

---

# University of Southampton Research Repository

Copyright © and Moral Rights for this thesis are retained by the author and/or other copyright owners. A copy can be downloaded for personal non-commercial research or study, without prior permission or charge. This thesis and the accompanying data cannot be reproduced or quoted extensively from without first obtaining permission in writing from the copyright holder/s. The content of the thesis and accompanying research data (where applicable) must not be changed in any way or sold commercially in any format or medium without the formal permission of the copyright holder/s.

When referring to this thesis and any accompanying data, full bibliographic details must be given e.g.

Thesis: AUTHOR (year of submission) “Full thesis title”, University of Southampton, name of the University Faculty or School or Department, PhD Thesis, pagination.

Data: Author (Year) Title. URI [dataset]



---

**UNIVERSITY OF SOUTHAMPTON**

FACULTY OF ENGINEERING AND PHYSICAL SCIENCES

INSTITUTE OF SOUND AND VIBRATION RESEARCH

**MODELLING OF RAIL CORRUGATION GROWTH IN  
CURVED TRACK**

by

**Jiawei Wang**

ORCID: 0009-0000-7844-6238

Thesis for the degree of Doctor of Philosophy

November 2023



---

# UNIVERSITY OF SOUTHAMPTON

## ABSTRACT

FACULTY OF ENGINEERING AND PHYSICAL SCIENCES

Institute of Sound and Vibration Research

Doctor of Philosophy

Modelling of rail corrugation growth in curved track

by Jiawei Wang

Railway corrugation is a frequent wavy wear pattern on the running surface of the rails. The corrugation generated on curved tracks is investigated through numerical modelling. A time-domain simulation model is developed that allows the growth of the corrugation to be simulated through models of the coupled vibration of the railway vehicle-track system and the wheel-rail rolling contact mechanics. The simulation tool that is developed consists of several models connected in a feedback loop to account for both the short-term dynamic vehicle-track interaction and the long-term damage. Steady-state curving conditions of the railway vehicle-track system are first obtained by means of a steady-state curving model. The vehicle-track interaction model comprises a finite element wheelset model, a frequency-domain semi-analytical track model with discrete supports and a non-Hertzian non-steady-state 3D wheel-rail contact model based on the variational theory by Kalker. The wheel-rail interaction forces are also obtained from the contact model. Wear calculations are performed using the contact parameters obtained from the wheel-rail contact model. Several case studies applying the current prediction model are also investigated. The frequency range of interest for the dynamic response is up to about 5000 Hz while for corrugation it is up to around 1000 Hz.

Multiple mechanisms can contribute to the formation and development of the rail corrugation, such as transient dynamic interaction and stick-slip self-excited vibration caused by falling friction or mode coupling. The relative contribution of each mechanism is investigated using the simulation model by comparisons of results from different cases and the dominant resonances of the system are identified. In addition, the effect of the coupling between the two rails and wheels as well as the effect of multiple wheel/rail

---

interactions are investigated. The coupling between the two rails and wheels is found to have little effect on the resultant roughness growth. The multiple wheel/rail interaction effect has a significant effect on the track responses. Wave reflections between the wheels generate fluctuations in the track responses at high frequency. However, from the time domain results, the presence of multiple wheels also has little effect on the roughness growth.

A series of case studies are carried out to investigate the influences of operational, track and vehicle parameters on the resultant wear and roughness growth on the low rail of curves. In this situation, the creep force at the wheel/rail contact is usually in the saturation region. Thus, in most cases, the self-excited vibration caused by falling friction is the main mechanism. The corresponding frequencies of the corrugation are related to wheelset modes which are associated with rutting corrugation or to the P2 resonance.

---

# Table of Contents

<b>Table of Contents</b> .....	<b>vii</b>
<b>Table of Tables</b> .....	<b>xi</b>
<b>Table of Figures</b> .....	<b>xiii</b>
<b>List of Symbols</b> .....	<b>xxi</b>
<b>Research Thesis: Declaration of Authorship</b> .....	<b>xxv</b>
<b>Acknowledgements</b> .....	<b>xxvii</b>
<b>1 Introduction</b> .....	<b>1</b>
1.1 Background .....	1
1.2 Rail corrugation.....	2
1.3 Review of rail corrugation prediction models .....	5
1.3.1 Wheel-rail contact .....	6
1.3.2 Transient dynamic interaction .....	7
1.3.3 Stick-slip self-excited vibration due to falling friction .....	11
1.3.4 Stick-slip self-excited vibration due to mode coupling.....	12
1.3.5 Alternative mechanism based on flexibility differences .....	13
1.4 Research on effects of critical aspects .....	14
1.4.1 Discussions in the literature .....	15
1.4.2 Summary of critical aspects .....	18
1.5 Research target and contributions .....	20
<b>2 Steady-state curving model</b> .....	<b>23</b>
2.1 Introduction .....	23
2.2 Review of railway vehicle dynamics .....	23
2.3 Steady-state curving model from Huang [69].....	25
2.3.1 Creepages .....	25
2.3.2 Rolling friction.....	26
2.3.3 Wheel-rail interaction.....	27
2.3.4 Vehicle dynamics .....	29
2.3.5 Curving behaviour.....	30
2.4 Modification of the steady-state curving model.....	33
2.4.1 Applied traction under constant friction.....	33
2.4.2 Applied traction under velocity-dependent friction .....	33
2.5 Steady-state curving results.....	35
2.6 Summary .....	40
<b>3 Track model</b> .....	<b>43</b>

3.1	Introduction.....	43
3.2	Review of track models .....	43
3.3	Frequency domain model .....	46
3.3.1	Rail model.....	47
3.3.2	Rail pad model.....	54
3.3.3	Flexible sleeper model.....	54
3.3.4	Receptance-coupling.....	57
3.3.5	Track decay rate .....	62
3.3.6	Transfer mobility under excitation on the other rail .....	63
3.3.7	Effect of the torsion and warping on the track response.....	66
3.4	Time-domain model.....	67
3.4.1	Continuously supported track .....	68
3.4.2	Discretely supported track .....	70
3.5	Summary.....	73
<b>4</b>	<b>Wheel/rail interaction model .....</b>	<b>75</b>
4.1	Introduction.....	75
4.2	Wheelset model.....	75
4.2.1	Finite element model .....	76
4.2.2	State-space model .....	79
4.3	Dynamic interaction model.....	81
4.3.1	Wheel/rail displacements.....	81
4.3.2	Contact forces .....	83
4.3.3	Contact filter .....	85
4.3.4	Validation by simple cases.....	86
4.3.5	Comparison of Hertzian spring and variational contact model ..	91
4.4	Summary.....	94
<b>5</b>	<b>Contact and wear model.....</b>	<b>97</b>
5.1	Introduction.....	97
5.2	Review of contact models.....	98
5.3	Stress distribution in the wheel-rail contact.....	99
5.3.1	Contact geometry .....	99
5.3.2	Stick and slip zones .....	101
5.3.3	Calculation of stress distribution .....	102
5.3.4	Results.....	106
5.4	Rolling contact.....	108
5.4.1	Transient stress distribution .....	108



---

5.4.2 Numerical example .....	110
5.4.3 Application of real contact surface profile .....	111
5.4.4 Calculation of slip and slip velocity in the contact patch.....	112
5.4.5 Normal interaction force in rolling with a rough rail .....	113
5.5 Wear model .....	116
5.5.1 Wear model based on frictional work .....	116
5.5.2 Wear model from Archard's work.....	118
5.5.3 Wear model by multiple mechanisms .....	119
5.6 Summary .....	120
<b>6 Numerical investigation of corrugation growth .....</b>	<b>122</b>
6.1 Introduction.....	122
6.2 Possible roughness growth mechanisms .....	123
6.2.1 Input roughness .....	123
6.2.2 Falling friction.....	124
6.2.3 Vertical-lateral coupling.....	126
6.3 Preliminary results .....	128
6.3.1 Identification of P2 resonance.....	128
6.3.2 Identification of pinned-pinned resonance.....	131
6.4 Identification of dominant mechanism.....	133
6.4.1 Basic case with only initial roughness input.....	133
6.4.2 Case considering both initial roughness and vertical-lateral coupling .....	136
6.4.3 Case considering both initial roughness and falling friction.....	137
6.4.4 Case considering all three mechanisms.....	140
6.5 Effect of coupling between two wheels and rails.....	143
6.6 Effect of multiple wheel/rail interactions.....	145
6.6.1 Relationship between the contact force and track dynamics ....	146
6.6.2 Track responses .....	146
6.6.3 Numerical example .....	149
6.6.4 Time-domain results.....	150
6.7 Summary .....	152
<b>7 Influence of different parameters on roughness growth.....</b>	<b>155</b>
7.1 Introduction.....	155
7.2 Influence of operational parameters.....	155
7.2.1 Curve radius .....	155

---

7.2.2 Vehicle speed .....	159
7.2.3 Friction coefficient.....	161
7.3 Influence of track parameters .....	165
7.3.1 Influence of rail pad stiffness .....	165
7.3.2 Comparison with slab track .....	167
7.3.3 Influence of cant deficiency and cant excess.....	169
7.4 Influence of vehicle parameters .....	170
7.4.1 Different wheelset designs.....	170
7.4.2 Axle load .....	172
7.4.3 Traction force.....	173
7.5 Summary.....	174
<b>8 Conclusions and Recommendations .....</b>	<b>177</b>
8.1 The updated and newly assembled time-domain prediction model.....	177
8.2 Corrugation growth mechanisms .....	178
8.3 Effect of relevant parameters on corrugation .....	179
8.4 Summing up.....	180
8.5 Recommendations for future work .....	180
<b>Appendices.....</b>	<b>183</b>
Appendix A. Flexible sleeper model [84].....	183
Appendix B. Fundamentals of beam theories [84] .....	189
B.1 Classical beam theory .....	190
B.2 Timoshenko beam theory .....	190
B.3 Warping and arbitrary excitation forces [79] .....	192
Appendix C. Initial broadband roughness .....	196
Appendix D. Effect of track curvature on rolling noise .....	198
<b>References.....</b>	<b>203</b>

---

## Table of Tables

Table 1.1 Types of rail corrugation and their characteristics according to Grassie [5]..	3
Table 1.2 Summary of mechanisms of corrugation assumed in the literature .....	6
Table 1.3 List of critical aspects that affect the rail corrugation investigated in the literature .....	15
Table 2.1 Bogie vehicle parameters provided by Wickens [70].....	36
Table 3.1 Rail section parameters for 60E1 rail (inertial properties relative to centroid) [84] .....	51
Table 3.2 Properties used for the rail pads [84] .....	51
Table 3.3 Monobloc sleeper properties [84] .....	55
Table 3.4 Parameters used for the predictions .....	60
Table 4.1 Steady-state curving parameters used .....	91
Table 5.1 Wear regimes and wear rate .....	119
Table 6.1 Roughness growth rate per 1000 passages in different frequency bands under different mechanisms .....	142
Table 6.2 Steady-state curving parameters for low and high rails .....	144
Table 7.1 Steady-state curving parameters for leading inner wheel under various curve radii .....	156
Table 7.2 Steady-state curving parameters under various vehicle speed .....	159
Table 7.3 Steady-state curving parameters under various values of extra cant height .....	170
Table 7.4 Steady-state curving parameters under various vehicle speed .....	173



---

## Table of Figures

Figure 1.1 Rail corrugation examples [4] .....	2
Figure 1.2 Different types of short-pitch rail corrugation on low rail of curves [7] .....	3
Figure 1.3 Structure of simulation tool .....	20
Figure 2.1 Rolling contact of two elastic bodies [75] .....	25
Figure 2.2 Body on the ground [44] .....	26
Figure 2.3 Slip and adhesion area in wheel-rail contact [44] .....	27
Figure 2.4 Creep force with micro-slip and saturation [44] .....	27
Figure 2.5 Lateral offset of a wheelset on a canted track [69] .....	28
Figure 2.6 Definition of the reference points and coordinate systems of main components of an idealised bogie vehicle, under the condition in which the primary suspension springs are relaxed and the secondary suspension springs are in their initial positions [69] .....	30
Figure 2.7 Rear view of the bogie vehicle [69] .....	30
Figure 2.8 A free wheelset passing the curve [44] .....	31
Figure 2.9 Outer wheel rolling radius when running in a curve [44] .....	31
Figure 2.10 Creep coefficients .....	34
Figure 2.11 Convergence to steady-state curving behaviour of the leading and trailing wheelsets of a bogie .....	37
Figure 2.12 Convergence to steady-state creepages at wheel-rail contacts of a bogie vehicle .....	38
Figure 2.13 Convergence to steady-state normal loads of the wheels of a bogie vehicle .....	39
Figure 2.14 Convergence to steady-state creepages of the wheels of a bogie vehicle at wheel-rail contacts with applied traction .....	39
Figure 2.15 Convergence to steady-state longitudinal creep force of the wheels of a bogie vehicle with applied traction .....	40
Figure 3.1 The coordinate system, shear centre S and centroid C of the rail cross-section .....	46
Figure 3.2 (a) Side view of track model, where $L_s$ is the sleeper spacing; $F_i$ is the force transmitted at the $i$ th discrete support; (b) front view of track model, showing two rails connected to the sleeper .....	47
Figure 3.3 Point mobilities for 60E1 rail: (a) Vertical mobility; (b) Lateral mobility .....	52
Figure 3.4 Axial point mobility for track .....	53
Figure 3.5 Vertical-lateral cross mobility for track excited in vertical direction .....	53

Figure 3.6 G44 sleeper design [84].....	55
Figure 3.7 Point mobility of concrete monobloc sleeper for vertical excitation at the centreline of the sleeper upper surface .....	56
Figure 3.8 Predicted vertical point mobility at the rail seat of the sleeper in ballast... 57	
Figure 3.9 Source and receiver structures coupled at multiple connection points through massless resilient elements [85] .....	57
Figure 3.10 Vertical point mobility of the track. (a) Predicted; (b) measured.....	61
Figure 3.11 Lateral point mobility of the track. (a) Predicted; (b) measured .....	62
Figure 3.12 Predicted mobility of the track excited at different positions. (a) Axial mobility; (b) vertical-lateral cross mobility .....	62
Figure 3.13 Track decay rate compared with measured results from [84]. (a) Vertical direction; (b) lateral direction .....	63
Figure 3.14 Comparison of the predicted transfer mobility between two rails with the measurement and with the predicted point mobility, all results for excitation above a sleeper. (a) Vertical direction; (b) lateral direction. ....	66
Figure 3.15 Lateral results with or without torsion and warping. (a) Lateral point mobility above a sleeper, (b) lateral track decay rate .....	66
Figure 3.16 Non-moving vertical Green's functions for different distances between the excitation and response points .....	68
Figure 3.17 Vertical receptances for different distances between the excitation and response points.....	69
Figure 3.18 Moving Green's functions of the continuous track system in the vertical direction for different moving speeds .....	69
Figure 3.19 Magnitude of the track point and transfer vertical receptances for excitation: (a) above a sleeper position; (b) at mid-span between two sleeper positions....	70
Figure 3.20 The vertical non-moving Green's functions of the discretely supported track system for different excitation points (response point coincides with the excitation point).....	71
Figure 3.21 The vertical non-moving Green's functions of the discretely supported track, (a) response point is fixed above the sleeper; (b) response point is fixed at the mid- span between sleepers.....	71
Figure 3.22 The vertical moving Green's functions of the track with different excitation points and moving velocity 20 m/s .....	72
Figure 3.23 The vertical moving Green's functions of the track with different moving velocity and the same excitation point which is above the sleeper: (a) excited above the sleeper; (b) excited at the mid-span between sleepers.....	73

Figure 3.24 The vertical moving Green's functions of the track for excitation above the sleeper under different moving speeds plotted against distance .....	73
Figure 4.1 Half of the rotating cross-section of the wheelset in ANSYS .....	77
Figure 4.2 Mode shapes of some identified modes.....	77
Figure 4.3 Radial, axial and cross mobilities of wheelset: (a) radial mobilities; (b) axial mobilities; (c) cross mobilities .....	79
Figure 4.4 Impulse response of the wheelset in the radial direction.....	81
Figure 4.5 Moving reference frame containing the wheel-rail interactions.....	82
Figure 4.6 Impulse response of the mass-spring system.....	87
Figure 4.7 Roughness in the time domain used in simple cases of this section.....	88
Figure 4.8 Predicted interaction contact force, WSS-RGF: combination of the Green's function with the state-space method; Green's Function: the full Green's function method .....	88
Figure 4.9 Impulse response of the two degree-of-freedom mass-spring system representing the track .....	90
Figure 4.10 Interaction contact force predicted in the combination of the Green's function with the state-space method and the full state-space method .....	90
Figure 4.11 Interaction force in time domain for the contact between SDOF system and the continuously supported track.....	92
Figure 4.12 Interaction force spectrum for the contact between SDOF system and the continuously supported track .....	93
Figure 4.13 Contact filter effect derived from current results compared with DPRS results .....	93
Figure 4.14 Normal interaction force in time domain for the contact between SDOF system and the discretely supported track.....	94
Figure 4.15 Normal interaction force spectrum for the contact between SDOF system and the discretely supported track.....	94
Figure 5.1 Geometry of wheel and rail in the contact.....	100
Figure 5.2 Contact area under a longitudinal creepage calculated by FASTSIM [13] .....	101
Figure 5.3 Geometry of the potential contact area in the x-y plane.....	103
Figure 5.4 Normal stress distribution results in three-dimensional form.....	106
Figure 5.5 Normal stress distribution results on the centreline in the potential contact area .....	107
Figure 5.6 Tangential stress distribution results on the centreline in the potential contact area, $Q=0.25\mu P$ , $\mu=0.3$ .....	107

Figure 5.7 Tangential stress distribution results on the centreline in the potential contact area for different element size, $Q=0.25\mu P$ , $\mu=0.3$ .....	108
Figure 5.8 Shift in potential contact area in each time-step [107].....	109
Figure 5.9 Transient tangential stress distribution under constant normal, longitudinal and lateral force from static to steady-state conditions, --- limiting stress $\mu p$ , — tangential stress distribution at centreline of the potential contact area .....	110
Figure 5.10 Transient tangential stress distribution under constant longitudinal creepage from static to steady-state, --- limiting stress $\mu p$ , — tangential stress distribution at centreline of the contact area .....	111
Figure 5.11 Practical wheel and rail smooth contact surface profiles in MATLAB: (a) cross-section; (b) 3D view .....	112
Figure 5.12 Normal stress distribution obtained from variational methods in three-dimensional form for practical wheel and rail profiles. Units in figures are all millimetre. ....	112
Figure 5.13 Slip and stress distribution in steady-state rolling with $Q=0.25\mu P$ and 1 mm element size. Upper: slip velocity; Lower: tangential stress distribution, where --- is the friction limit. ....	113
Figure 5.14 Normal stress distribution of the potential contact area in three-dimensional form: (a) calculated by penetration; (b) calculated by normal load .....	114
Figure 5.15 Normal stress distribution of the potential contact area centre line in two-dimensional form .....	115
Figure 5.16 Wear rate for different values of the wear index [134]: $K_1$ ‘mild wear’; $K_2$ ‘severe wear’; $K_3$ ‘catastrophic wear’. ....	119
Figure 5.17 Wear depth variation with creepage value for different wear models ....	120
Figure 6.1 Velocity-dependent friction curve .....	124
Figure 6.2 Ratio of creep force to normal load varying with the creepage .....	125
Figure 6.3 Iteration loop for inclusion of velocity-dependent friction coefficient ....	126
Figure 6.4 Two-degree-of-freedom system on moving belt [138].....	126
Figure 6.5 Real part (growth rate) and imaginary part (frequency) of eigenvalues plotted against the friction coefficient [44].....	127
Figure 6.6 Time histories with (a) $\mu = 0.7$ and (b) $\mu = 0.8$ ; blue solid line: lateral direction; red dashed line: vertical direction [44].....	128
Figure 6.7 Vertical receptances of the wheelset, ballasted track and contact spring .	129
Figure 6.8 Roughness development in one third octave bands of the basic case applying rigid wheelset: (a) passage step size investigation; (b) wheel and rail vibration spectra .....	130



---

Figure 6.9 Roughness level development in one third octave bands of: (a) the discretely supported track with nominal sleeper spacing; (b) the continuously supported track.....	132
Figure 6.10 Roughness development in one third octave bands of the basic case applying 0.75 m sleeper spacing .....	132
Figure 6.11 The wheel/rail contact force due to initial surface roughness: (a) Time history; (b) Frequency spectra in one third octave bands .....	134
Figure 6.12 Displacement spectra in one third octave bands due to initial surface roughness of (a) wheel; (b) rail .....	134
Figure 6.13 Wheel/rail surface roughness development after different passages with initial surface roughness in one third octave bands .....	135
Figure 6.14 Frequency spectra of the wheel/rail contact force with initial surface roughness and vertical-lateral coupling compared with only initial roughness in one third octave bands .....	136
Figure 6.15 Displacement spectra in one third octave bands of (a) wheel; (b) rail for the case with initial surface roughness and vertical-lateral coupling.....	137
Figure 6.16 Wheel/rail surface roughness development after different passages with initial surface roughness and vertical-lateral coupling in one third octave bands .....	137
Figure 6.17 Velocity-dependent friction coefficient with maximum value 0.3 plotted against creepage .....	138
Figure 6.18 Frequency spectra of the wheel and rail contact force with initial surface roughness and falling friction in one third octave bands .....	139
Figure 6.19 Displacement spectra in one third octave bands of (a) wheel; (b) rail for the case with initial surface roughness and falling friction.....	139
Figure 6.20 Wheel/rail surface roughness development after different passages with initial surface roughness and falling friction in one third octave bands .....	140
Figure 6.21 Frequency spectra of the wheel and rail contact forces considering all three mechanisms in one third octave bands.....	140
Figure 6.22 Displacement spectra in one third octave bands of (a) wheel; (b) rail for this case .....	141
Figure 6.23 Wheel/rail surface roughness development after different passages considering all three mechanisms in one third octave bands .....	142
Figure 6.24 Wheel/rail surface roughness growth rate of first 10,000 passages with all three mechanisms and different wheelset modes removed in one third octave bands.....	143
Figure 6.25 Wheel/rail surface roughness development on the low rail applying all three mechanisms including the coupling between high and low rails in one third octave	

bands .....	144
Figure 6.26 Wheel/rail surface roughness development on the high rail applying all three mechanisms including the coupling between high and low rails in one third octave bands .....	145
Figure 6.27 A track with four wheels on the rail [75].....	146
Figure 6.28 Amplitude of point and transfer mobility and passive interaction force at different wheel positions. Soft pads are used. A unit excitation force acts at the wheel 1 position and the excitation is above one of the sleepers. ....	150
Figure 6.29 Roughness level spectra applying all three mechanisms considering multiple wheel-rail interactions in one third octave bands: (a) First wheel-rail interaction; (b) Second wheel-rail interaction.....	151
Figure 6.30 Roughness growth rates of first 10k passages applying all three mechanisms considering multiple wheel-rail interactions in one third octave bands: (a) First wheel-rail interaction; (b) Second wheel-rail interaction.....	152
Figure 7.1 Effects of curve radius on steady parameters when curving .....	156
Figure 7.2 Roughness level spectra variation with number of the passages applying all three mechanisms on curved track with radius: (a) 200 m; (b) 300 m; (c) 500 m; (d) 800 m .....	157
Figure 7.3 Roughness growth rates of first 10k passages under different track curve radii applying (a) only initial roughness; (b) initial roughness and vertical-lateral cross terms; (c) initial roughness and falling friction; (d) initial roughness, vertical-lateral cross terms and falling friction .....	158
Figure 7.4 Traction coefficient against creepage .....	159
Figure 7.5 Roughness level spectra variation with the number of passages applying all three mechanisms for train speed of: (a) 15 m/s; (b) 20 m/s; (c) 30 m/s .....	160
Figure 7.6 Roughness growth rates of the first 10,000 passages under different mechanisms under (a) 20 m/s; (b) 30 m/s; (c) 40 m/s .....	161
Figure 7.7 Roughness level spectra variation with number of the passages applying all three mechanisms and velocity-dependent friction coefficient whose actual value of (a) 0.2; (b) 0.3; (c) 0.5; (d) 0.8 .....	162
Figure 7.8 Roughness growth rates of the first 10,000 passages under different mechanisms and constant friction coefficient of 0.5 .....	163
Figure 7.9 Wheel and rail vertical displacement spectra for case of friction coefficient of 0.5 due to: (a) initial surface roughness and vertical-lateral cross terms; (b) initial surface roughness and falling friction.....	163
Figure 7.10 Roughness growth rates of the first 10,000 passages under all three	

mechanisms and different constant friction coefficient .....	164
Figure 7.11 Traction coefficient against creepage with different friction coefficient	164
Figure 7.12 Point mobilities of tracks with different values of vertical pad stiffness: (a) vertical; (b) lateral.....	165
Figure 7.13 Roughness level development of the first 10,000 passages for different pad stiffnesses: (a) 60 MN/m; (b) 120 MN/m; (c) 300 MN/m; (d) 800 MN/m.....	166
Figure 7.14 Roughness growth rates of the first 10,000 passages for different pad stiffnesses with initial roughness, cross terms and falling friction .....	167
Figure 7.15 Vertical mobility of slab track and ballasted track with rail pad stiffness 60 MN/m.....	168
Figure 7.16 Roughness of the first 10,000 passages under all three mechanisms of a slab track with 60 MN/m pad stiffness: (a) Roughness level of concrete track; (b) Roughness level of slab track; (c) Roughness growth rate comparison between ballasted track and slab track.....	168
Figure 7.17 Roughness growth rates of the first 10,000 passages under all three mechanisms with various values of cant.....	170
Figure 7.18 Mobilities of wheelset whose wheel (a) with straight web; (b) with curved web .....	171
Figure 7.19 Roughness variation with the passage number with all three mechanisms of ballasted track in contact with wheel with curved web: (a) Roughness level spectra; (b) Comparison of roughness growth rate with results for wheel with straight web.....	171
Figure 7.20 Roughness growth rates of first 10,000 passages under different wheel loads with all three mechanisms .....	172
Figure 7.21 Tangential/Normal force ratio variation with creepage .....	173
Figure 7.22 Roughness growth rates of first 10,000 passages under different tractions with all three mechanisms.....	174
Figure A.0.1 Lateral/torsional waves on a sleeper excited by a point force at $x_0$ [69] .....	183
Figure B.0.2 Forces and moments on an infinitesimal element.....	189
Figure B.0.3 Bending of beam with shear.....	191
Figure B.0.4 Excitation forces applied with offsets from the centroid .....	194
Figure C.0.5 Broadband roughness spectrum of the initial roughness generated.....	197
Figure D.0.6 Interaction force spectra comparison of different track types: (a) Curved track with radius 300 m and tangent track; (b) Curved track with radius 300 m with and without coupling between two wheels/rails .....	199
Figure D.0.7 Total sound pressure level comparison: (a) between curved track and	

---

tangent track; (b) among curved tracks with different radii .....	200
Figure D.0.8 A-weighted SPL of each component plotted against curve radius .....	201
Figure D.0.9 Sound pressure level of each part of: (a) tangent track; (b) curved track with 300 m radius .....	201

---

## List of Symbols

$A$	Cross-section area
$A_s$	ratio of the limit friction coefficient at infinity slip velocity to the maximum friction coefficient $\mu_s$
<b>A</b>	System matrix for state-space solution
$a$	semi-axis of the contact ellipse in the longitudinal direction
$B_s$	coefficient of exponential friction decrease, s/m
<b>B</b>	System matrix for state-space solution
$b$	semi-axis of the contact ellipse in the lateral direction
$C_H$	Hertzian constant
$C_{ij}$	normal ‘influence coefficient’ matrices
<b>C</b>	Global damping matrix for track
<b>C<sub>w</sub></b>	Global damping matrix for vehicle/wheels
$c_{11}, c_{22}, c_{23}$	Kalker’s coefficients
$D_{ij}$	tangential ‘influence coefficient’ matrices
$E$	Young’s modulus
$E^*$	Combined Young’s modulus in contact
$e_y, e_z$	lateral and vertical offset between shear centre and centroid
$F_e$	external force
$F_s$	static friction force
$F_N$	normal force
$F_x, F_y, F_z$	forces of respective axis
$f_w$	warping displacement measure
$G$	shear modulus
$G_g$	gravity force of the body
$h$	undeformed distance between the bodies
$I_y, I_z$	second moment of area about the respective axis
$I_{yz}$	product moment of area
$I_p$	polar moment of area
$I_w$	warping constant
$I_{wy}, I_{wz}$	warping product moments of area
$J$	torsional constant
$J_t$	secondary torsional constant
$k$	variable reduction factor
$k_{re}$	variable stiffness reduction factor

---

$k_0$	initial value of Kalker's reduction factor at creep values close to zero
$k_x, k_y, k_z$	translational stiffness per unit length along the respective axis
$k_{rx}, k_{ry}, k_{rz}$	corresponding rotational stiffnesses
$L_s$	sleeper spacing
$L_p$	Rail pad length along rail
$l$	half of the lateral distance between the contact points of the two wheels
$M_x, M_y, M_z$	moment of respective axis
$M_x^p$	Saint-Venant torsional moment due to the uniform torsion
$M_x^E$	non-uniform torsion moment due to warping
<b>M</b>	Global mass matrix for track
<b>M<sub>w</sub></b>	Global mass matrix for vehicle/wheels
$N_x$	element number of potential contact area in the $x$ direction
$N_y$	element number of potential contact area in the $y$ direction
$O$	Origin of axes
$P$	normal force
$p$	normal pressure
$Q$	tangential force
$\dot{q}$	modal velocity
$q_i$	modal displacement
$q$	tangential stress
$R$	curve radius
$R_{out}$	wheel radii of outer wheels
$R_{in}$	wheel radii of inner wheels
$r_0$	nominal wheel radius
$S$	the contact area
$s$	relative tangential displacement between two initially coincident points in the contacting structures
$\dot{s}$	magnitude of the slip velocity vector
$U_E$	Elastic strain energy
$U_E^*$	Internal complementary energy
$u_x, u_y, u_z$	displacements of respective axis
$u'_{it}$	prior displacement difference between the surfaces due to elastic deformation
$V^*$	Total complementary energy of contact system
$V_0$	vehicle speed
$v$	total creepage
$v_w, v_r$	linear velocities of wheel and rail surface

---

$W_{it}$	rigid tangential shift
$x, y, z$	longitudinal, lateral and vertical directions
$y_e, z_e$	lateral and vertical offset between the excitation point and the centroid
$y_r, z_r$	lateral and vertical offset between the response point and the centroid
$\Delta t$	time increment
$\Delta x$	distance increment
$\Delta y$	lateral offset of the wheelset
$\Delta v$	sliding velocity
$\gamma$	creep ratio
$\gamma_x$	longitudinal creepage
$\gamma_y$	lateral creepage
$\gamma_\phi$	relative spin, rad/m
$\gamma_{xy}$	angle between the normal to the plane and the tangent to the beam centerline
$\mu$	coefficient of friction
$\mu_s$	static friction coefficient
$\mu_m$	maximum coefficient of friction
$\phi_0$	cant angle
$\phi$	roll angle about the $x$ -axis
$\theta_y$	angle between the $x$ -axis and the normal to the plane
$\psi$	yaw angle
$\rho$	density
$\delta$	approach of distant points in the two bodies
$\delta_0$	conicity of the wheel
$\alpha$	receptance
$\alpha_{inf}$	fraction of the initial value of Kalker's reduction factor at creep values approaching infinity
$\beta_{re}$	non-dimensional parameter related to the decrease of the contact stiffness with the increase of the slip area size
$\epsilon_{re}$	parameter describing the gradient of the tangential stress in the stress distribution transformed to a hemisphere which also represents the ratio of the slip area to the area of adhesion
$\epsilon_{yy}, \epsilon_{zz}, \gamma_{yz}$	strains
$\zeta$	damping ratio
$\eta$	damping loss factor
$\xi$	complex wavenumber
$\omega$	circular frequency

---

$\kappa_y, \kappa_z$	shear coefficient accounts for the effective shear area in the $y$ and $z$ direction
$\kappa_s$	correction factor for the effective shear area undergoing torsion
$\varnothing$	mode shape
$\varnothing_s^p$	primary warping functions
$\varnothing_s^s$	secondary warping functions
$\nu$	Poisson's ratio



---

# Research Thesis: Declaration of Authorship

Print name: Jiawei Wang

Title of thesis: Modelling of rail corrugation growth in curved track

I declare that this thesis and the work presented in it are my own and have been generated by me as the result of my own original research.

I confirm that:

1. This work was done wholly or mainly while in candidature for a research degree at this University;
2. No part of this thesis has previously been submitted for a degree or any other qualification at this University or any other institution;
3. Where I have consulted the published work of others, this is always clearly attributed;
4. Where I have quoted from the work of others, the source is always given. With the exception of such quotations, this thesis is entirely my own work;
5. I have acknowledged all main sources of help;
6. Where the thesis is based on work done by myself jointly with others, I have made clear exactly what was done by others and what I have contributed myself;
7. Some of this work has been published before submission:
  - (1) Rolling noise on curved track: an efficient time domain model including coupling between the wheels and rails. IWRN14, Shanghai, December 2022.
  - (2) A semi-analytical model of a discretely supported railway track. Accepted by Journal of Rail and Rapid Transit, 2023.

Signature: .....Date:.....



---

## Acknowledgements

It has been a long journey for me to study in ISVR and finally finish this thesis. I really enjoyed this special journey in my life and also very appreciate the help and support obtained from people I met. The PhD project has received funding from CAF (Construccionesy Auxiliar de Ferrocarriles) for which I am very grateful. I would like to thank Professor Luis Baeza for his kind assistance.

First of all, I would like to give many thanks to my first supervisor, Prof. David Thompson. He is always a very kind and nice person from the first day I knew him. During the last four years, I learned a lot of things from him, both in academic area and in life. The enthusiasm for the research, hard-working, rigorous attitude and the patience, are the most outstanding character and moral of him that I admired. He is not only my academic supervisor, but also my life model. The days we spent together will be a precious memory for me and the things I learned from him will inspire me to be a good man in both academic area and life. It's a great honour to be one of his students.

I would also like to thank my second supervisor, Dr. Giacomo Squicciarini for the help and supervision in these years. Especially when I have problems with programming, he is always there to help and explain everything in detail with lots of patience. When conducting the measurements, I also learned many skills from setting up to carrying out measurement. He is always enthusiastic, hardworking, and full of energy and humour, which always inspire me to move on.

On a more personal note, I would like to express my appreciation towards all friends and colleagues from the Dynamics Group and the University of Southampton, who made every day special and unique. The same PhD journey we had together are valuable memories to me. My roommates also gave great support to me that made my days colourful. I hope all of them can graduate smoothly and have a bright future.

Lastly and most importantly, I deeply appreciate the support from my family. The endless love from them is crucial power for me to finish this journey.



---

# 1 Introduction

## 1.1 Background

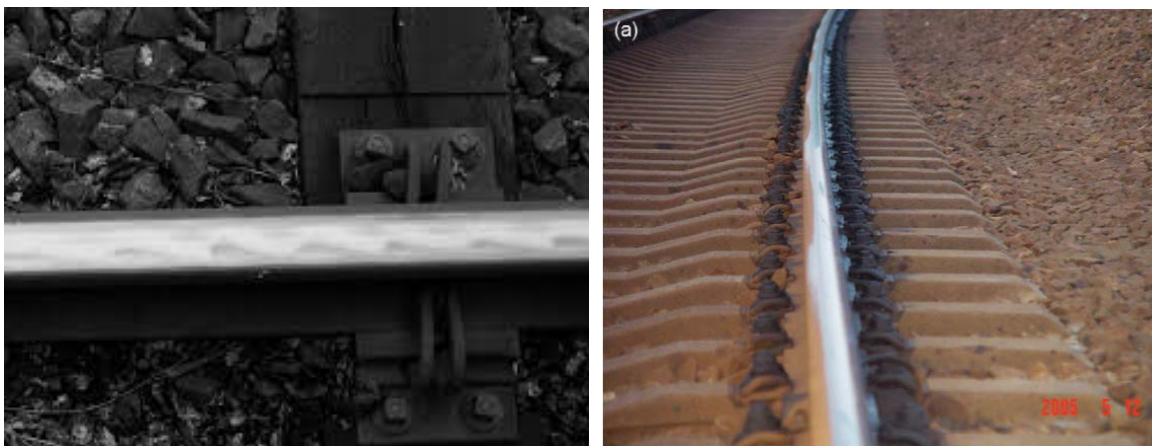
Since the introduction of steam locomotives in the 1820s, railways have always been an important form of transportation. In recent decades, high-speed trains and metros have developed rapidly and become more and more popular and widespread. Gradually, the level of development of high-speed trains and metros becomes a criterion to measure the social and economic growth level of a city, region or country. Due to the high capacity and high efficiency of railways, the population becomes increasingly mobile. There are higher demands for travel and tourism as well as fast logistics for diverse products. For example, the freight transport volume and average number of kilometres travelled by people increase year by year. In addition, railways are also an environmentally friendly form of transportation compared to road vehicles and air traffic. Under the need to reduce carbon emissions in recent years, railways are more desirable as a priority choice.

Nevertheless, the railway has negative impacts on the environment, which mostly concern noise and vibration. Furthermore, concerning the physiological response of humans, vibration and noise can have significant effects for people living near railway and metro lines as well as for passengers and staff. High noise levels are not only harmful to mental health, but also interfere with the performance of daily activities and sleep at night. Thus, great attention should be paid to the noise levels when developing railways and metros in densely populated areas.

There are various sources of railway noise and two main mechanisms can be identified [1]. One is the aerodynamic fluctuations due to air turbulence. This kind of noise only dominates the noise of high-speed trains with an operational speed of 300 km/h or above. The other is the rolling noise generated by the vibration of wheel and rail. This is the main noise source for most trains that run below 300 km/h. This vibration is induced by the vertical relative displacements between wheel and rail because of the roughness on their surfaces. A particularly severe form of roughness is known as corrugation (examples are shown in Figure 1.1).

Relative vertical motion at the contact due to rail and wheel roughness results in dynamic interaction forces and thus, vibration and noise of the wheel and track. High roughness levels lead to high vibration and noise levels. Thompson [2] presented experimental

evidence from a number of sources to confirm the linear relation between roughness and noise. The assumption made in theoretical models that the wheel and rail roughness spectra may be added to give the total excitation was therefore also confirmed. Grassie [3] found a satisfactory correlation between ground-borne noise levels and railhead roughness in the 100-1000 mm wavelength range. From measurements carried out on different types of railway system, the largest irregularities were found on the low rail of metro curves (i.e. on the inside of the curve) while lower levels were found on the high rails or on high-speed lines.



(a) on tangent track

(b) on curved track

Figure 1.1 Rail corrugation examples [4]

The maintenance of railways includes re-profiling the wheels and grinding the rails [5]. But the process of rail grinding to reduce roughness is time-consuming and expensive and corrugation can re-appear. Thus, it is important to understand the mechanisms of rail roughness development in order to optimize the methods to minimise rail roughness growth as well as the costs of noise and vibration control and maintenance.

## 1.2 Rail corrugation

Rail corrugation is an important type of surface roughness, which refers to the undesirable periodic wave-shaped irregularities on the contact surface of the rails. A series of dynamic, vibration, and noise problems are caused by rail corrugation. Rail corrugation is typically caused by uneven wear [5], due to the variations of wheel-rail contact stresses. The wavelength and severity of corrugation are dependent on the track structure, track geometry, traction system, rail vehicle behaviour, and wheel-rail interaction. Often such irregularities can be observed on the low rail (inner rail of a curve) of small-radius curves (further examples are shown in Figure 1.2). Rail corrugation is difficult to study because of the variety of initiation and evolution mechanisms, and also the variety of operational

situations. Different types of track generate corrugation with different wavelengths and amplitudes according to different wavelength fixing mechanisms and damage mechanisms [5] as shown in Table 1.1.

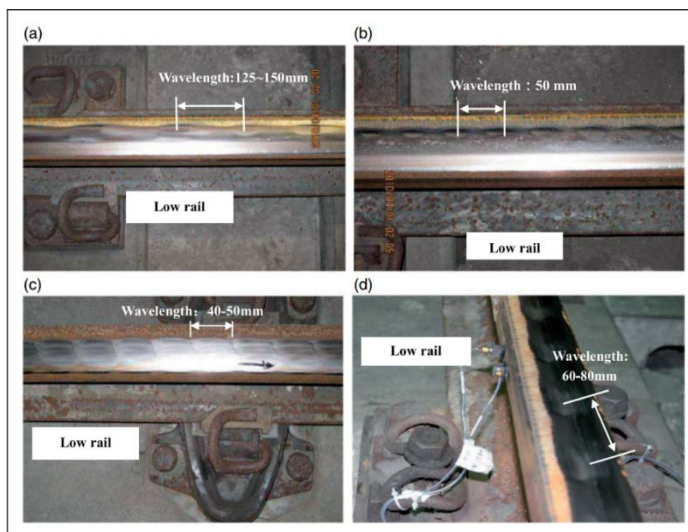


Figure 1.2 Different types of short-pitch rail corrugation on low rail of curves [7]

Table 1.1 Types of rail corrugation and their characteristics according to Grassie [5]

Type	Wavelength-fixing mechanism	Where	Typical frequency (Hz)	Damage mechanism
Pinned-pinned resonance ('roaring rails')	Pinned-pinned resonance	Straight track, high rail of curves	400-1200	Wear
Rutting	Second torsional resonance of axles	Low rail of curves	250-400	Wear
Other P2 resonance	P2 resonance	Straight track or high rail in curves	50-100	Wear
Heavy haul	P2 resonance	Straight track or curves	50-100	Plastic flow in troughs
Light rail	P2 resonance	Straight track or curves	50-100	Plastic bending
Trackform-specific	Trackform-specific	Straight track or curves	-	Wear

Although it is a problem that has been known since the beginning of the railways, the mechanisms that cause corrugation are still not fully understood, so there are no decisive measures to control its growth. Understanding of the initiation and development mechanisms of rail corrugation is essential for the long-term noise control and railway maintenance. Through investigating the factors that affect rail corrugation, it will be possible to find appropriate strategies to control rail corrugation growth and, thus, result in a reduction in the generated noise and vibration.

---

Among the many known rail corrugation forms, the most common ones are those associated with the pinned-pinned resonance (also known as roaring rails), P2 resonance, and rutting (Table 1.1) [5]. The pinned-pinned resonance corrugation is associated with a resonance of the vertical vibration of the rails as if they were pinned at the sleepers and occurs at frequencies around 1000 Hz depending on the sleeper spacing. P2 resonance corrugation is associated with the vibration of the unsprung mass of the vehicle (i.e. the wheelset and axleboxes) on the track stiffness and occurs at frequencies between 50 and 100 Hz. These two corrugation types are commonly found in straight lines or on the high rail in curves. More recently, Grassie has suggested that rutting corrugation is more likely associated with a bending mode of the leading wheelsets of a bogie around 80-110 Hz [6]. Rutting corrugation is typically found on sharp curves, although it can also be found in straight lines when the traction or braking forces are sufficiently high. It appears most commonly on the low rail of curves. The damage mechanism for rutting, pinned-pinned resonance corrugation and P2 resonance corrugation is most commonly identified as wear.

The mechanisms of rail corrugation have been investigated using field observations and measurements, theoretical and numerical modelling, and laboratory experiments [5]. Based on the test results and field observations, the opinion is widely accepted that the transient dynamic interaction of the wheel-rail system induced by the original roughness of the rail and wheel surfaces leads to the formation of corrugation. It is thereby assumed that variations in the frictional work, due to lateral or longitudinal relative motion, and caused by the transient dynamic interaction, lead to the appearance of corrugation. Some corrugation phenomena can be reasonably well explained based on these existing generation mechanisms, but there are still situations that cannot be explained satisfactorily.

Recently, many researchers have supported the hypothesis that the corrugation on curves is probably caused by a stick-slip process of the wheel on the rail [4,7]. When the creepage (ratio of relative velocity to the vehicle speed) at the wheel-rail contact patch is large enough to overcome the friction limit at the wheel-rail interface, the wheel will slide on the rail. If the kinetic friction coefficient is lower than the static friction coefficient, this would result in a reduction of the friction force. The reduction of the wheel-rail friction force during wheel sliding sometimes triggers a resonant response, reducing forces and making the wheel stick to the rail again. The stick-slip process would generate rail corrugation on the running surfaces of rails. Oscillation of the wheel load caused by wheel-rail irregularities and rail rolling vibration can also cause stick-slip oscillation and periodic wear.



---

A negative slope of the traction-creep curve for saturated creep forces brings about friction-induced oscillation of the wheel-rail system. Additionally, the wheel/rail coupling can also cause stick-slip oscillation. The oscillation of the rail is coupled with that of the wheels in the action of the saturated creep forces. When the wheel/rail coupling is strong, self-excited oscillation of the wheel-rail system occurs which causes variation of the contact forces between the wheels and rails. Vertical/lateral coupling of the wheel and rail may also give contributions to this self-excited oscillation. Then the frictional work also varies and if it is in phase with the existing roughness, corrugation will develop. Mode coupling is also a form of instability that has become a focus of attention in curve squeal research and may also play a role in corrugation.

In order to explain some corrugation phenomena, such as the short-pitch corrugation that generally occurs on the low rail of tightly curved tracks and the fact that a reduced friction coefficient can eliminate rail corrugation, the mechanism of self-excited vibration of the wheelset-track system induced by the saturated creep force has been presented by a group of researchers [8-9].

A possible alternative mechanism to describe the cause of short-pitch corrugation is the wheel-rail dynamic flexibility difference, demonstrated in [10-12]. This mechanism means the excitation in the wheel/rail contact is due to the variation of the wheel and rail stiffness over a sleeper span. In some other contexts, this is also called ‘parametric excitation’. This possible mechanism still needs further investigation and validation. Categorised by the mechanisms described above, models of rail corrugation initiation and development are reviewed in the next section.

### **1.3 Review of rail corrugation prediction models**

As the transient dynamic interaction and the slip-stick vibration are widely accepted among several wavelength-fixing mechanisms of short-pitch rail corrugation, the discussion of rail corrugation initiation and growth is divided into these two categories. Since the slip-stick vibration can be generated by falling friction and wheel-rail dynamic mode coupling, models in this part are further divided into two categories. Finally, research on a possible mechanism associated with wheel-rail dynamic flexibility difference is also shown. An overview table is shown in Table 1.2.

Table 1.2 Summary of mechanisms of corrugation assumed in the literature

Mechanism	Description	Corrugation type applied	Typical frequency (Hz)	Review in
Transient dynamic interaction	The original roughness of the rail surface causes transient dynamic interaction and then induces variation of frictional work	Roaring rails, rutting or 'other P2 resonance' corrugation	50-1200	Section 1.3.2
Falling friction stick-slip vibration	Large creepage causes wheel sliding and friction force reduction, which lead to stick-slip oscillation	Roaring rails or rutting	250-1200	Section 1.3.3
Mode coupling stick-slip vibration	Saturated creep force causes coupling between the oscillations of rail and wheels. Strong coupling causes self-excited oscillation and then leads to variation of contact forces	Roaring rails or rutting	250-1200	Section 1.3.4
Wheel-rail dynamic flexibility difference	Dynamic flexibility difference of different positions of action points lead to the change and cyclical fluctuation of wheel-rail contact force	Roaring rails	400-1200	Section 1.3.5

### 1.3.1 Wheel-rail contact

An important aspect of the modelling of rail corrugation initiation and growth is the representation of the wheel-rail contact. One of the most widely used models for tangential wheel-rail contact problems is called FASTSIM [13]. It was developed by Kalker for calculating the total force in rolling contact from a given creepage and spin. The model divides the contact area into strips, treating each strip as a two-dimensional problem. The method neglects the interaction between the strips and works best if the contact patch width is much greater than the length in the rolling direction. The surface displacement at a point is determined only by the surface traction at the same point in this model, whereas in reality the displacement at a point depends on the traction at all points on the surface. The main advantage of FASTSIM is its calculation speed and accuracy for cases where the

---

normal problem can be described by the Hertzian model. However, it is less accurate when the Hertzian assumptions do not apply. The Hertzian assumptions include: the contact surface profiles must be parabolic and any higher terms are neglected; surfaces must be smooth, non-conforming and frictionless; elastic half-space theory must be valid, that is the contact dimensions must be small compared with radii of curvature of the undeformed surfaces; the contact stress must not depend on the shape of the bodies away from the contact patch.

Kalker also developed an exact method for all contact problems of bodies that can be described by half-spaces, as described in [14]. The computer program implementing the method is called CONTACT. CONTACT works by a variational method, minimising a strain energy function subject to the constraint that the contact pressure is positive everywhere and approaches zero at the edges of the contact. It can be used for both Hertzian or non-Hertzian contact problems, and takes account of transient effects by calculating step by step from given initial conditions, following the loading history of the particular problem. The main limitation of CONTACT is the computation time. An extremely fine discretisation of the potential contact area is required to deal with micro-roughness of the surface. Also, CONTACT is limited to elastic problems and does not include plastic deformation of any asperities.

### **1.3.2 Transient dynamic interaction**

Many scholars have carried out numerous investigations into the modelling of rail corrugation initiation and growth based on the mechanism of transient dynamic interaction. Grassie and Johnson [15] proposed approximate methods for calculating wear which results in roaring rails above 200 Hz, in terms of frictional dissipation as a wheel rolls over a sinusoidal corrugated rail, but they did not find any mechanism. This was because the frictional dissipation was not maximum at the corrugation troughs, which they suggested may be because of the omission of flexible dynamics in the contact plane. Many aspects of the causes of rail corrugation were discussed by Frederick [16], such as the initial surface roughness, the impedance of the rails and the lateral creep of the wheel. The pinned-pinned frequency was pointed out to have undesirable effects on short-pitch corrugation and roaring rails.

Based on this investigation, Hempelmann and Knothe [17] developed a linear model to predict short-pitch corrugation and roaring rails in the range 160-1600 Hz based on the idea of feedback between structural dynamics and wear. The structural dynamics model

---

only considered lateral and vertical dynamics and only excitation by profile irregularities. They found that stiff situations caused by anti-resonances within the structures, mainly in the vertical structural dynamics of the track, cause high contact forces and can lead finally to corrugation.

The statement that the cause of corrugation is related to the vertical track dynamics started to draw attention. Müller [18] linked the presence of high lateral rail receptance and low vertical rail receptance to short-pitch corrugation development in the range 80-2000 Hz. A contact mechanical filtering function was proposed, to limit the corrugation wavelength to a particular band. This may explain the observation that corrugation wavelengths are largely independent of train speed in some cases. Nielsen et al. [19] presented a time-stepping model for the interaction force to predict the short-pitch rail corrugation growth in the range 200-2000 Hz. The P2 resonance was also considered. The wear constant and model parameters were obtained from measurements. The corrugation growth they predicted showed good agreement with measured data. A strategy of adding damping to the rail to increase the track receptance around the pinned-pinned frequency above a sleeper was proposed to prevent the corrugation growth. They also pointed out the possibility of other damage mechanisms apart from wear.

Andersson and Johansson [20] developed a three-dimensional time-domain interaction force model based on Hertz theory. Kalker's algorithm program FASTSIM [13] was used to assess the spatial variations of creep and traction. The overall wear was calculated by multiplying the wear for each wheel passage by the number of passages. It was found that vertical dynamic properties are of greater importance to short-pitch corrugation initiation in the range 200-1200 Hz in tangent track compared to the lateral motion. For rail corrugation in curves, the importance of the lateral track dynamics was believed to increase. Robles et al. [21] introduced a combined vertical/lateral model which includes the vertical wheel-rail dynamic interaction with a Hertzian spring and the FASTSIM [13] algorithm is used to study tangential contact. The importance of the consideration of lateral dynamics in models studying corrugation in sharp curves was validated by experimental measurements.

Jin et al. [4,22] presented a three-dimensional train-track system model. The combined influences of the corrugation development, the vertical and lateral coupled dynamics of the vehicle and the curved track were taken into account. The discrete track support caused fluctuations of the normal loads and creepages at the passing frequency of the sleepers. The

---

excited track resonance frequencies resulted in the initiation and development of rail corrugation with several specific wavelengths. Gomez and Vadillo [23] presented a linear model using the finite element (FE) method to explain short-pitch rail corrugation formation in the range 100-1000 Hz. The main mechanism of corrugation initiation was identified to be vertical anti-resonances and regions of high lateral dynamics of the wheel-rail structure.

By investigating four types of slab track under identical operational conditions through field measurements and numerical simulation, Li et al. [7] found that the characteristics of the tracks were associated with the formation of short-pitch corrugation below 1000 Hz rather than high-frequency torsional or bending resonances of wheelsets. Wheel-rail interaction and creepage together with track resonances also contribute to the initiation.

Different from former authors' conclusions, other causes of rail corrugation have been investigated. Nielsen [24] used a pure contact model considering a cylinder rolling over a periodically varying surface to study the initiation of corrugation. He found that the characteristic wavelength of corrugation development in the range of 0.025-0.1 m is determined by the creep magnitude and contact patch length of the passing wheels, and is independent of the initial amplitudes of the surface irregularities.

An alternative mechanism for the initiation of rail corrugation in the wavelength range 20-80 mm has been proposed by Ciavarella [25-26]. The simple analytical model suggested a pure longitudinal creepage mechanism. The presence of much larger values of longitudinal creepage compensates for the effect that lateral creepage shows more growth than longitudinal creepage. For corrugation at high frequency, the mechanism is more like a constant-wavelength one than a constant-frequency one and this wavelength only depends on the geometry and loading conditions. The vertical resonances of the systems, even the pinned-pinned resonance associated with the effect of discrete supports, showed little effects on the growth of corrugation.

Consideration has also been given to the unsteady rolling effect. Wu and Thompson [27] used the two-dimensional quasi-static contact approach from Grassie and Johnson [15] in a frequency domain model to study the effect of multiple wheel passages on rail corrugation in the range 400-1500 Hz. The unsteady rolling contact problem was considered in which the normal contact force and surface curvature vary. The wheel-rail contact forces were assumed to be responsible for the rail corrugation. It was found that wear is heavier at

---

shorter wavelengths and increases with the amplitude of the dynamic contact force. This also confirmed the conclusion that stiff rail pads would result in higher corrugation growth than soft pads [28].

Baeza et al. [29-30] investigated the importance of applying a transient rolling contact model. When the forces applied are constant, the results obtained from transient and stationary models are identical, but when applying varying forces, significant differences occur and thus the wear estimation is affected. Alonso and Gimenez [31] and Knothe and Gross-Thebing [32] also studied the effects of transient contact mechanics. However, apart from Kalker's CONTACT program [14], most models assume that the stress distribution between the wheel and rail at one position inside the contact is independent of the distribution at previous locations.

Xie and Iwnicki [33] developed a three-dimensional contact model based on Kalker's variational method which included non-linear effects, transient effects and non-Hertzian effects. It was found that when these effects are included, the maximum wear always occurred close to corrugation peaks and thus resulted in roughness being suppressed rather than developing into a sinusoidal pattern. When the model was extended with the time-domain wheel-rail interaction [34], calculations were presented of a free wheel subject to a constant longitudinal creepage and a driven wheel subject to a dynamic longitudinal creepage and a broadband roughness. The wear spectrum was found to be mostly independent of both the wheel speed and the initial roughness spectrum.

Wheelset dynamics should also be considered. A simulation tool comprising a cyclic finite track model, a flexible and rotating wheelset model and a wheel-rail contact model has been presented by Vila et al. [35-36] to study the evolution of the rail roughness in the range 50-1500 Hz. They identified the vibration modes of the wheelset responsible for a complex dynamic behaviour able to produce high forces and wear at the wheel-rail contact. The coupled influence of the third bending mode of the wheelset and various wheel modes on the growth of rail corrugation was analysed and it was found that the possible wavelength-fixing mechanism that was identified depends on the speed of the vehicle. It was also found that when a mean positive longitudinal creepage is considered, roughness growth is predicted only on the low rail.

A model which comprises a finite element (FE) track model, rigid vehicle, flexible wheelset and non-Hertzian non-steady contact model was applied by Torstensson et al. [37-

---

38] to predict long-term roughness development on small radius curves in the range 25-1500 Hz and was validated by measured data. It was found that corrugation wavelengths on curves are related to excitation of the first symmetric and antisymmetric bending modes of the leading wheelset in a bogie.

### **1.3.3 Stick-slip self-excited vibration due to falling friction**

Clark et al. [39] investigated self-excited vibration of a flexible wheelset and a discretely supported track system under high creepage conditions. They derived the interaction force including vertical and lateral dynamics, since they found that lateral creep had more effect on the short wavelength corrugation development than longitudinal creep. A significant improvement in their model was the wear prediction which considered varying lateral creep as well as varying random speeds of wheel pass-bys. It was found that a friction characteristic with a negative slope leading to self-excited vibration could promote short pitch corrugation growth.

An analytical model based on Clark et al.'s work [39] was introduced by Brockley and Ko [40] to derive a formula linking corrugation wear with friction-induced vibration and to investigate its effect on corrugation initiation and development. They found that corrugations in the range 40-80 mm are formed by wear resulting from torsional vibration of the driven wheels and by longitudinal vibration of the rails.

More recently, Matsumoto et al. [41] studied the growth process of short wavelength corrugation on curved track by numerical simulation together with full-scale stand tests and commercial line experiments. It was found that the wheelset vertical vibration induced by wheel-rail irregularities would cause a fluctuation of the normal force between wheels and rails. This fluctuation, and a large creepage, would generate stick-slip vibration in the contact of the wheel-rail system with the torsional vibration of the axle and thus generate rail corrugation in curved sections of track. They also gave an explanation of the phenomenon that corrugation occurs on the low rail. As the normal wheel load on the low rail is smaller, the stick-slip process happens more easily.

Considering the varying normal forces caused by track features such as welds and joints, Grassie and Edwards [42] used a simplified analytical model to investigate the effect of normal force fluctuation. It was found that a varying normal load with constant tangential load, where the tangential load is a small fraction of those which can be sustained by friction, would result in variations of slip in the contact and thus, affect the corrugation

---

growth. If a wheel is close to slipping, corrugation in the 100–300 mm wavelength range is more likely to arise from variations in tangential forces that would be associated with a torsional resonance of wheelsets.

Sun and Simson [43] developed a nonlinear vehicle-track model which comprised a wheelset with two wheels coupled in torsion and bending, a discretely supported distributed-parameter track model and a wheel-rail interaction model based on Kalker's linear creep theory [14]. It was found that the frequency of the wheel stick-slip process corresponded to the wavelength of rail corrugation. This was related to the sleeper-passing frequency and the combined torsional and bending frequency of the wheelset. If the static friction coefficient has a low value, the creepage can easily overcome the wheel–rail interface's ability to accommodate it, leading to the wheel stick-slip process. Furthermore, a low kinetic friction coefficient intensifies the wheel stick-slip process.

#### **1.3.4 Stick-slip self-excited vibration due to mode coupling**

The falling friction characteristic discussed above was also believed to be the main cause of the stick-slip self-excited vibration in curve squeal, but recently the mode-coupling mechanism has also gained popularity as another possible cause [44]. Similarly, in rail corrugation, the mode-coupling mechanism may also be an important mechanism. Coupling between different wheel modes, also known in other contexts as flutter, results in instability at a frequency which is normally between those of the two coupled modes [44]. In such a situation, vertical and lateral vibrations exhibit a phase difference and can be characterised by beating.

Kurzeck [45] set up a vehicle-track simulation model using the commercial multi-body software SIMPACK. Through numerical simulations, the initiation mechanism for corrugation at a frequency of 80 Hz was identified as the bending mode-coupling instability in friction-induced oscillations. The oscillation of the rail was coupled with that of the wheels under the action of the saturated creep forces. When the coupling was strong, self-excited oscillation of the wheel-rail system occurred which caused variation of the contact forces between wheels and rails. The oscillation was characterized by high vertical amplitudes at the axle-box of the inner wheel of the leading wheelset without the need of an excitation by the rails.

At a similar time, Chen et al. [8,46,47] used a finite element model to investigate the formation mechanism of rail corrugation from the viewpoint of mode-coupling self-excited



---

vibration of the wheelset-track system. Creep forces were assumed to be saturated. A complex eigenvalue method and a transient dynamics method were utilized to study the stability of the wheel-rail system and the unstable transient dynamics. The normal contact force between the wheel and rail fluctuated at the same frequency as the wheel and rail vibration when the self-excited vibration occurs, leading to corrugation in the range 50-600 Hz. A negative friction-velocity slope was found to have a small influence on the occurrence of rail corrugation. Besides, it was found that when the vertical rail fastener stiffness was increased, the possibility of wheel slipping decreased and the propensity for rail corrugation to occur also decreased.

Later field measurements and numerical studies were carried out by Cui et al. [9]. Vertical vibration acceleration had significant fluctuations when a wheelset passed. They suggested this implies the occurrence of frictional-coupling self-excited vibration caused by a saturated creep force. This was linked to unstable vibration mainly on the low rail of curves causing rail corrugation in the range 100-500 Hz. Cui et al. [48] further showed that friction-induced oscillation was the main cause of rail corrugation through a study of a particular phenomenon in which corrugation wavelengths differ in different track sections when using Cologne egg fasteners and fixed dual short sleepers. Unstable oscillation occurs on the low rail of the Cologne egg section at a frequency of about 422 Hz, but occurs on the low rail of the fixed dual short sleeper section at a frequency of about 201 Hz. They also stated that the reason why rail corrugation rarely occurred on the rails of tangential or curved track of larger radius was that the creep forces are not saturated.

### **1.3.5 Alternative mechanism based on flexibility differences**

Apart from the wheel-rail contact, another viewpoint to investigate the corrugation mechanism has been considered in [10-12]. Previously, for the pinned-pinned resonance corrugation, it has been widely accepted that this is associated with a mode of the track in which the rail vibrates as if it is a beam almost pinned at the periodic sleepers or rail fastenings. Then the rail vibration causes the variation of dynamic loads and thus corrugation. However, through an experimental study of rail dynamic frequency response functions for different trackforms,

Vadillo et al. [49] examined a case of inside rail corrugation where curvature is sharp. The corrugation was found to develop quickly in the area between one sleeper and the next. The explanation lay in the high lateral creep of the first bogie wheelset on the curve, especially in the mid-span between sleepers. Modal analysis indicated the first mode of

---

lateral bending in the rail was the wavelength-fixing mechanism.

Wang et al. [10] considered that variations of dynamic loads or contact force were not only due to rail vibration. They found that the transfer functions clearly showed opposite trends when the wheels are running above the fasteners and at the middle of a span between two fasteners and demonstrated that the discontinuous support could be a main cause of short-pitch (25–80 mm) corrugation of the rail. This is the basis of the proposed mechanism of wheel-rail dynamic flexibility difference.

Zhao et al. [11] later studied the relationship between the change of discontinuous support stiffness of the track system and the dynamic flexibility (receptance) of wheel and track. Due to dynamic flexibility difference between different positions, a cyclical fluctuation of the wheel-rail contact force was generated. The mechanism of wheel-rail dynamic flexibility difference for corrugation initiation was then presented. To control the growth of rail corrugation below 1200 Hz, the optimal vertical and lateral stiffness of the fastener was calculated through numerical examples. Later, Zhao et al. [12] verified this mechanism through field observations and simulation analysis. It was found that installation of a novel rail damper can shift the pinned-pinned frequency to a lower frequency and reduce the difference in wheel-track receptance which sharply minimises the wheel-rail interaction force and thus the rail corrugation.

This mechanism is similar to the mechanism of the pinned-pinned resonance since they both consider the wheel-rail system vibration which results in corrugation, and they both correspond to sleeper or fastening spacing and fastener stiffness. However, there is a difference in the vibration generation mechanism. The mechanism of wheel-rail dynamic flexibility difference may be able to explain the corrugation initiation when the train speed is fixed and the frequency is away from the pinned-pinned resonance of the rails.

## **1.4 Research on effects of critical aspects**

As well as investigations of the mechanism and prediction of rail corrugation, figuring out and understanding the effects of possible critical aspects is also important to set appropriate strategies for rail corrugation prevention and control. Many parameter studies and sensitivity analyses have been carried out by various authors. Initial sinusoidal roughness is often used to excite particular modes of the wheelset, track system or the coupling of the wheel and rail to investigate the effects of the particular modes on the development of the rail corrugation. The sinusoidal roughness is assumed to be present on the running surfaces

of rails with a wavelength calculated as the velocity divided by the frequency corresponding to the particular modes. Here, only recent works are reviewed, some considering new aspects and some verifying the influence of critical aspects found by former authors. These aspects are listed in Table 1.3.

Table 1.3 List of critical aspects that affect the rail corrugation investigated in the literature

Critical aspects	Reference
Friction coefficient	[50],[53],[61],[62],[63],[68]
Modal damping of wheel-rail system	[50],[64],[65],[68]
Wheel-rail profile	[43]
Wheel-rail contact angle	[67]
Direction of saturated creep force	[67]
Coupled bogie/track system	[55]
Bogie design	[66]
Multiple wheels	[27],[56],[57],[58],[59]
Operational speed	[52],[53],[58],[59],[60],[61]
Train axle load	[52]
Track parameters	[43]
Fastening parameters	[6],[27],[28],[51],[52],[53]
Discrete supports	[6],[22],[52],[54]

#### 1.4.1 Discussions in the literature

Meehan et al. [50] developed an analytical model based on the mechanism of transient dynamic interaction and performed a sensitivity analysis to determine the influence of various railway parameters on the growth rate of wear-type corrugation (such as rutting and roaring rails). It was shown that the wear coefficient, friction coefficient and the ratio of tangential load to the friction limit had positive correlation with the corrugation growth rate, whereas the modal damping of the wheel-rail system had a negative correlation with rail corrugation growth.

Sun and Simson [43] used a nonlinear vehicle-track model based on the mechanism of stick-slip vibration to investigate the effects of the curved track parameters, the wheel-rail friction characteristics and the wheel-rail profiles on the wheel stick-slip process and thus on corrugation. Among the parameters investigated, larger track curvature, higher static friction coefficient, higher kinetic friction coefficient and worn wheel-rail profiles were found to have significant effect in suppressing the rail corrugation growth (assuming the creep force remains constant in all cases).

---

Yan et al. [51] introduced the floating ladder track to control track vibration in the Beijing subway and found the second-order bending resonance of the ladder sleeper occurred at 134 Hz that causes vibration and trackform-specific corrugation. Change of the fastening parameters and resilient material affected the high and low frequency range separately. Thus, increasing the vertical damping and decreasing vertical fastening stiffness could improve the vibration and reduce rail corrugation.

Song et al. [52] investigated the effect of several factors on wear-type rail corrugation, including operational speed, rail pad stiffness, rail pad damping, sleeper spacing and train axle load. Among these, changing the rail pad stiffness was considered the most practical and effective solution and was verified by field measurements. A lower rail pad stiffness was shown to reduce roughness growth as found in previous studies [27,28]. Robles et al. [53] predicted the development of corrugation using a new developed time/space domain model. Apart from the finding that lower pad stiffness reduces corrugation growth rate, it is also found that the greater the deviation of the vehicle speed distribution, the smaller the extent of wear and the less corrugation is developed. Different friction coefficients were also studied.

Apart from component parameters, other aspects also draw much attention. Sheng et al. [54] used a two-dimensional Hertzian-based wear model, which was different from Jin et al. [22], to investigate the effect of discrete supports but the results led to the same conclusion that the discrete supports significantly affect the initiation of short-pitch rail corrugation. This conclusion was obtained because the Hertzian contact stiffness varied due to discrete supports when the wheels moved on periodically supported rails. Maximum corrugation growth was found to occur near the pinned-pinned frequency.

Iceland [55] used a linear vehicle model with a nonlinear Hertzian contact stiffness moving over a linear track model, discretely supported by flexible sleepers to calculate the vertical wheel/rail contact forces. The vertical dynamic behaviour was assumed to be independent of the friction forces and creep. It was found that resonances in the coupled bogie/track system, occurring due to wave reflections between the two wheels on the rail, may have a considerable influence on the vertical dynamic interaction between the vehicle and the track and thus on the roaring rail corrugation growth. Later, Manabe [56] used an analytical model without discrete rail supports to investigate the effect of the standing waves in the rail between multiple wheels. Wu and Thompson [27] also investigated the effect of multiple wheels. The significant effect of the standing waves in the rail between

---

two wheels of a bogie was further verified by Johansson and Nielsen [57].

The effect of train speed and the frequency of successive wheels on wear-type rail corrugation formation were investigated by Meehan and Daniel [58] and Bellette et al. [59]. It was found that in some cases a wider spread of vehicle speeds was effective in controlling rail corrugation growth while the wheel passing frequency (wheels passing per second within a train) also had some effects on it. Nonlinear behaviour was not taken into account so the influence was limited to small amplitude corrugation growth. Later Meehan et al. [60] used a frequency-domain corrugation growth model to investigate the effects of asymmetric speed distribution on maximum growth rate for trains in cornering. Positive skew (higher distribution at low speeds) caused a decrease in rail corrugation, thus speed control via manipulation of the distribution skew was believed to be effective.

Bellette and Meehan [61] carried out validation experiments and showed that speed variation and the use of friction modifiers can have a great effect on the reduction in corrugation growth rates which is consistent with theoretical predictions. High steady wear would increase the corrugation growth at first, but it would also quickly create a more conformal contact, which resulted in a reduction in the change in steady-state profile per pass, thus limiting the corrugation growth. The effect of friction modifiers on short-pitch corrugation growth in curves was also studied by Eadie et al. [62]. The friction modifiers can change the friction coefficient of the rail contact surface and eliminate the negative slope at high creepage. Field measurements showed that a friction modifier was effective in controlling the corrugation growth rate and the effectiveness would not be much influenced by changes in contact conditions.

Grassie [6] described a metro project and identified the types of corrugation that were considered to be most likely to occur. To avoid trackform-specific corrugation and P2 resonance corrugation, the fastening system of the track was used with a relatively stiff railpad and a resilient baseplate pad. The choice of the fastener spacing was also justified to mitigate pinned-pinned resonance corrugation. No specific preventions were made to mitigate rutting corrugation which could best be treated by installing friction modifier in the sections of track where it occurred. The measures proposed and adopted were indeed successful to minimize corrugation occurrence as the results of monitoring were undertaken [63].

Croft et al. [64] developed a simple time-stepping FE model to calculate the interaction

---

forces between the wheel and the rail for a track with and without rail dampers to study the effects of rail dampers on short-pitch rail corrugation growth. Through numerical analysis, it was found that the rail dampers could reduce the dynamic interaction forces and shift the force spectrum to lower frequencies, i.e. longer wavelengths. Thus, the short-pitch corrugation growth was attenuated. Wu [65] used a time-domain model including the track with rail dampers to reach similar conclusions. He studied short-pitch rail corrugation from the viewpoint that friction-induced self-excited vibration of a wheel–rail system causes corrugation.

Later Wu et al. [66] established an FE model based on the commercial software ABAQUS with bogies with different axlebox arrangement to obtain parameters of interest to study the effects of several aspects by complex modal analysis. A design of bogie with inner axleboxes was found to be favourable for suppressing the rail corrugation. The lateral spacing between the primary suspension points of a bogie with inner axleboxes had a positive correlation with the possibility of rutting rail corrugation occurrence. Lower vertical stiffness of the primary suspension was also found to be beneficial in the suppression of the corrugation. Too low or too high vertical damping of the primary suspension or a heavier vehicle or bogie increased the possibility of corrugation occurrence.

Based on the viewpoint of frictional-coupling self-excited vibration of the wheelset-track system, the effect of wheel-rail contact angle and direction of saturated creep force on short-pitch corrugation were studied by Cui et al. [67] through an FE model and analysed by the complex eigenvalue method. Contact angles smaller than  $8.41^\circ$  would result in self-excited vibration and then rail corrugation. Higher longitudinal creep resulted in a lower propensity for corrugation. It was shown that the creep force in the lateral direction more easily generates corrugation than the force in the longitudinal direction. Corrugation more easily occurred in tightly curved track than tangent track. Beshbichi et al. [68] used an FE wheelset and track model in ABAQUS to investigate the formation of railhead corrugation in sharp curves. The effective damping ratio of the coupled system was obtained through complex eigenvalue analysis. For higher values of friction coefficient, the effective damping ratio associated with unstable vibration increased in magnitude while the frequency shifted towards lower values.

### **1.4.2 Summary of critical aspects**

Many possible aspects of the wheel-rail system have been identified over the years with

---

varying success based on the mechanisms introduced in Section 1.3. Thus, many effective treatments and methods related to these aspects have been developed to control the initiation and growth of the wear-type rail corrugation.

Since the damage mechanism of the various types of rail corrugation, such as roaring rails, rutting and track-form specific corrugation, is wear, improving these aspects related to frictional work is directly effective in suppressing the initiation and growth of rail corrugation. This treatment includes lubrication, which improves the wear coefficient, static and kinetic friction coefficient, and the use of friction modifiers, which reduces or eliminates the falling friction characteristics. Increasing the modal damping of the wheel-rail system is also an alternative treatment.

When the corrugation generation mechanism is considered to be stick-slip self-excited vibration caused by falling friction, the parameters that are related to the track, such as the track curvature, the rail pad stiffness and rail vibration absorber, have a significant effect on roaring rails or rutting corrugation. The fastener spacing, however, has a significant effect on the pinned-pinned resonance. The vehicle speed, wheel passing frequency, wheel-rail contact angle, the direction of saturated creep force and the worn wheel-rail profile also contribute to the wheel-rail system dynamics and therefore affect the initiation and growth of roaring rails or rutting corrugation.

When the dominant corrugation generation mechanism is considered to be stick-slip self-excited vibration caused by mode-coupling, the aspects which affect the vehicle and track vibration modes should be taken into account to control the initiation and growth of roaring rails or rutting corrugation. For the track, the parameters of the discrete supports are important. For the vehicle, the design of bogies with inner axleboxes with reduced lateral spacing between the primary suspension points, the vertical stiffness and damping of the primary suspension and the mass of the bogie are critical.

For trackform-specific corrugation, increasing the damping of vertical resilient supports and decreasing the vertical fastening stiffness can improve the vibration performance and reduce rail corrugation in low and high frequency range, respectively.

The choice of a treatment for a specific situation requires many considerations to be taken into account, especially the generation mechanism of the rail corrugation. Thus, identifying the dominant mechanism of the rail corrugation is the key point and will contribute to the

decision of corrugation growth control strategy.

### 1.5 Research target and contributions

So far, short-pitch rail corrugation including roaring rails, rutting and other wear-type corrugation has been widely investigated, but some railway roughness phenomena are still not satisfactorily explained. There are still considerable difficulties in identifying the causes of the rail corrugation at particular locations. That means further investigations and research are needed to solve this problem. One of the most damaging types of corrugation is known as rutting which usually appears on the inner rail of curves and produces intense noise in a low frequency range.

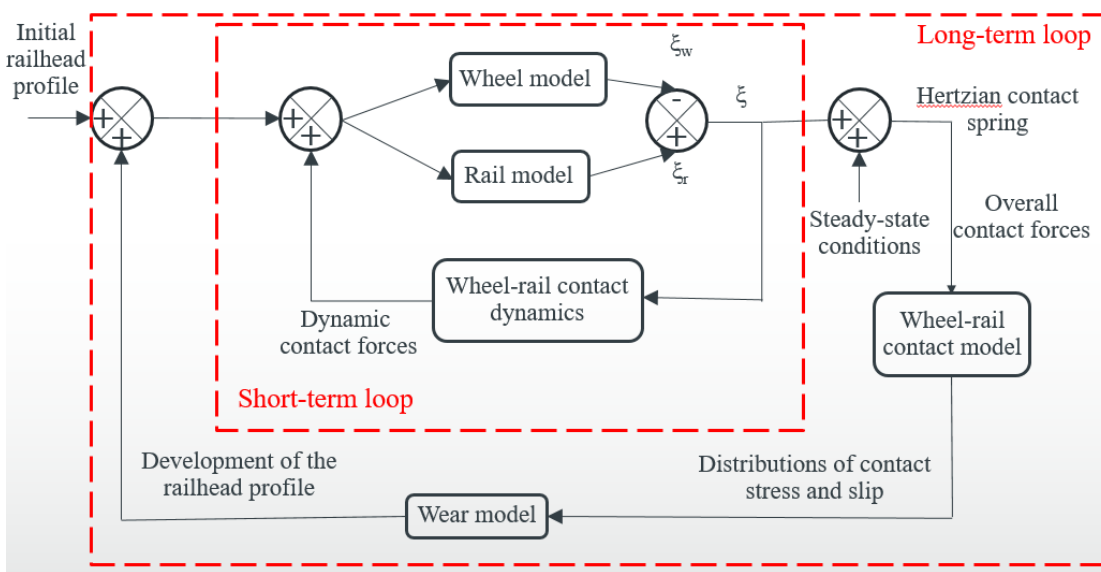


Figure 1.3 Structure of simulation tool

In this research, the aim is to develop a time domain model of the wheel-rail coupled system that allows a thorough investigation of rutting corrugation. In Figure 1.3, the time domain model of the wheel and rail are obtained from their frequency domain models. Then together with other sub-models, these models are assembled and used all in the time domain. Such model is then used to perform extensive parametric studies that allow evaluating and comparing the most important parameters that are associated to roughness growth. Hence, the objectives of the work are set out below:

- 1) To develop a simulation tool to predict corrugation growth through models of the coupled vibration of the railway vehicle-track system and the wheel-rail rolling contact mechanics. The developed simulation tool will consist of several models



---

connected in a feedback loop (as shown in Figure 1.3) to account for both the short-term dynamic vehicle-track interaction and the long-term damage.

- 2) To develop a track dynamic model based on the existing rail model developed by Kostovasilis [84] and obtain the impulse responses in the time domain, combining them with a state-space modal model of the wheelset in a time-stepping approach.
- 3) To extend the steady-state curving model developed by Huang [69] to include the effects of falling friction and traction force.
- 4) To implement the 3D contact model to obtain the contact forces and then the wear, then to identify the dominant resonance and mechanism of the corrugation initiation in a specific case.
- 5) To investigate the effect of wheel/rail couplings between two wheels and rails, and also the effect of multiple wheel/rail interactions on the corrugation initiation.
- 6) To investigate the effects of some key parameters in order to mitigate rail corrugation.

Most vehicle-track interaction models may be categorized as either time-domain or frequency-domain models. Historically, time-domain models have required a large computational capacity whereas frequency-domain models are usually more efficient, albeit less flexible. Frequency-domain models can take account of multiple wheels and parametric excitation, but their main limitation is the inherent assumption of linearity, which is valid only when the roughness excitation of the system is low. They also usually neglect spatial variations in track properties. In comparison, time-domain models are developed to study cases where non-linear effects are significant such as in modelling rail corrugation. As advances occur in computational capabilities, it is becoming possible to do time-domain analysis for increasingly complex models. Considering the frequency range and parameters of interest, a time-domain vehicle-track interaction model is used in this research.

The time-domain vehicle-track interaction model should comprise a flexible wheelset model, a semi-analytical track model with discrete supports and the non-Hertzian non-steady-state 3D wheel-rail contact model based on the variational theory by Kalker [14]. The dynamic interaction between the vehicle and the track is solved in the time domain to take into account the nonlinearities of the coupled vehicle-track system. Wear calculation is performed with Braghin's wear model [134] by using the contact parameters obtained from the wheel-rail contact model, which is able to represent adequately the distributions of contact stress and slip velocity. These distributions are required as input data to the wear model to compute the material loss on the running surfaces of the two rails. The frequency

---

range of interest for the rail corrugation is up to about 1500 Hz. Due to the use of a time-domain prediction model, to get more precise results, the sampling frequency used in the time-domain model is higher. Thus, the frequency range of interest for the wheelset and track need to be up to about 5000 Hz.

The main original contributions in this thesis can be summarised as follows:

- 1) An existing steady-state curving model is extended to include the effects of falling friction and applied traction on the calculation of contact forces, contact positions and creepages.
- 2) A new analytical track model is developed based on an existing rail model and the receptance-coupling method to account for discrete supports. The transfer responses between the two rails of the track are also obtained. The dynamic responses of the new track model are validated by measured results. The effects of the inclusion of torsion and warping for the rail on the overall lateral track responses are investigated.
- 3) A new combination of the time-domain track and wheelset responses is applied in the wheel/rail interaction model. For the track, a moving Green's function method is used to get the track response in the time domain, while for the wheelset, the state-space method is used based on modal coordinates. This combination is found to be effective and sufficient to model the wheel/rail interaction.
- 4) For a vehicle with a specific speed passing a curved track with a specific radius, different mechanisms are evaluated and the dominant mechanism for the corrugation initiation is identified. The dominant resonances in such a case are also identified.
- 5) The effects of the coupling between the two wheels and rails, and also of the presence of multiple wheels on each rail on the dynamic responses and on corrugation growth are investigated.
- 6) Parametric studies are performed, including varying the friction coefficient, radius of curved track, vehicle speed, rail pad stiffness, cant angle, wheelset design and axle load. For a wide range of conditions, the dominant mechanism is determined. Furthermore, some general conclusions in determining the dominant mechanism are obtained.

---

## 2 Steady-state curving model

### 2.1 Introduction

The wheelsets of railway vehicles usually consist of two wheels joined by a rigid axle. The bogie is a frame in which two such wheelsets are mounted. When trains are travelling through a curve, the wheelsets (especially the leading one) exhibit a non-zero angle of attack to the rail and consequently a sliding velocity is generated in longitudinal and lateral directions at the wheel-rail contact. The lateral sliding motion causes lateral creep forces, and the longitudinal sliding causes longitudinal creep forces. These forces also change the wheel/rail contact positions and normal load applied to the rail.

In a curve of constant radius, without any external input, the vehicle-track system would achieve a steady-state behaviour. The contact position between the wheel and rail, the creepages and the normal load in the steady state are needed for the following calculations. The steady-state curving model used in this thesis was established by Huang [69] and is extended in this thesis to include falling friction and applied traction. A general description of this model will be given in this chapter. Detailed information about this steady-state curving model is given by Huang [69].

### 2.2 Review of railway vehicle dynamics

In modelling rail corrugation for curved track, some steady-state curving parameters, such as creepages, contact positions and normal loads, are required. A steady-state curving model presented in this section can provide these parameters. This is mainly based on the description in the book of Wickens [70].

The theoretical analysis of railway vehicle dynamics started in the 19<sup>th</sup> century. First theoretical analysis represented the situation of the unconstrained wheelset in a moderate curve. To maintain stability in practical situations, the wheelsets of the vehicle must be constrained by the suspension stiffness, which connects the wheelset to other parts of the vehicle, or by the wheel flange. In the unconstrained wheelset case, the guidance is provided by the linear conicity only for slightly curved track. For tightly curved tracks, the essential mode of guidance is found to be the wheel flanges [70]. Mackenzie [71] later developed the first practical theories, which considered the friction forces. He investigated this based on sliding friction, neglecting the effect of wheelset conicity on curving. It was assumed that the wheelsets run under flange contact on the outer rails of curves.

---

The principal consideration is that a vehicle is supported on multiple wheelsets, and in each wheelset, two wheels are connected rigidly by the axle. Their running surfaces have conicity. Wheel/rail forces are developed by sliding friction forces at all the wheel treads and at the flange contacts (where applicable). The curving behaviour can be divided into two kinds [72]. One is referred to as constrained curving for small curve radii where the leading outer and trailing inner flanges contact the rail. The other is referred to as free curving where only the leading outer wheel is in flange contact.

On most curves, the analysis of curving behaviour of conventional vehicles must involve a consideration of important nonlinearities, i.e. the saturation of the friction forces and realistic wheel-rail geometric interaction in flange contact [70]. Elkins and Gostling [73] gave a comprehensive nonlinear treatment of practical vehicles on curves. The numerical solutions were found to have a good agreement with experimental results. The nonlinearities caused by the contact patch movement along the rail and subsequent change in contact patch shape, friction saturation and large wheel/rail contact angle in flange contact were considered, while the inertia terms were not included as the research was focused on steady-state behaviour.

From the 1980s, the simulations of vehicle dynamics gradually became available in powerful, validated and user-friendly commercial software packages, such as ADAMS, VAMPIRE and SIMPACK with which it is possible to carry out simulations of the dynamic behaviour of the railway vehicles running on the track. Although the commercial software packages are available, to satisfy the demands of curve corrugation research and provide insight into the mechanism of the corrugation initiation, it is useful to have a self-contained vehicle simulation model.

In this steady-state curving model, rigid bodies representing the vehicle are connected to each other by flexible components of the suspensions, i.e. springs and dampers. The vehicle is considered to run on a constant track section, which has a fixed curve radius and cant angle. The cross-section profiles of the wheel tread and railhead are based on measured data and assumed constant through the whole simulation process. The nonlinear creepage-creep force relationship is also considered in the steady-state curving but this does not include the falling region. The definitions of sliding velocities and creepages are slightly different from the linear creepage-creep force relationship. Under most circumstances, the rigid motion of a wheelset is much more significant than that of the

track. Therefore, the rail motion can be ignored for determining the vehicle dynamics. This is a treatment consistent with the definitions in the commercial software.

## 2.3 Steady-state curving model from Huang [69]

The steady-state curving model used here is based on Huang's work [69]. Here a brief introduction is given to state the basic structure, settings and assumptions.

### 2.3.1 Creepages

As defined by Johnson [74], rolling is a relative angular motion between two bodies in contact about an axis parallel to their tangent plane, as shown in Figure 2.1. In the contact frame, the contact surfaces 'flow' through the contact zone with tangential velocities in the  $x$  (longitudinal) and  $y$  (lateral) directions. The bodies can also have angular velocities about the  $z$  (vertical) direction which are in the  $x$ - $y$  plane. In tractive rolling contact, which refers to the cases with non-zero tangential force, tangential loading can lead to a difference in elastic deformation of the two bodies. The difference in elastic deformation or strain in the contact yields the overall relative slip, which is known as creep [74]. Creep can occur in the longitudinal and lateral directions and in the form of spin, where the relative slip between wheel and rail is rotational. For rolling without sliding or spin, the motion is called 'pure rolling' which is an ideal case.

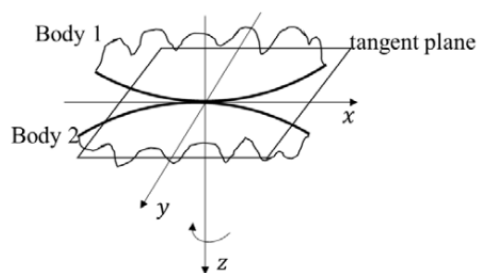


Figure 2.1 Rolling contact of two elastic bodies [75]

Johnson [74] defined the creep ratio  $\gamma$  as the difference between the distance travelled in one revolution by the deformed and undeformed wheels, divided by the undeformed circumference. It may also be expressed in terms of the velocities of the contact surfaces and is also known as creepage. If the velocity of a point on the surface of the wheel, relative to the contact patch, is  $v^w$  and the contact moves along the rail with an overall velocity  $v^r$ , then the longitudinal, lateral creepages and spin can be written as

$$\gamma_x = \frac{v_x^w - v_x^r}{V_0}, \gamma_y = \frac{v_y^w - v_y^r}{V_0}, \gamma_\phi = \frac{v_\phi^w - v_\phi^r}{V_0} \quad (2.1)$$

where  $V_0$  is the vehicle speed. The longitudinal and lateral creepages are dimensionless whereas the spin creepage has a dimension of  $m^{-1}$ .

### 2.3.2 Rolling friction

Consider first a body at rest on the ground, as shown in Figure 2.2. The normal force  $F_N$  given by the ground to the body is equal in magnitude and opposite in direction to the gravity force acting on the body  $G_g$ . The external force  $F_e$  gives the body a trend to move forward. The static friction force  $F_s$  is equal in magnitude and opposite in direction to the external force applied to the body until the friction limit between the two contact surfaces is reached; this is equal to the value of the static friction coefficient multiplied by the normal force  $\mu_s F_N$ . Thus, the friction force can take any value from zero to the friction limit before the body starts to slide. When the external force  $F_e$  is larger than the friction limit  $\mu_s F_N$ , sliding motion occurs. At this point, the friction force is equal to the friction limit.

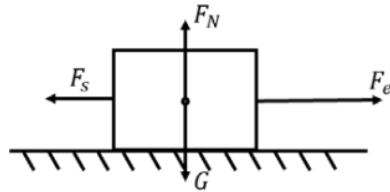


Figure 2.2 Body on the ground [44]

For a rolling wheel, the wheel and rail are not rigid. When the two elastic bodies are in contact, a deformation exists in the contact area which is fundamental to rolling friction [76]. In the contact area, there is some local slip before gross sliding occurs. This phenomenon is called micro-slip [77]. At this micro-slip stage, there are areas of adhesion and slip in the contact area, as shown in Figure 2.3. When entering the contact area, the surface particles of the wheel and rail lock together and move towards the rear. The front zone of the contact area is the adhesion zone. In the trailing zone of the contact area, where surface particles leave the contact area, a slip region occurs. When the global sliding velocity (or creepage) is very small, the contact is mainly in adhesion, with elastic deformation that builds up through the contact zone until micro-slip occurs near the trailing edge. As the creepage is increased, the size of the slip zone increases and the tangential force in the contact increases linearly from zero, until it reaches its saturation value. When

reaching saturation, the rolling contact is under gross sliding and the tangential force is equal to the friction limit (shown as dashed line in Figure 2.4).

It is widely known that friction coefficients are different in static and dynamic situations. The dynamic friction coefficient depends on the sliding velocity between the surfaces and higher slip velocities can result in a lower friction coefficient. Consequently, the slope of the curve of tangential force against creep ratio is not always positive. For high values of creep, the falling friction coefficient causes the slope of the creep-force relationship to become negative (shown as solid line in Figure 2.4. In the figure, the line has a positive slope due to the sign convention adopted. In this region, with increasing sliding velocity, the magnitude of the force is decreasing but with a negative sign). In the following calculations, the friction coefficient is assumed to be either constant or velocity dependent. The velocity-dependent friction is introduced in detail in Chapter 6.

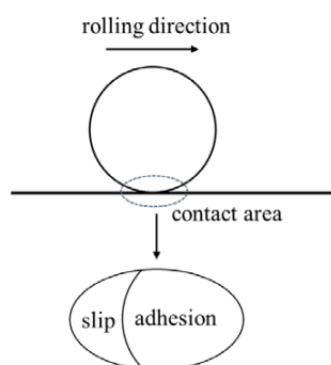


Figure 2.3 Slip and adhesion area in wheel-rail contact [44]

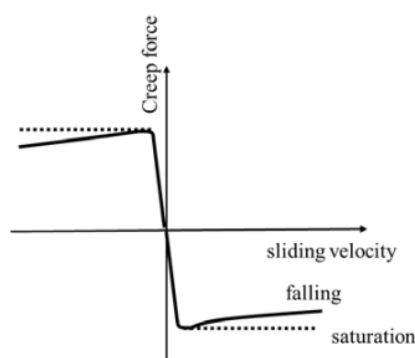


Figure 2.4 Creep force with micro-slip and saturation [44]

### 2.3.3 Wheel-rail interaction

Figure 2.5 shows the rear view of a wheelset on a track in a right-hand curve with a cant angle  $\phi_0$ . The wheelset reference frame  $oxyz$  is defined on the track, with the origin  $o$  at the centre point of the line that connects the top points on the two rail profiles. The  $z$ -axis is normal to the cant plane and the  $y$ -axis is parallel to the cant plane. The lateral offset of the

wheelset in the reference coordinates is  $u_2$ , and the roll angle about the  $x$ -axis is  $\phi$ .

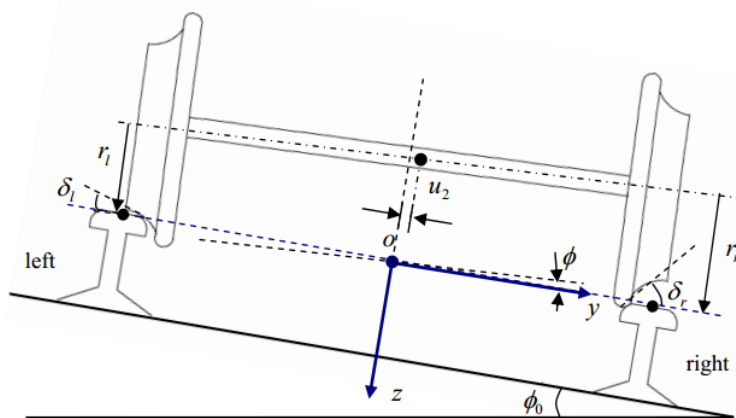


Figure 2.5 Lateral offset of a wheelset on a canted track [69]

The lateral offset of the wheelset will result in variations in the wheel-rail contact positions. Using an iterative process, the roll angle and the contact positions for a specific value of the lateral offset can be found. Variations in the wheel-rail contact positions will also lead to changes in other contact parameters. These contact results are calculated using the measured profiles of a S1002 wheel profile and a standard UIC 60 rail (with 1:20 inclination, installed on a canted ground plane). The wheel-rail contact results are smoothed with a curve fitting method and tabulated in terms of the lateral offset of the wheelset. In the simulations in this vehicle dynamics model, the contact results for each wheelset are found from the table according to the lateral position of the wheelset.

In the wheel-rail contact, the normal load is applied, and the contact area is formed. The elastic deformation in the vicinity of the contact area is small enough to be neglected in the geometrical analysis compared to the wheel and rail profiles. Then assuming the wheel and rail surfaces are smooth, their curvatures are approximately constant in the vicinity of the contact patch and the conditions for using the Hertz theory for the contact patch calculation are satisfied. This is not necessarily true for worn profiles, but the Hertz theory can be used as an approximation. The contact patch size depends on the normal load applied. For the measured wheel and rail profiles adopted in the current simulations, the curvatures of the wheel and rail are not continuous. Therefore, the form of the contact patch may be discontinuous at some positions. When flange contact occurs, the Hertz theory is not satisfied. But since the error caused by using Hertz theory for the curving analysis is acceptable, the Hertz theory is adopted in the steady-state curving model.

The steady-state creepages at the wheel-rail contacts are important input parameters in the



---

rail corrugation prediction model. The detailed realisation of the creepages in the steady-state curving calculation is presented in [69]. In the curving analysis, flange contact with large spin may occur at some wheel-rail contacts. Hence, FASTSIM [13] which accounts for the effects of large spin, can be used for the friction model in the steady-state curving model instead of the full variational method which is more computationally demanding.

When a vehicle is running on the track, the external forces are mainly due to the interaction between the wheel and rail. The wheel-rail interaction forces exist in the contact plane, including the contact force normal to the contact plane, the spin moment about the normal to the contact plane and the tangential forces in the contact plane. To calculate the tangential forces, the normal contact force is determined first; this also determines the size of the contact patch. In steady-state curving analysis, if the position of a wheelset is near the track centreline, the contact angles of both left and right contacts are small and the normal forces are approximately equal to the resultant value of gravity and centripetal forces. However, if one of the contact points is close to the flange zone, the difference between left and right wheel/rail contact angles is large enough to make the normal force at each contact patch different. The assumed normal force is therefore adjusted using an iterative process.

### **2.3.4 Vehicle dynamics**

Most modern railway vehicles are four-axle vehicles with a car body and two bogies. Each bogie has a frame and two wheelsets. The wheelsets and the bogie frame are connected through a primary suspension. The bogies support the vehicle body, usually by means of a secondary suspension, but there is no direct connection between the bogies. In Figure 2.6 and Figure 2.7, a bogie vehicle is shown under its initial conditions in a curve. The curving behaviour of all components, including the four wheelsets (denoted '1' to '4'), the two bogies (denoted 'b' and 'd') and the vehicle body (denoted 'c'), are analysed in their local coordinates, with the origins at their mass centre, the  $y$ -axes pointing inwards along the radial direction of the curved track, and the  $z$ -axes normal to the canted track plane and pointing downwards. The positions of the suspension components are shown in Figure 2.6 and Figure 2.7 by springs (with dampers, not shown, installed in parallel). The bogie vehicle under these initial conditions may not be in equilibrium. The steady-state curving behaviour can be obtained by step-by-step integration.

The minimum number of degrees of freedom (DOF) required to describe the steady-state curving behaviour of this bogie vehicle is 17, including the lateral motion  $y$ , yaw  $\psi$  and roll

$\phi$  of the vehicle body, the two bogies, and the lateral motion and yaw of the four wheelsets<sup>1</sup>. The vertical and pitch motions mainly result from the vertical undulation of the track in the running direction. This is avoided in the steady-state curving analysis by assuming a constant smooth profile of track. Hence, the motion of the bogie vehicle is defined by a set of 17 generalised coordinates. The equations of motion in these generalised coordinates are

$$[\mathbf{A}_v]\{\ddot{\mathbf{Q}}_v\} + [\mathbf{D}_v]\{\dot{\mathbf{Q}}_v\} + [\mathbf{E}_v]\{\mathbf{Q}_v\} = \{\mathbf{F}_v\} \quad (2.2)$$

where  $[\mathbf{A}_v]$  is the inertia matrix,  $[\mathbf{D}_v]$  is the damping matrix,  $[\mathbf{E}_v]$  is the stiffness matrix and  $\{\mathbf{F}_v\}$  is the external force vector.

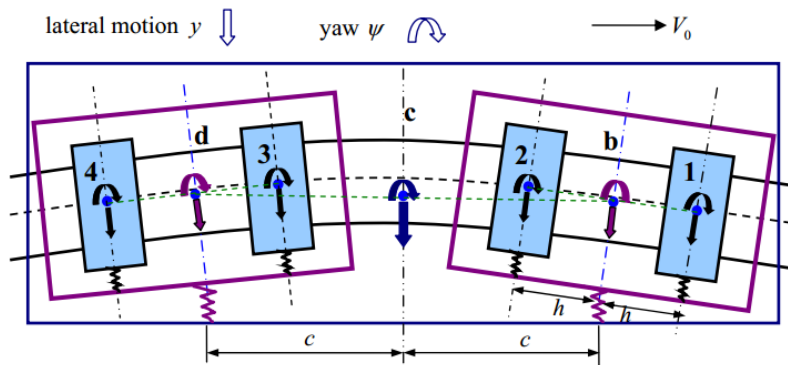


Figure 2.6 Definition of the reference points and coordinate systems of main components of an idealised bogie vehicle, under the condition in which the primary suspension springs are relaxed and the secondary suspension springs are in their initial positions [69]

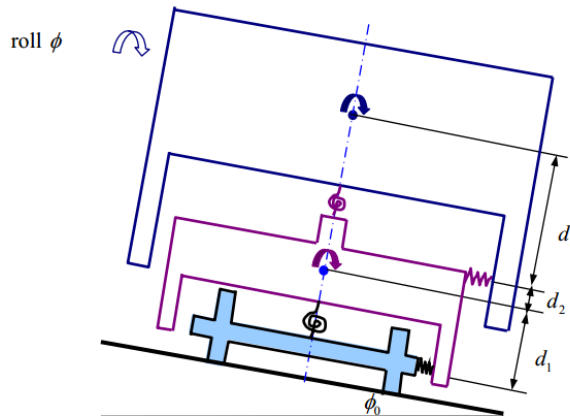


Figure 2.7 Rear view of the bogie vehicle [69]

### 2.3.5 Curving behaviour

To introduce the curving behaviour, first a free wheelset is considered. The running surface of the wheel has an approximately conical geometry to keep the motion of the train aligned

<sup>1</sup> In the commercial software or other models, a conventional vehicle model will include the vertical motions of the wheelsets, bogies and vehicle body, and the pitch motions of the bogies and vehicle body, as well as the motions included in the current steady-state curving model.

with the track. A schematic view of a free wheelset running on a curved track is shown in Figure 2.8.

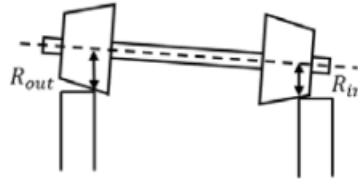


Figure 2.8 A free wheelset passing the curve [44]

To achieve the radial steering and to pass the curve, the wheelset axis points outwards from the centre of the curve. Thus, the outer wheel of the wheelset rolls a longer distance compared with the inner wheel. To balance this distance difference, the wheel radii of outer and inner wheels should also have a difference and satisfy the relationship:

$$\frac{R_{out}}{R_{in}} = \frac{R+l}{R-l} \quad (2.3)$$

where  $R_{out}$  and  $R_{in}$  are the wheel radii of the outer and inner wheels, respectively,  $l$  is half the lateral distance between the contact points of the two wheels and  $R$  is the curve radius.

If the wheel is conical, as indicated in Figure 2.6, the wheel radii of the outer and inner wheels can also be given as:

$$R_{out} = r_0 + \delta_0 \Delta y \quad (2.4)$$

$$R_{in} = r_0 - \delta_0 \Delta y \quad (2.5)$$

where  $r_0$  is the nominal wheel radius,  $\Delta y$  is the lateral displacement of the wheelset, and  $\delta_0$  is the conicity of the wheel (see Figure 2.9 as an example for the outer wheel). Substituting Equations (2.4) and (2.5) into Equation (2.3), the lateral displacement  $\Delta y$  of the wheelset can be written as:

$$\Delta y = \frac{r_0 l}{\delta_0 R} \quad (2.6)$$

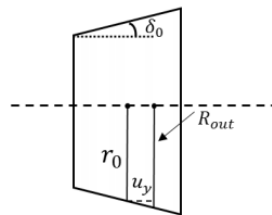


Figure 2.9 Outer wheel rolling radius when running in a curve [44]

If the lateral displacement  $\Delta y$  is achieved exactly, the free wheelset would curve along the

---

equilibrium rolling line.

As observed by Wickens [70], when a free wheelset is running on a straight track, it would exhibit a kinematic oscillation instead of stable running. Thus, the wheelsets of railway vehicles are mounted in bogies. To ensure the stability, usually two wheelsets are connected by a rigid frame within a bogie. Therefore, the curving behaviour of a bogie will differ from that of a free wheelset.

Due to the rigid frame of the bogie, the wheelsets are fixed in the longitudinal direction. The axles of the two wheelsets are also constrained and cannot take up a radial position in the curve. This will cause a considerable angle of attack (yaw angle of the wheelset relative to the rail) of the wheelsets. In practice, the wheelsets, as well as the rigid frame, are connected by the suspensions including springs and dampers in the vertical, lateral and longitudinal directions. They not only stabilize the tendency of the wheelsets to oscillate, but also facilitate the motion of the vehicle when negotiating curves.

Many parameters can affect the curving behaviour of a bogie or vehicle, such as the curve radius, the cant angle and the vehicle speed. Cant deficiency is present when the cant angle of the track in a curve provides less centripetal acceleration than that required to achieve the balanced cant by a specific curve radius  $R$  and vehicle speed  $V_0$ :

$$\phi_0 < \tan^{-1} \left( \frac{V_0^2}{R_0 g} \right) \quad (2.7)$$

Cant (and therefore cant deficiency) is often defined in terms of the height difference between the two rails. The usual maximum allowed cant is 150 mm. Thus, for some cases, zero cant deficiency is not realistic. If the required cant to achieve zero cant deficiency is larger than the maximum value, the cant angle (which is the inverse tangent of the ratio of the cant to the gauge) is smaller than required and cant deficiency exists.

For a small radius curve, if the vehicle runs at a low speed, the leading wheelsets move outwards in the curve while the trailing wheelsets move inwards. Thus, the outer wheel of the leading wheelset and the inner wheel of the trailing wheelset are very likely to be in flange contact. When the vehicle runs at a much higher speed, the trailing wheelset would also tend to move outwards. From this it can be seen that the angle of attack of the leading wheelset in small radius curves is higher than that in larger radius curves.

---

## 2.4 Modification of the steady-state curving model

In the steady-state curving model described above, the creep forces are calculated by the FASTSIM algorithm [13]. In Huang's work [69], the conventional FASTSIM algorithm without falling friction is adopted and no traction or braking forces are applied. In some practical analyses, the traction applied to the wheel is also considered as it is an important factor in the formation of the rail corrugation [3]. In addition, large creepages or spin may be present. In this situation, some modifications are needed in FASTSIM to consider the contact nonlinearity and falling friction coefficient.

### 2.4.1 Applied traction under constant friction

Firstly, the effect of an applied traction is considered under a constant friction coefficient in the steady-state curving model. The effect of braking can be found in a similar manner. To include the effect of the applied traction, an iteration process is added in the FASTSIM algorithm. The exact relationship between the creepage and the creep force is not known, so an estimated additional longitudinal creepage is initially added to the original one. Through the iteration process, the resultant longitudinal creepage is obtained for which the longitudinal creep force attains an increase of the same value as the applied traction.

This iteration process is effective whether the longitudinal creep force saturation is reached or not and used to find the estimated resultant longitudinal creepage. When the sum of the original longitudinal creep force and the applied traction is beyond the saturation, the exact value of the longitudinal creepage is hard to obtain since the relationship between the creepage and the creep force is nonlinear here. Fortunately, the final parameter needed for the following calculation is the creep force, not the creepage. As Figure 2.4 shows, when the creep force saturation is reached under a constant friction coefficient, the ratio of the creep force to the normal load is also constant. The resultant longitudinal creep force is then equal to the value of saturated creep force in this case. Since the outputs of the FASTSIM algorithm used for the steady-state curving simulation are the creep forces, the error of the resultant longitudinal creepage can be neglected.

### 2.4.2 Applied traction under velocity-dependent friction

For large creepage, including the situations with tractions applied to the wheels, the wheel-rail friction coefficient is considered as velocity-dependent, reducing with increasing slip velocity. An assumption has been made that the velocity-dependent friction coefficient is different for each point in the contact patch since the local slip is different on each point in

---

the contact area. This is described in more detail later in Section 6.2.2.

Since the FASTSIM algorithm is used for tangential creep force calculation in the current steady-state curving model, the local slip of each point on the contact area is hard to obtain. The friction coefficient for each point is also hard to determine. Thus, the assumption above has been adjusted and the variable friction coefficient can instead be taken as the same for each point in the contact [79]. In FASTSIM,  $c_{ij}$ , the creep coefficient which is a function of the contact aspect ratio, is used to get the contact flexibility coefficient  $L$  defined by Kalker [13] and further the creep force. The creep coefficients  $c_{ij}$  apply to the linear region of the creep force-creepage relation. When using these coefficients, FASTSIM is sufficient in the linear region. The creep coefficient values are tabulated by Kalker [13] and are plotted in Figure 2.10 for a Poisson's ratio of 0.3.

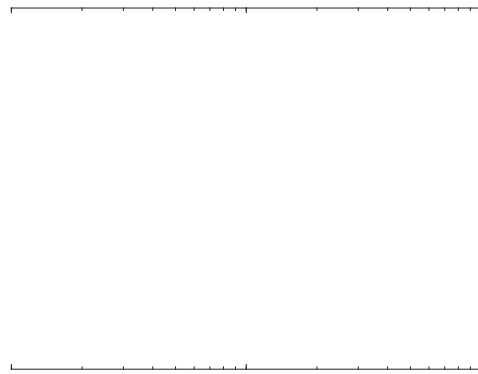


Figure 2.10 Creep coefficients

To realise the creepage-creep force relationship under a velocity-dependent friction coefficient in the FASTSIM algorithm, a replacement of contact flexibility parameter  $L$  used in the algorithm is carried out. For very small creep values in the micro-creep domain, the contact deforms elastically, and the traction stress distribution corresponds to Kalker's theory [13]. With increasing traction, the contact deforms elastically and plastically, and the contact flexibility parameter  $L$  becomes lower. The nonlinear deformation and corresponding nonlinear tangential stress distribution which exist when the creep force saturation is reached, can be represented by a linear deformation using a lower flexibility parameter. To achieve the effect of the contact nonlinearity, a variable reduction factor  $k$  [80,81] is applied to reduce Kalker's coefficients  $c_{11}$ ,  $c_{22}$ ,  $c_{23}$ .

It is assumed that the factor  $k$  reduces with increasing ratio of the slip area to the adhesion area. Therefore, it requires a mathematical description of the change of the ratio between

the slip area and the adhesion area as a function of creepage. For the variable stiffness reduction factor  $k_{re}$  the expression proposed in [79] is used

$$k_{re} = k_0 \left( \alpha_{inf} + \frac{1-k_{inf}}{1+\beta_{re}\varepsilon_{re}} \right) \quad (2.8)$$

where  $k_0$  is the initial value of Kalker's reduction factor at creep values close to zero,  $0 < k_0 \leq 1$ ; Kalker's reduction factor is dependent on the surface roughness [82,83] and contamination [82];  $\alpha_{inf}$  is the ratio of the reduction factor at creep values approaching infinity to Kalker's initial value,  $0 < \alpha_{inf} \leq 1$ ;  $\beta_{re}$  is a non-dimensional parameter related to the decrease of the contact stiffness with the increase of the slip area size,  $0 \leq \beta_{re}$ ;  $\varepsilon_{re}$  is a parameter describing the gradient of the tangential stress in the stress distribution transformed to a hemisphere which also represents the ratio of the slip area to the area of adhesion:

$$\varepsilon_{re} = \frac{1}{4} \frac{G\pi ab k_0 c_{11} \gamma_{total}}{Q\mu} \quad (2.9)$$

where  $G$  is the shear modulus,  $a$  is the semi-axis of the contact ellipse in the longitudinal direction;  $b$  is the semi-axis of the contact ellipse in the lateral direction;  $c_{11}$  is Kalker's coefficient;  $Q$  is the wheel load;  $\mu$  is the coefficient of friction;  $\gamma_{total}$  is the total creepage, which can be defined as

$$\gamma_{total} = \sqrt{\gamma_{x\varphi}^2 + \gamma_y^2} \quad (2.10)$$

where  $\gamma_{x\varphi} = \gamma_x + a\gamma_\varphi$ , in which  $\gamma_\varphi$  is the relative spin, rad/m. If the values of lateral creepage and spin have opposite signs and the total lateral creepage is lower than the pure lateral creepage, the higher absolute value of  $\gamma_\varphi$  and  $\gamma_x$  is selected.

Finally, the contact flexibility coefficient  $L$  defined by Kalker [13] is increased and the new value  $L^*$  is calculated as

$$L^* = \frac{L}{k_{re}} \quad (2.11)$$

or Kalker's coefficients  $c_{11}$ ,  $c_{22}$ ,  $c_{23}$  are reduced through multiplying by the stiffness reduction factor  $k_{re}$ .

## 2.5 Steady-state curving results

The steady-state curving simulation involves simulating a quasi-steady time-history of vehicle motion in a curve; convergence at the steady state is achieved via step-by-step integration. If the simulation process is convergent, the integration process can start from arbitrary reasonable initial conditions and will finally provide the quasi-steady results. Considering the nonlinear characteristics of the wheel-rail contact forces, a fourth order Runge-Kutta integration algorithm is applied in the integration.

Table 2.1 Bogie vehicle parameters provided by Wickens [70]

Parameter	Value	Units
Nominal wheel radius $r_0$	0.45	m
Half distance of the track gauge $l_0$	0.75	m
Half distance between two wheelsets in a bogie $h$	1.25	m
Half distance between two bogies in a vehicle $c$	8.75	m
Vertical distance between the bogie and primary suspension $d_1$	0.20	m
Vertical distance between the bogie and secondary suspension $d_2$	0.40	m
Vertical distance between the vehicle body and primary suspension $d_3$	1.00	m
Mass of the wheelset $m_w$	1250	kg
Yaw inertia of the wheelset $I_{zw}$	700	kgm <sup>2</sup>
Mass of the bogie $m_b$	2500	kg
Yaw inertia of the bogie $I_{zb}$	3500	kgm <sup>2</sup>
Roll inertia of the bogie $I_{xb}$	1000	kgm <sup>2</sup>
Mass of the vehicle body $m_c$	22000	kg
Yaw inertia of the vehicle body $I_{zc}$	10 <sup>6</sup>	kgm <sup>2</sup>
Roll inertia of the vehicle body $I_{xc}$	30000	kgm <sup>2</sup>
Lateral stiffness of the primary suspensions $k_y$	40	MN/m
Lateral damping of the primary suspensions $C_y$	0	kNs/m
Yaw stiffness of the primary suspensions $k_\psi$	40	MNm
Yaw damping of the primary suspensions $C_\psi$	0	kNms
Roll stiffness of the primary suspensions $k_\phi$	1	MNm
Roll damping of the primary suspensions $C_\phi$	10	kNms
Lateral stiffness of the secondary suspensions $k_{yb}$	0.45	MN/m
Lateral damping of the secondary suspensions $C_{yb}$	1	kNs/m
Yaw stiffness of the secondary suspensions $k_{\psi b}$	0	MNm
Yaw damping of the secondary suspensions $C_{\psi b}$	0	kNms
Roll stiffness of the secondary suspensions $k_{\phi b}$	1	MNm
Roll damping of the secondary suspensions $C_{\phi b}$	60	kNms

In curving, the wheelsets in the bogie cannot move freely to the equilibrium position or rotate to achieve radial alignment like unconstrained wheelsets, but they are constrained by the stiffness between the bogie frame and the wheelsets. The steady-state curving behaviour of the bogie can be reached when all the external forces and torques acting on both wheelsets are balanced. For a bogie vehicle, since the resistance of the secondary suspension to the bogie rotation is relatively low, the curving behaviour of the leading and trailing bogies is similar.

For verification, a bogie vehicle described by the parameters in Table 2.1 is simulated. It has two bogies connected to the vehicle body through secondary suspensions. The right-



hand curve radius is of  $R_0 = 150$  m, which is tight enough to generate rail corrugation. The vehicle speed is  $V_0 = 10$  m/s and the cant deficiency is zero (i.e. the cant angle is set such that the resultant of gravity and centripetal accelerations is directed normal to the track plane). The Coulomb friction coefficient is taken as  $\mu_0 = 0.3$ . The tangential force model is based on the modified FASTSIM [79] described in Section 2.4.2. The simulation is started from initial conditions with every coordinate in its zero position and lasts 1 second until steady-state conditions are reached. In this case, the yaw stiffness between the bogies and the vehicle body is set to zero, so that the curving behaviour of the leading and trailing bogies is identical. Only the results of the leading bogie are shown in Figures 2.11-2.13.

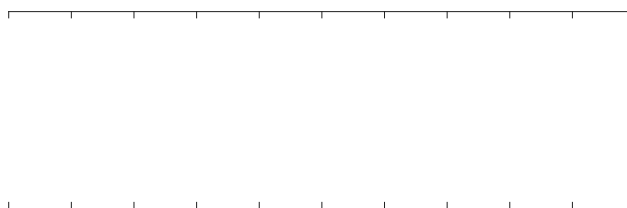


Figure 2.11 Convergence to steady-state curving behaviour of the leading and trailing wheelsets of a bogie

The lateral displacements and yaw angles of the two wheelsets are shown in Figure 2.11. The leading wheelset moves outward into flange contact and has a yaw angle of -14 mrad, while the trailing wheelset moves inward in the curve without flange contact and has almost zero yaw angle. The behaviour of the bogie frame (not shown) is almost the average of that of the two wheelsets. The steady-state results are reached after about 0.5 seconds.

Figure 2.12 shows the steady-state creepages at each contact. In Figure 2.12(a), as in the discussion of curving behaviour of the bogie (given in [69]), the left and right longitudinal creepages of the leading wheelset are opposite to the corresponding ones in the trailing wheelset. Thus, two frictional torques with opposite directions are in balance within the bogie. In Figure 2.12(b), the negative yaw angle of the leading wheelset produces negative lateral creepages at both left and right wheel/rail contacts. As the leading left (outer) wheel is in flange contact with a large contact angle, the lateral creepage at the leading left

contact is greater than that at the leading right contact. Due to the zero yaw angle of the trailing wheelset there is no lateral creepage (Lateral creepage of trailing left and right wheels are identical). As shown in Figure 2.12(c), significant spin can be found in the leading outer (left) wheel/rail contact.

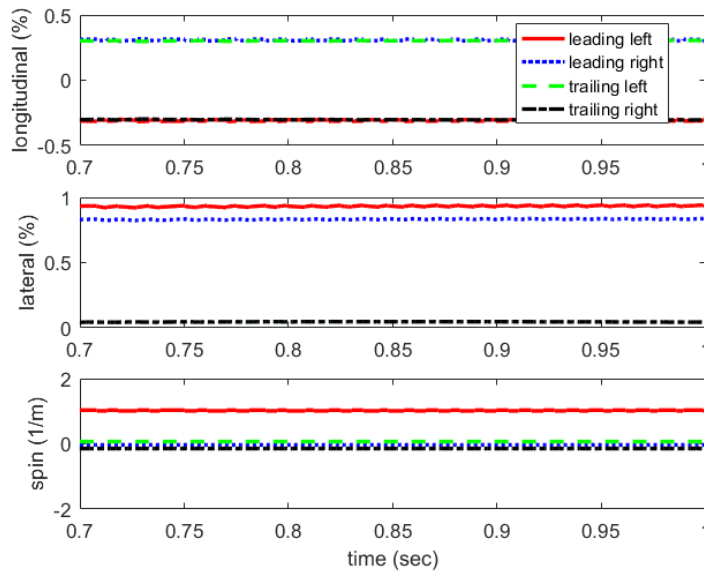


Figure 2.12 Convergence to steady-state creepages at wheel-rail contacts of a bogie vehicle

The normal load is obtained through an iteration process starting from the nominal normal load value, as shown in Figure 2.13. The nominal normal force in the current case is 39.2 kN which is the one-eighth of the weight of the whole vehicle. Usually, the greater the contact angle, the larger the normal force, i.e. there is a large normal force at the leading outer contact due to flange contact. Additionally, the flange contact at the leading outer wheel can induce a roll angle of the leading wheelset, and consequently the bogie. The contact angle is not considered in the wheel-rail interaction model.

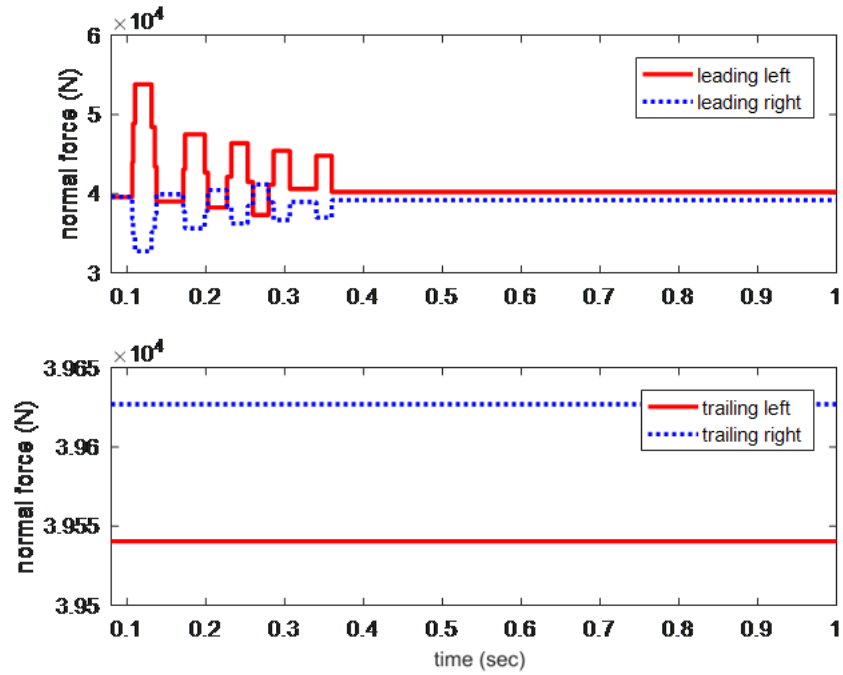


Figure 2.13 Convergence to steady-state normal loads of the wheels of a bogie vehicle

The steady-state curving simulation given above considers the vehicle running on a curved track without any external forces or moments. In practice, traction or braking forces are often applied to the wheelset. It is known that the traction or braking forces can also exacerbate the rail corrugation. So, the modification described in Section 2.4 has been applied in the steady-state curving model.

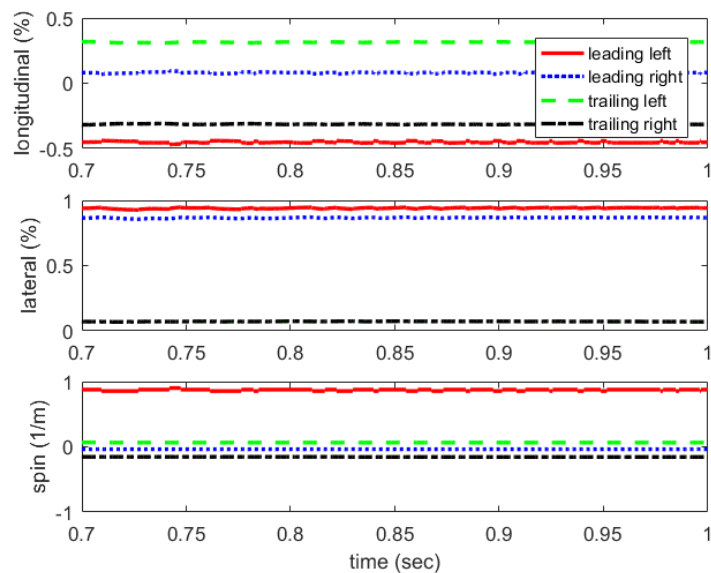


Figure 2.14 Convergence to steady-state creepages of the wheels of a bogie vehicle at wheel-rail contacts with applied traction

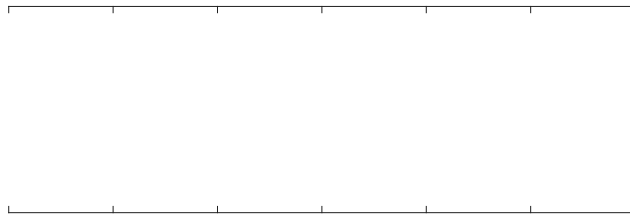


Figure 2.15 Convergence to steady-state longitudinal creep force of the wheels of a bogie vehicle with applied traction

Normally, the traction would be applied to both wheelsets of a bogie. For demonstration, however, the traction is assumed here to be applied only to the leading wheelset of the leading bogie. The traction will directly increase the longitudinal creepage and creep force. Since equilibrium within the bogie needs to be achieved, when an external traction force applied, the wheelsets will generate higher longitudinal creep forces. An example is shown in Figure 2.14-2.15 in which a 2 kN traction force is applied (for simplicity the vehicle is assumed not to accelerate). Other parameters used in the simulation are the same as previously.

The leading wheelset which has the applied traction shows obvious differences. The longitudinal creepage and creep force of the left and right wheel of the leading wheelset are no longer opposite to each other. The value of the longitudinal creepage is shifted to a larger negative value, which makes the longitudinal creep force increase in the direction opposite to the running direction. For the trailing wheelset, for which no traction was applied, the longitudinal creepage and creep force of the left and right wheel are also affected in order to achieve the balance within the bogie. The falling of the friction forces at large sliding velocities does not play a significant role in the vehicle dynamics [78]

## 2.6 Summary

This chapter gives a general introduction to the steady-state curving model developed by Huang [69], including the wheel-rail interaction and vehicle dynamics. The curving behaviour of a free wheelset and bogie are also briefly introduced. To give better

---

understanding of the steady-state curving model, the definitions of creepage and rolling friction are also introduced. The difference between static and dynamic friction is explained and will be used in Chapter 5 to explain stick-slip phenomena. In the steady-state curving model, the vehicle dynamics are more important than the track system dynamics. Thus, the results, i.e., contact position, creepages, spin and normal loads, are mainly dependent on the vehicle dynamics. Some modifications are also applied to the steady-state curving model developed by Huang [69] in this work. As the model will be applied in a tightly curved track, a velocity-dependent friction coefficient and reduction factor are applied in the calculation of the creep force. The effect of traction forces applied to the wheelset is also considered in the current work since the traction is also believed to be an important factor in the initiation of rail corrugation.



---

## 3 Track model

### 3.1 Introduction

A mathematical representation of the track dynamic behaviour is required in modelling the high frequency dynamic interaction between the vehicle and the track. Much work has been done in this area and many track system models have been established in both frequency and time domains. The complexity of these track system models has a wide range, starting from simple beams on a continuous elastic support to complex multiple degree-of-freedom models with discrete supports beneath each rail including variable constraints and additional components applied to the rail.

A combination of two previously-established modelling approaches in the frequency domain [84,85] is firstly used as the basis for the work in the current research. Kostovasilis [84] represented the rail as an infinite Timoshenko beam including bending, torsion (with warping) and extension. The modelling of the rail dynamic behaviour considered 7 degrees of freedom (3 displacements, 3 rotations and 1 for the warping). The sleeper was similarly represented as a finite Timoshenko beam, including bending, torsion and extension, considering 6 degrees of freedom. It is supported on a continuous foundation representing the ballast. The rail was supported by an equivalent continuous support consisting of the sleepers, ballast and rail pads. In the present model, the rail is instead attached to discrete sleepers. The coupling between the rail and the sleepers through the rail pads is based on the method of Zhang et al. [85]. Then the frequency response functions of this analytical track model are transformed from the frequency domain to the time domain by applying a Fourier transform. These time-domain impulse responses are sampled appropriately to obtain moving Green's functions using the method of [86]. The time-domain moving Green's functions are used throughout the thesis to determine the dynamic displacement of the rail, required as the input to calculate the dynamic normal interaction force in the contact model.

In this chapter, the development process of the track model is presented in detail. For each part of the model, numerical examples are presented. To validate the current model, results are compared with published results.

### 3.2 Review of track models

A typical ballasted track consists of rails, rail pads, sleepers and ballast. A suitable model

---

for this kind of railway track should consider the discrete nature of the support as well as the coupling between the vertical and lateral directions. Many authors have used analytical beam models to study the vertical dynamics of the rail and have commonly assumed an equivalent continuous support, e.g. [87,88]. They mainly focused on the vertical vibration but paid less attention to the lateral vibration or the coupling between the vertical and lateral directions [89]. Thompson et al. [90,91] used a Timoshenko beam on a two-layer foundation to model both the vertical and lateral track dynamics and estimated the cross receptance between vertical and lateral directions from the geometrical average of the vertical and lateral receptances, using an empirical scaling factor.

The effect of the discrete nature of the support is most evident around the ‘pinned-pinned’ frequency, at which the sleeper spacing corresponds to half a bending wavelength in the rail. Grassie et al. [92] proposed a discretely supported track model, in which the sleepers were represented by lumped masses and the rail pads and ballast by damped springs. Compared with the continuously supported track model, a resonance peak was found at the pinned-pinned frequency for excitation between sleepers and a corresponding dip for excitation above the sleepers. Heckl [93] introduced a discretely supported track model in which an infinite Timoshenko beam was used to represent the vertical vibration of the rail, while a finite number of discrete supports were considered, which were replaced by point reaction forces acting on the infinite rail. Heckl [94] later developed a model of a Timoshenko beam, including torsional and extensional waves, with an infinite number of periodically spaced supports, and studied coupled waves in all three directions. Wu and Thompson [95,96] developed continuously supported multiple beam models to explore the vertical and lateral response including an approximation for cross-sectional deformation. However, the effect of vertical/lateral coupling was not considered.

At higher frequencies cross-sectional deformation of the rail becomes important [97]. Numerical methods can be used to include the effects of cross-sectional deformation in the track response. Thompson [97] modelled a short slice of rail on a continuous support using finite elements and used periodic structure theory to obtain the dispersion relationship and receptances. Knothe et al. [98] used the finite strip method, in which only the cross-section of the rail is discretised, to study the free wave propagation in a rail. Similarly, Ryue et al. [99] determined the waves propagating in a continuously supported rail up to 80 kHz using the waveguide FE method (also known as the 2.5D FE method). Nilsson et al. [100] used the waveguide FE and boundary element methods to calculate the vibration and sound radiation of an infinite continuously supported rail. A similar



---

approach has been used for a continuously supported rail with multiple layer support [101].

Numerical methods also have disadvantages, however, particularly the more extensive computational capacity and increased calculation time required compared with analytical or semi-analytical models. The rail is effectively infinite in length but a finite element model necessarily has to be truncated, leading to reflections from the ends, although this can be avoided with 2.5D models. Besides that, analytical models have their own advantages of offering increased physical insight.

Bhaskar et al. [102] introduced an analytical model that accounted for the lateral and torsional motion of the rail up to around 2 kHz. The rail head was represented as a beam which was allowed to bend in three directions and rotate around the axial direction. The rail web and foot were represented by three plates, one for the web and one for the foot on each side of the web. The rail responses were obtained by Fourier integrals. Betgen et al. [103] showed, in comparison with measurements and a detailed finite element (FE) model, that the analytical beam models of [92] were unable to capture some key characteristics of the response, particularly the vertical-lateral cross mobility and track decay rates. The lateral position of the vertical excitation force was shown to have a great influence on the cross mobility. To overcome the disadvantages of numerical models, Kostovasilis et al. [84] introduced a semi-analytical rail model which accounts for vertical and lateral bending, extension and torsion. Although cross-section deformation was not considered, the inclusion of torsion and corrections for shear deformation, shear centre eccentricity and warping improved the lateral response of the track. In comparison with measurements and the results from a waveguide FE model, good agreement was found for the vertical and lateral mobilities for frequencies up to 3 kHz and for the decay rates up to 2 kHz. There was also generally good agreement for the vertical-lateral cross mobility.

In the track models discussed above, the sleeper was either neglected or was modelled as a rigid mass. This simplification ignores the bending modes that monobloc sleepers exhibit in the frequency range above 100 Hz. Grassie and Cox [104] modelled the sleepers as finite uniform Timoshenko beams supported by an elastic layer, while Nielsen and Igeland [105] used beam finite elements to account also for the variable cross-section. Grassie [106] proposed a simple uniform Timoshenko beam model for a freely suspended sleeper and a similar model was subsequently used in the TWINS model [91], but including an elastic layer beneath the sleeper to represent the ballast. Usually, the rail pads

are presented by a model with a single spring-damper or a spring using a loss factor damping. The effects of using loss factor on causality have been verified. Ferrara et al. considered the rail pads as a series of massless spring-damper finite elements placed across the width of the sleepers and along the rail [107]. Zhang et al. [85] established a rail model by applying the 2.5D finite element method and predicted the overall track system responses and decay rates by using a receptance-coupling approach similar to [93]. The effects of different sleeper models and the number of springs used to represent the rail pad on the responses of the track system were also studied.

In the present work, a semi-analytical model of a discretely supported track is introduced with the aim of better predicting the track dynamics without resorting to fully numerical models. The model includes both rails and considers the vertical/lateral coupling as well as the axial dynamics. Infinitely long rails are modelled using the semi-analytical approach of Kostovasilis et al. [84]. The rails are connected to a finite number of sleepers through damped springs. The sleepers are represented by flexible beams, supported on a viscoelastic layer representing the ballast. A receptance coupling method [85, 93] is used to couple the rails to the sleepers. The point mobilities and track decay rates are obtained using this model and compared with results from measurements. The effect of the inclusion of torsion and warping on the lateral track response is also investigated. Finally, the response of one rail to excitation on the other is presented.

### 3.3 Frequency domain model

For mainline tracks the rail cross-section, for example 60E1 rail, is symmetric about the vertical mid-plane but is asymmetric about the horizontal mid-plane. This results in the shear centre, through which the shear forces are considered to act, not being coincident with the centroid through which the inertial forces are considered to act, as shown in Figure 3.1. This introduces a coupling between the lateral bending and torsion.

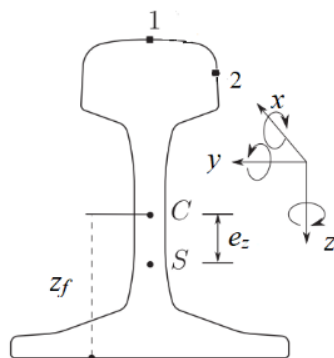


Figure 3.1 The coordinate system, shear centre  $S$  and centroid  $C$  of the rail cross-section

Various methods are available to model the vibration of a track with discrete supports, Figure 3.2(a). The approach applied here is based on the advanced beam model of Kostovasilis et al. described in Appendix B, which includes bending, torsion, warping and extension [84]. This beam model is implemented in the discrete support framework proposed by Heckl [93]. This latter approach replaces the discrete rail supports by a set of point forces acting on an infinite free rail. To implement this method, the point and transfer receptances of the free rail are required, as well as the receptances of the sleepers and rail pads. In the current model, two rails are coupled to flexible sleepers, as shown in Figure 3.2(b).

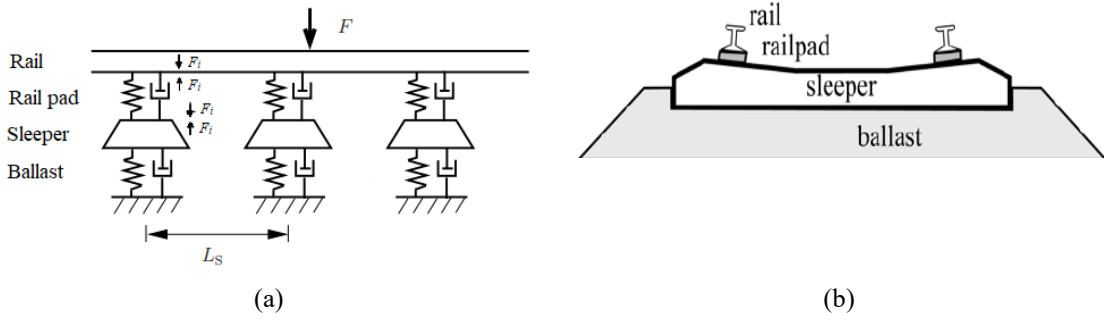


Figure 3.2 (a) Side view of track model, where  $L_s$  is the sleeper spacing;  $F_i$  is the force transmitted at the  $i$ th discrete support; (b) front view of track model, showing two rails connected to the sleeper

### 3.3.1 Rail model

The semi-analytical rail model developed by Kostovasilis [84] is used, which considered various sources of vertical-lateral coupling. Cross-section deformation is not taken into account but instead the rail is treated as a simple beam cross-section, accounting for vertical and lateral bending, extension and torsion. This is sufficient for the frequency range of interest up to 3000 Hz. Corrections for shear deformation, shear centre eccentricity and warping are included.

By extending the classical Timoshenko beam model and taking the sum of the stress resultants including forces and moments acting on the centroid of an infinitesimal element in all three directions, as well as the bi-moment in the axial direction due to warping, seven equations of motion for the fully coupled rail are obtained in matrix form [84]:

$$\mathbf{K}_0 \mathbf{U} + \mathbf{K}_1 \frac{\partial \mathbf{U}}{\partial x} + \mathbf{K}_2 \frac{\partial^2 \mathbf{U}}{\partial x^2} + \mathbf{M} \frac{\partial^2 \mathbf{U}}{\partial t^2} = \mathbf{F} \quad (3.1)$$

where  $\mathbf{U}(x,t)$  is a vector of the seven components (i.e. 3 displacements, 3 rotations and 1 warping) of vibration at the centroid. The matrices  $\mathbf{K}_0$ ,  $\mathbf{K}_1$ ,  $\mathbf{K}_2$ ,  $\mathbf{M}$  for the fully coupled model are given by

$$\mathbf{K}_0 = \begin{bmatrix} 0 & 0 & 0 & 0 & 0 & 0 & 0 \\ 0 & 0 & 0 & 0 & 0 & 0 & 0 \\ 0 & 0 & 0 & 0 & 0 & 0 & 0 \\ 0 & 0 & 0 & 0 & 0 & 0 & 0 \\ 0 & 0 & 0 & 0 & G\kappa_z & 0 & G\kappa_z e_y \\ 0 & 0 & 0 & 0 & 0 & G\kappa_y & G\kappa_y e_z \\ 0 & 0 & 0 & 0 & G\kappa_z e_y & G\kappa_y e_z & J_t \end{bmatrix} \quad (3.2)$$

$$\mathbf{K}_1 = \begin{bmatrix} 0 & 0 & 0 & 0 & 0 & 0 & 0 \\ 0 & 0 & 0 & 0 & 0 & -G\kappa_y & -G\kappa_y e_z \\ 0 & 0 & 0 & 0 & G\kappa_z & 0 & G\kappa_z e_y \\ 0 & 0 & 0 & 0 & -G\kappa_z e_y & -G\kappa_y e_z & -J_t \\ 0 & 0 & -G\kappa_z & G\kappa_z e_y & 0 & 0 & 0 \\ 0 & G\kappa_y & 0 & G\kappa_y e_z & 0 & 0 & 0 \\ 0 & G\kappa_y e_z & -G\kappa_z e_y & J_t & 0 & 0 & 0 \end{bmatrix} \quad (3.3)$$

$$\mathbf{K}_2 = \begin{bmatrix} -EA & 0 & 0 & 0 & 0 & 0 & 0 \\ 0 & -G\kappa_y & 0 & -G\kappa_y e_z & 0 & 0 & 0 \\ 0 & 0 & -G\kappa_z & G\kappa_z e_y & 0 & 0 & 0 \\ 0 & -G\kappa_y e_z & G\kappa_z e_y & -G(J_t + J) & 0 & 0 & 0 \\ 0 & 0 & 0 & 0 & -EI_y & EI_{yz} & EI_{wy} \\ 0 & 0 & 0 & 0 & EI_{yz} & -EI_z & -EI_{wz} \\ 0 & 0 & 0 & 0 & EI_{wy} & -EI_{wz} & -EI_w \end{bmatrix} \quad (3.4)$$

$$\mathbf{M} = \begin{bmatrix} \rho A & 0 & 0 & 0 & 0 & 0 & 0 \\ 0 & \rho A & 0 & 0 & 0 & 0 & 0 \\ 0 & 0 & \rho A & 0 & 0 & 0 & 0 \\ 0 & 0 & 0 & \rho I_p & 0 & 0 & 0 \\ 0 & 0 & 0 & 0 & \rho(I_y + I_{wy}) & 0 & -\rho I_{wy} \\ 0 & 0 & 0 & 0 & 0 & \rho(I_z - I_{wz}) & \rho I_{wz} \\ 0 & 0 & 0 & 0 & -\rho I_{wy} & \rho I_{wz} & \rho I_w \end{bmatrix} \quad (3.5)$$

where  $\mathbf{K}_0$  is the classical stiffness matrix,  $\mathbf{K}_1$  and  $\mathbf{K}_2$  contain stiffness terms related to the first and second derivatives in the  $x$  direction and  $\mathbf{M}$  is the inertial matrix.

In the matrices presented in Equation (3.2)-(3.5),  $E$  is the Young's modulus,  $G$  is the shear modulus,  $A$  is the cross-section area,  $\rho$  is the density,  $\kappa_y$  and  $\kappa_z$  are the lateral and vertical shear coefficients,  $e_y$  and  $e_z$  are the lateral and vertical shear centre eccentricity,  $J$  is the torsional constant,  $I_y$  and  $I_z$  are the second moments of area about the  $y$ -axis and  $z$ -axis,  $I_{yz}$  is the product moment of area,  $I_p$  is the polar moment of area,  $I_w$  is the warping constant,  $I_{wy}$ ,  $I_{wz}$  are warping product moments of area, and  $J_t$  is the second torsional constant, representing the effective shear due to restrained warping shear stresses including the effects of eccentricity in the  $y$  and  $z$  axes, which is calculated by

$$J_t = J_{rs} + A\kappa_z e_y^2 + A\kappa_y e_z^2 \quad (3.6)$$

The effective shear area is given by Equation (B.23). Since the value of the correction factor will not affect the response of the beam significantly, the  $\kappa_s = 1$  is used here.

The responses are assumed to be harmonic both in space and time with circular frequency  $\omega$  and complex wavenumber  $\zeta$  as

$$\mathbf{U} = \tilde{\mathbf{U}} e^{i\omega t} e^{-i\zeta x} \quad (3.7)$$

in which  $\tilde{\mathbf{U}} = [\tilde{U}_x, \tilde{U}_y, \tilde{U}_z, \tilde{\theta}_x, \tilde{\theta}_y, \tilde{\theta}_z, \tilde{U}_w]^T$  is a vector of complex amplitudes, consisting of seven components of vibration (three displacements, three rotations and warping) at the centroid.  $\mathbf{F}$  is the corresponding vector of the external forces and moments, which is assumed to act at  $x = 0$ , and is given as  $\mathbf{F} = \tilde{\mathbf{F}} e^{i\omega t} \delta(x)$  with  $\tilde{\mathbf{F}}$  the vector of the corresponding amplitudes in the wavenumber domain.

By substituting above expressions for  $\mathbf{U}(x,t)$  and  $\mathbf{F}$ , the equation of motion is obtained in the wavenumber domain as

$$((\mathbf{K}_0 - \omega^2 \mathbf{M}) - i\zeta \mathbf{K}_1 - \zeta^2 \mathbf{K}_2) \tilde{\mathbf{U}} = \tilde{\mathbf{F}} \quad (3.8)$$

which can be written as  $\mathbf{A}(\zeta, \omega) \tilde{\mathbf{U}} = \tilde{\mathbf{F}}$ .

To solve Equation (3.8), the case of free vibration,  $\tilde{\mathbf{F}} = \mathbf{0}$ , is first considered. This can be viewed as a linear eigenvalue problem in squared frequency  $\omega^2$  for a given wavenumber  $\zeta$ , or equivalently as a quadratic eigenvalue problem in squared wavenumber  $\zeta^2$  for a given frequency  $\omega$ . Equation (3.8) is rewritten as:

$$\mathbf{A}_1 \mathbf{v} + i\zeta \mathbf{A}_2 \mathbf{v} = \mathbf{0} \quad (3.9)$$

where  $\mathbf{v} = [\tilde{\mathbf{U}}, i\zeta \tilde{\mathbf{U}}]^T$ ,

$$\mathbf{A}_1 = \begin{bmatrix} \mathbf{K}_0 - \omega^2 \mathbf{M} & -\mathbf{K}_1 \\ \mathbf{0}_{7 \times 7} & \mathbf{I}_{7 \times 7} \end{bmatrix} \quad (3.10)$$

and

$$\mathbf{A}_2 = \begin{bmatrix} \mathbf{0}_{7 \times 7} & \mathbf{K}_2 \\ -\mathbf{I}_{7 \times 7} & \mathbf{0}_{7 \times 7} \end{bmatrix} \quad (3.11)$$

Equation (3.9) can be solved to give complex wavenumbers  $\xi_n$ , which occur in pairs  $(\pm \xi_n)$ , and the corresponding  $(1 \times 7)$  left eigenvectors  $\mathbf{U}_{nL}$ , and  $(7 \times 1)$  right eigenvectors,  $\mathbf{U}_{nR}$ , for each frequency. To obtain the response in the spatial domain, the inverse Fourier transform is used:

$$\mathbf{U}(x) = \frac{1}{2\pi} \int_{-\infty}^{\infty} \tilde{\mathbf{U}} e^{-i\zeta x} d\zeta \quad (3.12)$$

This integration is performed analytically using the contour integration method from the theory of complex variables. For  $x \geq 0$ , the solution to the integral is given by the sum of the residues of the poles lying in the lower half plane,  $\text{Im}(\zeta_n) < 0$ . The poles are the eigenvalues determined from equation (3.9). The solution in the spatial domain is given for

$x \geq 0$  as [90]

$$\mathbf{U} = -i \sum_{n=1}^N \frac{\mathbf{U}_{nL} \tilde{\mathbf{F}}}{\mathbf{U}_{nL} \mathbf{A}'(\xi_n) \mathbf{U}_{nR}} \mathbf{U}_{nR} e^{-i\xi_n x} \quad (3.13)$$

where the dash means the derivative with respect to  $\xi$  and  $\xi_n$  are the  $N$  eigenvalues on the lower half-plane with  $\text{Im}(\xi_n) < 0$ . From Equation (3.8) the derivative can be written as

$\mathbf{A}'(\xi_n) = -2\xi_n \mathbf{K}_2 - i\mathbf{K}_1$ .  $x$  is the longitudinal distance between excitation and response points.

Finally, if the force vector in Equation (3.13) is set to unity in one direction and zero in the others, the mobility can be calculated from the response as  $\mathbf{V} = \frac{\partial \mathbf{U}}{\partial t} = i\omega \mathbf{U}$ .

To validate the implementation of the model, the forced response is firstly considered in terms of the point mobility in both vertical and lateral directions and compared with Kostovasilis's results. The rail section parameters used are listed in Table 3.1. As Kostovasilis's results included the support from rail pads, the above equations are extended to include an additional stiffness matrix  $\mathbf{K}_p$  to represent the effect of the rail pads. The support stiffness matrix  $\mathbf{K}_p$  includes the effect of the vertical and lateral distance between the rail centroid and the centre of the top surface of the rail pads which is shown in Figure 3.1 as  $z_f$  and  $y_f$ . The matrix can be given as:

$$\mathbf{K}_p = \mathbf{T}_f^T \mathbf{K}_{pf} \mathbf{T}_f \quad (3.14)$$

where

$$\mathbf{K}_{pf} = \text{diag}(k_x, k_y, k_z, k_{xr}, k_{yr}, k_{zr}, k_w) \quad (3.15)$$

contains the stiffness in each direction, and  $\mathbf{T}_f$  is a transformation matrix similar to Equation (B.26).

The rail pad parameters used are listed in Table 3.2. Damping loss factors are introduced for the rail and rail pads, making the corresponding Young's modulus, shear modulus and rail pad stiffness complex. The stiffness values in three directions given in Table 3.2 are for a single pad. For a continuously supported track, the equivalent stiffness per unit length is derived from the stiffness per pad divided by the sleeper spacing. For a discretely supported track, the stiffness of the pad can be used directly without finding the equivalent value.

For simplicity the rotational stiffnesses are estimated from the translational stiffness per pad, assuming a homogeneous material for the pad [93], as

$$k_{xr} = k_{yr} = \frac{l_p^2}{12} k_z \quad (3.16)$$

in which it is assumed that the pad is square with length  $l_p$ . Similarly, the rotational stiffness about a vertical axis can be given by

$$k_{zr} = \frac{l_p^2}{12} k_x + \frac{l_p^2}{12} k_y \quad (3.17)$$

The foundation resistance to warping is similarly defined as

$$k_w = (\kappa_w e_s)^2 \frac{l_p^2}{12} k_x \quad (3.18)$$

where  $\kappa_w$  is a factor relating the axial deformation of the rail foot due to warping to the warping amplitude (assuming a linear profile) and  $e_s$  is the vertical distance between the rail foot and the rail shear centre ( $z_f - e_z$ ) as shown in Figure 3.1.

Table 3.1 Rail section parameters for 60E1 rail (inertial properties relative to centroid) [84]

Parameter	Value	Units
Young's modulus $E$	210	GPa
Shear modulus $G$	80.769	GPa
Density $\rho$	7860	kg/m <sup>3</sup>
Poisson's ratio $\nu$	0.3	-
Cross-section area $A$	$7.670 \times 10^{-3}$	m <sup>2</sup>
Second moment of area about z-axis $I_z$	$512.7 \times 10^{-8}$	m <sup>4</sup>
Second moment of area about y-axis $I_y$	$3037 \times 10^{-8}$	m <sup>4</sup>
Product moment of area $I_{yz}$	0	m <sup>4</sup>
Polar moment of area $I_p$	$3.550 \times 10^{-5}$	m <sup>4</sup>
Torsional constant $J$	$2.212 \times 10^{-6}$	m <sup>4</sup>
Vertical shear coefficient $\kappa_z$	0.393	-
Lateral shear coefficient $\kappa_y$	0.538	-
Vertical shear centre eccentricity $e_z$	0.033	m
Lateral shear centre eccentricity $e_y$	0	m
Warping constant $I_w$	$2.161 \times 10^{-8}$	m <sup>6</sup>
Warping product moment of area $I_{wz}$	$1.6971 \times 10^{-7}$	m <sup>5</sup>
Warping product moment of area $I_{wy}$	0	m <sup>5</sup>
Warping factor for rail foot $k_w$	-0.6016	-

Table 3.2 Properties used for the rail pads [84]

Parameter	Value	Units
Rail pad axial stiffness $k_x^p$	40	MN/m
Rail pad vertical stiffness $k_z^p$	120	MN/m
Rail pad lateral stiffness $k_y^p$	40	MN/m
Pad damping loss factor	0.25	-
Rail pad width (rail foot) $l_p$	150	mm
Foot to centroid distance $z_f$	81	mm

Foot to centroid distance $y_f$	0	mm
Sleeper spacing $l_{sp}$	0.65	m

To validate the current rail model, numerical examples from [84] are considered. The parameters for the rail section and the rail pads are listed in Table 3.1 and 3.2. As Kostovasilis did in Ref. [84], the 60E1 rail is excited at various positions as shown in Figure 3.1. The calculation results are shown in the form of mobility, including three directions and the vertical-lateral cross mobility.

The first case (Figure 3.3(a)) shows the vertical point mobility at the rail centreline on the railhead (Position 1). The peak which occurs at about 290 Hz in the mobility curve is at the cut-on frequency of the vertical bending wave. The result from the Timoshenko beam model has a good agreement with the current model. However, for vertical excitation at Position 2, which is 10 mm from the web centreline, as well as the peak at about 290 Hz, a small peak at 100 Hz is also seen in the current model.

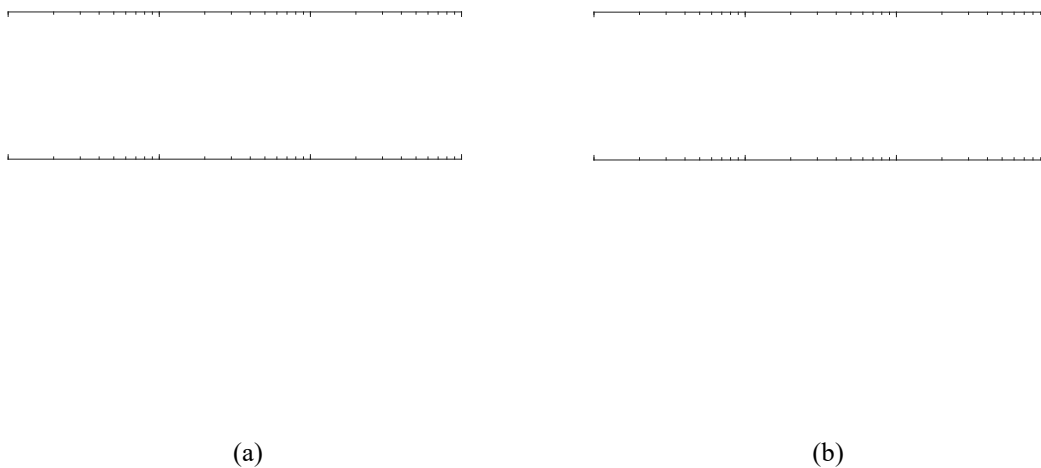


Figure 3.3 Point mobilities for 60E1 rail: (a) Vertical mobility; (b) Lateral mobility

The second case (Figure 3.3(b)) shows the lateral point mobility at Position 1, i.e. at the top of the railhead, and at Position 2, a point whose distance from the rail centreline on the railhead is  $\Delta y=36$  mm,  $\Delta z=20$  mm. Two peaks can be identified at low frequencies in both curves, one at about 100 Hz corresponding to the cut-on frequency of the lateral bending wave and the other at about 300 Hz corresponding to the torsional wave. The phase is similar in each case, but the magnitude of the lateral mobility at the top of the railhead is higher than at the side of the railhead.

Figure 3.4 shows the axial (longitudinal) mobility of the rail when excited at the centre of



---

the railhead (Position 1). A peak is seen at about 170 Hz, corresponding to the cut-on frequency of the first-order axial wave. A further peak occurs at about 5 kHz, corresponding to the cut-on of a higher order wave in the Timoshenko beam.

The cross mobility is the response in one direction when excited at the same position in another direction. Figure 3.5 shows the lateral response at the side of the railhead due to a vertical force for an offset of 10 mm or 20 mm from centre of the railhead. The results for 20 mm offset are a factor of 2 larger than the ones for 10 mm offset; for an offset of 0 the cross mobility is zero. For frequencies above 1 kHz, especially for an offset of 20 mm, cross-section deformation starts to become important and to influence the response of the rail [86]. Since the current model does not contain cross-section deformation, the results above 1 kHz will have some differences compared with practical results.

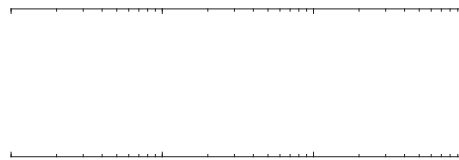


Figure 3.4 Axial point mobility for track

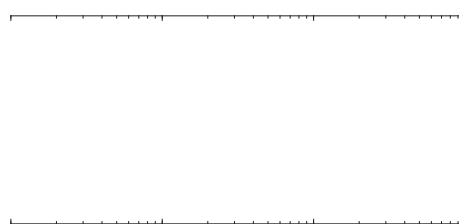


Figure 3.5 Vertical-lateral cross mobility for track excited in vertical direction

The mobilities presented above are calculated using the same parameters as Kostovasilis including the rail pad as a continuous support. The results show good agreement with those from Kostovasilis [84]. The implementation of this beam model in a discretely supported track will now be described.

---

### 3.3.2 Rail pad model

The rail pad connects the rail to the sleeper dynamically. Measurements have shown that the rail pad damping is well approximated by using a dynamic stiffness with a constant loss factor [97].

Each rail pad is considered here as a single damped spring in each direction. The dynamic stiffness of the rail pads has six components.  $k_x$ ,  $k_y$ ,  $k_z$  are used to represent the longitudinal, lateral and vertical stiffness as introduced in Equations (3.16-18).

### 3.3.3 Flexible sleeper model

The sleeper is represented as a finite uniform Timoshenko beam [106] with length  $L$  and is assumed to be supported on a continuous viscoelastic foundation which represents the ballast. The modelling approach for the sleeper is similar to that described by Thompson [97], in which the receptance is obtained from a wave approach. This model assumes a uniform cross-section of the sleeper along its length and was extended by Kostovasilis [84] to account for the sleeper flexibility not only in vertical bending, but also in the axial, lateral and torsional directions. This has been achieved in a similar manner to that for the rail modelling, i.e., considering models for the extension, torsion and bending in vertical and lateral directions but in this case with no coupling between them through the beam. As the sleeper cross-section is symmetric, the sleeper model can be seen as two separate models, one involving the axial sleeper response (lateral to the rail) and vertical sleeper bending, and the other involving the torsional response and lateral sleeper bending (axial to the rail). Note that the axial direction of the sleeper is coincident with the lateral direction of the rail, while the lateral direction of the sleeper is coincident with the axial direction of the rail. Thus, the receptance of the sleeper needs to be transformed to match the coordinate system of the rail when assembling the track model.

In the sleeper model, there is coupling between vertical and axial responses and between lateral and torsional responses; this originates from the foundation eccentricity, in which the ballast is assumed to act at the bottom of the sleeper as a continuous damped elastic foundation. Finally, appropriate consideration of the boundary conditions is taken into account to accommodate the finite length of the sleeper. The detailed modelling process is presented in Appendix A.

In order to validate the sleeper model, a pre-stressed type G44 concrete sleeper is

considered. Kostovasilis [84] conducted a series of mobility measurements using an impact hammer on such a sleeper. The design of the G44 sleeper is depicted in Figure 3.6.

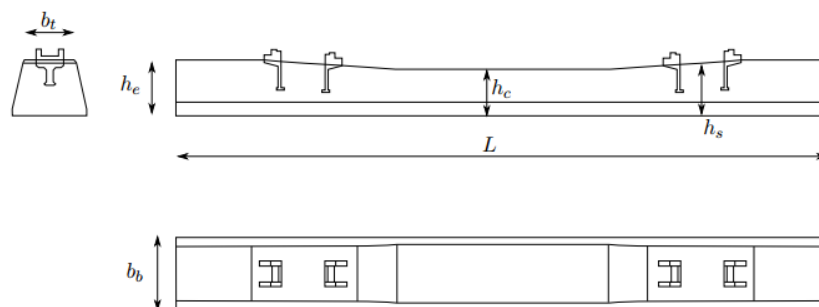


Figure 3.6 G44 sleeper design [84]

The parameters used for the monobloc sleeper are listed in Table 3.3. All the geometric parameters are derived from the actual geometry of the sleeper. The only exception was the torsional constant which, due to the varying cross-section of the sleeper, was selected to provide a good fit with the measured data for the torsional resonances. In the model, the elastic layer below the sleeper is continuous, here with a constant stiffness value. This mainly affects the rigid body mode of the sleeper. The sleeper support stiffness was adjusted accordingly to provide a good fit to the first peak from the measured data. The fitting was performed accounting for the three displacement directions as well as the torsional responses. The parameters in Table 3.3 will also be used for the monobloc sleeper in subsequent chapters.

In the measurements of Kostovasilis [84], the sleeper was supported on soft rubber mounts under each rail seat giving a bounce mode natural frequency of 20 Hz. An example of the mobility of the sleeper when it is excited vertically at one end is shown in Figure 3.7. Figure 3.7 shows the prediction obtained by the current model with the foundation stiffness assumed as 5 MN/m. The first peak at 20 Hz corresponds to the rigid body mode of the sleeper while the peaks at 100 Hz and above correspond to the vertical bending modes. Good agreement is found between it with the measured results obtained by Kostovasilis [84].

Table 3.3 Monobloc sleeper properties [84]

Parameter	Value	Units
Young's modulus $E$	57.0	GPa
Shear modulus $G$	23.8	GPa
Density $\rho$	7860	kg/m <sup>3</sup>

Mass (full sleeper) $m$	303	kg
Poisson's ratio $\nu$	0.2	-
Length $L$	2.5	m
Damping loss factor $\eta$	0.0083	-
Second moment of area about z-axis $I_{p,z}$	$1.27 \times 10^{-4}$	$m^4$
Second moment of area about y-axis $I_{p,y}$	$2.24 \times 10^{-4}$	$m^4$
Polar moment of area $I_p$	$3.51 \times 10^{-4}$	$m^4$
Torsional constant $J$	$2.70 \times 10^{-4}$	$m^4$
Vertical shear coefficient $\kappa_z$	0.83	-
Lateral shear coefficient $\kappa_y$	0.83	-
Vertical shear centre eccentricity $e_z$	0	m
Height at centre $h_c$	0.172	m
Height at rail seat $h_s$	0.197	m
Breadth at centre (top) $b_{c,t}$	0.210	m
Breadth at centre (bottom) $b_{c,b}$	0.282	m
Breadth at rail seat (top) $b_{s,t}$	0.203	m
Breadth at rail seat (bottom) $b_{s,b}$	0.283	m

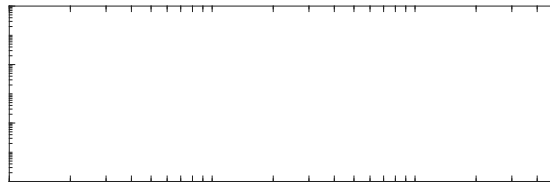


Figure 3.7 Point mobility of concrete monobloc sleeper for vertical excitation at the centreline of the sleeper upper surface

A visco-elastic model is used for the ballast. Here the stiffness (per unit length of the sleeper) is chosen to be  $50 \text{ MN/m}^2$  and damping is  $120 \text{ kNs/m}^2$ . As the stiffness and damping of ballast vary considerably from one position to another, they will be chosen in the following section according to the site measurements in [90].

Using the sleeper properties listed in Table 3.3, the point mobility of the sleeper at the rail seat when located in ballast is presented in Figure 3.8. Compared with the result shown in [85] this has a good agreement. The ballast support causes the sleeper natural frequencies

to increase compared with the free sleeper (in Figure 3.7), and their damping is also much greater.

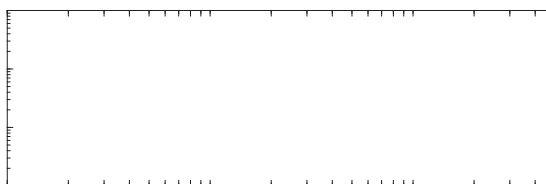


Figure 3.8 Predicted vertical point mobility at the rail seat of the sleeper in ballast

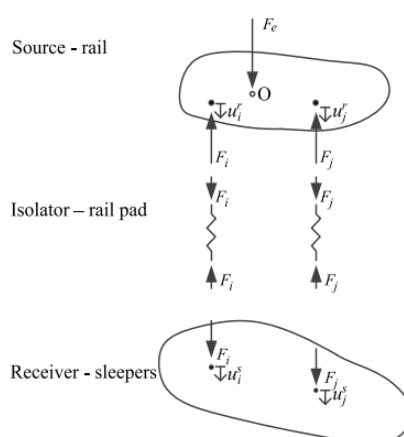


Figure 3.9 Source and receiver structures coupled at multiple connection points through massless resilient elements [85]

### 3.3.4 Receptance-coupling

There are various ways to model the vibration of a track with discrete supports. The approach adopted by Zhang et al. [85] is based on that proposed by Heckl [93]. The discrete rail supports are replaced by corresponding reaction forces, so that the rail is considered as an infinite structure with many point forces acting on it. This has not previously been combined with the rail model of Kostovasilis [84].

For a coupled system, consisting of a source structure and a receiver, connected by flexible isolators, the dynamic response can be determined in terms of the receptances of the various systems at the interface. This is illustrated in general terms in Figure 3.9.

In the present case, the source structure represents the rail, the receiver the sleepers and the isolators the rail pads. An external force  $F_e$  is applied on the rail at an arbitrary point  $O$ . Interactions occur between the source, the isolator and the receiver as shown in Figure 3.9. For simplicity this shows vertical interaction forces but at each connection point the forces can act in multiple directions. The isolators are assumed to be massless so that the same forces act on both the source and receiver structures but in opposite directions.

Assuming harmonic motion at circular frequency  $\omega$ , the displacement of a point  $i$  on the rail can be expressed as

$$u_i^r = \alpha_{ie}^r F_e - \sum_j \alpha_{ij}^r F_j \quad (3.19)$$

where  $\alpha_{ie}^r$  is the transfer receptance of the free rail, giving the response at the connection point  $i$  due to a unit force at the excitation point;  $\alpha_{ij}^r$  is the transfer receptance of the free rail, giving the response at the connection point  $i$  due to a unit force at the connection point  $j$ ;  $F_j$  is the interaction force at point  $j$ , and  $F_e$  is the external force at the excitation point.

The relative displacement of the springs connecting the rail and the sleepers is given by

$$u_i^r - u_i^s = \sum_j \alpha_{ij}^p F_j \quad (3.20)$$

where  $u_i^s$  is the displacement of the sleepers at the point  $i$ ;  $\alpha_{ij}^p$  is the receptance of the spring connection giving the relative displacement at the point  $i$  due to the force acting at the attachment point  $j$ . In practice  $\alpha_{ij}^p = 0$  for  $i \neq j$ . For the sleepers, the displacement at the connection points is given by

$$u_i^s = \sum_j \alpha_{ij}^s F_j \quad (3.21)$$

For the connection points on different sleepers, which are assumed to be uncoupled from one another,  $\alpha_{ij}^s = 0$ , but multiple connection points on one sleeper are allowed in which case  $\alpha_{ij}^s$  would be non-zero. Considering all the connection points, the equations of motion can be written in matrix form for the three structures

$$\mathbf{u}_r = \boldsymbol{\alpha}_e^r F_e - \boldsymbol{\alpha}^r \mathbf{F} \quad (3.22)$$

$$\mathbf{u}_r - \mathbf{u}_s = \boldsymbol{\alpha}^p \mathbf{F} \quad (3.23)$$

$$\mathbf{u}_s = \boldsymbol{\alpha}^s \mathbf{F} \quad (3.24)$$

where  $\mathbf{u}_r$  are the displacements on the rail foot at the positions of every rail pad, while  $\mathbf{u}_s$  are the displacements on the top surface of the sleepers at the corresponding points.  $\boldsymbol{\alpha}^r$ ,  $\boldsymbol{\alpha}^p$  and  $\boldsymbol{\alpha}^s$  are matrices of the receptances at every connection point of the rail, rail pad and the

sleeper respectively due to the force at the rail pad positions.  $\alpha_e^r$  is the vector of receptances of the rail at the connection points due to the external force  $F_e$ .

Adding Equations (3.23) and (3.24) gives

$$\mathbf{u}_r = (\alpha^p + \alpha^s) \mathbf{F} \quad (3.25)$$

Substituting Equation (3.25) into Equation (3.22) and rearranging, the rail displacement can be obtained as

$$\mathbf{u}_r = (\mathbf{I} + \alpha^r (\alpha^p + \alpha^s)^{-1})^{-1} \alpha_e^r F_e \quad (3.26)$$

where  $\mathbf{I}$  is the unit matrix.

It should be noted that the cross receptance between the axial direction (also some rotations) and other directions at the connection positions at the left side of the excitation position should have opposite signs compared with the cross receptance at the connection positions at the right side of the excitation position. This is due to the wave propagation assumption.

Equation (3.26) can be used to obtain the interaction forces  $\mathbf{F}$  from Equation (3.25). The displacement at an arbitrary point  $k$  on the rail can finally be calculated as

$$u_k^r = \alpha_{ke}^r F_e - \alpha_k^r \mathbf{F} \quad (3.27)$$

where  $\alpha_k^r$  is the vector of receptances giving the response at point  $k$  on the rail to a unit force at each spring location on the rail foot;  $\alpha_{ke}^r$  is the transfer receptance from the external force  $F_e$  to the response point  $k$ . Note that the sleeper spacing is not specified in the above formulation; this implies that the coupled track system could have discrete supports with arbitrary spacing.

To apply this coupling method to a discretely supported railway track, the infinite rail is coupled to a finite number of sleepers as shown in Figure 3.5. The infinite free rail is modelled by using the rail model introduced in Section 3.4.1. It is connected through elastic supports for each rail pad to a flexible sleeper model including the ballast beneath it. For the coupling of the rail and the sleeper, the top surfaces of the monobloc sleepers are connected to the rail via springs attached to the bottom of the rail foot. Each rail pad is initially considered as a single damped spring in each direction. To ensure the waves generated are sufficiently attenuated at the ends of the finite supported region, 120 rail supports are used in the longitudinal direction to represent the infinite supported rail.

Table 3.4 Parameters used for the predictions

<b>Rail parameters</b>	Value	Units
Rail cross section	60E1	-
Rail mass per unit length	60	kg/m
Rail loss factor	0.02	-
<b>Rail pad parameters</b>	Value	Units
Pad vertical stiffness	300	MN/m
Pad axial and lateral stiffness	40	MN/m
<b>Sleeper parameters</b>	Value	Units
Sleeper spacing	0.63	m
<b>Ballast parameters</b>	Value	Units
<b>(per unit length along the sleeper)</b>		
Ballast vertical stiffness	68	MN/m <sup>2</sup>
Ballast axial and lateral stiffness	58	MN/m <sup>2</sup>
Ballast vertical damping	82	kNs/m <sup>2</sup>
Ballast axial and lateral damping	68	kNs/m <sup>2</sup>

The receptance-coupling method is applied to obtain the response of the discretely supported railway track. At this stage only a single rail is included. The rail type is CEN 60E1. Table 3.4 lists the parameters used for the rails and rail pads, which are mainly derived from [84], although the rail pad properties are adjusted to match the measurements described below. The frequency range used in the predictions is from 50 Hz to 6000 Hz, with a constant spacing of 1 Hz.

For a vertical force, the excitation position is at the centre of the rail head (position 1 in Figure 3.1). Figure 3.10(a) compares the point mobilities of the track, for vertical excitation at mid-span between sleepers and directly above a sleeper. Pronounced differences can be seen between the results for the two excitation points, especially in the frequency range between 500 Hz and 2000 Hz. For the vertical mobility at mid-span, three obvious peaks can be identified. The first peak at 100 Hz corresponds to the resonance of the rail and sleeper mass on the vertical ballast stiffness, while the second peak at 470 Hz is the resonance of the rail mass on the vertical rail pad stiffness. There are also some oscillations due to the bending modes of the sleepers. The peak at 980 Hz is the vertical ‘pinned-pinned’ frequency; a dip appears just above this frequency in the mobility above the sleeper.

Corresponding measured results are shown in Figure 3.10(b). These were measured on a test track of length 32 m at Chilworth, Southampton, UK. The track consists of 60E1 rails and monobloc concrete sleepers. A PCB 086C03 hammer and an accelerometer with a



magnetic fixing attached to the rail were used in the measurement. The mobilities were obtained using an average of 5 impacts in each case. The coherence was always above 0.8 above 50 Hz and close to 1 for most frequencies. The predictions show good agreement with the measured results below 4 kHz. Similar comparisons of vertical track dynamics were done between whole-track FE model and experiments by Oregui et al [111].

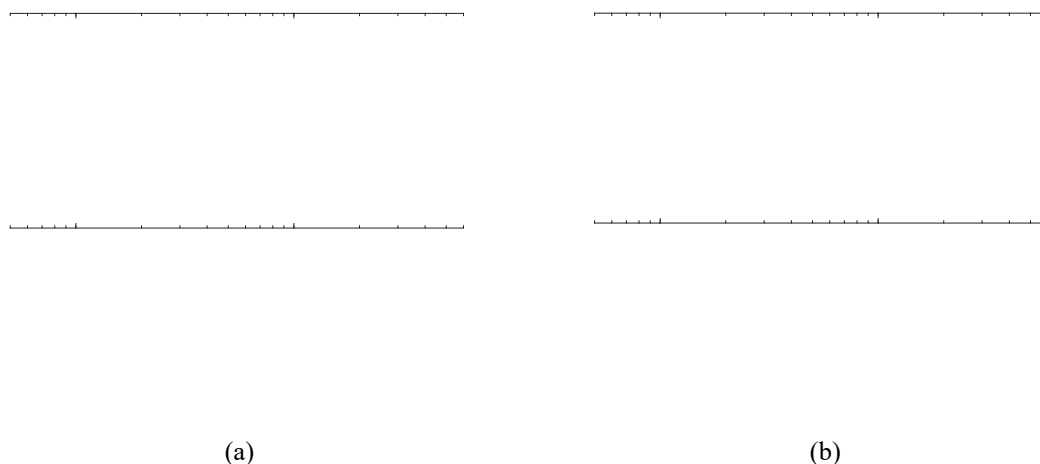
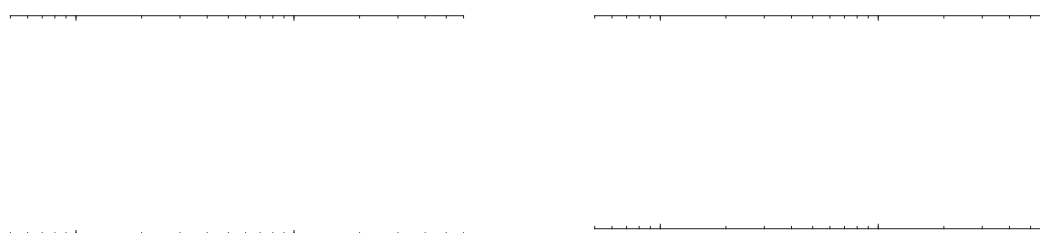
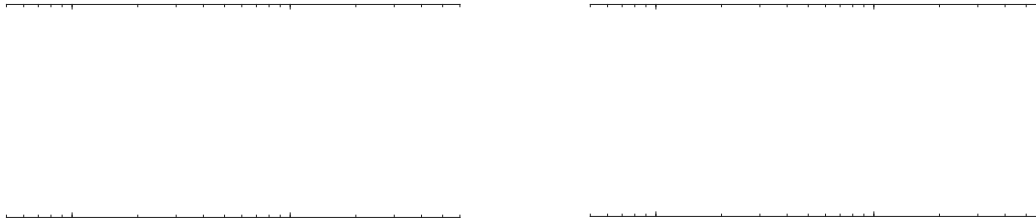


Figure 3.10 Vertical point mobility of the track. (a) Predicted; (b) measured

For the lateral direction, the excitation position is at the side of the rail head (position 2 in Figure 3.1). The predicted lateral point mobility is shown in Figure 3.11(a) and the corresponding measured results in Figure 3.11(b). A distinct peak can be observed in the lateral mobility at 140 Hz, corresponding to the resonance of the rail and sleeper mass on the lateral ballast stiffness. The peak at 470 Hz at mid-span is the lateral ‘pinned-pinned’ resonance and that at 670 Hz is the torsional ‘pinned-pinned’ resonance. Dips are found at these two frequencies in the point mobility above the sleeper. The large oscillations in the measured results between 600 and 1500 Hz are due to the finite length of the test track, as there is a low decay rate in this frequency region. Apart from this, there is reasonably good agreement between measurements and predictions.



(a) (b)  
Figure 3.11 Lateral point mobility of the track. (a) Predicted; (b) measured



(a) (b)  
Figure 3.12 Predicted mobility of the track excited at different positions. (a) Axial mobility; (b) vertical-lateral cross mobility

Figure 3.12(a) shows the predicted axial mobility at mid-span and above a sleeper for excitation at the centre of the rail head (position 1 in Figure 3.1). This rises to a peak at 200 Hz, which is the cut-on frequency of longitudinal waves. Above this frequency it is approximately flat, apart from the influence of the sleeper modes, until rising to a sharp peak at 5 kHz, which is the cut-on of the higher order wave of the Timoshenko beam.

Figure 3.12(b) shows the predicted cross mobility (lateral response due to a vertical force) at a position with an offset of 10 mm from position 1 and at a position with an offset of 20 mm. For the offset of 10 mm, results are shown at mid-span and above a sleeper. The characteristics are very similar to the vertical and lateral point mobilities, with clear differences between mid-span and above a sleeper at the pinned-pinned resonances. For the larger offset, the magnitude of the cross mobility increases at all frequencies.

### 3.3.5 Track decay rate

The track decay rate is determined from the transfer mobilities at different positions along the rail [112]. The overall decay rate in each one-third octave band is evaluated from predicted transfer mobilities according to the standard measurement method as [113]:

$$\Delta_{\text{tot}} = \frac{4.343}{\sum_{x=0}^{x_{\text{max}}} \frac{|Y(x_n)|^2}{|Y(x_0)|^2} \delta x_n} \quad (3.28)$$

where  $Y(x_n)$  is the transfer mobility in one-third octave bands at a distance  $x_n$  away from the excitation point,  $Y(x_0)$  is the mobility at the excitation point and  $\delta x_n$  is the distance between the midpoints of each grid interval on either side of the location  $n$ .

The vertical decay rate is plotted in Figure 3.13(a), and the lateral one in Figure 3.13(b). These results are compared with measurements obtained on the same test track by Kostovasilis et al. [84].

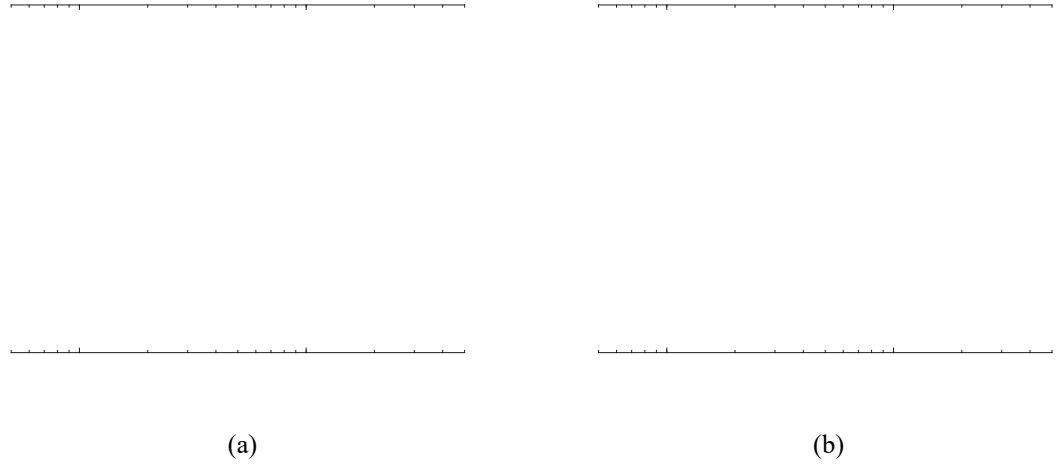


Figure 3.13 Track decay rate compared with measured results from [84]. (a) Vertical direction; (b) lateral direction

Although the track was the same as used for the measurements of point mobilities, the measured decay rates were obtained in warmer weather, which results in the rail pad being softer. Thus, the pad stiffnesses used in these predictions are adjusted to 120 MN/m for the vertical direction and 40 MN/m for the longitudinal and lateral directions, as given in [84]. At low frequencies, the vertical decay rate is high due to the blocking effect of the support stiffness. It drops at around the cut-on frequency of the rail vertical bending wave, which is around 300 Hz for these parameters. The lateral decay rate drops at a lower cut-on frequency. The agreement with measurements is very good up to 2 kHz, but at higher frequencies the measurements rise more rapidly due to cross-section deformation of the rail, which is not included in the model.

### 3.3.6 Transfer mobility under excitation on the other rail

In the above, following the method of Refs [85, 93], the infinite rail is coupled to a finite number of sleepers through the rail pads, see Figure 3.5(a). This approach is extended here to include both rails. The two rails are denoted left and right and it is assumed that the external force  $F_e$  is applied to the left rail.

The vectors of displacement on the rail foot of the left and right rail at the connection points with the rail pads (three displacements and three rotations) are denoted  $\mathbf{u}_{rL}$  and

$\mathbf{u}_{rR}$ . The corresponding displacement vectors on the sleepers are denoted  $\mathbf{u}_{sL}$  and  $\mathbf{u}_{sR}$ . If there are  $N$  sleepers, these vectors have dimension  $6N \times 1$ . These are combined into  $12N \times 1$  vectors  $\mathbf{u}_r = [\mathbf{u}_{rL}^T \ \mathbf{u}_{rR}^T]^T$  and  $\mathbf{u}_s = [\mathbf{u}_{sL}^T \ \mathbf{u}_{sR}^T]^T$ .  $\mathbf{F}_L$  and  $\mathbf{F}_R$  are the corresponding vectors of interaction forces at the left and right connection points, which are combined into a single force vector  $\mathbf{F} = [\mathbf{F}_L^T \ \mathbf{F}_R^T]^T$ . The sleepers are represented by  $12N \times 12N$  matrices of receptances (displacement for a unit force)

$$\boldsymbol{\alpha}^s = \begin{bmatrix} \boldsymbol{\alpha}_L^s & \boldsymbol{\alpha}_{LR}^s \\ \boldsymbol{\alpha}_{RL}^s & \boldsymbol{\alpha}_R^s \end{bmatrix} \quad (3.29)$$

in which  $\boldsymbol{\alpha}_L^s$  is the matrix of receptances of the sleepers at the points connected to the left rail, which are given by

$$\boldsymbol{\alpha}_L^s = \begin{bmatrix} \ddots & & 0 \\ & \boldsymbol{\alpha}_{L,i}^s & \\ 0 & & \ddots \end{bmatrix} \quad (3.30)$$

where  $\boldsymbol{\alpha}_{L,i}^s$  is the  $6 \times 6$  receptance matrix for a single sleeper. Similarly,  $\boldsymbol{\alpha}_R^s$  are the matrices of receptances of the sleeper at the points connected to the right rail and  $\boldsymbol{\alpha}_{LR}^s$ ,  $\boldsymbol{\alpha}_{RL}^s$  contain the transfer receptances between the left and right connection points.

Similarly, the connection points on the left rail are described by the matrix  $\boldsymbol{\alpha}_L^r$  and those on the right rail by  $\boldsymbol{\alpha}_R^r$ , giving a combined receptance matrix for both rails as:

$$\boldsymbol{\alpha}^r = \begin{bmatrix} \boldsymbol{\alpha}_L^r & \mathbf{0} \\ \mathbf{0} & \boldsymbol{\alpha}_R^r \end{bmatrix} \quad (3.31)$$

The rail pads are represented by a  $12N \times 12N$  diagonal matrix of receptances  $\boldsymbol{\alpha}^p$ .

Considering all the connection points on both rails, the equations of motion can be written in matrix form as:

$$\mathbf{u}_r = \boldsymbol{\alpha}_e^r F_e - \boldsymbol{\alpha}^r \mathbf{F} \quad (3.32)$$

$$\mathbf{u}_r - \mathbf{u}_s = \boldsymbol{\alpha}^p \mathbf{F} \quad (3.33)$$

$$\mathbf{u}_s = \boldsymbol{\alpha}^s \mathbf{F} \quad (3.34)$$

where  $\boldsymbol{\alpha}_e^r$  is the vector of transfer receptances of the rail from the external force  $F_e$  at a position on the left rail head to the responses at the connection points (for positions on the right rail it contains zeros). Combining Eq. (3.33) and (3.34) gives

$$\mathbf{u}_r = (\boldsymbol{\alpha}^p + \boldsymbol{\alpha}^s) \mathbf{F} \quad (3.35)$$

Substituting this into Eq. (3.32) and rearranging, the rail displacements at the connection points can be obtained as:

$$\mathbf{u}_r = (\mathbf{I} + \boldsymbol{\alpha}^r (\boldsymbol{\alpha}^p + \boldsymbol{\alpha}^s)^{-1})^{-1} \boldsymbol{\alpha}_e^r F_e \quad (3.36)$$

where  $\mathbf{I}$  is the unit matrix.

The rail displacements  $\mathbf{u}_r$  are used to obtain the interaction forces  $\mathbf{F}$  by inverting Eq. (3.57). The displacement at an arbitrary point  $k$  on the left rail can finally be calculated as

$$u_{L,k}^r = \alpha_{L,ke}^r F_e - \boldsymbol{\alpha}_{L,k}^r \mathbf{F}_L \quad (3.37)$$

where  $\boldsymbol{\alpha}_{L,k}^r$  is a vector of transfer receptances of the free rail, giving the response at the point  $k$  to a unit force at each rail pad location on the rail foot;  $\alpha_{L,ke}^r$  is the transfer receptance of the free rail from the external force  $F_e$  to the response point  $k$ . By applying a unit force on the rail head, in each direction in turn, the responses  $u_{L,k}^r$  correspond to the receptances of the assembled track. They can be expressed as mobilities by using  $Y = i\omega u_k^r$ . Similarly, the responses at an arbitrary point  $k$  on the right rail to excitation on the left rail are given by

$$u_{R,k}^r = -\boldsymbol{\alpha}_{R,k}^r \mathbf{F}_R \quad (3.38)$$

The model is now used to predict the response of the right rail to a force on the left rail. The same parameters are used as shown in Table 3.4. For the vertical direction, the excitation is at position 1 on the left rail and the response is at position 1 on the right rail. For the lateral direction, the excitation is at position 2 on the left rail head and response is at position 2 on the right rail head.

Figure 3.14 compares the transfer mobility with the point mobility for both vertical and lateral directions for excitation above a sleeper. The magnitudes of the point and transfer mobilities have a roughly constant difference at low frequency but the difference increases at high frequency. Nevertheless, there are some narrow frequency regions where the difference between point and transfer mobilities is rather small, for example around 400 Hz and 1 kHz for the vertical direction.

In Figure 3.14 the predicted transfer mobility between the two rails is also compared with the corresponding measured results which were obtained on the test track. Good agreement can be seen between the measured and predicted mobilities. As the transfer mobility between the two rails is much lower than the point mobility, the coupling between the two rails is found to have little effect on the track mobilities on the excited rail or on the track decay rates.

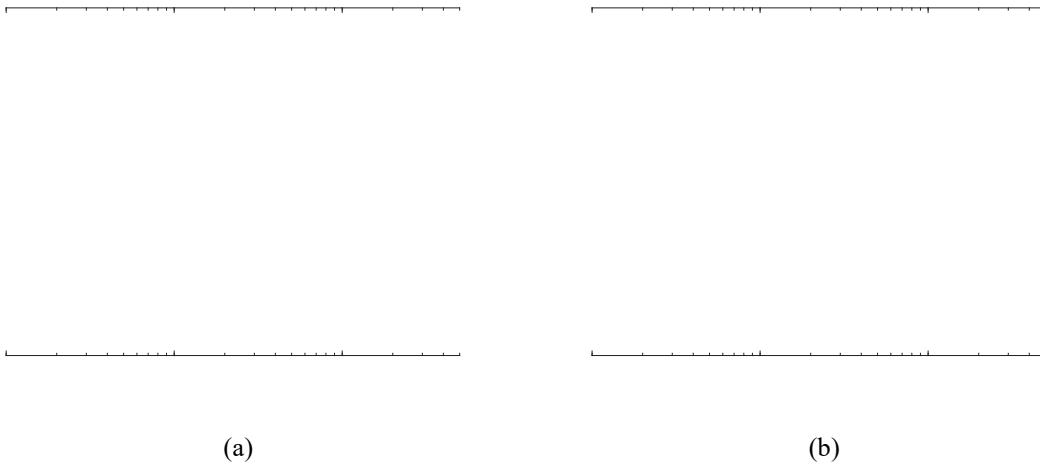


Figure 3.14 Comparison of the predicted transfer mobility between two rails with the measurement and with the predicted point mobility, all results for excitation above a sleeper. (a) Vertical direction; (b) lateral direction.

### 3.3.7 Effect of the torsion and warping on the track response

The beam model used includes the effects of torsion and warping on the lateral responses [84]. To investigate their effects, results are obtained from the current model with and without the torsion and warping. The track parameters from Table 3.4 are used and the excitation and response points are the same as considered above.

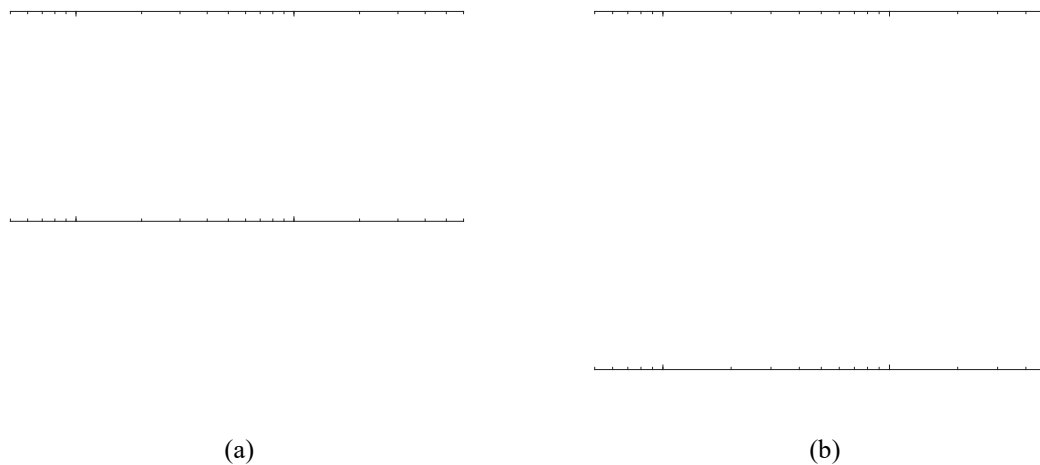


Figure 3.15 Lateral results with or without torsion and warping. (a) Lateral point mobility above a sleeper, (b) lateral track decay rate

The vertical point mobility and decay rate are unaffected by the inclusion of torsion and warping, so are not shown here. Figure 3.15(a) shows the lateral point mobility above a sleeper and Figure 3.15(b) shows the corresponding track decay rate. The inclusion of torsion and warping both have significant effects on the lateral response over the whole frequency range. The inclusion of torsion lowers the cut-on frequency of the lateral wave from 200 Hz to 150 Hz, which can be seen in both the mobility and the decay rate. The inclusion of warping then leads to a further increase in the magnitude of the mobility. The

dip related to the lateral pinned-pinned resonance can be found even when only lateral bending is considered but the one related to the rotational pinned-pinned resonance is only found when warping is introduced. For groove rails in trams, the rail section is asymmetric which is different from the rail investigated here. The effect of torsion and warping would be more important to the track response of the groove rails in trams in the vertical and lateral directions.

### 3.4 Time-domain model

To predict corrugation growth with a time-domain approach, a track model is required in the time domain. Clark et al. [114] used a rail model with 20 sleeper bay length, represented by Euler beam elements with fixed boundary conditions at the ends. The track was assumed to be finite in length and a modal summation technique was used in this time-domain model. Baeza et al. [115] proposed a modal substructuring approach, where the rail and sleeper are modelled by modal coordinates. Other components such as the rail pads and ballast are introduced by means of the forces in connecting elements. The drawback of this method is its high computational cost.

In this thesis, Pieringer's method [86], which is based on Heckl's work [116], is used. In the frequency domain, the track system is presented by its receptances

$$\tilde{\alpha}^R(f) = \frac{u^R(f)}{F(f)} \quad (3.39)$$

which indicate the displacement response,  $u^R(f)$ , to a harmonic excitation force,  $F(f)$  at frequency  $f$ . The tilde  $\sim$  above the parameter signifies non-moving functions, the superscript  $R$  signifies the rail.

This method uses inverse fast Fourier transformation to transform the receptance of the discretely supported track system from the frequency domain into the time domain. The impulse-response functions obtained are the so-called Green's functions:

$$\tilde{g}_{ij}^R(t) = F^{-1} \left( \tilde{\alpha}_{ij}^R(f) \right) \quad (3.40)$$

where the subscript  $i, j = x, y, z$ . When  $i = j$ , it is the Green's function of the point receptance. When  $i \neq j$ , it is the Green's function of the cross receptance.

The non-moving Green's functions, in which the excitation and response points are fixed, can be obtained directly from Equation (3.40) as a continuous function. However, for an excitation point that is moving along the rail, moving Green's functions are required, for which the excitation (or response) points are moving at a particular speed. The moving

---

Green's functions can be obtained from a discrete version of Equation (3.40) with values extracted at each time step corresponding to different positions. Depending on the track system, the moving and non-moving Green's functions may have significant differences. The Green's functions presented in this chapter are all obtained by transforming the point receptances in the vertical direction but the same approach can be used for other directions.

### 3.4.1 Continuously supported track

For a continuously supported track, the non-moving Green's functions are independent of the excitation and response point positions, and depend only on the distance between them.

The continuously supported track considered here uses the same rail as in the example presented in Section 3.3.1, while the supports under the rail are two-layer supports with parameters equivalent to the rail pad and sleeper examples presented in Section 3.3.2 and Section 3.3.3. Non-moving vertical Green's functions of the continuously supported track are shown in Figure 3.16 for three different distances between the excitation and response points: 0 m, 0.325 m (half the sleeper spacing for discrete supports) and 0.65 m (the sleeper spacing for discrete supports). Figure 3.16 shows that the amplitude of the non-moving Green's functions is decreasing with increasing distance between the excitation and response points. This corresponding receptances are shown in Figure 3.17. Since a constant loss factor model has been used for the damping, the impulse responses will be non-causal – i.e. the impulse response has a nonzero value before  $t=0$ . This effect is small, and can be neglected when the impulse response value is set to 0 before  $t=0$ .

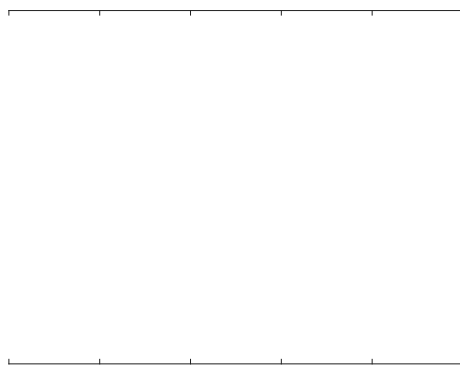


Figure 3.16 Non-moving vertical Green's functions for different distances between the excitation and response points



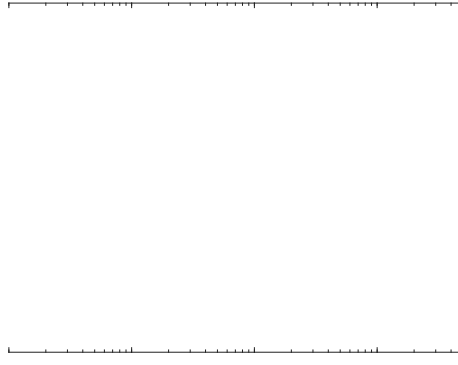


Figure 3.17 Vertical receptances for different distances between the excitation and response points

The moving Green's functions of the continuously supported track are constructed from a series of track transfer receptances,  $\tilde{G}_{ij}^{R,\Delta x_{er}}(f)$ . Here the superscripts specify the distance between the excitation point and the response point,  $\Delta x_{er}$ . The Green's functions,  $\tilde{g}_{ij}^{R,\Delta x_{er}}(t)$  corresponding to these track receptances, are obtained by inverse Fourier transform

$$\tilde{g}_{ij}^{R,\Delta x_{er}}(t) = F^{-1} \left( \tilde{\alpha}_{ij}^{R,\Delta x_{er}}(f) \right) \quad (3.41)$$

Exploiting the relation,  $\Delta x = v\Delta t$ , between the time increment,  $\Delta t$ , and the spatial increment,  $\Delta x$ , the discrete moving Green's functions are constructed as [86]

$$g_{ij}^R(t) = \tilde{g}_{ij}^{R,[n-1]\Delta x}([n-1]\Delta t) \quad (3.42)$$

Thus, at each time step, a different non-moving Green's function is sampled. The moving Green's function consists of the values of different non-moving Green's functions at different time. The total number of samples  $N_R$  is chosen such that the moving Green's functions have decayed sufficiently at  $N_R\Delta t$ .

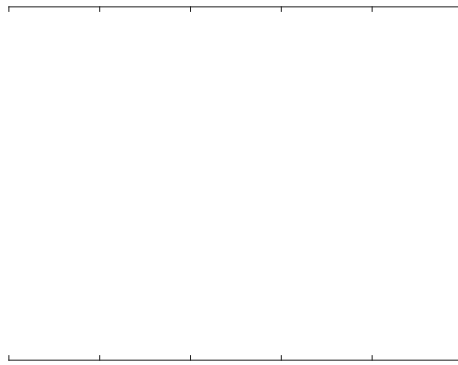


Figure 3.18 Moving Green's functions of the continuous track system in the vertical direction for different moving speeds

Figure 3.18 shows the moving Green's functions of the continuously supported track under different moving speeds. Under different moving speeds, the moving Green's functions of the continuously supported track do not change much.

### 3.4.2 Discretely supported track

For a discretely supported track, the non-moving Green's functions depend on both the excitation and response point positions, as well as the distance between them.

For the discretely supported track model presented in Section 3.3.4, the magnitude of the vertical point receptances are shown in the Figure 3.19. In Figure 3.19(a), the excitation point is above the sleeper. The vertical point receptance is shown along with two examples of transfer receptances. In Figure 3.19(b), the excitation point is changed to the mid-span between the sleepers. The vertical point receptance is again shown along with two examples of transfer receptances. For excitation at mid-span between two sleepers, a sharp peak is observed at around 1000 Hz, which is the pinned-pinned resonance frequency. Correspondingly, the receptances for excitation over a sleeper show an anti-resonance in this frequency range, at a slightly higher frequency. Additionally, the point receptances for both excitation positions have an anti-resonance at about 2400 Hz, which is the second pinned-pinned frequency.

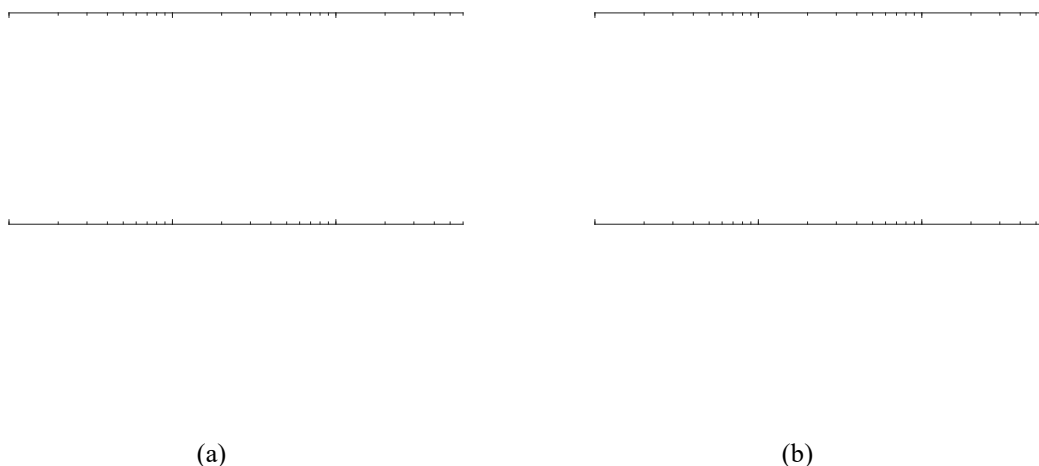


Figure 3.19 Magnitude of the track point and transfer vertical receptances for excitation: (a) above a sleeper position; (b) at mid-span between two sleeper positions

Examples of the non-moving Green's functions are presented in Figure 3.20. The excitation and response points of the non-moving Green's functions are at the same location. Two cases are considered, in which the excitation points are above the sleeper and at mid-span between sleepers. Results show large differences in amplitude and decay rate,

with a strong oscillation at around 1000 Hz at the mid-span position.

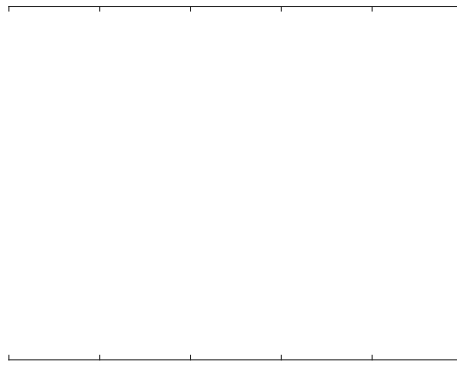


Figure 3.20 The vertical non-moving Green's functions of the discretely supported track system for different excitation points (response point coincides with the excitation point)

Figure 3.21 compares the non-moving Green's functions for the same response point but different excitation points, one of which is above the sleeper and the other is at mid-span between sleepers. In Figure 3.19(a) when the response point is above the sleeper, the non-moving Green's functions do not vary much in amplitude and decay rate for the different excitation points. But in Figure 3.19(b) when the response point is at the mid-span between sleepers, the non-moving Green's functions show larger differences.

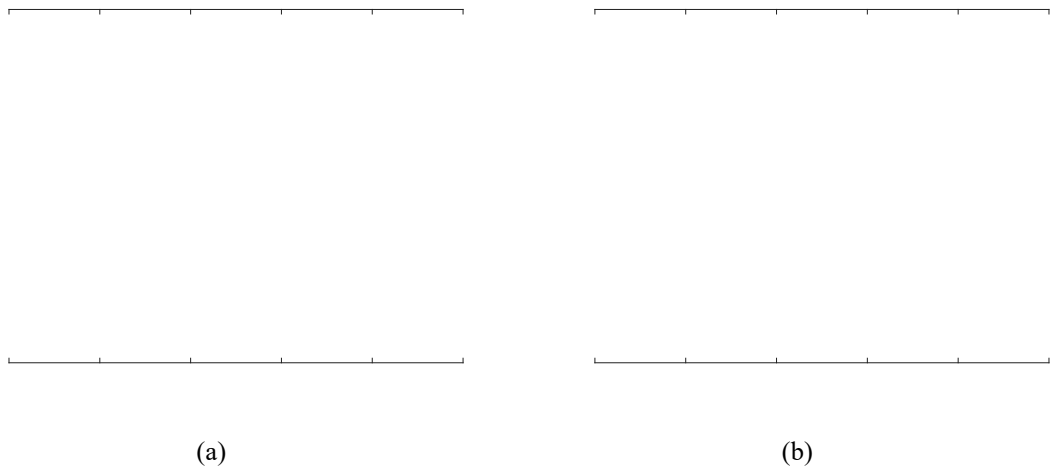


Figure 3.21 The vertical non-moving Green's functions of the discretely supported track, (a) response point is fixed above the sleeper; (b) response point is fixed at the mid-span between sleepers

As in the previous section, the discrete version of the moving Green's functions  $\tilde{g}_{ij, V_0}^{R, x_0}(t)$ , denoted  $g_{ij, V_0}^{R, x_0}(n)$ , is constructed from a series of the track system transfer receptances,  $\tilde{\alpha}_{ij}^{R, x_0, x_0+\chi}(f)$ . Here the superscripts specify the excitation point,  $x_0$ , and the response point  $x_0+\chi$ . The Green's functions,  $\tilde{g}_{ij}^{R, x_0, x_0+\chi}(t)$  corresponding to these track receptances, are

obtained by inverse Fourier transform

$$\tilde{g}_{ij}^{R,x_0,x_0+\chi}(t) = F^{-1} \left( \tilde{\alpha}_{ij}^{R,x_0,x_0+\chi}(f) \right) \quad (3.43)$$

Exploiting the relation,  $\Delta x = V_0 \Delta t$ , between the time increment,  $\Delta t$ , and the spatial increment,  $\Delta x$ , the discrete moving Green's functions are constructed as

$$g_{ij,V_0}^{R,x_0}(n) = \tilde{g}_{ij}^{R,x_0,x_0+[n-1]\Delta x}([n-1]\Delta t) \quad (3.44)$$

The total number of samples  $N_R=325$  is again chosen such that the moving Green's functions of the rail have decayed sufficiently at  $N_R \Delta t$ .

Examples of the moving Green's functions for two different excitation positions are presented in Figure 3.22. The moving speed is 20 m/s. The response points are moving away from the excitation point with each time step. The additional high-frequency oscillations for excitation at mid-span between sleepers in comparison with excitation above the sleeper are again related to the pinned-pinned resonance. Figure 3.23 shows the moving Green's functions of the discretely supported track excited at the same position but with different moving speeds. The moving Green's functions at the same excitation position with different moving speeds have little difference in the time domain when excited above the sleeper, as shown in Figure 3.23(a). In Figure 3.23(b), the moving Green's functions have differences in the decaying part when excited at the mid-span between sleepers. When the distance passed is considered instead of the time, the resultant moving Green's functions at the same excitation position with different moving speeds show obvious differences, as shown in Figure 3.24.

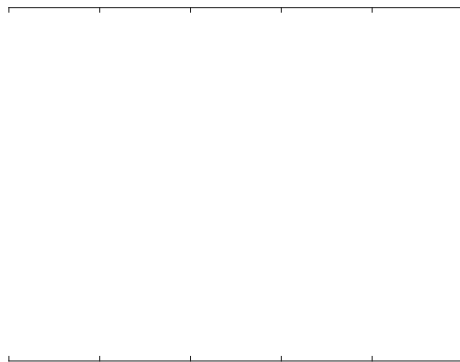


Figure 3.22 The vertical moving Green's functions of the track with different excitation points and moving velocity 20 m/s

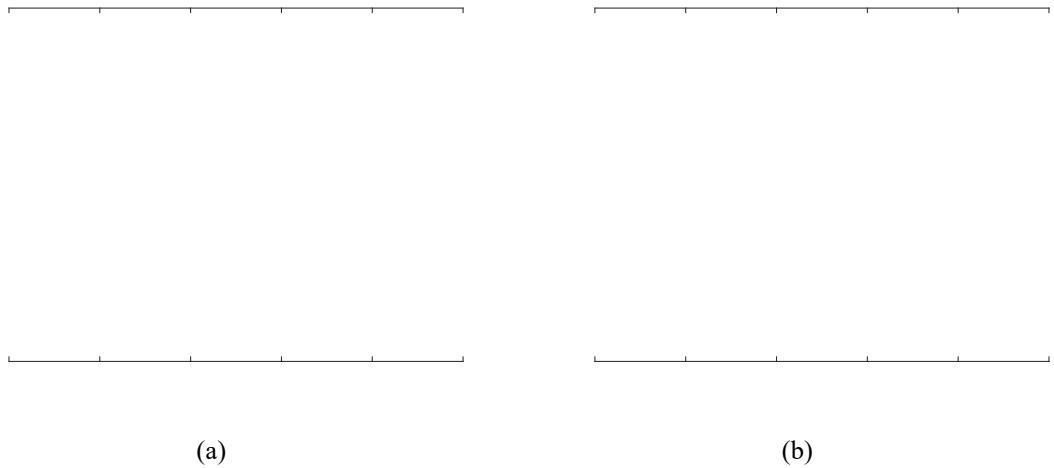


Figure 3.23 The vertical moving Green's functions of the track with different moving velocity and the same excitation point which is above the sleeper: (a) excited above the sleeper; (b) excited at the mid-span between sleepers

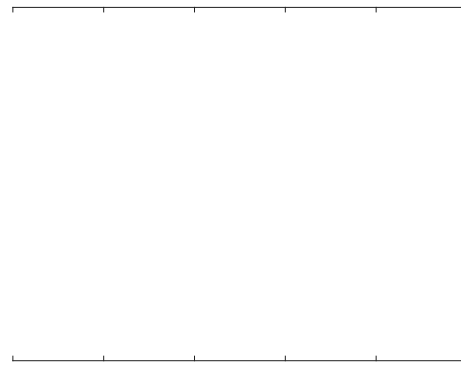


Figure 3.24 The vertical moving Green's functions of the track for excitation above the sleeper under different moving speeds plotted against distance

Due to the periodicity of the track, for a particular moving speed  $v$  and a particular time interval  $\Delta t$ , the number of different moving Green's functions required to represent the dynamics of the discretely supported track system is equal to  $L_s/\Delta x$ , where  $\Delta x$  is the distance passed in one time interval  $\Delta t$ ,  $\Delta x = V_0\Delta t$ . For example, with the parameters  $L_s = 0.65$  m and  $\Delta x = 1$  mm, this leads to 650 moving Green's functions that are required to represent fully the dynamics of the discretely supported track system.

### 3.5 Summary

For the purpose of calculating the interaction forces between the wheel and rail, a discretely supported track model is established. The rail model is developed in the frequency domain by using a semi-analytical method considering seven degrees of freedom, including three displacements, three rotations and warping. The rail pad is modelled using damped springs with a constant value of stiffness and damping loss factor.

---

The sleeper is modelled using a similar method to the rail with a continuous support layer. By applying the receptance-coupling method, the frequency domain response of the discretely supported track system is obtained. Each part of the model is validated with the examples from the literature.

Based on this railway track model, the point and transfer responses in different directions on one rail can be accurately obtained, as well as the cross responses between different directions. The decay rates of the track in different directions are obtained based on the transfer mobility at different positions along the track. Besides these, the transfer responses between two coupled rails are also investigated based on the receptance coupling approach. Thus, the effect of this coupling between rails on the decay rate can also be investigated. Moreover, the inclusion of torsion and warping are found to have significant effects on the lateral track responses.

By applying the inverse FFT, the frequency domain response of the discretely supported track is transformed into the time domain, allowing the moving Green's functions to be obtained. The time-domain results of the continuously and discretely supported track are presented. With a specific value of the sleeper spacing and distance interval, the dynamic behaviour of the discretely supported track can be represented by a series of moving Green's functions. These can be pre-calculated for use in the time-domain wheel-track interaction model, which is introduced in the next chapter.

---

## 4 Wheel/rail interaction model

### 4.1 Introduction

This chapter establishes the interaction model to calculate the normal interaction force between the wheel and rail. The tangential problem will be solved in the next chapter. To calculate the normal interaction force, the dynamic displacements of the wheel and rail need to be calculated. The penetration between the wheel and rail, which is the difference between wheel and rail vertical displacements, is used as input to the wheel-rail contact model that follows to find the normal interaction force. A representation of the vehicle dynamic properties and the coupling between the wheel and the rail are needed together with the track model.

The semi-analytical model of the discretely supported track system has been described in Chapter 3. In this chapter, a finite element model of the wheelset is introduced. The coupling between the wheelset and the track system can take place through the nonlinear Hertzian contact spring between the wheel and the rail. Another way to calculate the interaction force between the wheel and rail is to apply the detailed wheel-rail contact model that follows. The Hertzian contact spring is used in this chapter for presenting the contact force results and the detailed contact model for following calculations is introduced in the next chapter.

After the Hertzian contact spring is introduced, the interaction force between the wheel and rail can be obtained. The method using time-domain models to get the penetration between the wheel and rail and to apply the Hertzian spring to calculate the interaction force is based on Pieringer's work [86]. Here, however, although the moving Green's functions are used for the track system, the state-space method is used for the wheelset; this combination is believed to be innovative.

### 4.2 Wheelset model

The wheelset is a fundamental component of the train system. It consists of two wheels that are rigidly connected to a common axle, and is the part of the vehicle which is directly in contact with the track. The structural flexibility of the wheelset has a major influence on the high frequency vehicle-track interaction, such as the fluctuation of wheel-rail forces. A flexible but non-rotating wheelset model was presented by Gomez and Vadillo [23]. Fayos et al. [117] presented a method for obtaining the dynamic response of rotating flexible

---

solids. This model takes account of the inertial and moving load effects due to rotation. The technique was applied to the case of a railway wheel in [118]. In [38], the flexibility was taken into account, but only the wheelset axle was modelled as flexible and rotating whereas the wheels were represented as rigid bodies.

The methods used to model the structural flexibility of wheelsets include continuous models [119,120], finite element models [121,122] and lumped models [123]. The continuous models use analytical approaches to obtain exact solutions for the structural flexibility. The lumped models use discrete masses and springs to represent the structural flexibility and the characteristics of the natural damping. The FE models consider different element types, such as beam elements for the axle, plate or shell elements for the wheel disc or three-dimensional solid elements. Axisymmetric models are particularly useful in which only the cross-section is meshed. The structural flexibility of wheelsets is usually considered in numerical simulations in terms of eigenmodes derived from the respective models. Considering the frequency range of interest and the number of modes of the wheelset in this range, a finite element model is used in this research.

#### **4.2.1 Finite element model**

In this thesis, a typical wheelset from a multiple unit train is studied. This wheel has a straight web and a diameter of 0.84 m. The finite element axi-symmetric model is produced by using the FE analysis software ANSYS. Modal analysis can provide modal parameters (natural frequencies and mode shapes) from which the mobility or receptance at the wheel-rail contact point can be obtained.

Half of the axisymmetric cross-section of the wheelset established in ANSYS is shown in Figure 4.1, making use of symmetry at the centre of the axle. The rigid body modes of the wheelset with non-zero natural frequencies are included which are adjusted afterwards as well as the axle modes. To obtain modes that include motion of the axle, a complete model of the wheelset is required. To achieve this, symmetric and antisymmetric boundary conditions are invoked at the centre of the axle between the two wheels. The frame of reference is positioned with the origin of the lateral axis located at the nominal contact point and the origin of the vertical axis at the axle centre.



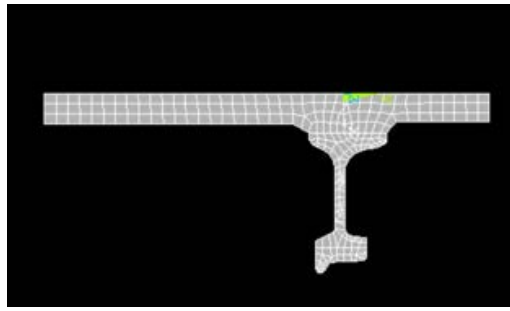






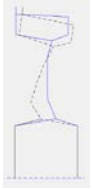



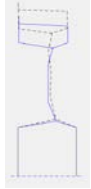
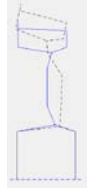








Figure 4.1 Half of the rotating cross-section of the wheelset in ANSYS

From the modal analysis, several modes are obtained for each applicable number of nodal diameters in the mode shape. The mode shapes are mass-normalized. From the modal information of the wheelset a modal parameter file is created, as used for the input to the TWINS [91] software. The eigenfrequencies and corresponding eigenmodes from this finite element model are calculated in the range up to 5 kHz.

Figure 4.2 Mode shapes of some identified modes

Number of nodal diameters	0	1	2	3	4
0 nodal circle					
	258.62 Hz	80.83 Hz	402.74 Hz	1065.8 Hz	1919.3 Hz
1 nodal circle					
	1784.6 Hz	720.5 Hz	4070.5 Hz	4615.6 Hz	3561.3 Hz
Radial					
	3240.5 Hz	3620.6 Hz	2333.6 Hz	2770 Hz	3464.6 Hz
Circumferential					
	887.43 Hz	2252.8 Hz	4779.4 Hz		

In addition to the number of nodal diameters, the mode types are identified by viewing the mode shapes in the solution in ANSYS. The eigenmodes of the wheelset are classified according to their predominant motion into axial, radial and circumferential modes, which have  $n$  nodal diameters and  $m$  nodal circles [97]. Within the frequency range of interest, the mode types are identified such as 0 nodal circle mode, 1 nodal circle mode, 2 nodal circle mode, radial mode and circumferential mode. Some examples of mode shapes are shown in Figure 4.2.

The eigenmodes are assigned a modal damping ratio  $\zeta$  using the approximate values proposed by Thompson [97]:

$$\zeta = \begin{cases} 10^{-3} & \text{for } n = 0 \\ 10^{-2} & \text{for } n = 1 \\ 10^{-4} & \text{for } n \geq 2 \end{cases} \quad (4.1)$$

Considering the importance of the wheelset rigid body modes for the dynamics of the wheelset, their natural frequencies and damping ratios are adjusted to the expected values according to the primary suspension for the current wheelset; the adjusted frequencies are 20 Hz, 30 Hz and 40 Hz, while the corresponding damping ratios are 0.01. Starting from the modal basis, the mobilities of the wheel at the pre-determined contact point on the wheel tread are calculated by modal superposition. According to the superposition principle of modal summation [125], the frequency response function between a force at location  $c$  and the velocity response at location  $d$  can be found as

$$Y_{dc} = \sum_r \frac{i\omega \phi_{dr} \phi_{cr}}{m_r (\omega_r^2 - \omega^2 + 2i\zeta_r \omega \omega_r)} \quad (4.2)$$

where  $\phi_{dr}$  is the modeshape of mode  $r$  at location  $d$ ,  $m_r$  is the modal mass,  $\zeta_r$  is the damping ratio,  $\omega_r$  is the angular natural frequency,  $\omega$  is the frequency of the external force, and  $i$  is the imaginary unit given by  $i^2 = -1$ . Regardless of the modal identification, radial and axial mobilities at the nominal contact point on the wheelset are calculated using the modal superposition method based on all modes obtained from the modal analysis in ANSYS. The point mobilities in the radial and axial directions are shown in Figure 4.3. The cross mobility, which refers to the coupling between radial and axial directions, is also presented.

The corresponding mobilities at the nominal contact point for a single wheel are also given for comparison with the results for the full wheelset. In this case the axle is omitted, and the wheel is constrained at the inner edge of the hub. Although these results neglect the axle bending modes, the rigid body modes of the full wheelset have been included in the

modal summation. Comparing these results with the results for the wheelset, the peaks below 300 Hz are different from those for the wheelset because of the exclusion of the flexible axle. For frequencies above 300 Hz, the mobilities in both cases are similar because the wheel-dominated modes frequencies are dominant. Some peaks in the wheelset mobilities cannot be found in the wheel-only mobilities since these peaks correspond to the dynamic characteristics of the axle. Thus, in the frequency range of interest, the results from the full wheelset model contain more modal information than the wheel model and the response of the wheelset model will be more accurate. Around 30 modes are included in wheel model below 5 kHz while there are more than 40 modes in the wheelset model.

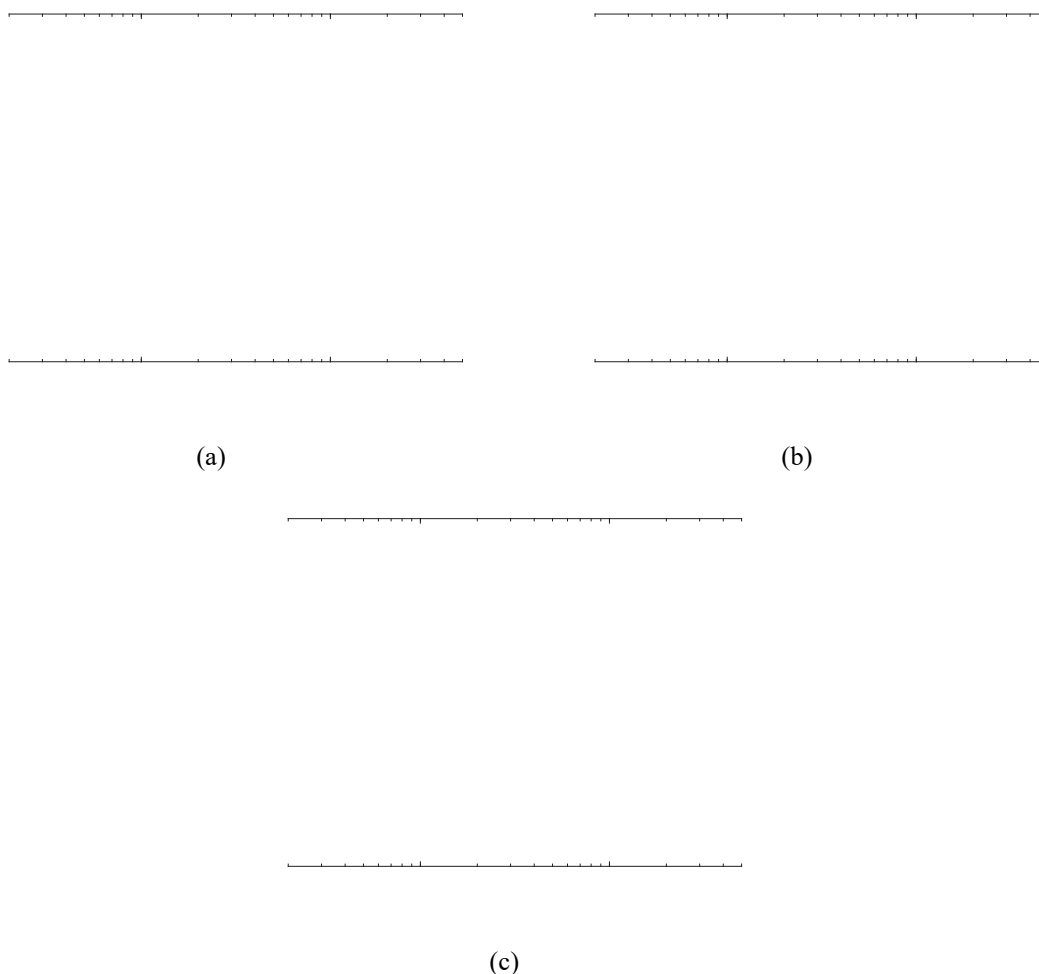


Figure 4.3 Radial, axial and cross mobilities of wheelset: (a) radial mobilities; (b) axial mobilities; (c) cross mobilities

#### 4.2.2 State-space model

For a nonlinear problem, the method of step-by-step integration in the time domain is appropriate. Although the wheelset model is linear, the contact model contains nonlinearities. Thus, besides the mobilities, a time-domain model of the wheelset is required. In this thesis, a state-space model derived from the modal analysis method is adopted. This model can retain recognizable modal information, which is of benefit to the

analysis. Impulse responses could also be used, as for the rail, but due to the light damping of the wheel modes, they would be impracticably long.

Consider a wheelset with  $n$  modes,  $j$  input dynamic forces  $\{\mathbf{f}^w\} = [f_1^w, f_2^w, \dots, f_j^w]^T$ , and  $i$  output dynamic velocities  $\{\mathbf{v}^w\} = [v_1^w, v_2^w, \dots, v_i^w]^T$ . This can be represented by a state equation and an output equation:

$$\{\dot{\mathbf{w}}\} = [\mathbf{A}^w]\{\mathbf{w}\} + [\mathbf{B}^w]\{\mathbf{f}^w\} \quad (4.3)$$

$$\{\mathbf{v}^w\} = [\mathbf{C}^w]\{\mathbf{w}\} \quad (4.4)$$

where the  $2n$ -order state-variable vector consists of the modal velocity  $\dot{q}_r$  and the modal displacement  $q_r$  of modes  $r$  (1 to  $n$ )

$$\{\mathbf{w}\} = [\dot{q}_1, \dot{q}_2, \dots, \dot{q}_n, q_1, q_2, \dots, q_n]^T = [w_1, w_2, \dots, w_{2n}]^T \quad (4.5)$$

The system matrix  $[\mathbf{A}^w]$  is given by

$$[\mathbf{A}^w] = \begin{bmatrix} -2\zeta_1\omega_1 & 0 & \dots & 0 & -\omega_1^2 & 0 & \dots & 0 \\ 0 & -2\zeta_2\omega_2 & \dots & 0 & 0 & -\omega_2^2 & \dots & 0 \\ \vdots & \vdots & \ddots & 0 & \vdots & \vdots & \ddots & 0 \\ 0 & 0 & \dots & -2\zeta_n\omega_n & 0 & 0 & \dots & -\omega_n^2 \\ & 1 & 0 & \dots & 0 & 0 & \dots & 0 \\ & 0 & 1 & \dots & 0 & 0 & \dots & 0 \\ & \vdots & \vdots & \ddots & 0 & \vdots & \ddots & \vdots \\ & 0 & 0 & \dots & 1 & 0 & \dots & 0 \end{bmatrix} \quad (4.6)$$

where  $\zeta_r$  is the damping ratio of mode  $r$  (1 to  $n$ ) and  $\omega_r$  is the natural frequency (in rad/s) of mode  $r$ . The input matrix  $[\mathbf{B}^w]$  can transform external forces into modal forces for each mode, while the output matrix  $[\mathbf{C}^w]$  sums modal velocities of each mode into velocities in physical coordinates. Both matrices are formed with mode shapes of the wheelset:

$$[\mathbf{B}^w] = \begin{bmatrix} \phi_{11} & \phi_{12} & \dots & \phi_{1r} & 0 & 0 & \dots & 0 \\ \phi_{21} & \phi_{22} & \dots & \phi_{2r} & 0 & 0 & \dots & 0 \\ \vdots & \vdots & \ddots & \vdots & \vdots & \vdots & \ddots & \vdots \\ \phi_{j1} & \phi_{j2} & \dots & \phi_{jr} & 0 & 0 & \dots & 0 \end{bmatrix}^T \quad (4.7)$$

$$[\mathbf{C}^w] = \begin{bmatrix} \phi_{11} & \phi_{12} & \dots & \phi_{1r} & 0 & 0 & \dots & 0 \\ \phi_{21} & \phi_{22} & \dots & \phi_{2r} & 0 & 0 & \dots & 0 \\ \vdots & \vdots & \ddots & \vdots & \vdots & \vdots & \ddots & \vdots \\ \phi_{i1} & \phi_{i2} & \dots & \phi_{ir} & 0 & 0 & \dots & 0 \end{bmatrix} \quad (4.8)$$

where  $\phi_{ir}$  and  $\phi_{jr}$  are the mass-normalised mode shapes of the mode  $r$  in the  $i$  and  $j$  directions. In a Cartesian coordinate system, there are up to three forces and three moments at a point and six corresponding motions. Hence,  $i$  and  $j = 1$  to 6.

For the wheelset considered in the previous section, the impulse response in the time

---

domain is obtained from the state-space matrix of the wheelset and is shown in Figure 4.4. The dominant frequency of the impulse response is around 5 Hz corresponding to the rigid body modes.

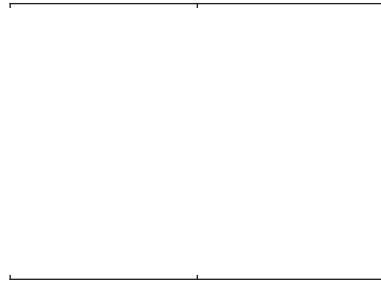


Figure 4.4 Impulse response of the wheelset in the radial and axial directions

## 4.3 Dynamic interaction model

### 4.3.1 Wheel/rail displacements

In the literature, many models of the interaction between the wheel and the rail have been developed and refined. The vertical interaction problem in particular has been studied in great detail, including the experimental validation of a two-dimensional time-domain model by Nielsen [126]. Andersson and Abrahamsson [127] carried out a three-dimensional analysis using a more complex time-domain model. In addition, the impulse response function approach of Pieringer et al. [128] has the potential to make a significant reduction in calculation times compared with more established time-domain techniques.

Based on the dynamic characteristics obtained from the wheelset (Section 4.2.2) and track models (Section 3.5) presented in previous sections, the wheel-rail contact forces can be expressed as a function of the wheelset and track displacements. The calculation of the displacements and contact forces is performed within the time stepping integration of the

equations of motion for the wheelset and the track. Using the time-domain models of the wheelset and the rail, the vectors of wheel and rail displacements at the contact points are computed including the initial irregularities of wheel and rail.

In order to describe the variables in the contact zone, a moving reference frame  $(x', y', z')$  is introduced, shown in Figure 4.5, which moves with the nominal contact point along the rail. The nominal point is the point where the rigid profiles of wheel and rail would touch first, when contact is initiated. Its lateral position is assumed constant in the simulation. The  $x'$ -axis points in the rolling direction along the rail, the lateral direction is the  $y'$ -direction pointing towards the field side of the wheel and the vertical  $z'$ -coordinate points downwards into the rail.  $F_z$ ,  $F_y$  and  $F_x$  represent the vertical, lateral and longitudinal contact forces acting at the nominal contact point between the wheel and rail.

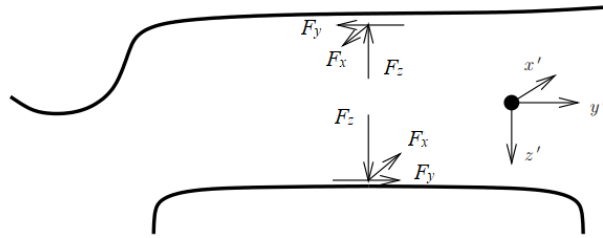


Figure 4.5 Moving reference frame containing the wheel-rail interactions

In the interaction model, for a wheel rolling velocity of  $V$ , the vertical displacement of the track at the nominal contact point,  $\zeta_z^R(t)$ , is calculated by a convolution of the vertical contact forces with the moving Green's functions of the discretely supported track

$$\zeta_z^R(t) = \int_0^t \sum_{i=1}^3 F_i(\tau) g_{iz, V}^{R, V\tau}(t-\tau) d\tau \quad (4.9)$$

where here  $1=x$ ,  $2=y$ ,  $3=z$ . The discrete version of Equation (4.9) formulated at time step  $m$  reads

$$\zeta_z^R(m) = \sum_{n=1}^{\min(N_R, m)} \sum_{i=1}^3 \Delta t g_{iz, V}^{R, V[m-n]\Delta t}(n) F_z(m-n+1) \quad (4.10)$$

where the moving Green's functions of the discretely supported track  $g_{iz, V}^{R, x_0}(n)$  are presented in Section 2.4.

The vertical displacement of the wheel at the nominal contact point,  $\zeta_z^W(t)$ , is calculated by the state-space matrix of the wheel and the fourth order Runge-Kutta integration algorithm between each time interval. Different from the track system, the axle load is applied to the wheel. Taking the effect of the axle load into account, the resultant force that leads to the

vertical displacement of the wheel is  $P-F_z$ , where  $P$  is the axle load applied to the wheel due to the vehicle weight. If the wheel displacement is given by a convolution, it can be written as

$$\xi_z^W(t) = \int_0^t \sum_{i=x}^z (P-F_i(\tau)) g_{iz}^W(t-\tau) d\tau \quad (4.11)$$

where  $i=x,y,z$ . The discrete version of Equation (4.11) formulated at time step  $\alpha$  reads

$$\xi_z^W(\alpha) = \sum_{n=1}^{\min(N_R, \alpha)} \sum_{i=x}^z \Delta t g_{iz}^W(n) (P-F_z(\alpha-n+1)) \quad (4.12)$$

where the impulse response of the wheelset  $g_{iz}^W(n)$  is given in Section 4.2.2. However, this method described by Equation (4.11) and (4.12) is not used here. The wheel displacement is obtained as follows.

In the time stepping procedure to calculate the wheel displacement, the rail displacement obtained by Equation (4.10), initial wheel displacement, the state-space matrix of the wheel and the equivalent contact spring stiffness are used as inputs to the fourth order Runge-Kutta integration algorithm. Meanwhile, a self-established function used inside the fourth order Runge-Kutta integration algorithm is then used to obtain the wheel/rail contact forces. Here ‘ode45’ solver is used for numerical convergence and the time step is constant throughout the calculation to obtain the correct rail displacement.

Inside the self-established function, the output matrix  $[C^w]$  is adjusted to sum modal displacement of each mode into displacements in physical coordinates.

$$[C^w] = \begin{bmatrix} 0 & 0 & \cdots & 0 & \phi_{11} & \phi_{12} & \cdots & \phi_{1r} \\ 0 & 0 & \cdots & 0 & \phi_{21} & \phi_{22} & \cdots & \phi_{2r} \\ \vdots & \vdots & \ddots & \vdots & \vdots & \vdots & \ddots & \vdots \\ 0 & 0 & \cdots & 0 & \phi_{i1} & \phi_{i2} & \cdots & \phi_{ir} \end{bmatrix} \quad (4.13)$$

Then this physical wheel displacement is combined with rail displacement obtained in advance and the surface roughness to obtain the contact force as introduced in detail in the next section. The contact force is used in Equation (4.3) to obtain the  $2n$ -order state-variable vector  $\{\mathbf{w}\}$  consisting of the modal velocity  $\dot{q}_r$  and the modal displacement  $q_r$  of modes  $r$  (1 to  $n$ ). Since the wheelset modal damping is low, when using the convolution for the wheelset to get its impulse response, it takes more time than using the state-space method. For efficiency, the state-space method is used for the wheelset.

### 4.3.2 Contact forces

In most wheel-rail interaction models to calculate the contact forces, the effect of the discrete size of the contact patch is limited to filtering the roughness excitation of the

system. Hertz's solution [129] is often used for the contact patch calculation. This solution is based on the linear elastic relation between the stress and small deformation of the contacting bodies.

The Hertz theory is restricted to frictionless surfaces and is based on a half-space assumption (semi-infinite elastic body bounded by the contact surfaces) and the assumption that the surfaces can be approximated by a constant radius of curvature in orthogonal directions. According to this theory, the contact area is elliptical since the contact surfaces are continuous and non-conforming. Its shape and orientation are sensitive to the wheel/rail curvatures in the vicinity of the contact. The size of the contact area is determined by the normal load. The strains are assumed to be small, so linear elasticity theory is applicable; only normal stress is considered in the contact region.

As the contact area increases with increasing normal load, the local elastic deformation at the wheel/rail contact has a non-linear relationship to the normal load. Hertz [129] first defined the load-deflection relation between contacting bodies described by their radii of curvature at the contact. The contact area is commonly replaced by a non-linear Hertzian spring acting at a single point. This is adequate for the determination of the overall normal force. By applying the Hertzian contact spring and the initial roughness of the wheel and rail,  $r$ , the normal wheel-rail contact force  $F_z$  can be calculated by

$$F_z = \begin{cases} C_H [\xi^w - \xi^R - r]^{3/2} & \xi^w - \xi^R - r > 0 \\ 0 & \xi^w - \xi^R - r \leq 0 \end{cases} \quad (4.14)$$

where  $C_H$  is the Hertzian constant which depends on the radii of curvature [129], in the study of this thesis, according to the radius curvature, the Hertzian constant value is  $93.7 \text{ GN/m}^{3/2}$ .

These models which apply the Hertz theory for the normal problem are usually applied in the FASTSIM algorithm to solve the tangential problem. FASTSIM is developed based on the Hertz theory for the normal problem. For the simple cases studied in this chapter, the Hertz theory and FASTSIM algorithm are used which are sufficient.

However, for curved track the contact conditions are not as ideal as assumed in the Hertz theory. Kalker's variational method [14] considers the wheel/rail contact as a 3-D contact problem and can solve both the normal and tangential problems. It considers the displacements in the wheel/rail contact as a penetration in the normal direction and a sliding in the tangential direction. The stress distribution in the contact patch is predicted



---

and the sum of the stresses would be the resultant contact forces. This wheel-rail contact model for more realistic situations is described in detail in the next chapter and applied for the calculations of the rest of this thesis.

Kalker's variational method [14] can also be used to calculate the interaction contact forces between the wheel and the rail. Prior to the simulation, the wheel-rail contact geometry is processed starting from measured or theoretical wheel and rail profiles. The contact parameters required, such as contact position, normal load and steady-state creepages, to compute wheel-rail contact forces are obtained from the steady-state curving model, which was described in Chapter 2. An undeformed distance calculated from the transverse profiles, which is equal to zero for the geometric contact point and greater than zero for the other potential contact points, is also needed.

The position of the contact point and the contact parameters at each time step of the numerical integration are computed considering the vibration of the wheelset and the track. Then an elastic penetration is computed by projecting the relative wheel-rail displacements in the contact point along the direction normal to the contact plane. Together with the roughness of the wheel and rail, the distance between the wheel and rail is modified. The points inside the potential contact area, for which the distance between wheel and rail is negative, form the actual contact area. Through the contact model which follows, the normal pressure of all the points inside the potential contact area can be obtained. By multiplying the normal pressure of each element in the contact area by the corresponding area of the element and summing the normal force of each element, the total normal and tangential contact forces between wheel and rail can be obtained.

### **4.3.3 Contact filter**

In both kinds of interaction model (single-point contact model and distributed contact model), the surface roughness is assumed to excite the wheel/rail system at the contact point or inside the contact patch. This roughness may be present on the wheel or the rail with the same effect. A relative displacement between the wheel and rail is introduced. When the roughness is present on both surfaces, they can be safely assumed to be incoherent [92]. To obtain the response due to both the wheel and rail surfaces roughness, their spectra can be added in terms of mean-square values.

In three-dimensional analysis, the contact between the wheel and rail exists over an area. In Hertz theory, this contact area is assumed to be elliptical with semi-axes  $a$ , and  $b$ , while in

---

practice the geometry of the contact area can be more complex. Roughness with wavelengths shorter than the contact length in the rolling direction,  $2a$ , tends to be attenuated in its excitation of the wheel/rail system. This effect is known as the ‘contact filter effect’. Moreover, in the lateral direction, the roughness profile differs across the width of the contact area. Its effect will be averaged out to some extent.

In the literature, there are two ways to introduce the contact filter. Remington [130] developed an analytical model for the contact filter. For a circular contact patch with radius  $a$ , the filter transfer function can be approximated in a simple way:

$$|H(k)|^2 = \left(1 + \frac{\pi}{4} (ka)^3\right)^{-1} \quad (4.15)$$

where  $k=2\pi/\lambda$  is the roughness wavenumber in the longitudinal direction,  $\lambda$  is the wavelength.

A numerical method for the contact filter was developed in [130], in which the contact zone between the wheel and rail is approximated by a series of distributed point-reacting springs (DPRS). The stiffness behaviour of these springs is assumed to be nonlinear in which the force is assumed to be proportional to the square root of the local deflection. In this way, the correct overall relationship between force and deflection is given. To maintain the correct contact area, the radii of curvature of the wheel and rail also have to be modified. The DPRS model produced a blocked force induced by the roughness passed between the wheel and rail. To avoid the excessive forces or loss of contact due to large amplitudes at long wavelengths, a high pass filter was built into the model by representing the wheel as a mass supported on a damper [131].

The contact filter effect should be added to the roughness used in the point contact models. The distributed contact models, such as the variational method used in the wheel/rail contact model in this research, implicitly include a dynamic contact filter. Thus, in the following calculations using this model there is no need to add an external contact filter.

#### 4.3.4 Validation by simple cases

Previous models have used either the Green’s functions [86] or the state-space method [116] to obtain the dynamic response of the track system and wheelset. The present approach involves the combination of these two approaches. This can keep the accuracy of the results, and also save computation time. The current model can be validated by comparison with these two established methods through some simple cases. Only the normal interaction problem is solved in the results presented here; the tangential problem

will be solved by the following wheel-rail contact model in Chapter 5. Thus, for the simple cases in this section, the Hertzian contact spring is used instead of Kalker's variational method for solving the normal contact force problem.

In the first case the wheelset is considered as a simple mass-spring-damper system. Since the damping of the wheelset is small compared with the track, it takes longer for the impulse response of the wheelset to decay to zero. This means the length of the Green's function used for the wheelset would be longer. Here, the wheelset is considered as single-degree-of-freedom system. Under this assumption, the full Green's functions for both the wheelset and the track can be adopted without high demand of computation capacity. The mass of half the wheelset  $m_w$  considered here is 550 kg, while the damping  $c_w$  is 13.2 kNs/m and the stiffness  $k_w$  is 1.12 MN/m, chosen to give a natural frequency of about 7 Hz and a damping ratio of 0.012.

For the simple mass-spring-damper system considered here, its receptance is given by:

$$G^w = \frac{1}{-m_w \omega^2 + k_w + i c_w \omega} \quad (4.16)$$

where  $\omega$  is the angular frequency and  $i$  is the imaginary unit given by  $i^2 = -1$ .

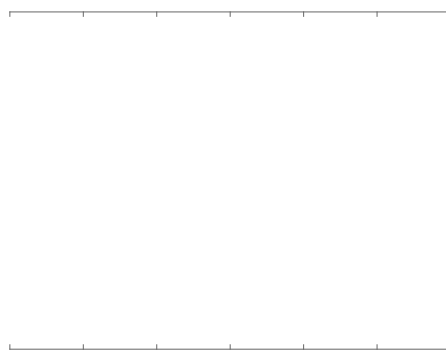


Figure 4.6 Impulse response of the mass-spring system

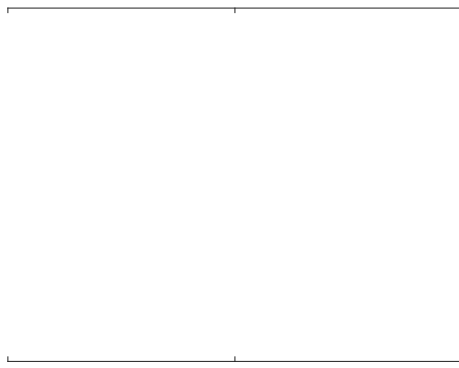


Figure 4.7 Roughness in the time domain used in simple cases of this section

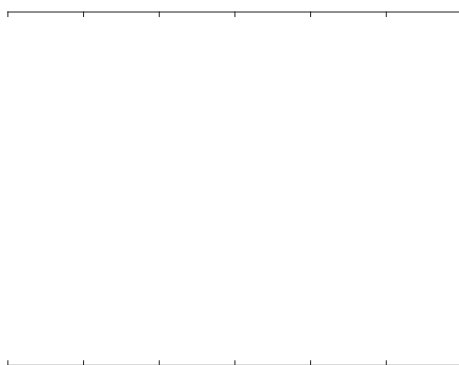


Figure 4.8 Predicted interaction contact force, WSS-RGF: combination of the Green's function with the state-space method; Green's Function: the full Green's function method

The impulse response, or Green's function, of the simple mass-spring-damper system obtained from the Fourier transform of Equation (4.16) is shown in Figure 4.6. In the following example simulations, the dynamic displacement of the mass-spring-damper system is calculated by a convolution of the normal contact forces with this impulse response.

The dynamic behaviour of the discretely supported track system is the same as in Section 3.4, using the moving Green's functions. The roughness is assumed to be an instantaneous dip with amplitude of 0.02 mm over 5 mm as shown in Figure 4.7. This is input at 0.6 second in the simulation in the Hertzian contact between the discretely supported track system and the single DOF system which represents the wheelset. The simulation under a speed of 20 m/s lasts for one second and the result is shown in Figure 4.8.

In the Figure 4.8, the legend 'WSS-RGF' represents the state-space method for the wheelset and the moving Green's functions for the track. 'Full GF' indicates that the Green's functions are applied to both the wheelset and the track. Before the roughness dip,

the wheel/rail contact force reaches steady-state. After the impulse roughness input, the contact force hardly oscillates and quickly returns to the steady-state value. The results of the two methods to calculate the interaction forces show good agreement, with a root mean-square error of 3.3 N.

In the second case, both systems are represented by a state-space formulation. The discretely supported track is too complex to be represented by a state-space matrix, so it is replaced by an equivalent two degree-of-freedom system. The rail and the sleeper are considered as masses while the rail pad and the ballast are considered as damped springs. Under this assumption, the full state-space method for both the wheelset and the track system can be adopted.

For the simple 2 DOF mass-spring-damper system considered here, using the state-space method, the system matrix  $[\mathbf{A}^r]$ , input matrix  $[\mathbf{B}^r]$  and output matrix  $[\mathbf{C}^r]$  are:

$$\mathbf{A}^r = \begin{bmatrix} 0 & 0 & 1 & 0 \\ 0 & 0 & 0 & 1 \\ -\frac{k_p}{m_r} & \frac{k_p}{m_r} & -\frac{c_p}{m_r} & \frac{c_p}{m_r} \\ \frac{k_p}{m_s} & \frac{-(k_p+k_b)}{m_s} & \frac{c_p}{m_s} & \frac{-(c_p+c_b)}{m_s} \end{bmatrix} \quad (4.16)$$

$$\mathbf{B}^r = \begin{bmatrix} 0 \\ 0 \\ 1 \\ 0 \end{bmatrix}$$

$$\mathbf{C}^r = [1 \quad 0 \quad 0 \quad 0]$$

where  $m_r = 60 \times 0.65$  kg and  $m_s = 300$  kg are the masses,  $k_p = 400$  MN/m,  $c_p = 400$  kN/m are the stiffness and damping between two masses and  $k_b = 104$  MN/m,  $c_b = 215.8$  kN/m are the stiffness and damping between the lower mass and the ground. These values are derived from Table 3.1 and 3.4 for a single sleeper bay. The impulse response of the 2-DOF system which contains the main features of the impulse responses in Section 3.4, is shown in Figure 4.9.

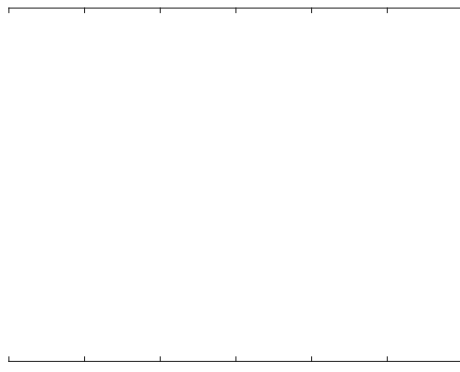


Figure 4.9 Impulse response of the two degree-of-freedom mass-spring system representing the track

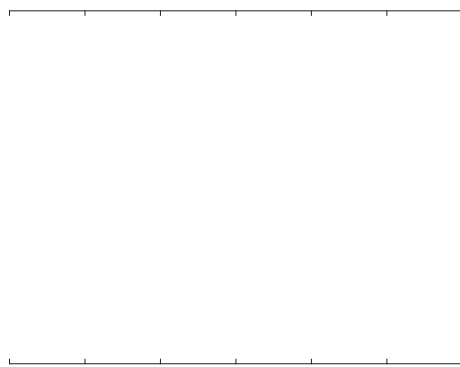


Figure 4.10 Interaction contact force predicted in the combination of the Green's function with the state-space method and the full state-space method

The system matrix of the 2-DOF system is combined with the system matrix of the wheelset. The system matrices are used in the fourth order Runge-Kutta integration algorithm to obtain the dynamic interaction force between these two systems.

In this case, the dynamic behaviour of the wheelset corresponds to the full set of wheelset modes, obtained from the finite element model in Section 4.2.2. With an input roughness of an instantaneous dip with amplitude 0.02 mm at 0.6 second (as shown in Figure 4.8), the simulation lasts for 1 second and the result is shown in Figure 4.10.

In Figure 4.10, the legend 'WSS-RGF' represents the state-space method for the wheelset and the moving Green's functions for the track system as previously. 'Full SS' indicates that the state-space method is applied to both the wheelset and the track. After the dip roughness input, the interaction contact force hardly oscillates and quickly returns to the steady-state value. The results of the two methods used to calculate the interaction forces again show good agreement, with a root mean-square error of 3.27 N.

After the calculation of these two cases, the current method, using the combination of the state-space and moving Green's function methods, can be considered to be verified.

### 4.3.5 Comparison of Hertzian spring and variational contact model

In this section a comparison is given between results obtained using the nonlinear Hertzian spring model and the full variational contact model. Only normal contact is considered. Two cases are considered: one with a continuously supported track and the other with a discretely supported one.

#### 4.3.5.1 SDOF wheel model and continuously supported track

This case considers the wheel as a mass supported by a damped stiffness in contact with a continuously supported track. The train speed is 20 m/s. The steady-state curving parameters, i.e. normal wheel load, wheel-rail contact position based on the yaw angle and the lateral displacement of the wheelset, longitudinal creepage in the wheel-rail interaction, are obtained for a case in Section 2.3 and are listed in Table 4.1.

Table 4.1 Steady-state curving parameters used

Parameter	Value	Units
Normal load	38.08	kN
Lateral displacement	7.595	mm
Yaw angle	7.222	mrاد
Longitudinal creepage	0.2381%	-
Lateral creepage	0.7211%	-
Spin	-0.03561	1/m
Speed	20	m/s
Curve radius	300	m
Longitudinal semi-length $a$	5.1	mm
Lateral semi-length $b$	3.7	mm

For the time-domain model of the continuously supported track system, a single moving Green's function is used. This is because the track is on a continuous support, so the impulse responses are independent of the position of the excitation and response point, and only depend on the distance between them. The dynamic displacement of the track is obtained by the time-stepping integration of the dynamic wheel-rail interaction force together with the Green's function. Due to starting transients in the numerical integration, the dynamic interaction force needs to be calculated for a long enough time period to reach

---

a steady-state value, before calculating the response to the roughness. This procedure done here is to obtain the time history in steady-state of these necessary parameters.

The calculations are performed using both the Hertzian and variational contact models. The SDOF wheel system is considered to move over the continuously supported track system for around 200 m. Figure 4.11 shows the normal interaction force between the wheel and rail in the time domain obtained by the two interaction models. The simulation is run for 4 s with a smooth rail to allow the process to reach a steady-state and then the broadband initial roughness obtained based on the limit curve given in ISO 3095-2013 [133] is introduced. The way to generate the roughness profile and its spectrum in comparison with the ISO 3095-2013 curve are introduced in detail in Appendix C. The broadband initial roughness obtained here is applied on all lines across the width of the contact zone. The fluctuation of the interaction force obtained by the variational contact model is smaller than that obtained by the Hertzian contact spring model. The corresponding 1/3 octave band force spectra from the two models are shown in Figure 4.12, from which it can be seen that the differences are mainly at high frequencies due to the contact filter effect. Figure 4.13 gives the difference between these two spectra which can be taken as the contact filter effect of the current variational contact model. This is compared with the DPRS contact filter result [97].

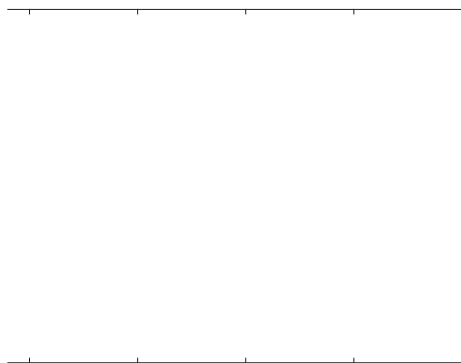


Figure 4.11 Interaction force in time domain for the contact between SDOF system and the continuously supported track



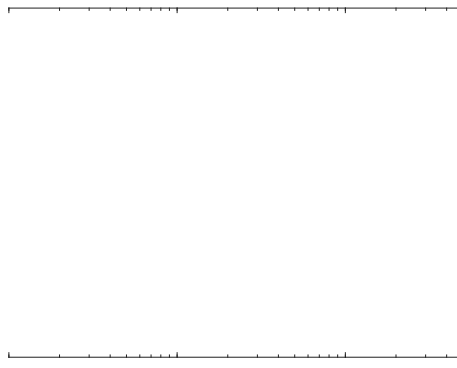


Figure 4.12 Interaction force spectrum for the contact between SDOF system and the continuously supported track

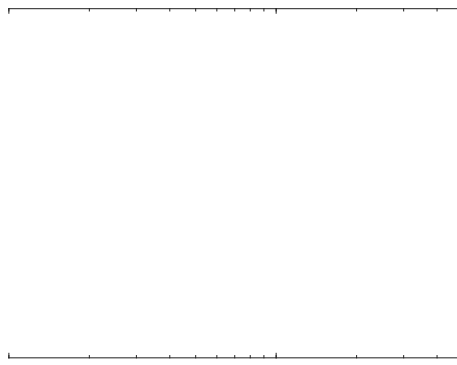


Figure 4.13 Contact filter effect derived from current results compared with DPRS results

#### 4.3.5.2 SDOF wheel model and discretely supported track

This case again considers the wheel as a mass supported by a damped stiffness, but it is now in contact with a discretely supported track in a tight curve. The steady-state curving parameters are again obtained from the case without applied traction in Section 2.3. Since the steady-state curving model mainly considers the dynamic behaviour of the vehicle, not the track, the same steady-state curving parameters are used as in the last section. The train speed is 20 m/s, as in the previous section.

For the time-domain model of the discretely supported track, a certain number of moving Green's functions are used (here 325) to describe the dynamic behaviour of the track. As in the previous case, the dynamic interaction force is calculated for a long enough time period to reach a steady-state value before calculating the response to the roughness.



Figure 4.14 Normal interaction force in time domain for the contact between SDOF system and the discretely supported track



Figure 4.15 Normal interaction force spectrum for the contact between SDOF system and the discretely supported track

Both Hertzian and variational contact models are again used for this case. Figure 4.14 shows the normal wheel/rail interaction force in the time domain obtained by the two interaction models. As before, an initial calculation is performed with a smooth rail for 4 s to reach steady-state and then the broadband initial roughness obtained based on the limit curve given in ISO 3095-2013 [133] is introduced. Similar to the previous case, the fluctuation of the interaction force obtained by the variational contact model is smaller than that obtained by the Hertzian contact spring. The spectra of the normal interaction force from the two models shown in Figure 4.15, showing similar trends to those in Figure 4.12.

#### 4.4 Summary

The semi-analytical track model described in Chapter 3 has been combined with a numerical wheelset model to obtain the wheel-rail interaction forces. The equations of motion of the wheelset are solved in the time domain using a state-space approach.

---

Two methodologies to calculate the dynamic interaction force are introduced. Both of them need the dynamic penetration in the wheel-rail contact. The dynamic penetration is calculated using the moving Green's functions for the track system and the state-space approach for the wheelset. After obtaining the dynamic penetration at each time step, the wheel-rail interaction force can be calculated by either the Hertzian contact spring used in this chapter or the wheel-rail contact model used here as well but introduced in detail in the next chapter. The interaction model has been validated for two example cases, one based entirely on the Green's functions and the other based entirely on the state-space approach. The normal interaction force between the wheel and the rail is required as an input to the contact model which follows to solve the tangential problem and to the wear model which follows to predict the wear depth.

When a railway vehicle negotiates a tight curve, high levels of vibration and noise usually arise. The rolling noise radiated by the vibration of the wheel and rail is generally more severe than on straight track. The effect of track curvature on rolling noise is also investigated based on the current wheel/rail interaction model. This is introduced in Appendix C.



---

## 5 Contact and wear model

### 5.1 Introduction

The previous chapter has concentrated on describing the model of the overall normal interaction force between the wheel and the rail. For this purpose, it is sufficient to model the wheel-rail contact as a Hertzian spring. However, to predict the wear of the rail surface resulting from the passage of the wheels, a more detailed model of the wheel-rail contact is required. The size and shape of the contact area and the distribution of normal and tangential stresses throughout the wheel-rail interface are then obtained.

In the current wheel-rail contact model, the variational method [14] is used which is more universal than the simpler Hertz theory. Starting from static cases, which consider constant normal and tangential forces in stationary contact, the method of calculating the stress distribution in the wheel-rail contact is introduced. The rolling contact problem is considered as an extension of the model for static contact, which includes transient effects. For rolling, the model is applied in a ‘time-stepping’ fashion and the contacting surface is stepped along the wheel and railhead surfaces. The stresses and displacements at each time-step in rolling depend on the values at the previous position.

The distribution of normal and tangential stresses in the contact and the identification of stick and slip zones when rolling are also of interest. In the situation that parts of the contacting surfaces slip, the relative sliding velocity of the contacting structures in the slip zone is important for the calculation of rail (and wheel) wear (In the current study only the effect on rail wear is considered). Thus, the calculation of the slip velocity at each location in the contact area is described. Tangential loading of the wheel-rail contact occurs especially during acceleration, braking or during curving.

When using the variational method, steady rolling can be considered as a special case that develops over a period of time through transient rolling from a set of initial conditions with unchanging external loads. Considering non-Hertzian effects in the form of rail roughness is important when determining the distribution of normal and tangential stresses which will be included at end of this chapter.

In this chapter, various wear models are also introduced. A common feature of these wear models is that the amount of material removed in the contact patch is determined by the

---

severity of normal and tangential stresses and the slip displacement or velocity in the slip region. These parameters can be obtained from the wheel/rail contact model and are linked to the wear models described in this chapter. In this thesis, the wear model developed by Braghin [134] is used, which contains several wear mechanisms.

## 5.2 Review of contact models

Hertz theory is widely used for the calculation of normal stress distributions in contact. However, it has many restrictions or assumptions [136]: the contact surface profiles must be parabolic in two dimensions and any higher terms are neglected; the surfaces must be smooth, non-conforming and frictionless; elastic half-space theory must be valid, that is the contact dimensions must be small compared with the radii of curvature of the undeformed surfaces; the contact stress must not depend on the shape of the bodies away from the contact patch.

Due to these restrictions, Hertz theory is not strictly applicable for the wheel-rail contact since the roughness of the surface in practice is likely to contain wavelengths (including corrugation) that are of comparable length to the dimensions of the contact patch. Kalker developed a variational method [14] which was based on minimising a strain energy function subject to the constraint that the contact pressure is positive inside the contact patch and presumed to be zero outside the contact. It can be used for both Hertzian and non-Hertzian contact problems and takes account of transient effects. Its main limitations are the computational time and neglect of plastic deformation.

Johnson [135] presented an approximation to the elastic half-space assumption in which the contact between the two bodies was replaced by a Winkler elastic foundation. This approximation avoided the difficulty in elastic contact stress theory that the displacement at any point on the contact surface depends on the distribution of pressure throughout the whole contact. Instead, it was assumed that the contact pressure at any point depends only on the displacement at that point. However, it had the difficulty that the contact area was not calculated correctly, similar to the DPRS method [97].

Surface adhesion effects in rolling contact have been analysed by Hao and Keer [136]. These effectively contribute to friction in the contact. However, in railway applications, the normal forces are high and the surface adhesion effects are not significant. The effect of surface roughness in a rolling contact analysis has also been studied [137]. It was found that a high roughness level reduced the tangential force that can be supported in the contact

---

and effectively modified the stress distribution and creep.

Among these models, non-Hertzian models give better and more practical results than the Hertzian ones, within the elastic half-space assumption. The accuracy of the results is limited by the computational capacity and the element size used to solve the problem. Transient effects are also considered to be important since high frequency responses are of interest. Thus, a non-Hertzian non-steady-state rolling contact model is used in this research based on Kalker's variational theory [14]. The friction coefficient is assumed to be constant, at least initially.

### **5.3 Stress distribution in the wheel-rail contact**

The work of Johnson [135] has been used as a source for much of the background material to describe the contact problem. The variational method developed by Kalker [14] is used for the analysis of wheel-rail contact. Kalker implemented this theory in his CONTACT program, which remains recognized as the benchmark solution to the rolling contact problem [138]. However, until recently, the application of CONTACT to determine the distribution of stresses in three dimensions between railway wheels and rails in the time domain has been limited by the calculation time required for the analysis. This section describes the implementation in MATLAB of a contact model explained by Kalker in his variational theory in three-dimensional form. For verification of the model only static cases are considered here, such as stationary contact with constant normal and tangential forces. Rolling contact is considered in the next section.

The minimum inputs to a wheel/rail contact model are the overall normal forces between the wheels and rails, and the initial profiles of the wheel and rail surfaces which refer to the undeformed state before contact. The overall normal force between the wheels and rails can be obtained from the interaction force model presented in Section 4.3. For model verification at this stage, the normal and tangential forces are assumed to be constant.

#### **5.3.1 Contact geometry**

The original undeformed surface profiles of the wheel and rail are defined as  $z_w(x,y)$  and  $z_r(x,y)$  as shown in Figure 5.1. The undeformed distance between the wheel and rail surfaces is then given by  $h(x,y)$ , as the difference between  $z_w(x,y)$  and  $z_r(x,y)$ .

$$h(x,y) = z_w(x,y) - z_r(x,y) \quad (5.1)$$

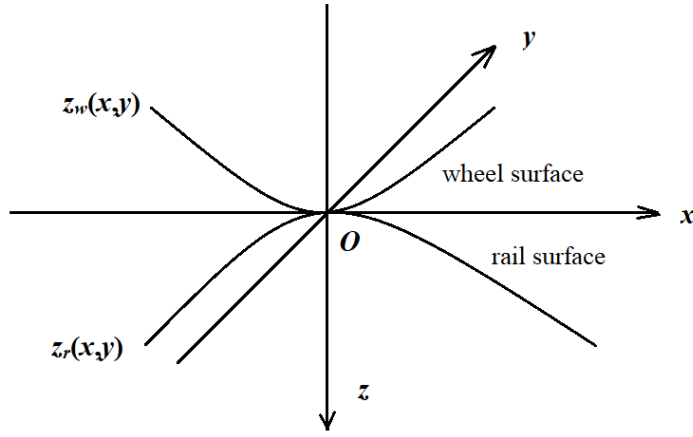


Figure 5.1 Geometry of wheel and rail in the contact

When the wheel and rail come into contact, the contact area is generated due to the normal interaction force. The relative motion of two surfaces in contact may be defined in terms of sliding, rolling and spin [86]. Sliding occurs when a relative linear velocity  $\Delta v$  is present between the two surfaces at the contact point.

$$\Delta v = v_w - v_r \quad (5.2)$$

where  $v_w(x,y)$  and  $v_r(x,y)$  are the linear velocities of the wheel and rail surfaces relative to the origin  $O$ . The sliding velocity  $\Delta v$  may have components in the  $x$  and  $y$  directions, but not in the  $z$  direction as the bodies are assumed to remain in contact. Rolling is a relative angular velocity  $\Delta \omega$  between the two bodies about an axis lying in the tangent plane. Spin is a relative angular velocity about the common normal, here the  $z$  axis.

The overall forces that may be transmitted through the contact area  $S$  are the compressive normal force  $P$  and the tangential force  $Q$  due to friction. The tangential force includes components in the longitudinal direction along the  $x$  axis and in the lateral direction along the  $y$  axis. The forces  $P$  and  $Q$  are related by the coefficient of friction  $\mu$  such that the magnitude of  $Q$  is less than or equal to the friction limit.

$$|Q| \leq \mu P \quad (5.3)$$

The normal force  $P$  and the tangential force  $Q$  are the resultants of stresses distributed across the interface area which lies in the  $x$ - $y$  plane. This distribution corresponds to a normal pressure vector  $p(x,y)$  and a tangential stress vector  $q(x,y)$  across the surface area such that

$$P = \int_S p dS \quad (5.4)$$

$$Q = \int_S q dS \quad (5.5)$$



### 5.3.2 Stick and slip zones

If the magnitude of the tangential force is less than  $\mu P$ , then the contact is not purely sliding. A relative movement or slip can occur between the surfaces in part of the interface, and another part of the interface will stick, or deform without relative motion between wheel and rail surfaces. The contact patch is then divided into stick and slip zones as shown in Figure 5.2, based on a calculation by FASTSIM for illustration.

At points in the stick zone, the tangential stress must be less than the limiting value due to friction,

$$|q(x,y)| < \mu p(x,y) \quad (5.6)$$

whereas in the slip zone the tangential stress is at its maximum and is equal to the friction limit.

$$q(x,y) = \mu p(x,y) \quad (5.7)$$

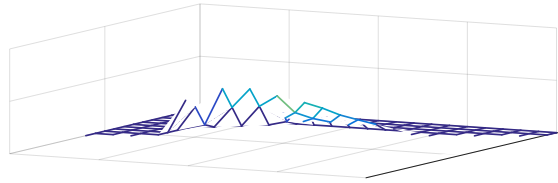


Figure 5.2 Contact area under a longitudinal creepage calculated by FASTSIM [13]

Upper: tangential stress distribution; Lower: tangential stress for the centreline,

--- limit stress  $\mu p$ , — tangential stress  $q$

The slip  $s$  is defined as the relative tangential displacement between two initially coincident points in the contacting structures. Slip is taken to be positive when the upper structure moves in the positive  $x$  direction or  $y$  direction relative to the lower structure. The tangential stress is in the direction opposing the direction of slip,

$$\frac{q(x,y)}{|q(x,y)|} = - \frac{s(x,y)}{|s(x,y)|} \quad (5.8)$$

---

while the slip is zero in a stick region. The solution of the contact problem gives the distribution of normal and tangential stresses as well as the location of the stick and slip regions in the contact area. In general, the normal stresses depend on the tangential stresses due to the presence of friction. In this case, the identification of the stick and slip zones would be more complex and slip may occur even when the tangential force does not reach the friction limit. However, if the materials of the two contacting structures are identical, an assumption can be made that the tangential displacements resulting from the normal force are identical in both structures. That means the normal stress distribution is independent of the tangential stress [13].

### 5.3.3 Calculation of stress distribution

Hertz developed his analytical theory describing the contact between parabolic surfaces in 1880. The normal stress distribution throughout the contact area can be obtained by this theory. The equations are summarized by Johnson [135] for general profiles within the limitations of the theory. From Hertzian contact, if the undeformed surface profiles of two structures  $z_w(x,y)$  and  $z_r(x,y)$ , and the overall normal force  $P$  over the contact area, are known, it is possible to evaluate the size and shape of contact area and the distribution of the normal stresses. However, for surfaces which are rough or not parabolic, the Hertz theory is no longer applicable.

For more general contact geometry, numerical methods for the evaluation of the stress distributions are usually either a direct method such as [135], where boundary conditions are satisfied exactly at specified matching points, or a variational method such as [14], where the values of traction at the elements are chosen to minimize an appropriate energy function. For both kinds of method, a potential area of contact is first defined in the  $x$ - $y$  plane that is greater than the actual contact area.

The direct method is also known as the matrix inversion method. However, it is not suitable for calculating the contact stress distribution in detail at many positions due to the computational cost required for the inversion of large matrices at each position of interest. Thus, in the present research, the variational method based on Kalker's CONTACT algorithm [14] is used.

In the variational method (also in the direct method), the potential contact area is divided into  $N$  elements, each of length  $\Delta x$  and width  $\Delta y$ . The normal elastic displacement  $u_z$  at the

centre of each element satisfies the relation

$$u_z + h(x,y) - \delta \begin{cases} = 0 & \text{in contact} \\ > 0 & \text{outside contact} \end{cases} \quad (5.9)$$

where  $\delta$  is the approach distance of distant points in the two bodies and  $h$  is the undeformed distance between the bodies as shown in Equation (5.1). The centre of each element may also undergo a tangential elastic displacement  $u_x$  or  $u_y$ . To determine the elastic displacements  $u_z$ ,  $u_x$  and  $u_y$ , normal and tangential ‘influence coefficient’ matrices  $C_{ij}$  and  $D_{ij}$  are required. The expressions of the influence coefficients are described here based on the approach of Kalker [14].

Figure 5.3 shows the relevant geometry of the potential contact area.  $a_e$  is defined as the half length of each element in the  $x$  direction and  $b_e$  as the half length of each element in the  $y$  direction. For each of the  $N \times N$  possible combinations of elements, influence coefficients  $C_{ij}$  and  $D_{ij}$  are calculated as follows. The distance in the  $x$  and  $y$  directions between the centres of elements  $i$  and  $j$  is denoted  $x_{ij}$  and  $y_{ij}$ . The distances in the  $x$  and  $y$  directions between the centre of one element and the four corners of another element are then given by

$$\begin{aligned} x_1 &= x_{ij} + a_e & y_1 &= y_{ij} + b_e \\ x_2 &= x_{ij} - a_e & y_2 &= y_{ij} - b_e \\ x_3 &= x_{ij} - a_e & y_3 &= y_{ij} + b_e \\ x_4 &= x_{ij} + a_e & y_4 &= y_{ij} - b_e \end{aligned} \quad (5.10)$$

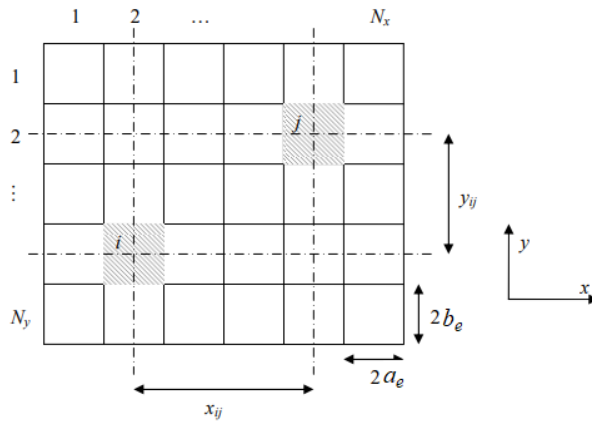


Figure 5.3 Geometry of the potential contact area in the  $x$ - $y$  plane

The straight-line distances between the centre of one element and four corners of another element are expressed as:

$$\begin{aligned}
L_1 &= \sqrt{x_1^2 + y_1^2} \\
L_2 &= \sqrt{x_2^2 + y_2^2} \\
L_3 &= \sqrt{x_3^2 + y_3^2} \\
L_4 &= \sqrt{x_4^2 + y_4^2}
\end{aligned} \tag{5.11}$$

The normal influence coefficient  $C_{ij}$  between any two elements is given by:

$$C_{ij} = \frac{(1-\nu)}{\pi G} [(f_1 + g_1) + (f_2 + g_2) - (f_3 + g_3) - (f_4 + g_4)] \tag{5.12}$$

and the tangential influence coefficient  $D_{ij}$  between any two elements is given by:

$$D_{ij} = \frac{1}{\pi G} [(f_1 + g_1) + (f_2 + g_2) - (f_3 + g_3) - (f_4 + g_4) - \nu (f_1 + f_2 - f_3 - f_4)] \tag{5.13}$$

Here  $\nu$  is Poisson's ratio and  $G$  is the shear modulus of the material. The functions  $f_{1-4}$  and  $g_{1-4}$  represent terms involving the geometrical distances derived in Equation (5.10) and (5.11). The functions  $f_{1-4}$  and  $g_{1-4}$  are defined as

$$\begin{aligned}
f_1 &= x_1 \log_e (L_1 + y_1) & g_1 &= y_1 \log_e (L_1 + x_1) \\
f_2 &= x_2 \log_e (L_2 + y_2) & g_2 &= y_2 \log_e (L_2 + x_2) \\
f_3 &= x_3 \log_e (L_3 + y_3) & g_3 &= y_3 \log_e (L_3 + x_3) \\
f_4 &= x_4 \log_e (L_4 + y_4) & g_4 &= y_4 \log_e (L_4 + x_4)
\end{aligned} \tag{5.14}$$

These influence coefficients are valid for contact between identical materials. With different materials, or cases involving spin, combined lateral and longitudinal forces occur as well as normal forces. The element displacement in each direction is then affected by forces acting in other directions. The influence coefficients are then more complicated. Here just the simpler case is described.

These influence coefficient matrices give the displacement of the centre of an element  $i$  on the contact surface due to a unit pressure applied at another element  $j$ . The total displacement of each element can then be determined from the sum of the displacements due to the normal pressure  $p$  or tangential stress  $q$  acting on all the elements in the potential contact surface:

$$u_{zi} = \sum_{j=1}^N C_{ij} p_j \tag{5.15}$$

$$u_{xi} = \sum_{j=1}^N D_{ij} q_{xj} \tag{5.16}$$

$$u_{yi} = \sum_{j=1}^N D_{ij} q_{yj} \tag{5.17}$$

To find the values of normal stress  $p_j$  and tangential stress  $q_j$  for each element  $j$  in the potential contact area, a quadratic minimization problem is solved involving the total complementary energy  $V^*$ . For this, the internal complementary energy  $U_E^*$  is introduced, also known as the complementary strain energy or the stress energy. For linear elastic materials  $U_E^*$  can be expressed in terms of normal stresses and displacements of the elements in the contact surface.

$$U_E^* = \frac{1}{2} \int_S p u_z dS \quad (5.18)$$

The total complementary energy  $V^*$  for a normal load can be written in terms of the internal complementary energy of the two stressed bodies and expressed as

$$V^* = \frac{1}{2} \int_S p u_z dS + \int_S p(h-\delta) dS \quad (5.19)$$

Substituting the expression for displacements from equation (5.15), equation (5.19) can be written as

$$V^* = \frac{1}{2} \sum_{i=1}^N A_i p_i \sum_{i=1}^N A_i p_i + \sum_{i=1}^N A_i p_i (h_i - \delta) \quad (5.20)$$

The approach of the two bodies  $\delta$  is assumed to be the same for all elements, and  $A_i$  is the area of each element. These do not affect the minimization problem and the function to be minimized for the distribution of normal stress  $p$  in the contact patch may be written as

$$\min F_{\text{norm}} = \frac{1}{2} \sum_{i=1}^N \sum_{j=1}^N p_i C_{ij} p_j + \sum_{i=1}^N h_i p_i \quad (5.21)$$

For the tangential stress, the function to be minimized has a similar form to that of the normal stress distribution. The term for the undeformed distance between the bodies  $h$  is replaced by a rigid tangential shift  $W_{it}$  and the prior displacement difference between the surfaces due to elastic deformation  $u'_{it}$ :

$$\min F_{\text{tan}} = \frac{1}{2} \sum_{i=1}^N \sum_{j=1}^N q_{xi} D_{ij} q_{xj} + \sum_{i=1}^N (W_{it} - u'_{it}) q_{xi} \quad (5.22)$$

This is also valid for the  $y$  direction. As the materials of the contact surfaces are assumed identical, the normal stress distribution is not affected by the tangential stress distribution.

Two constraints apply to the solution of the minimization problem for the normal case. The first is that the normal contact pressure  $p_j$  must be positive (compressive) within the contact area and zero outside the contact area. The second is that the sum of the normal stresses  $p_j$  on all the elements multiplied by the element area  $A_j$  must be equal to the total normal force  $P$ ,

$$P = \sum_{i=1}^N A_i p_i \quad \text{and} \quad p_i \geq 0 \quad (5.23)$$

In the tangential direction the constraint on the solution is that the magnitude of the tangential stress within the contact area must be less than the friction limit. In addition, if the overall tangential traction  $Q$  is known it must be equal to the sum of the stresses on the individual elements multiplied by the element area  $A_j$ , similar to the normal case.

$$Q = \sum_{i=1}^N A_i q_i \quad \text{and} \quad |q_i| \leq \mu p_i \quad (5.24)$$

### 5.3.4 Results

A simple case is considered in which a smooth sphere of radius 0.46 m is in contact with a flat plane. Thus, the contact area is circular and it is suitable to apply Hertz theory for comparison. The stress distribution obtained from the variational method is compared with the analytical solution based on the Hertz theory, calculated with a resolution of 0.5 mm. Firstly the overall normal force  $P$  in the contact is set to be 100 kN. The material of the contacting bodies is chosen to be steel with Young's modulus  $E = 210$  GPa and Poisson's ratio  $\nu = 0.3$ . For shortening the calculation time, the element size of the potential contact area for the numerical method is chosen to be 1 mm. Results in three-dimensional form are shown in Figure 5.4. The two-dimensional form on the centre line, which is the cross-section of the three-dimensional form, is shown in Figure 5.5.

The results obtained from the variational method and Hertz theory are in good agreement. The noticeable difference between them is at the edges of the contact patch which is due to the coarser discretization of the contact area used in the variational method.

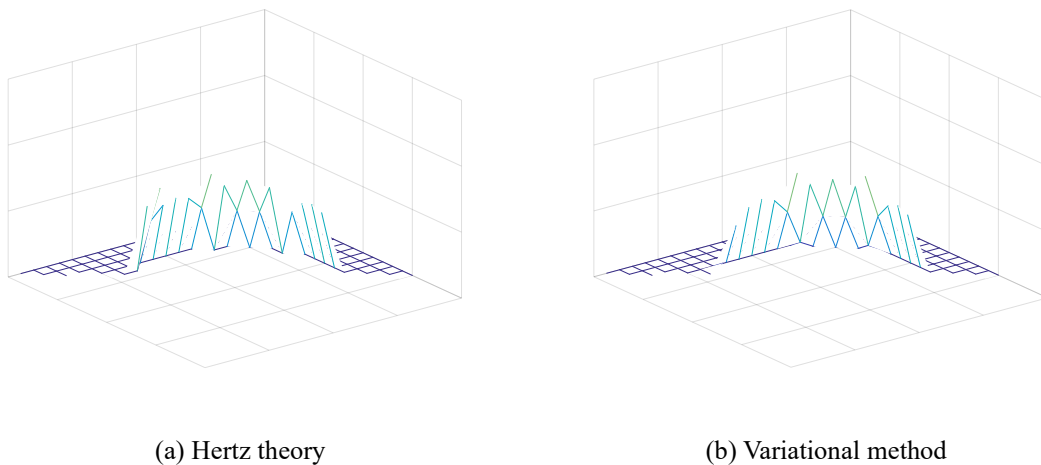


Figure 5.4 Normal stress distribution results in three-dimensional form

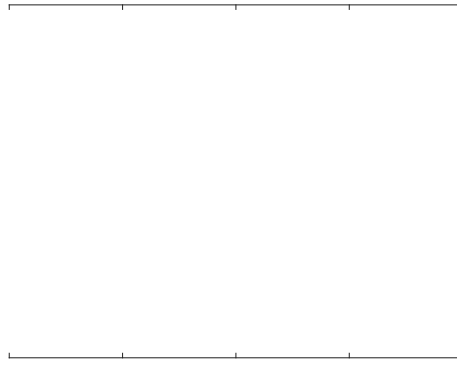


Figure 5.5 Normal stress distribution results on the centreline in the potential contact area

When applying a constant tangential force with value  $0.25\mu P$ , the division into stick and slip zones can be derived from the tangential stress distribution. The friction coefficient  $\mu$  is set equal to 0.3. An analytical expression for the tangential stress distribution is given by Johnson [102] based on a Hertzian normal stress distribution. Figure 5.6 shows the results obtained from the variational method and the analytical result from Johnson based on Hertz theory.

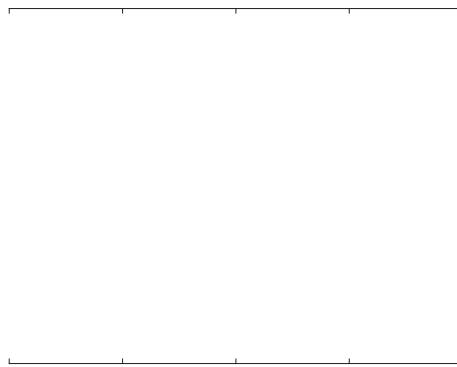


Figure 5.6 Tangential stress distribution results on the centreline in the potential contact area,  $Q=0.25\mu P$ ,  $\mu=0.3$

The differences between the variational method and Hertz theory in both normal and tangential cases are due to the discretization of the contact patch. The result accuracy can be improved by reducing the element size in the potential contact area; results for different element sizes are shown in Figure 5.7.

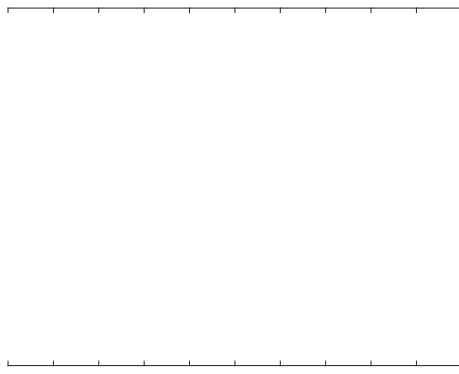


Figure 5.7 Tangential stress distribution results on the centreline in the potential contact area for different element size,  $Q=0.25\mu P$ ,  $\mu=0.3$

## 5.4 Rolling contact

### 5.4.1 Transient stress distribution

Analytical methods are limited to steady rolling contact problems. However, a wheel rolling over a rough rail is an unsteady or transient rolling contact problem since the forces and stresses in the contact vary with time. A quasi-static method is used in some models [27], in which the tangential stress distribution is calculated as steady state at each time step.

Actual transient effects are considered by using the variational method to calculate the stress distribution in rolling contact. In the variational method, the stress distribution in the contact patch at each time step depends on the stresses and displacements at the previous position. Steady rolling contact may then be considered as an extension or special case of the transient rolling contact theory.

The frame of reference is assumed to move with the contact patch. Rolling is assumed to take place in increments of time  $\Delta t$  with the current time given by  $t$  and the previous time by  $t'$ . In each time-step the wheel rolls forward a distance  $\Delta x=v\Delta t$  which is chosen to correspond to the length of an element in the potential contact area. The tangential loading on a rolling system may be represented by either an imposed overall tangential force  $Q$ , or an imposed rigid shift  $W_{it}$ . Acceleration or braking of a wheel corresponds to imposing an overall tangential force  $Q$ , while an imposed longitudinal creep may be described in terms of a rigid shift.

In general, if corresponding points on the rail and wheel are in contact in their deformed state at time  $t'=t-\Delta t$ , then the slip between their positions that occurs in a time-step  $\Delta t$  is the



sum of the rigid shift and the deformation shift given by

$$s_i(t-t') = (x_{wi} - x'_{wi}) - (x_{ri} - x'_{ri}) + (u_{wxi} - u'_{wxi}) - (u_{rx_i} - u'_{rx_i}) \quad (5.25)$$

where the  $x$  terms represent the rigid shift and the  $u_x$  terms represent the deformation shift. The deformation shift is the difference in the elastic displacement occurring in time  $\Delta t$  of the corresponding particles on the wheel and rail. The displacement difference  $u_{xi}$  is defined as the difference between the points on the two bodies at a particular time and is taken to be positive when the wheel moves in the positive longitudinal direction relative to the rail. The displacement difference  $u_{xi}$  is necessarily zero by definition in the stick zone although the tangential stress  $q$  and the deformations  $u_{wxi}$  and  $u_{rx_i}$  are not zero.

At time  $t'=0$ , the stress distribution  $q$  in the contact area is determined from the initial conditions of overall tangential loading or rigid shift. The elastic displacement difference in each element may then be determined, along with the division into stick and slip zones. The wheel then rolls forward a distance  $\Delta x$  in time  $\Delta t$ . The frame of reference moves along with the wheel. A slightly modified influence coefficient matrix  $D'_{ij}$  is required to relate the tangential stress at time  $t'$  to the displacement of the elements in the potential contact at time  $t$ .  $D'_{ij}$  is calculated by adding the distance  $\Delta x$  to the distance in the  $x$  direction between each element combination. In fact, the matrix  $D'_{ij}$  is identical to  $D_{ij}$  but with the first row dropped and an additional row added. Figure 5.8 shows the shift in terms of the potential contact area for a three-dimensional analysis.

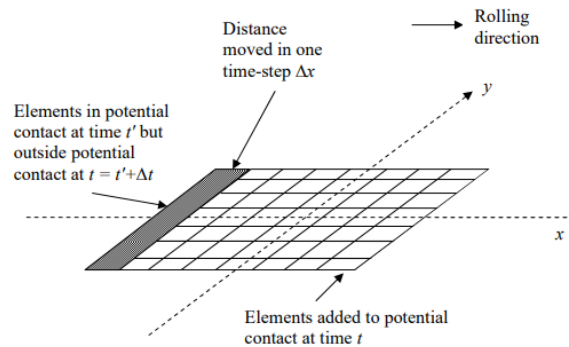


Figure 5.8 Shift in potential contact area in each time-step [64]

In each time-step, an element  $i$  of the  $N$  elements in the potential contact area is either in the contact zone or outside it. The normal stress of the elements outside the contact zone is zero while the normal stress of elements inside it is positive. In the contact zone, each element is also in either a stick zone or a slip zone. The tangential stress of the elements in the slip zone is equal to the friction limit value  $q_i = \mu p_i$  while the tangential stress of the elements in the stick zone is below the friction limit value.

## 5.4.2 Numerical example

A simple case is considered that is a smooth sphere with radius 0.46 m, as before, that is initially at rest on a flat plane. A normal load  $P$  of 100 kN is applied to the contact and this remains constant throughout rolling. The tangential force is considered in two directions: the longitudinal force  $Q_x$  has a value of  $0.75\mu P$  while the lateral force  $Q_y$  has a value of  $0.5\mu P$ . The friction coefficient  $\mu$  is 0.3. The initial rigid shift is zero. The sphere is then permitted to roll in the longitudinal direction upon the plane with a constant velocity  $V = 1$  m/s.

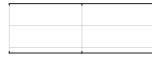


Figure 5.9 Transient tangential stress distribution under constant normal, longitudinal and lateral force from static to steady-state conditions, --- limiting stress  $\mu p$ , — tangential stress distribution at centreline of the potential contact area

The potential contact area is defined as a 20 mm  $\times$  20 mm square. This gives 400 elements in total, of length 1 mm in each direction, and the wheel will roll 1 mm in each time step. The development of the tangential stress distribution over 11 positions as rolling proceeds is shown in Figure 5.9. The stress distribution after rolling 10 mm is approaching a steady-state condition. In this case, the creep is initially zero when the sphere is at rest and increases to reach a constant value in the steady state.

In another case, only longitudinal creep is considered, which is assumed constant during rolling, while the initial tangential force applied is zero. With a constant assumed creep  $\gamma$  in a time-step of duration  $\Delta t$ , the rigid shift of the system  $W_{i\tau}$  ( $i$  expresses the  $i$ th element,  $\tau$  expresses the tangential direction which can be longitudinal or lateral direction) is given by

$$W_{i\tau} = \Delta x \gamma \quad (5.26)$$

---

It is the same for all the elements in the potential contact area. The tangential stress distribution is non-zero at first due to the existence of the longitudinal creep. There is no overall tangential stress  $Q$  applied and no constraint on the sum of the tangential stress over all the elements of the potential contact. Then the tangential force increases and becomes constant when steady-state conditions are reached. All other parameters are the same as in the previous example. The results are shown in Figure 5.10.

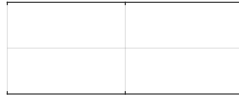


Figure 5.10 Transient tangential stress distribution under constant longitudinal creepage from static to steady-state, --- limiting stress  $\mu p$ , — tangential stress distribution at centreline of the contact area

With constant imposed creep, the system requires a longer time to reach a steady state than for the previous case with a constant imposed tangential traction  $Q$ . In each step shown in the figure the wheel has rolled 5 mm. The calculation step size is 1 mm, the same as in the previous example, but not all steps are shown. The steady state is reached after a distance of nearly twice the contact patch length.

### 5.4.3 Application of real contact surface profile

Model verification in the previous sections only considers simple contact surfaces. In practice, the wheel and rail surfaces are not just simple shapes and the initial roughness (corrugation) should also be included. Here, the S1002 wheel surface transverse profile and UIC60 rail surface profile are applied. Rail inclination is also included with a value of 1:40. The wheel and rail surface shape profiles without roughness, drawn in MATLAB, are shown in Figure 5.11.

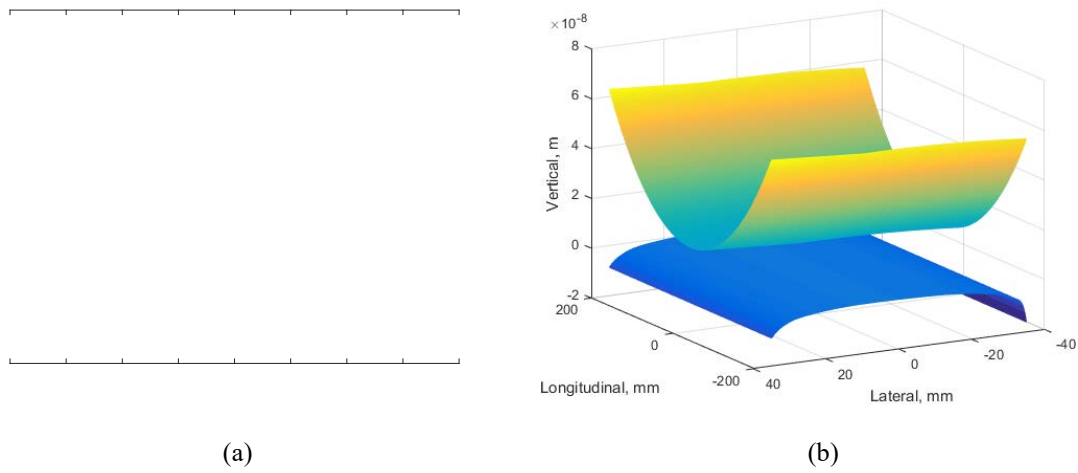


Figure 5.11 Practical wheel and rail smooth contact surface profiles in MATLAB: (a) cross-section; (b) 3D view

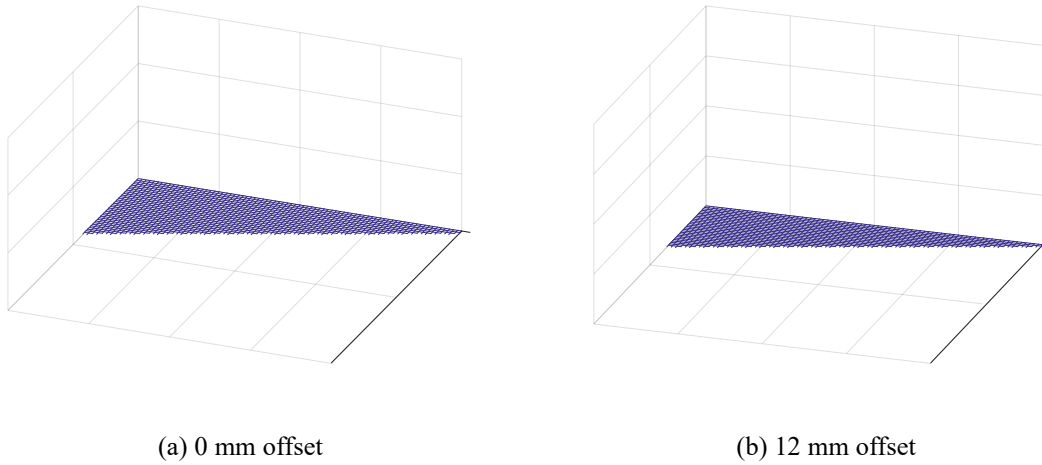


Figure 5.12 Normal stress distribution obtained from variational methods in three-dimensional form for practical wheel and rail profiles. Units in figures are all millimetre.

The normal stress distribution is shown in Figure 5.12. In the first case the nominal contact point on the wheel coincides with the vertical axis of symmetry of the rail. In the other case a lateral offset of 12 mm is applied to the wheel in the positive  $x$  direction compared with the first case. All other parameters are the same as in the previous example. The results show good agreement with results in the literature [139].

#### 5.4.4 Calculation of slip and slip velocity in the contact patch

At each position as the wheel rolls along the rail, the relative slip distance  $s$  between corresponding elements on the two bodies is given by the slip across the element  $W_{it}$  added to the change in the elastic displacement difference occurring in each time step. This is given by the elastic tangential displacement in the current time step  $u_{it}$  minus that from the previous time-step  $u'_{it}$ . Hence

$$s_i = W_{it} + u_{it} - u'_{it} \quad (5.27)$$

The slip velocity  $\dot{s}$  is determined by dividing the slip distance by the time-step interval  $\Delta t$ :

$$\dot{s}_i = \frac{s_i}{\Delta t} \quad (5.28)$$

In the stick zone there is no slip and the slip velocity is zero. In the slip zone, the slip velocity increases up to its maximum value at the trailing edge. Outside the contact zone the slip velocity is not considered. Although those elements which are outside the contact zone would experience elastic deformation as a result of the stresses on the elements within the contact zone, this cannot result in friction or wear. Therefore, the slip velocity in elements outside the contact patch is set to zero before calculating the wear depth in each time-step. This is not necessary if the stresses outside the contact are exactly zero, but the numerical minimisation technique can result in very small non-zero stresses outside the contact patch.

Figure 5.13 shows the slip velocity and corresponding tangential stress distribution calculated using the variational method after reaching a steady state under constant normal and tangential loading. The parameters are the same as used previously with a normal load of 100 kN, a constant tangential traction  $Q=0.25\mu P$ , a sphere wheel of radius 0.46 m, a contact width of 14 mm and a smooth flat plane. The coefficient of friction  $\mu$  is 0.3 and the rolling velocity  $v=1$  m/s. It can be seen that the slip is zero outside the contact patch. (The slip velocity in Figure 5.13 between -7 mm and -8 mm, as well as 7 mm and 8 mm is zero, but due to the element size chosen is 1 mm, the values shown is not zero)

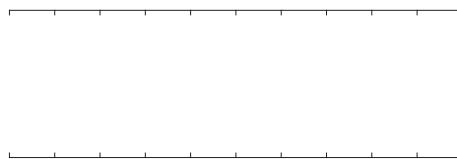


Figure 5.13 Slip and stress distribution in steady-state rolling with  $Q=0.25\mu P$  and 1 mm element size. Upper: slip velocity; Lower: tangential stress distribution, where --- is the friction limit.

#### 5.4.5 Normal interaction force in rolling with a rough rail

In Chapter 4 it is mentioned that the wheel-rail contact model introduced by Kalker in his

theory can be used to find the normal interaction force between the wheel and rail instead of the Hertzian contact spring. The normal problem is introduced in Section 5.3 and the tangential problem is introduced in Section 5.4. For practical investigation, the calculation of the contact force should take the roughness of the wheel and rail into consideration, as in the results shown in Section 4.3.5. Thus, in this section the wheel rolling on a rough rail is considered and the normal interaction force is obtained to check if the wheel-rail contact model introduced by Kalker in his theory is appropriate to be used.

However, in Section 5.3, the wheel-rail contact model is presented with the normal load known. In a time step of the time-domain model, the normal load is an output of the wheel-rail contact model. Before introducing the rough rail, it should be shown that the wheel-rail contact model is effective to calculate the normal stress distribution and resultant interaction force using vertical wheel-rail penetration instead of the normal load. A simple case is considered as previously of a sphere with 0.46 m radius in contact with a smooth plane. The initial distances between the wheel and rail of the elements inside the potential contact area are all positive and zero for the nominal contact point. A penetration of 0.1 mm is given to the potential contact area, which reduces all the initial distances between the two surfaces of the elements inside the potential contact area by 0.1 mm. Thus, the distance of the nominal contact point between the two surfaces is -0.1 mm. The distance after penetration obtained here is not the real value between the contact surfaces, it is a distance vector for the quadratic minimisation method to find stress distribution, which is based on the assumption that the contact surfaces do not deform. The elements with negative distance inside the assumed potential contact area between the wheel and rail would form the initial contact area.

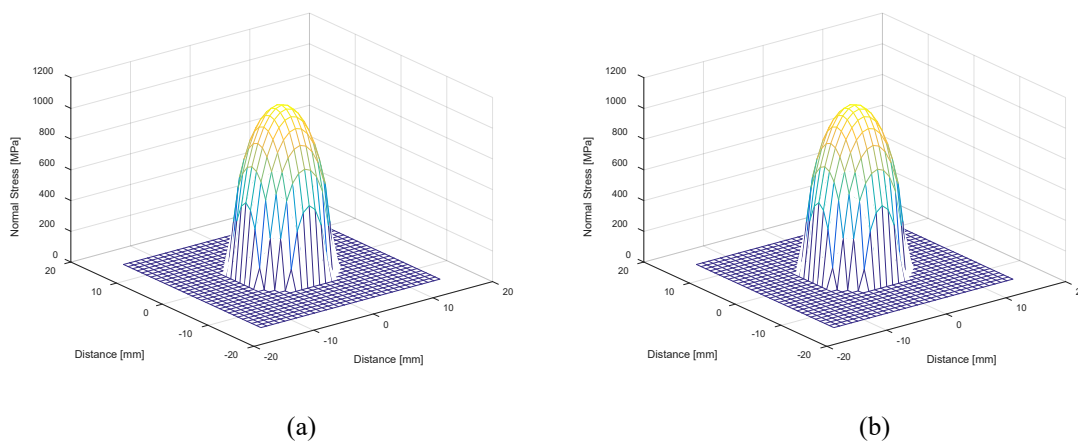


Figure 5.14 Normal stress distribution of the potential contact area in three-dimensional form: (a) calculated by penetration; (b) calculated by normal load

The constraints used to solve the quadratic minimization problem are therefore changed. The new initial distance vector is entered and the constraint of the normal load is removed. Figure 5.14(a) shows the normal stress distribution calculated by applying the penetration between the wheel and rail. The total normal load is calculated by the sum of the normal stress multiplied by the area of each element in the potential contact area. The total normal load calculated here is 104.46 kN.

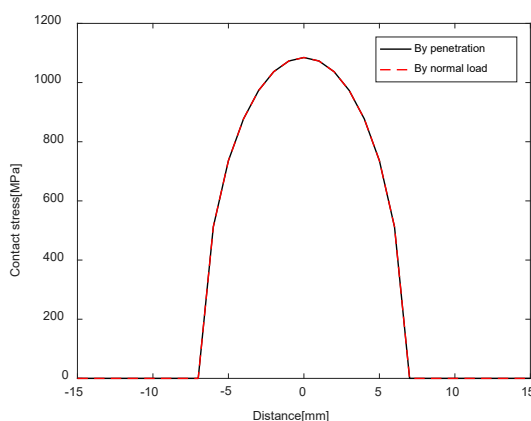


Figure 5.15 Normal stress distribution of the potential contact area centre line in two-dimensional form

By modifying the constraints used to solve the quadratic minimisation problem to use the previous initial distance vector, and applying a normal load with a value of 104.46 kN, the normal stress distribution calculated by applying the normal load is obtained, which is shown in Figure 5.14(b). Figure 5.15 compares the normal stress distribution on the centre line in these two cases and the results show good agreement. It is found that applying the penetration instead of the normal load in the wheel-rail contact model is effective to calculate the normal interaction force.

From Section 4.3.5 it can be seen that the roughness of the wheelset and the track is a factor that has a great effect on the normal interaction force. For a rough rail or wheel, the normal force varies in each time-step. The contact length and the distribution of the stresses and slip in the contact also vary with the contacting profile between the wheel and rail. For extreme contacting profiles, the nominal contact point may not be at a constant position in the lateral direction or longitudinal direction, as assumed in Chapter 4. The contact may also occur at more than one location in the potential contact area and there may be several zones of stick and slip.

---

## 5.5 Wear model

The wear model is an important part of the rail corrugation prediction since it directly determines the wear depth on the rail surface and affects the predicted rail corrugation growth. The wear only occurs in the slip region inside the contact patch between the wheel and rail. As the contacting surfaces have roughness and the contact force between the wheel and rail varies with the position and time, the amount of material removed also varies along the rail and with time. This uneven wear eventually results in the change in the surface profile of the rail after multiple wheel passages and may form corrugation on the rail surface.

The wear can occur by several different mechanisms depending on the contact conditions. It is common in roughness growth predictions to assume a single wear coefficient at all locations representing the frictional abrasive wear, or mild wear. However, the inclusion of non-Hertzian effects in the contact means that stress concentrations may arise from the roughness profile of the surfaces in contact. These stress concentrations may lead to higher wear rates in some parts of the contact area and trigger another, more severe wear mechanism.

For railway roughness development, abrasive wear and surface fatigue are the most relevant mechanisms [139]. Abrasive wear occurs when rough surfaces slide over one another, displacing material which forms loose wear particles. Surface fatigue wear is observed during repeated sliding or rolling, causing the formation of cracks which eventually result in the breakup of the surface. The wear mechanisms involved in corrugation development, rolling contact fatigue and general roughness growth are not necessarily the same, and it is likely that a combination of the various wear mechanisms occurs in many cases.

### 5.5.1 Wear model based on frictional work

One commonly used approach [140] to estimate wheel-rail contact wear is based on the frictional work, both lateral and longitudinal, which is the product of the tangential forces and the slip in the contact area. The frictional work hypothesis states that the wear is proportional to the amount of frictional work done in the contact patch, i.e.

$$\Delta m = k_0 \Delta W \quad (5.29)$$

where  $\Delta m$  is the mass of material removed in the contact patch in one time step,  $k_0$  is the wear coefficient and  $\Delta W$  is the frictional work, given by  $\Delta W = Q\gamma\Delta x$ .



It is found that the wear coefficient is largely constant for certain ranges of frictional power, with discontinuous jumps in wear coefficient between different wear regimes [141]. The value of the wear coefficient is considered to be a material parameter and is found by experiment to be in the range of  $(1-5) \times 10^{-9}$  kg/Nm for mild wear [141].

The change of vertical profile height at each point along the rail in one time step may be obtained by examining Equation (5.29) in the spatial domain and calculating the average height lost from the volume worn away,

$$\Delta z = \frac{\Delta m}{\rho A} = \frac{k_0 \Delta W}{\rho A} = \frac{k_0 Q \gamma \Delta x}{\rho A} \quad (5.30)$$

where  $\rho$  is the density,  $A$  is the contact area,  $Q$  is the tangential force,  $\gamma$  is the creepage and  $\Delta x$  is the distance passed in each time step.

To identify the height change in each area of the contact in a given time step, the ratio  $Q/A$  can be replaced by the tangential stress and the creepage in each area of the contact can be identified. From Equation (5.30), the wear depth of each element is

$$\Delta z_i = \frac{|k_0 q_i(x,y) \gamma_i \Delta x|}{\rho} = \frac{|k_0 q_i(x,y) \Delta s_i|}{\rho} \quad (5.31)$$

where  $\Delta s_i = \gamma_i \Delta x$  is the slip distance of  $i$ th element.

In some references, e.g. [142], the frictional power  $P_{\text{frictional}}$  is used instead of the frictional work (frictional power multiplied by the rolling time is the frictional work). In this way, the wear depth of each element of each time step can be written as

$$\Delta z_i = \frac{k_0 P_{\text{frictional}}}{2b\rho V_0} \quad (5.32)$$

where  $2b$  is the contact patch width,  $V_0$  is the running speed.

Brockley and Ko [143] presented a wear equation for the rail from the perspective of frictional work. The simplified form is as follows:

$$V_{\text{wear}} = K_b (H_b - C_b) \quad (5.33)$$

where  $V_{\text{wear}}$  is the wear volume,  $K_b$  is the wear constant used in Brockley and Ko's model,  $H_b$  is the friction work rate ( $H_b = Q\dot{s}$ ),  $Q$  is the creep force,  $\dot{s}$  is the slip velocity and  $C_b$  is the durability friction work rate. The parameters  $K_b$  and  $C_b$  can be set as constants.

In an example of tightly curved track, the creep forces on the inner and outer wheels of leading wheelset are generally saturated. When the creep force is saturated, it is equal to the friction limit, that is  $Q = \mu N$ . Meanwhile, the slip velocity ( $\dot{s}$ ) is approximately equal to

the attack angle ( $\psi_a$ ) multiplied by the forward speed of the wheelset ( $V$ ), and  $\mu$ ,  $\psi_a$ ,  $V$  can be set as constants when the wheelset passes through a tight curve.

The frictional work rate approach is an effective method for assessing relative wear damage under variable velocity conditions. In particular, it is useful in studying corrugation formation in relation to the vibration responsible for the damage.

### 5.5.2 Wear model from Archard's work

Archard's wear model [144] states that the volume of material which is removed from a surface due to wear is directly proportional to the normal load and the sliding distance between the bodies in contact.

According to the Archard wear model, the volume of worn material is calculated as

$$V_{\text{wear}} = k_w \frac{Ns}{H} \quad (5.34)$$

where  $k_w$  is the non-dimensional wear coefficient, which is different from the wear coefficient  $k_0$  with units of kg/Nm in the wear model discussed above, possibly equivalent to the product of the wear coefficient  $k_0$  and other parameters.  $N$  is the normal contact force with units of N,  $s$  is the slip distance with units of m and  $H$  is the hardness of the softer material in contact with units of N/m<sup>2</sup>. The parameter  $k_w$  is dependent on several factors, such as the normal contact pressure and the slip velocity. For wheel and rail steels, it varies in the range  $(1-400) \times 10^{-4}$ .

In the contact model, wear is calculated for a contact area discretized into  $N_c$  square elements with side length  $\Delta x$ . So based on Equation (5.34), the wear depth of an element inside the slip zone of the contact area in one time step can be calculated as

$$\Delta z_i = k_w \frac{p_i \Delta s_i}{H} \quad (5.35)$$

where  $p_i$  is the normal stress of each element inside the contact area. The distributions of slip distance and normal contact stress in the contact are obtained using the contact model.

In the following calculations, the wear coefficient  $k_w$  is assumed to be independent of the variations of the normal contact stress and the slip velocity in the contact patch. A wear coefficient of  $1.09 \times 10^{-4}$ , which corresponds to low slip velocities, and a hardness of 3.2 GPa have been used for the simulation of railhead wear. This makes the value of the ratio  $k_w/H$  equal to  $3.4 \times 10^{-14} \text{ m}^2/\text{N}$ .

### 5.5.3 Wear model by multiple mechanisms

For the prediction of roughness growth development in this research, alternative wear mechanisms are considered by using the wear model of Braghin et al. [134]. This wear model applies the Derby wear index  $Q\gamma/A$  ( $Q$  is the tractive force,  $\gamma$  is the creepage at the wheel-rail interface and  $A$  is the contact area) used by Pearce and Sherratt [141] which adopts an energy approach in the analysis of the relationship between wear rate and contact conditions. It is assumed that the wear rate  $K(Q\gamma/A)$  is proportional to the work done at the wheel-rail contact.

So the wear index in each element of the contact patch may be written in the units of  $N/mm^2$  as

$$\frac{Q\gamma}{A} = \frac{|\Delta s_i q_i|}{v} \times 10^{-6} = \frac{|\Delta s_i q_i|}{\Delta x} \times 10^{-6} \quad (5.36)$$

where  $\Delta x$  is the distance passed in each time-step,  $q_i$  is the tangential stress of each element in the contact patch. According to the wear index of each element, the wear rate in the units of  $\mu g/m/mm^2$  can be obtained from the relationship in Figure 5.16 and Table 5.1.

Table 5.1 Wear regimes and wear rate

Regime	$Q\gamma/A$ ( $N/mm^2$ )	Wear rate ( $\mu g/m/mm^2$ )
$K_1$	$Q\gamma/A < 10.4$	$5.3 Q\gamma/A$
$K_2$	$10.4 < Q\gamma/A < 77.2$	55.0
$K_3$	$77.2 < Q\gamma/A$	$61.9 Q\gamma/A$

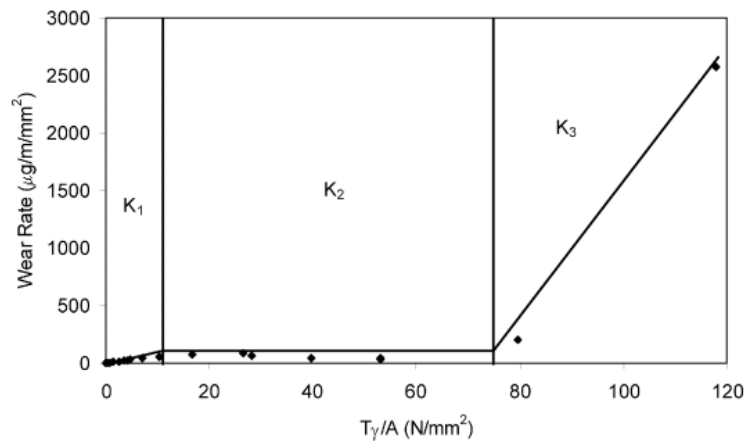


Figure 5.16 Wear rate for different values of the wear index [134]:  $K_1$  ‘mild wear’;  $K_2$  ‘severe wear’;  $K_3$  ‘catastrophic wear’.

It is assumed that the wear rate  $K(Q\gamma/A)$  is related to work done at the wheel-rail contact, where  $K(Q\gamma/A)$  represents a function of the wear index  $Q\gamma/A$ . This means the wear rate  $K$

can be considered as an equivalent wear coefficient value  $k_0$  multiplied by the wear index  $Q\gamma/A$ . After transforming to S.I. units, the depth of material  $\Delta z$  removed across the area of an element  $i$  in the slip zone in each time-step is given in metres by

$$\Delta z_i = K \frac{\Delta x}{\rho} \times 10^{-3} \quad (5.37)$$

In this way the wear coefficient is determined at each element of the contact based on the severity of the conditions at that location. The advantage of this approach is that the wear relationship has been validated using laboratory tests [134] under controlled conditions. It is a more comprehensive model than the single wear coefficient approach, which can only consider mild wear for all contact conditions. In any case the initial surface roughness levels used in the wear model should be chosen to prevent excessively high wheel-rail interaction forces that might lead to loss of elasticity.

To compare the wear depth obtained by the Archard and Braghin's wear models, an example is considered. The normal force is 40 kN, the constant friction coefficient is 0.3, the tangential force is saturated, thus it is 12 kN. The distance passed in each time-step  $\Delta x$  is 1 mm, the element area  $A$  is 1 mm<sup>2</sup> and the material is steel with a density of 7850 kg/m<sup>3</sup>. The value of the ratio  $k_w/H$  used in Archard's model is equal to  $2.03 \times 10^{-14}$  m<sup>2</sup>/N. As the creepage increases, the wear depth calculated by the two wear models is shown in Figure 5.17.

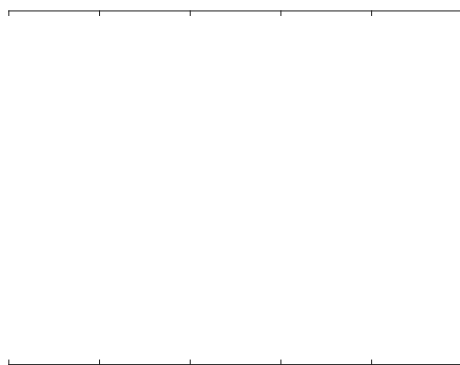


Figure 5.17 Wear depth variation with creepage value for different wear models

## 5.6 Summary

A three-dimensional contact model explained by Kalker in his variational method has been implemented in MATLAB. The contact model can determine normal and tangential stress distributions throughout the contact area. For a simple case of the contact between a

---

smooth sphere and a smooth flat plane, results from the current model have been compared with analytical results using the Hertzian theory. The accuracy of this numerical model is limited only by the size of the elements used to represent the potential contact area but a high computational capacity is demanded.

Transient rolling contact is the default calculation state when using the variational method. Results for steady-state rolling can be obtained by allowing the system to converge under constant forces. The input tangential forces can be either in the form of a constant overall tangential force, or in the form of prescribed creep.

The derivation of the slip velocity in rolling contact has been described. The roughness of the wheel and rail has a significant effect on the normal and tangential stress distributions. When considering a three-dimensional contact area, the current wheel-rail contact model is more accurate than the use of the Hertzian contact spring as it includes the contact filter effect directly. This is validated through a numerical example.

Some wear models are also introduced to calculate the wear depth in the contact patch. Among the many wear models, the model developed by Braghin et al. [134], which considers multiple wear mechanisms, is used in this thesis. Different from the typical situation of rolling contact on tangent track, the interaction force and roughness developed between the wheel and rail can easily reach high levels in tightly curved track. Thus, for the rolling contact between the wheel and the track system in practice, multiple wear mechanisms may be present due to the high-level broadband roughness and large values of longitudinal creepage. Other wear models introduced in this chapter considered only the mild wear, whereas the current model allows for the possibility of multiple wear mechanisms in different parts of the contact patch.

---

## 6 Numerical investigation of corrugation growth

### 6.1 Introduction

In this chapter, the models described in the preceding chapters are assembled and applied to a series of cases to examine the development of rail corrugation. Possible mechanisms accounting for the formation and development of the rail corrugation presented in the literature so far are briefly explained. After that, a series of roughness growth rate calculations are performed to examine the development of broadband acoustic roughness (roughness affecting the acoustic frequency range) over time under different mechanisms. Results are presented in the form of roughness level in 1/3 octave frequency bands and a roughness growth rate. This allows comparisons between the different implemented mechanisms.

When using the current rail corrugation prediction model in this chapter, the wear depth in the wheel-rail interaction is calculated for an example type of vehicle and track with an initial broadband roughness profile obtained according to the limit curve in ISO 3095:2013 [133]. The model has only been used to consider the effect of a single type of traffic on the roughness development. However, if the precise types of vehicle are given, the roughness level after multiple passages and the resultant roughness growth rate under mixed traffic could be obtained by applying each vehicle type individually. The modified roughness level in 1/3 octave frequency bands calculated over a passage time of 2 seconds (around 60 sleeper bays, 40 m) under the initial rail profile is sufficient to get a good approximation of predicted roughness development.

The case studied here shows the roughness development predicted by the wheel/rail interaction model which applies the variational contact model. Hertzian theory has been widely used to model rail wear depth and also the corrugation development historically. However, for the broadband roughness development, including the stress concentration effects, the non-Hertzian wear model is essential [33].

In order to study the relevance of different mechanisms, comparisons are made between a basic case in which only the initial roughness input is considered, a case in which a velocity-dependent friction coefficient is applied instead of a constant one and a case in which vertical-lateral coupling is included when calculating the displacements of the wheel and rail. Results in the form of interaction forces, roughness level and roughness growth

---

rate are compared to find the relative importance of the various mechanisms in the wheel/rail surface roughness development in the current situation.

This study further considers the effect of the coupling between two wheels and rails on roughness development and growth rate. The effect of including multiple wheel/rail interactions on a single rail is also investigated. The roughness development and growth rate results after including these effects are discussed in Section 6.5 and 6.6.

## **6.2 Possible roughness growth mechanisms**

This section gives a brief introduction to various possible mechanisms for the generation of rail corrugation, and how each mechanism generates vibration and contributes to the formation of the rail corrugation. The first mechanism is based only on the input roughness, in which roughness grows if the wear is in phase with the initial roughness. The second includes falling friction - the way to obtain it from the slip velocity in the contact is presented and how it causes the self-excited vibration is explained. Then, the way to apply this in the time-domain model is also introduced. The third involves mode coupling - to illustrate this, the equation of motion for an example two-degree-of-freedom system is shown and then the stability of the system is investigated to show how the self-excited vibration is generated by this mechanism.

### **6.2.1 Input roughness**

In the prediction of the rail corrugation development, there are two types of rail roughness which are often used. One is a sinusoidal roughness and the other is a broadband roughness.

Initial sinusoidal roughness is often used to excite particular modes of the wheelset, track system or the coupling of the wheel and rail to investigate the effects of the particular modes on the development of the rail corrugation. The sinusoidal roughness is assumed to be present on the running surfaces of rails with a wavelength calculated as the velocity divided by the frequency corresponding to the particular modes. However, rail roughness is generally broadband, so the selection of single wavelengths is unrealistic and not sufficiently general. The establishment of the initial broadband roughness profile of the rails from a typical 1/3 octave spectrum is introduced in Appendix C in detail.

---

## 6.2.2 Falling friction

Measurements of the creep-force relationship, for railway rolling situations [144-145], show that when the creep increases beyond saturation, the tangential forces that can be supported by the wheel/rail contact reduce. A falling creep-force relationship is attributed to the variation of the friction coefficient. The value of the dynamic friction coefficient is dependent on the sliding velocity between the wheel/rail contact surfaces. Consequently, for larger creep values, the slope of the creep-force relationship becomes negative.

In this thesis, the velocity-dependent friction law is implemented to apply the falling friction mechanism. The velocity-dependent friction coefficient is given as [146]

$$\mu = \mu_s \left[ \frac{50}{100 + |\dot{s}|^2} + \frac{0.1}{0.2 + |\dot{s}|} \right] \quad (6.1)$$

In [146], the static friction coefficient  $\mu_s$  is chosen as 0.3.  $s$  is the sliding distance in the contact while the  $\dot{s}$  is the sliding velocity. The resulting relationship between friction coefficient and slip velocity is shown in Figure 6.1 for  $\mu_s = 0.3$ . The traction coefficient, indicating the ratio of the creep force to the normal load, is given in Figure 6.2 as a function of the creepage under a vehicle speed of 20 m/s.

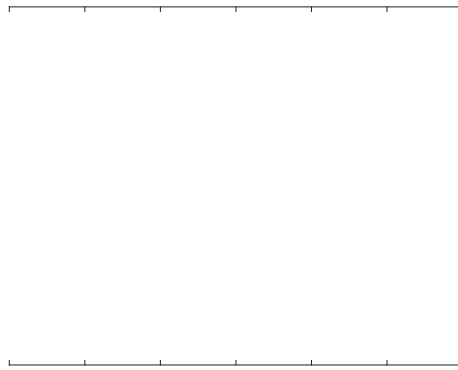


Figure 6.1 Velocity-dependent friction curve



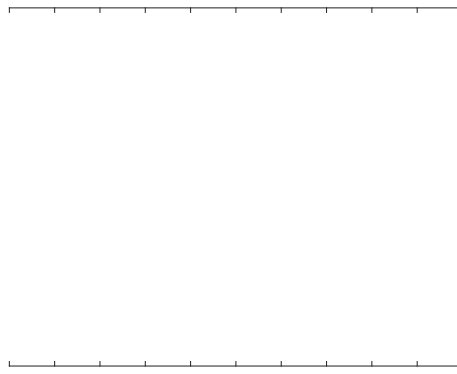


Figure 6.2 Ratio of creep force to normal load varying with the creepage

In [146], the contact problem was solved based on a modified version of FASTSIM with a velocity-dependent friction law. The implementation of the velocity-dependent friction law in FASTSIM required the elimination of a derivative term to ensure mathematical stability of the resulting stress distribution. In this thesis, the contact problem is solved based on the variational method [14] and no such mathematical difficulty is encountered.

The implementation of the velocity-dependent friction law in the variational method requires an iterative loop [139], as shown in Figure 6.3. With a constant friction coefficient, the slip velocity depends on the tangential stress distribution. With a variable friction coefficient, however, the tangential stress distribution is dependent on the slip velocity and vice versa, since the tangential stress results in the slip distance and slip velocity values, and the slip velocity affects the friction coefficient and modifies the tangential stress limit. Thus, considering the transient effect in the variational method, an iteration for finding the friction coefficient value is required at each time step in the time-domain prediction model. At the beginning, the stress distribution is calculated as before for a constant friction coefficient. Thus, the initial friction limit is set using the static friction coefficient in order to begin the rolling contact analysis. Once the rolling contact is underway, the friction limit is first calculated based on the slip velocity distribution in the contact at the previous time step. Based on this, the tangential stress distribution and the slip velocity are calculated as preliminary estimates for the current time step. The friction limit throughout the contact is then updated and the revised friction limit is used to obtain the new tangential stress and slip velocity.

Normally, the iterative loop ends when the friction coefficient is consistent with the value obtained by the new tangential stress and slip velocity. It has been found that five iterations of the tangential stress calculation at each time step are enough to ensure the system

converges to a solution in the current study case presented in this chapter.

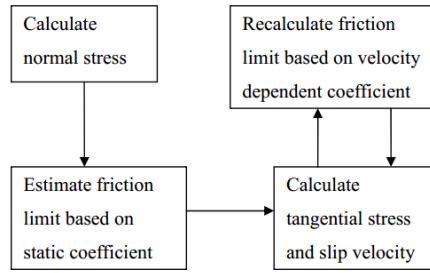


Figure 6.3 Iteration loop for inclusion of velocity-dependent friction coefficient

### 6.2.3 Vertical-lateral coupling

As discussed in Section 1.3.4, mode coupling is another type of friction-induced self-excited vibration. The mode coupling instability was explained by a two-degree-of-freedom mass-belt system developed by Hoffmann et al. [147-148]. This two-degree-of-freedom mass-belt system is briefly introduced here, as shown in Figure 6.4.

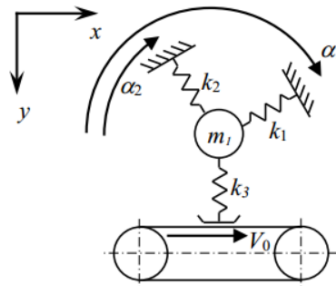


Figure 6.4 Two-degree-of-freedom system on moving belt [138]

As Figure 6.4 shows, the mass has two degrees of freedom,  $x$  and  $y$ . The moving velocity of the belt is assumed to take a constant value  $V_0$ . Since the friction coefficient between the mass and belt is also assumed to be constant, the friction force is given as  $\mu k_3 y$ . Thus, the equation of motion for the system shown in Figure 6.4 is

$$\begin{bmatrix} m_1 & 0 \\ 0 & m_1 \end{bmatrix} \begin{bmatrix} \ddot{x} \\ \ddot{y} \end{bmatrix} + \begin{bmatrix} k_{11} & k_{12} - \mu k_3 \\ k_{21} & k_{22} \end{bmatrix} \begin{bmatrix} x \\ y \end{bmatrix} = 0 \quad (6.7)$$

where the elements in the stiffness matrix are

$$k_{11} = k_1 \cos^2 \alpha_1 + k_2 \cos^2 \alpha_2 \quad (6.8)$$

$$k_{12} = k_{21} = -k_1 \sin \alpha_1 \cos \alpha_1 - k_2 \sin \alpha_2 \cos \alpha_2 \quad (6.9)$$

$$k_{22} = k_1 \sin^2 \alpha_1 + k_2 \sin^2 \alpha_2 + k_3 \quad (6.10)$$

Due to the term  $\mu k_3 y$ , the stiffness matrix in Equation (6.7) is asymmetric and this can lead

to instability [149]. The coupling between the vertical and lateral dynamics is introduced by the term  $k_{12} - \mu k_3$ . When considering the vertical-lateral coupling, the tangential friction force is also varying with the change of the normal displacement of the mass.

To show the features of mode coupling, in his case in relation to curve squeal, a simple case is considered by Ding [44]. This will also be briefly introduced here. In this case,  $m_1=50$  kg,  $k_1, k_2, k_3$  are assumed as  $1.8 \times 10^8$  N/m,  $2.5 \times 10^9$  N/m and  $1.33 \times 10^9$  N/m, respectively,  $\alpha_1=150^\circ$ ,  $\alpha_2=30^\circ$ .

By performing eigenvalue analysis of Equation (6.7), the stability of this system is investigated. The imaginary part (plotted as frequency) and real part (growth rate) of one of the eigenvalues are plotted against the friction coefficient  $\mu$  in Figure 6.5.

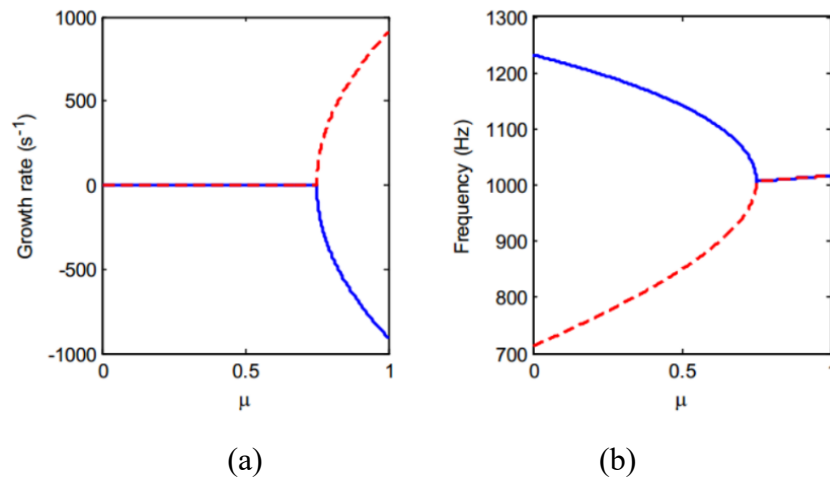


Figure 6.5 Real part (growth rate) and imaginary part (frequency) of eigenvalues plotted against the friction coefficient [44]

It can be seen from the figure that, when the friction coefficient is low, the real part of the eigenvalues both start from 0. When  $\mu > 0.75$ , the real part of one of the eigenvalues becomes positive while the other one becomes negative. As for the imaginary part, when  $\mu = 0$ , there are two different modes with distinct natural frequencies. As the friction coefficient increases, they become closer and closer and finally merge to one value which is not equal to either of the frequencies of the two modes when  $\mu = 0$ . This frequency shift is one of the basic features of mode coupling [147].

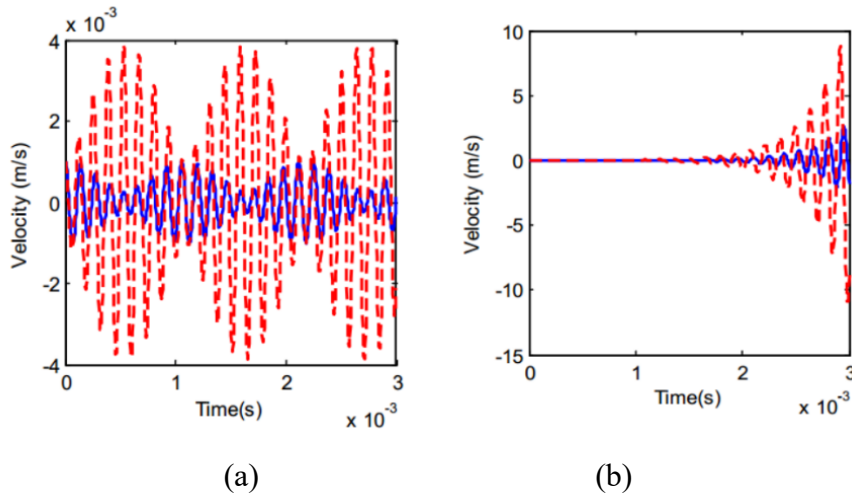


Figure 6.6 Time histories with (a)  $\mu = 0.7$  and (b)  $\mu = 0.8$ ; blue solid line: lateral direction; red dashed line: vertical direction [44]

Results of time-domain analysis are also displayed here to study the vertical and lateral vibrations. Results are shown in Figure 6.6 for two different values of the friction coefficient. One is 0.7 which is before the two modes merge into one and the other is 0.8 which is after the two modes merge. It can be seen from the figure that, for  $\mu = 0.7$ , the time histories show repeated oscillations, like a beating, for both directions, caused by the superposition of two close frequencies. When  $\mu = 0.8$ , the system is found to be unstable and the vibration in both directions keeps increasing. While in practice, the response does not grow infinitely due to the non-linearities. A phase difference exists between the velocities in the vertical and lateral directions. This is another feature that is typical of mode coupling [147]. The phase difference is necessary to transfer the energy from one direction to the other one and result in the instability.

The results here are shown in order to explain the phenomenon in a simplified manner. Damping is not included here, while in [148], this mass-belt system is used to investigate the effect of damping on mode coupling. In railway curve squeal, mode coupling could occur between two wheel modes or between a wheel mode and the rail. Based on this, it may indicate that also for the rail corrugation growth, mode coupling may exist and may occur between wheel modes or between a wheel mode and the rail.

## 6.3 Preliminary results

### 6.3.1 Identification of P2 resonance

As introduced in Section 1.2, apart from the wheelset modes, the P2 and pinned-pinned resonances are also believed to be important for the development of rail corrugation. The

---

identification of the P2 and pinned-pinned resonances helps the resonance identification in the following case studies.

The P2 resonance is related to both track and wheel dynamics, while the pinned-pinned resonance is dependent only on the track dynamics. This section aims to identify the P2 and pinned-pinned resonances of the wheel and track used in the basic case in this thesis which are described in Section 3.4.2 and Section 4.2.2. This gives assistance to identify the type of dominant resonance in the following cases.

Figure 6.7 compares the receptances of the wheel, track and the equivalent wheel/rail contact spring. The first crossing point of the wheelset and track receptances is identified as the P2 resonance, which in this case is at around 100 Hz.

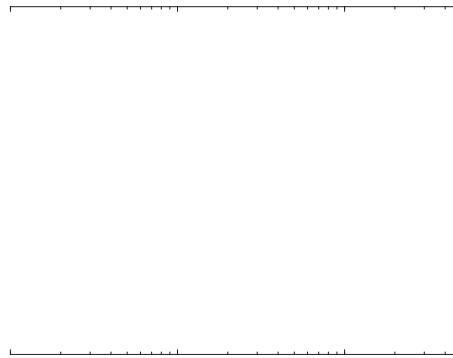


Figure 6.7 Vertical receptances of the wheelset, ballasted track and contact spring

The basic case considered in this thesis is a single wheel rolling over a discretely supported railway track with only the only mechanism being due to the initial wheel/rail surface roughness input. In this case, the dynamic characteristics of the wheel and track are same as those established in Section 3.5 and 4.2. The radius of the curve is chosen as 300 m. The wheel running speed is 72 km/h (20 m/s) and track cant is 50 mm (corresponding to a cant deficiency of 158 mm). The friction coefficient is set as a constant value here, which is taken as  $\mu_0 = 0.2$ . The analysis focuses on the low rail.

Before using the time-domain simulation model to predict the wheel/rail vibration, contact forces and the wear, some input parameters for this time-domain model are first obtained from the steady-state curving model, which was introduced in Chapter 2 and listed in Table 4.1.

---

Using these steady-state parameters, the prediction using the current time-domain simulation model is carried out. The pre-calculation time in the time-domain model to reach the steady-state of the wheel-rail rolling contact is 4 seconds. Then the wheel/rail surface roughness is introduced for the next 2 seconds, which is the section of interest. The frequency spectra displayed here are in the form of one-third octave bands and the magnitudes are shown in decibels.

Before this calculation, the effect of the passage step size used in the roughness growth calculation is evaluated. The passage step size is the multiplier used to predict the roughness after a certain number of passages by multiplying the wear results after one calculation. Here, results are obtained using a passage step size of 1 (assumed to be the correct result) and larger values of 10, 100, 500, 1000, 2000, 5000, 10000. The value is considered to be effective when the error compared with former result is below 1%. When comparing the results of two near values, the total passage number considered is 10 times of the larger value of the two. The error is the percentage of the difference of wear depth time histories between two results with the wear depth time history of the smaller value result. This error variation with the passage step size is given in Figure 6.8(a). Based on this, the passage step size is chosen to be 1000.

To check the influence of the P2 resonance in the time-domain results, all wheelset modes besides the rigid body modes are removed in the model. All the possible mechanisms of the corrugation development introduced above are also considered. The wheel and rail surface vibration spectra are given in Figure 6.8(b).

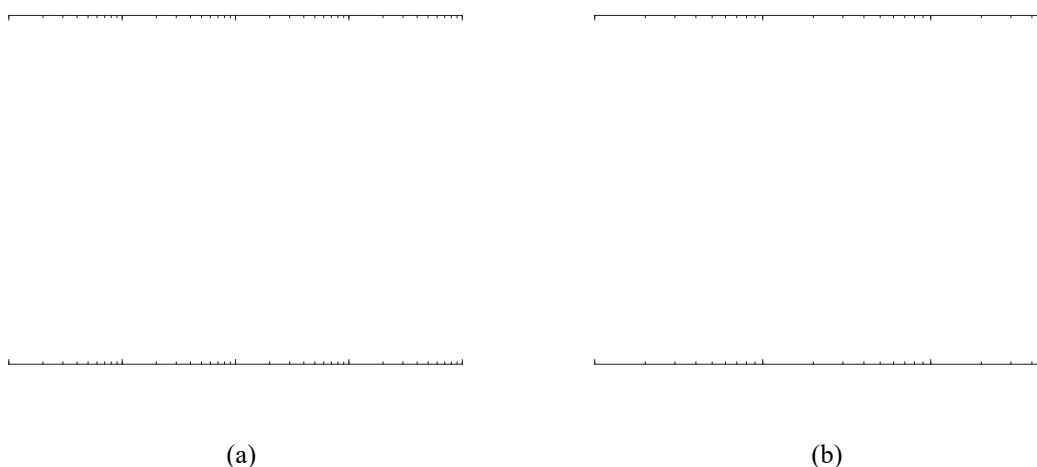


Figure 6.8 Roughness development in one third octave bands of the basic case applying rigid wheelset: (a) passage step size investigation; (b) wheel and rail vibration spectra

The significant peak identified in the vibration spectra is at 100 Hz, which is close to the

---

P2 resonance. It is found that below this frequency, the wheel vibration level is higher than the rail vibration, while above that frequency, the rail vibration level is higher. By identifying the P2 resonance value of the basic case, it is more convenient to identify which modes the significant peaks in roughness development related to in the following investigations. It can also check whether the P2 resonance is shifted due to the mode coupling.

### **6.3.2 Identification of pinned-pinned resonance**

The identification process of the pinned-pinned resonance is close to the one introduced in Section 6.3.2. In Figure 6.7 which compares the receptances of the wheel, track and the equivalent wheel/rail contact spring, The pinned-pinned resonance is found as a dip in the track receptance above a sleeper at around 1000 Hz. The basic case is also considered here and the steady-state input parameters for this time-domain model are listed in Table 4.1. The pre-calculation time in the time-domain model to reach the steady-state of the wheel-rail rolling contact is 4 seconds. Then the wheel/rail surface roughness is introduced for the next 2 seconds, which is the section of interest. The frequency spectra displayed here are in the form of one-third octave bands and the magnitudes are shown in decibels. The passage step size is chosen to be 1000 and applied in all following cases.

It is difficult to isolate the effect of the pinned-pinned resonance, since a wheelset mode also occurs around 1000 Hz. However, by using a continuously supported track the pinned-pinned mode is removed. The roughness development for the discretely supported track with the nominal sleeper spacing of 0.65 m and a continuously supported track are given in Figure 6.9. Peaks at 250 Hz and 400 Hz in Figure 6.9(a) correspond to wheelset modes. There is also a small peak at 1000 Hz but it is unclear if this is due to the pinned-pinned mode or a wheelset mode. For the continuously supported track in Figure 6.9(b), the peak at 160 Hz corresponds to the wheelset resonance, while the peak at 400 Hz corresponding to the wheelset mode is again present. The peak at 1000 Hz is smaller than in Figure 6.9(a), which may indicate that the wheelset mode contributes to this peak together with the pinned-pinned resonance.

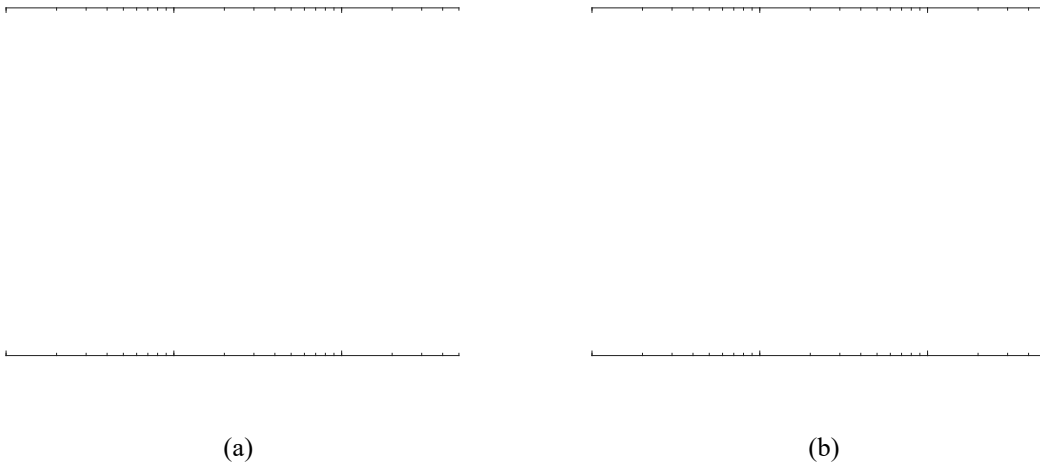


Figure 6.9 Roughness level development in one third octave bands of: (a) the discretely supported track with nominal sleeper spacing; (b) the continuously supported track

Next, the sleeper spacing of the discretely supported track is adjusted to 0.75 m. By doing this, the frequency of the pinned-pinned resonance is reduced to around 800 Hz. The rail surface roughness development and its variation with the number of passages after applying the new sleeper spacing are given in Figure 6.10.

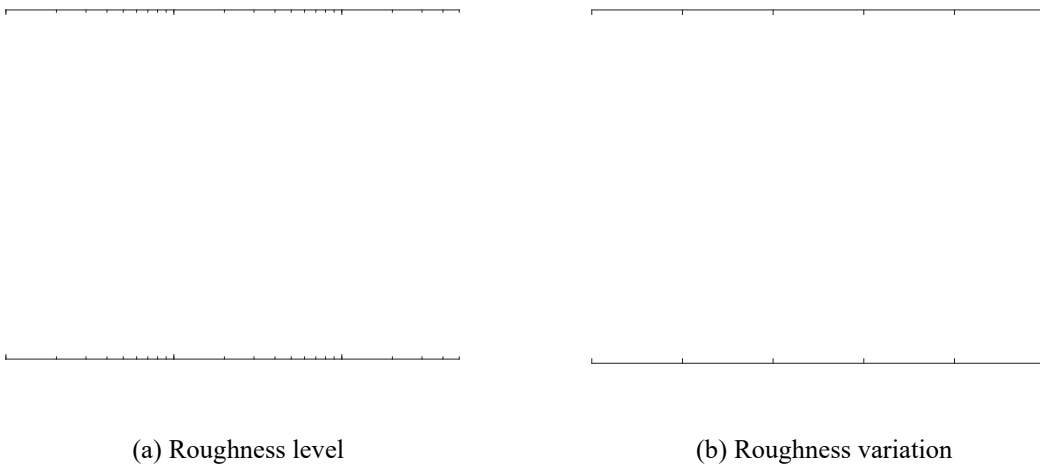


Figure 6.10 Roughness development in one third octave bands of the basic case applying 0.75 m sleeper spacing

It is found that, with the modified sleeper spacing, the roughness level at around 800 Hz increases, which may be associated with the pinned-pinned resonance. The roughness at 160 Hz also increases, but much less than in Figure 6.8. This may be because the dominant resonance changes after the sleeper spacing has been changed. The roughness growth at 160 Hz appears to be suppressed by the pinned-pinned resonance.

The identification of the P2 resonance and the pinned-pinned resonance of the basic case gives the exact values of these two resonances. These values are found to be similar to



---

some modal frequencies of the wheelset. In the following investigations, if significant peaks appear at these frequencies, it needs further investigations to identify which resonance contributes to the roughness development at this frequency.

## **6.4 Identification of dominant mechanism**

The generation of rail corrugation is associated with multiple mechanisms and it is unlikely that it can be explained satisfactorily by a single mechanism in all situations. Under specific conditions, a particular mechanism may be found to be dominant. Finding this mechanism would allow the corresponding actions to be taken to suppress the development of rail corrugation and would allow more optimal track maintenance. In this section, by isolating the occurrence of each mechanism, the contact and wear results under different mechanisms are obtained and compared. In this way, the role of each mechanism in the generation of rail corrugation can be identified.

The basic case considered is the same as introduced in Section 6.3.2, which is a single wheel rolling over a discretely supported railway track with only the initial wheel/rail surface roughness input. In this case, the dynamic characteristics of the wheel and track are the same as those established in Section 3.5 and 4.2. The radius of the curve is chosen as 300 m. The wheel running speed is 72 km/h (20 m/s) and track cant is 50 mm (corresponding to a cant deficiency of 158 mm). The friction coefficient is set as a constant value here, which is taken as  $\mu_0 = 0.2$ . The analysis focuses on the low rail.

### **6.4.1 Basic case with only initial roughness input**

The first case considered consists of only the initial surface roughness as a mechanism. Neither the vertical-lateral coupling for the track and wheel, nor the falling friction are applied. Figure 6.11(a) shows the relevant range of the time histories of the wheel/rail contact force in vertical and lateral directions for this case. It can be noticed from the negative sign of the lateral contact force that the low rail tends to deflect towards the inside of the curve. Due to the saturated tangential contact force, the lateral contact force spectrum has the same pattern as the vertical contact force spectrum, but with a lower level as shown in Figure 6.11(b). The 80 Hz peak is either due to the wheelset bending mode or the P2 resonance, or due to both, while the 200 Hz peak is related to the anti-resonance of the track dynamic response shown in Figure 3.8.

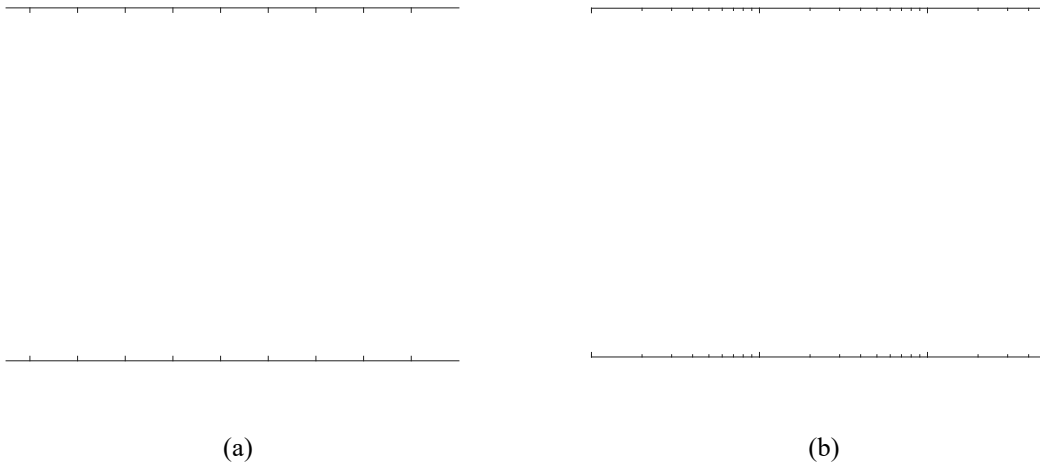


Figure 6.11 The wheel/rail contact force due to initial surface roughness: (a) Time history; (b) Frequency spectra in one third octave bands

The vertical wheel displacement spectrum shown in Figure 6.12(a) has very few specific characteristics. The lateral wheel displacement spectrum exhibits a peak at 30 Hz, which is the sleeper passing frequency, which is also visible in the vertical displacement spectrum. Strong peaks are present in the lateral response at 80 Hz and 160 Hz which are related to lateral wheelset modes, as shown in Figure 4.4(b). The peaks at 250 Hz, 400 Hz and 1000 Hz are related to lateral wheel modes. Figure 6.12(b) gives the rail displacement spectra due to the initial roughness. The vertical and lateral directions show similar patterns. The peak at 30 Hz is again the sleeper-passing frequency, whereas the peak at 100 Hz seems related to the P2 resonance since the wheel vertical displacement is higher below 100 Hz and the rail vertical displacement is higher above 100 Hz. The peak at 200 Hz is hard to explain.

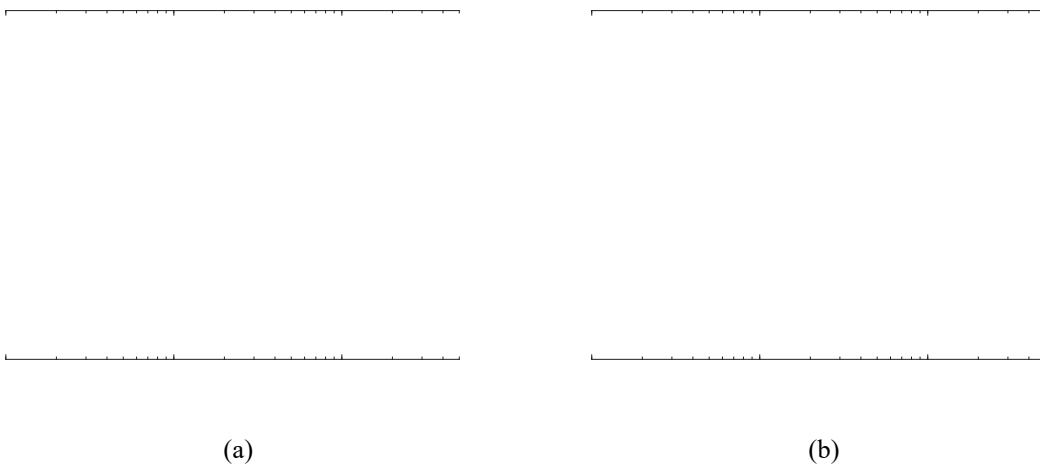


Figure 6.12 Displacement spectra in one third octave bands due to initial surface roughness of (a) wheel; (b) rail

Figure 6.13(a) shows the development of roughness for this case. As the number of wheel

passages increases, the roughness at 400 Hz grows significantly. There is also a small increase at 1000 Hz but there is no evidence of roughness growth at the P2 resonance (100 Hz). The roughness growth rate at 400 Hz shows a large increase. This peak is related to the wheelset mode at 402 Hz, which is the (2,0) axial mode and is prominent in the wheelset lateral receptance. The corresponding peak is also found in the wheel lateral displacement in Figure 6.12(a). The roughness level above around 1600 Hz tends to decrease. This may be due to the dynamic contact filter effect introduced in Section 4.3.3. The contact patch length is around 14 mm, which corresponds to a frequency of 1428 Hz for a velocity of 20 m/s.

A growth rate parameter is introduced here to quantify the global growth rate. For each wavelength band  $k$  this is calculated from the initial roughness amplitude  $A_{k,0}$  and the final roughness amplitude  $A_{k,n}$  after  $n$  wheel passages, assuming a linear increase in level. It is expressed as

$$\psi_k = \frac{20}{n} \log_{10} \frac{A_{k,n}}{A_{k,0}} \quad (6.11)$$

If the roughness level in a particular wavelength band increases after a number of wheel passages, the roughness growth rate is positive in that wavelength band. A negative roughness growth rate indicates the decrease of the roughness level in that wavelength band.

Figure 6.13(b) shows the average roughness growth rate of the first 10,000 passages throughout the frequency range for the present case. This shows clearly the large growth rate at 400 Hz.

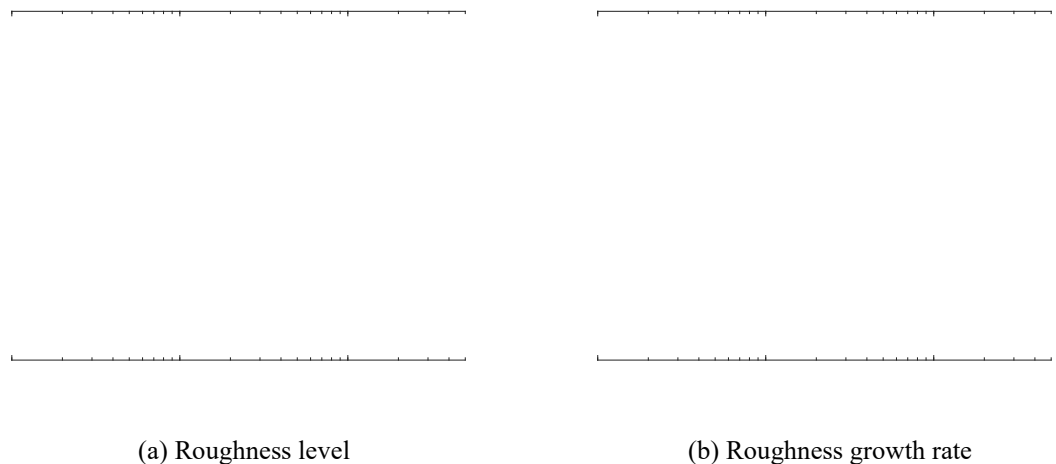


Figure 6.13 Wheel/rail surface roughness development after different passages with initial surface roughness in one third octave bands

---

## 6.4.2 Case considering both initial roughness and vertical-lateral coupling

The next case considered here includes not only the initial roughness input, but also the vertical-lateral coupling effect on the wheel and rail dynamics. The cross receptances between vertical and lateral directions of the wheel and track are obtained and transformed into corresponding impulse responses and moving Green's functions. The operational and steady-state curving parameters used in this case are the same as in the former basic case in the previous section. In this way, the effect of the vertical-lateral coupling on the roughness growth can be found by comparing the results with those of the basic case. The vertical-lateral coupling effect is only introduced in the section of interest in the time domain (where the roughness is introduced) to avoid any corrugation growth before steady state is reached.

The frequency spectra of the wheel/rail contact force in vertical and lateral directions are given in Figure 6.14. Compared with the case considering only initial roughness, the inclusion of the vertical-lateral cross terms has no significant effect on the contact force spectra except for a small increase to the peak at 80 Hz and at 400 Hz. The displacement spectra of the track and wheelset are shown in Figure 6.15. For the wheel displacement spectra, the inclusion of the vertical-lateral cross terms results in a small peak at 400 Hz in the vertical direction and considerably enhances that peak in the lateral direction. The rail displacement spectra follow a similar pattern to the contact force spectra, with a small increase at 80 Hz and for all the frequencies above 300 Hz.

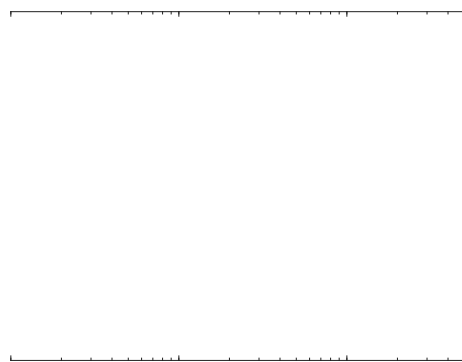


Figure 6.14 Frequency spectra of the wheel/rail contact force with initial surface roughness and vertical-lateral coupling compared with only initial roughness in one third octave bands

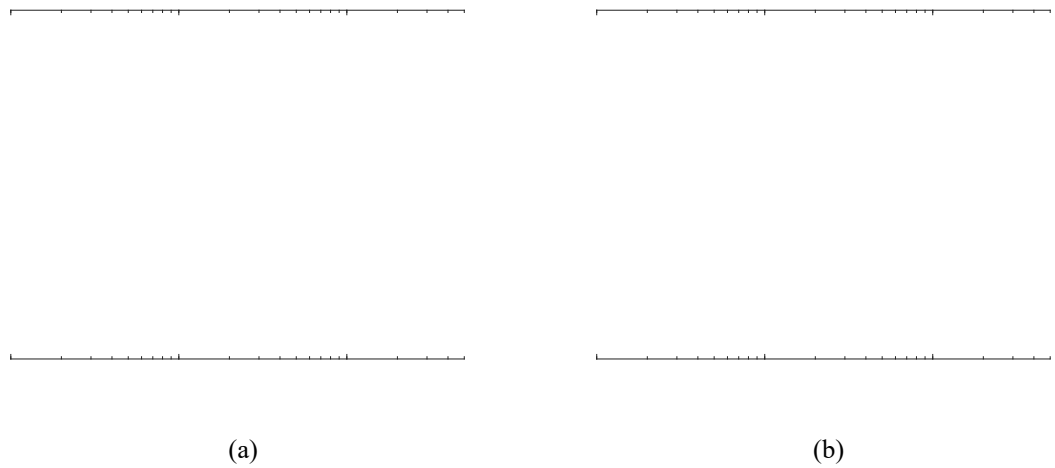


Figure 6.15 Displacement spectra in one third octave bands of (a) wheel; (b) rail for the case with initial surface roughness and vertical-lateral coupling

Figure 6.16(a) shows the roughness development with the number of wheel passages for this case. As before, the roughness at 400 Hz has a significant growth, while at 1000 Hz, the roughness only has a slight increase. Figure 6.16(b) shows the roughness growth rate based on the first 10,000 passages throughout the frequency range for the present case. Compared with Figure 6.13, the inclusion of the vertical-lateral coupling only gives a small increase in the roughness growth rate at 400 Hz and 1000 Hz.

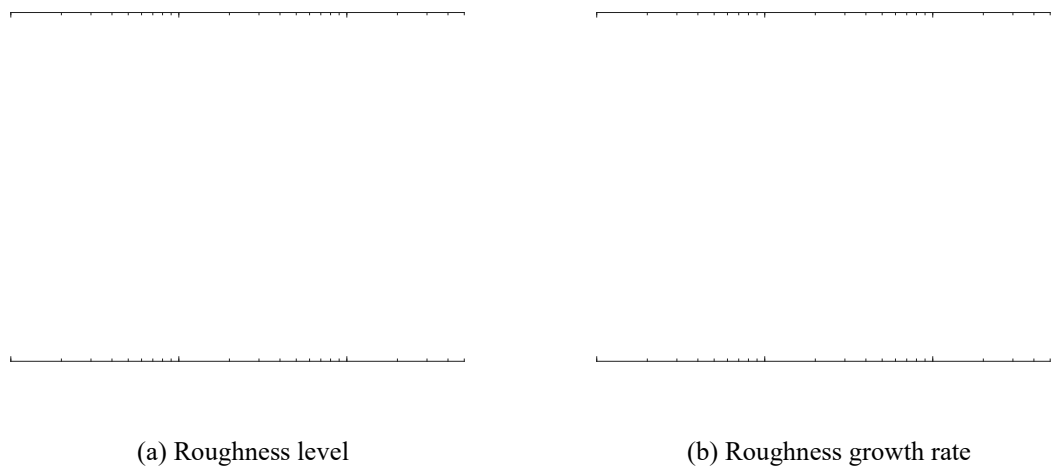


Figure 6.16 Wheel/rail surface roughness development after different passages with initial surface roughness and vertical-lateral coupling in one third octave bands

### 6.4.3 Case considering both initial roughness and falling friction

The next case considered includes both the initial roughness input and falling friction when calculating the lateral creep force, slip velocity and wear. The velocity-dependent friction coefficient introduced in Section 6.2.2 is used here. The operational and steady-state curving parameters used in this case are the same as the former basic case. However, the vertical-lateral coupling effect is omitted. In this way, the effect of the application of falling

---

friction on the roughness growth can be found by comparing with the results of the basic case. The velocity-dependent friction coefficient is only introduced in the section of interest in the time domain when the roughness is introduced.

The velocity-dependent friction coefficient used is shown in Figure 6.17. This is based on a maximum value of 0.3, which is chosen to allow direct comparison with the results of the basic case given in Section 6.4.1. Under the current lateral creepage, the value of the dynamic friction coefficient is similar to the value of the constant friction coefficient used in the basic case, i.e. 0.2.

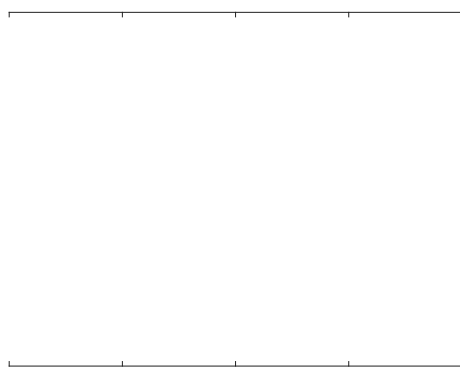


Figure 6.17 Velocity-dependent friction coefficient with maximum value 0.3 plotted against creepage

Figure 6.18 shows the frequency spectra of the vertical and lateral contact forces for the case with initial surface roughness and falling friction. Compared with the results without falling friction, from Figure 6.11(b), the vertical contact force spectrum has little change due to the inclusion of falling friction, since the falling friction only affects the tangential contact force whereas the vertical-lateral coupling is not included here. However, the lateral contact force spectrum has a large increase for frequencies above 80 Hz because of the inclusion of falling friction. Similar characteristics are found in Figure 6.19, which shows the displacement spectra of the wheel and rail. In the wheel lateral displacement spectrum, the peak at 80 Hz decreases in amplitude while the peaks at 160 Hz, 250 Hz, 400 Hz and 1000 Hz increase after including the falling friction. The vertical displacement spectrum is not affected. For the rail displacement spectra given in Figure 6.19(b), the characteristics are similar but with no significant peaks.

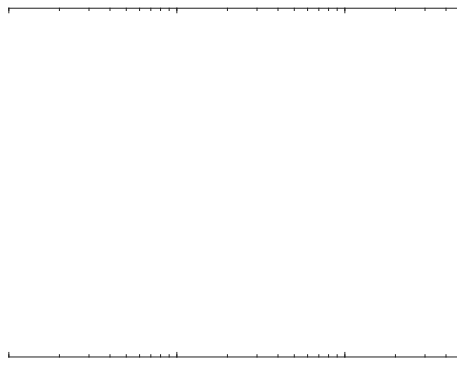


Figure 6.18 Frequency spectra of the wheel and rail contact force with initial surface roughness and falling friction in one third octave bands

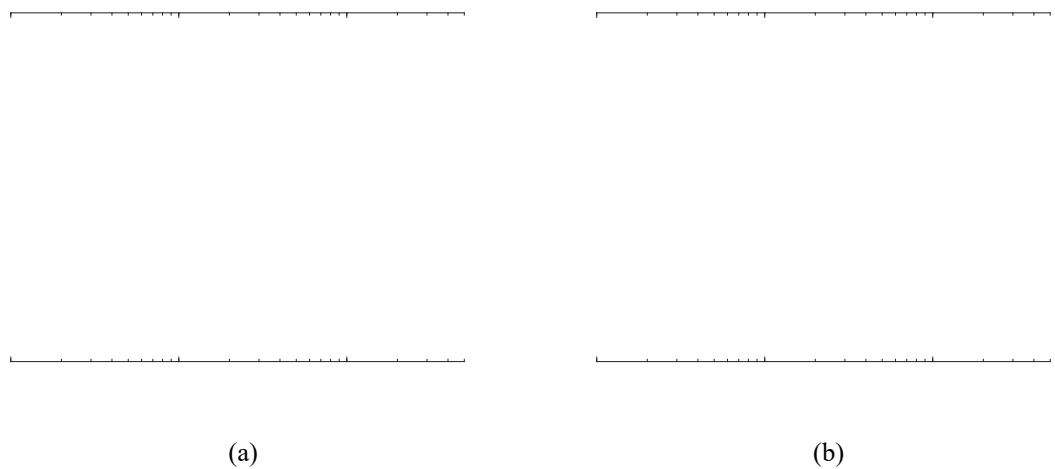


Figure 6.19 Displacement spectra in one third octave bands of (a) wheel; (b) rail for the case with initial surface roughness and falling friction

Figure 6.20(a) shows the roughness development with the number of wheel passages considering the falling friction as well as initial roughness. The roughness shows significant growth at 160 Hz, 250 Hz, 400 Hz and, to a lesser extent, at 1000 Hz. Comparing this with Figure 6.19, it can be identified that these peaks are related to the peaks in the wheel lateral displacement spectrum. This indicates that the modes contributing to the roughness growth are mainly the lateral wheelset modes. Figure 6.20(b) gives the roughness growth considering the falling friction and the initial roughness. Compared with the case considering only the initial roughness, the inclusion of the falling friction introduces two more peaks at 160 Hz and 250 Hz. The roughness growth at 400 Hz and 1000 Hz is also increased to a small extent. The inclusion of falling friction means that more lateral wheelset modes are involved in contributing to the roughness development.

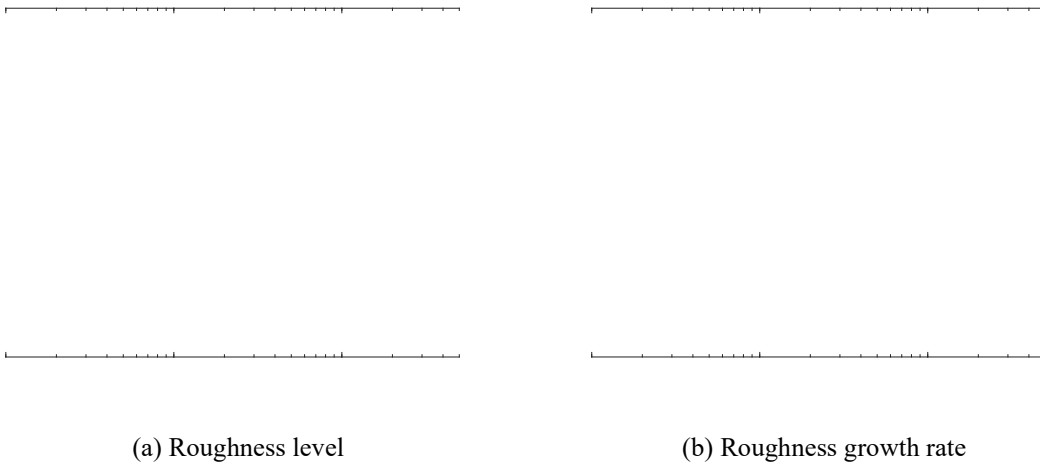


Figure 6.20 Wheel/rail surface roughness development after different passages with initial surface roughness and falling friction in one third octave bands

#### 6.4.4 Case considering all three mechanisms

The last case considered here includes all three mechanisms: the initial roughness input, the vertical-lateral coupling and the falling friction, when calculating the lateral creep force, slip velocity and wear. The operational and steady-state curving parameters used in this case are the same as in the former cases. This case is more similar to a practical case which includes multiple corrugation generation mechanisms. In this case, the mechanism that contributes to the most significant roughness growth rate would be the dominant mechanism.

Figure 6.21 shows the frequency spectra of the wheel/rail contact forces, considering all three mechanisms introduced in the thesis. In this case, the spectra resemble a combination of the former cases, in which the vertical force spectrum is slightly affected by the vertical-lateral coupling while the lateral force spectrum has a large increase mainly above 80 Hz due to the falling friction.

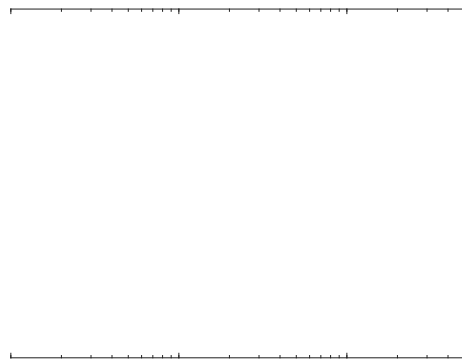


Figure 6.21 Frequency spectra of the wheel and rail contact forces considering all three mechanisms in one third octave bands



Figure 6.22 shows the displacement spectra of the wheel and rail. As in the case with falling friction (Figure 6.19), the wheel lateral displacement spectrum has strong peaks at 160 Hz, 250 Hz, 400 Hz and 1000 Hz, which are over 10 dB greater than those in the case with only initial roughness. The vertical displacement is slightly affected by the lateral displacement due to the vertical-lateral coupling.

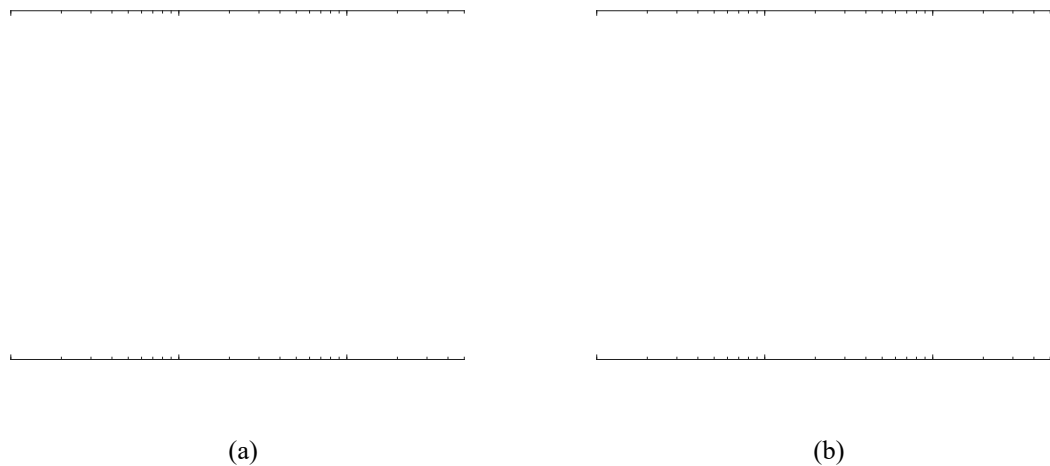


Figure 6.22 Displacement spectra in one third octave bands of (a) wheel; (b) rail for this case

Figure 6.23(a) shows the roughness spectra after different numbers of wheel passages. The roughness has a significant growth in the 160 Hz, 250 Hz, 400 Hz and 1000 Hz frequency bands. This indicates that the lateral wheelset modes are most dominant in the roughness development. To identify the responsible mechanism more precisely, Figure 6.23(b) compares the roughness growth rate with the different mechanisms and all the considered mechanisms. The roughness growth rates in the most important frequency bands are listed in Table 6.1. It can be identified that the roughness growth at 160 and 250 Hz is caused by the falling friction, while the growth at 400 Hz and 1000 Hz corresponds to the transient dynamic interaction mechanism (i.e. initial roughness). The vertical-lateral coupling contributes to the slight increase of the roughness growth rate at frequencies above 500 Hz.

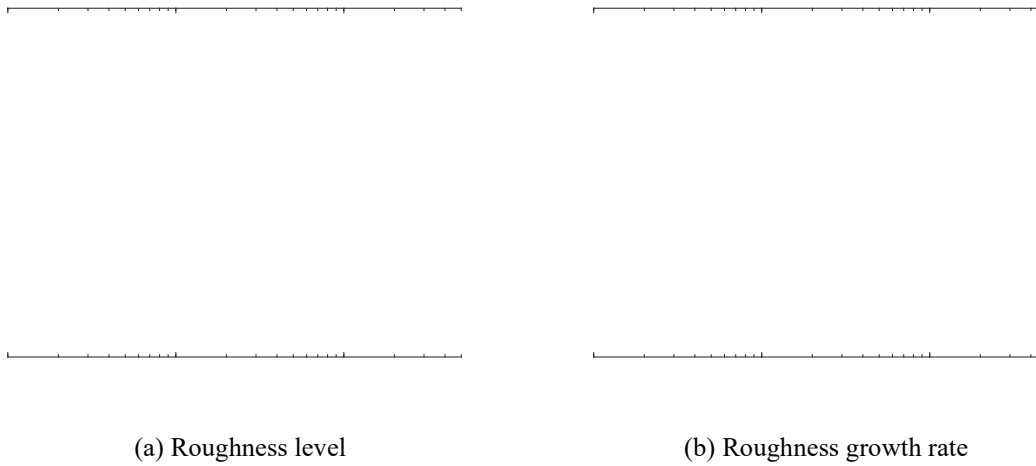


Figure 6.23 Wheel/rail surface roughness development after different passages considering all three mechanisms in one third octave bands

Table 6.1 Roughness growth rate per 1000 passages in different frequency bands under different mechanisms

Frequency band	160 Hz	250 Hz	400 Hz	1000 Hz
Corresponding mode	Wheelset mode	Wheelset mode	Wheelset mode	Wheelset mode or pinned-pinned resonance
Initial roughness		0.08	0.6	0.12
Initial roughness and vertical-lateral coupling		0.09	0.73	0.16
Initial roughness and falling friction	0.3	0.47	0.74	0.18
All three mechanisms	0.3	0.48	0.77	0.23

To identify the frequency peaks found in the roughness growth rate, several additional time-domain predictions are performed. The wheelset modes at 147, 276, 402 and 1065 Hz are removed from the wheelset modal information and the time-domain model is run again to predict the roughness growth. The results are shown in Figure 6.24. The growth rate at both 160 Hz and 250 Hz drops to nearly zero when either of the modes at 147 Hz or 276 Hz mode are removed from the wheelset model. In these two cases, the roughness growth rate at 400 Hz and 1000 Hz is not affected much. When the 402 Hz wheelset mode is removed, the roughness growth rate at 400 Hz drops to zero, as well as the rate at 160 Hz and 250 Hz, and instead much stronger roughness growth occurs at 1000 Hz. In this case, the remaining dominant mode is only the 1000 Hz mode and the effect of falling friction is eliminated.

---

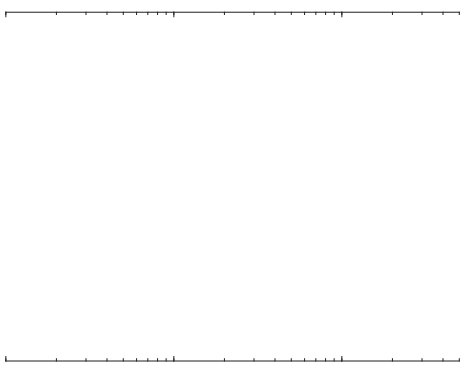


Figure 6.24 Wheel/rail surface roughness growth rate of first 10,000 passages with all three mechanisms and different wheelset modes removed in one third octave bands

The peak at 1000 Hz in the original case may be related to the 1063 Hz wheelset mode and/or the vertical pinned-pinned resonance. When removing the 1063 Hz wheelset mode, the resultant roughness growth at 1000 Hz is reduced but not to zero, suggesting that the roughness growth at 1000 Hz is due to both the wheelset mode and pinned-pinned resonance. These results indicate that, when all three mechanisms are present, under the simulation parameters introduced in this section, the lateral wheelset mode at 402 Hz and 1065 Hz, the stick-slip motion associated with the wheelset mode at 147 Hz and 276 Hz and pinned-pinned resonance all contribute to the dominant roughness growth. The transient dynamic interaction and stick-slip vibration due to falling friction are the main mechanisms on roughness development.

## 6.5 Effect of coupling between two wheels and rails

The effects of coupling between the two wheels and two rails on the wheel and track responses have been introduced in Section 3.4.6. This section investigates the effects of this coupling on the corrugation generation compared with the cases introduced in Section 6.4 which consider only the wheel/rail contact on the low rail in the curve.

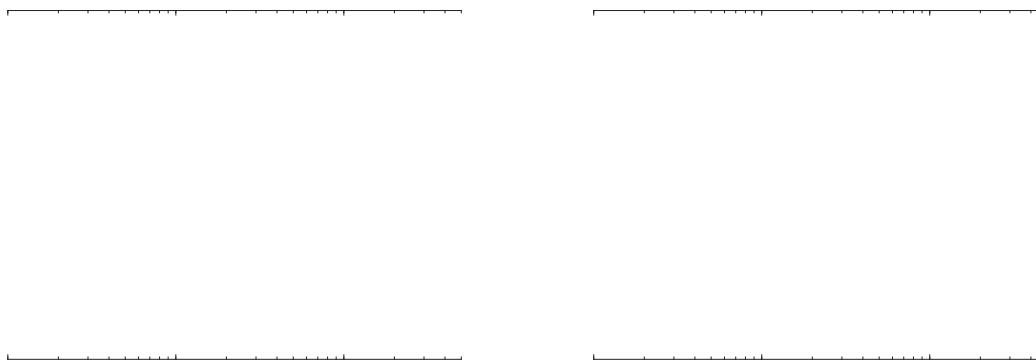
In this case, the dynamic characteristics of the wheel and track remain the same as those established in Sections 3.5 and 4.2. The radius of the curve is 300 m, the wheel running speed is 72 km/h (20 m/s) and the track cant is 50 mm with cant deficiency of 158 mm. The friction coefficient is set as a constant value of  $\mu_0 = 0.2$ . When applying the velocity-dependent friction coefficient, the maximum value of friction coefficient is chosen to be 0.3, as shown in Figure 6.17. The input parameters for the wheel/rail contact on the low rail in this time-domain model are the same as mentioned at the beginning of Section 6.4. The steady-state parameters of the wheel/rail contact on the high rail are also obtained

from the steady-state curving model introduced in Chapter 2, as shown in Table 6.2.

Table 6.2 Steady-state curving parameters for low and high rails

Parameter	Low rail	High rail	Units
Normal load	35.58	47.15	kN
Lateral displacement	7.755	7.755	mm
Yaw angle	7.347	7.347	mrاد
Longitudinal creepage	0.3984%	-0.3984%	-
Lateral creepage	0.732%	0.8645%	-
Spin	-0.034	1.22	1/m
Speed	20	20	m/s
Curve radius	300	300	m

The effects of coupling between the two tracks are investigated for the case with all three mechanisms: initial roughness, vertical-lateral coupling and falling friction. The contact forces and the surface roughness on the low rail are still the ones of interest and the high rail is also potentially of interest. Figure 6.25(a) shows the roughness development with the number of wheel passages. Compared with the results of the case without considering the coupling between two tracks in Section 6.4.4, the characteristics of the roughness development are similar but there are some differences. To illustrate these, the roughness growth rate of the first 10,000 passages is shown in Figure 6.25(b). Compared with the former case, the roughness growth rate at 250 Hz increases while the growth rates at 400 Hz and 1000 Hz decrease. The roughness growth rate at 160 Hz is not affected much. This may indicate that, when considering the coupling between two tracks, the stick-slip vibration due to falling friction contributes more to the roughness development on the low rail at curves than in the case without this coupling.



(a) Roughness level

(b) Roughness growth rate

Figure 6.25 Wheel/rail surface roughness development on the low rail applying all three mechanisms including the coupling between high and low rails in one third octave bands

Considering the roughness on the high rail, Figure 6.26 shows the roughness level after different passage numbers and roughness growth rate for the case in which all three mechanisms (initial roughness, vertical-lateral coupling and falling friction) are included together with the coupling between two tracks. For the high rail, under the current vehicle speed and track curve radius, the roughness is nearly not developing and no rail corrugation occurs on it.

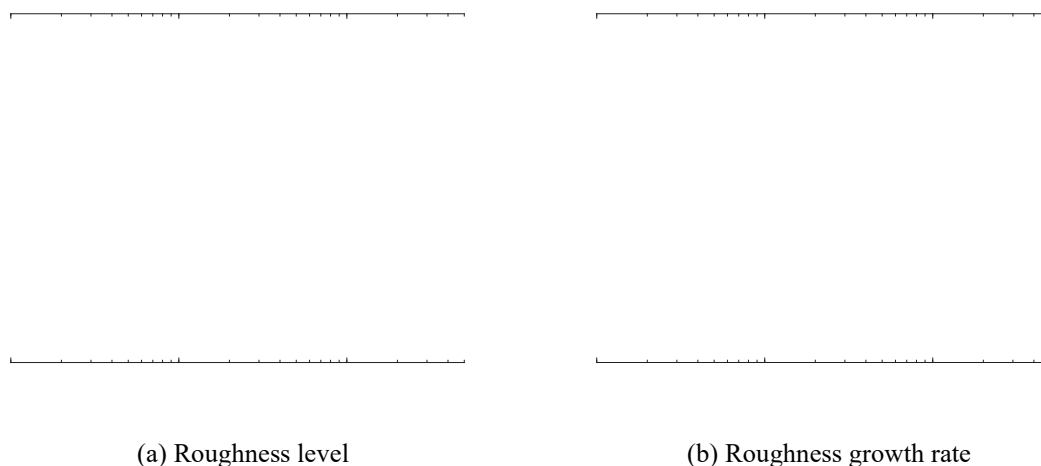


Figure 6.26 Wheel/rail surface roughness development on the high rail applying all three mechanisms including the coupling between high and low rails in one third octave bands

## 6.6 Effect of multiple wheel/rail interactions

The wheel/rail contact forces play a very important role in the formation of the rail corrugation. It has been found by previous authors that the spectrum of the vertical wheel/rail contact force may contain several peaks at different frequencies due to the wave reflections between the multiple wheels on the rail [55,75]. Wu and Thompson [151,27] introduced a model in the frequency domain of multiple wheels interacting with a rail and developed the concepts of active and passive wheel/rail interactions. Based on this, the superposition principle was used to calculate the wheel/rail contact force and the possible effect of multiple wheel/rail interactions on the formation of the short-pitch corrugation was explored.

In [151], only the vertical interactions between the wheels and track were considered. Based on this approach, the response of the discretely supported track under multiple wheel/rail interactions is investigated here using the receptance-coupling method introduced in the Section 3.4.4. In the following, some basic concepts and equations from references [151,27] are briefly introduced and the application of the receptance-coupling method in obtaining the response of the discretely supported track with multiple wheel/rail

interactions is introduced in detail.

### 6.6.1 Relationship between the contact force and track dynamics

In a simple case of vertical interaction between a single wheel and rail, the contact force  $F$  can be calculated in the frequency domain by a relative displacement (roughness) excitation model [90]

$$F(\omega) = -\frac{R(\omega)}{\alpha^W(\omega) + \alpha^C(\omega) + \alpha^R(\omega)} \tag{6.12}$$

where  $R$  is the relative displacement (roughness) between the wheel and rail,  $\alpha^W$ ,  $\alpha^C$ ,  $\alpha^R$  are the point receptances of the wheel, equivalent contact spring and rail respectively and  $\omega$  is the circular frequency of the excitation. The variables in Equation (6.12) are all complex, and the common term  $e^{i\omega t}$  is omitted.

Figure 6.27 shows a track interacting with four wheels, which represent a pair of bogies at the adjacent ends of two vehicles. The roughness excitation is only considered at one wheel, in this case wheel 1. This would cause an interaction force  $F_1$  at the position of wheel 1 and generate an incident wave propagating along the rail and interacting with other wheels. This would generate ‘passive’ interaction forces  $P_{ji}$  at the other wheel/rail interaction positions; here the subscript indicates that the generated passive force is at position  $j$  and caused by the excitation at position  $i$ . These passive interaction forces also generate waves propagating in both directions from the respective interaction positions. Thus, the vibration due to  $F_1$  is a combination of the vibration generated by  $F_1$  and the waves generated by  $P_{ji}$ .

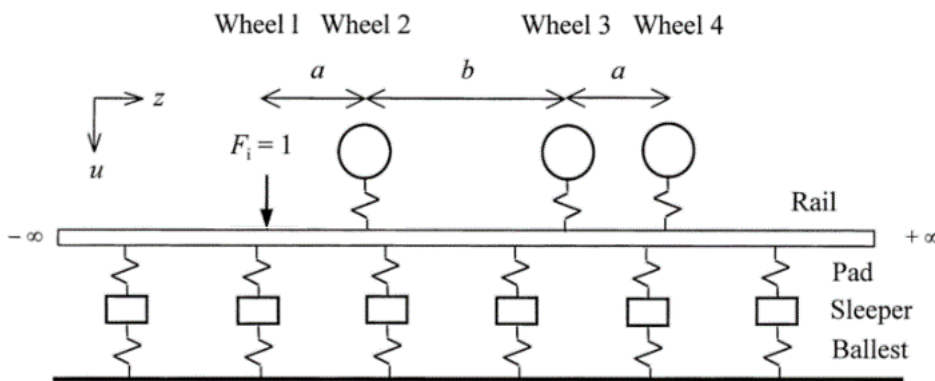


Figure 6.27 A track with four wheels on the rail [75]

### 6.6.2 Track responses

As mentioned in Section 3.5, to consider the track dynamics in the time domain, the moving Green’s functions of the track obtained from the track receptances are needed. In

order to calculate the track receptance considering the effect of multiple wheel/rail interactions, the track model introduced in Section 3.4 is extended here to include the passive wheel/rail interactions. Inserting this track receptance into Equation (6.12), the active contact force  $F_1$  can be calculated. The model developed by Wu and Thompson [75] considered the track dynamics for multiple wheels on the rail and calculated the point receptance and passive wheel/rail interactions. This model is briefly introduced here and then the expansion based on the receptance-coupling method is also introduced.

Figure 6.27 schematically shows a track with multiple wheels on the rail. The discrete supports and the wheels can all be replaced by interaction forces. The rail vibration can also be expressed as the superposition of the response to each passive force and the excitation force. When considering an excitation force at a wheel position  $i$ , the corresponding wheel should be omitted to determine the receptance. The transfer receptance of the rail at an arbitrary position can be obtained when the excitation force is a unit force:

$$\alpha(z_m) = \sum_{\substack{n=1 \\ n \neq i}}^M p_{wni} \alpha^{RT}(z_m, z_n) + \sum_{n=M+1}^{M+N} p_{sni} \alpha^{RT}(z_m, z_n) + \alpha^{RT}(z_m, z_i) \quad (6.13)$$

where  $m = 1, 2, \dots, M+N$ ,  $M$  is the number of wheel/rail interactions under consideration,  $N$  is the number of the discrete supports.  $\alpha^{RT}(z_m, z_n)$  is the transfer receptance of a free rail at  $z_m$  with the force acting at  $z_n$ .  $p_{wni}$  and  $p_{sni}$  are the passive forces at the wheel/rail interaction positions and discrete support positions respectively and given as

$$p_{wni} = -Z_w \alpha(z_n), \quad n=1, 2, \dots, M \quad \text{and} \quad n \neq i \quad (6.14)$$

$$p_{sni} = -Z_s \alpha(z_n), \quad n=M+1, M+2, \dots, M+N \quad (6.15)$$

where  $Z_s$  is the dynamic stiffness of the support.  $Z_w$  is the combined dynamic stiffness of the wheel and contact spring and may be calculated using

$$Z_w = \frac{1}{\alpha^C + \alpha^W} \quad (6.16)$$

where  $\alpha^C$  is the receptance of the wheel/rail contact spring, and  $\alpha^W$  is the wheel receptance at the contact point. When applying this in the current receptance-coupling method to get the track response, an equivalent linear contact spring is assumed. The wheel receptance in all directions can be obtained from the wheel modal information and modal summation method.

Comparing Equation (6.13) and Equation (3.41), the only difference is the first term on the right side of Equation (6.13). This term represents the vibration generated by the multiple wheel/rail interactions.

Considering a track with multiple wheels on the rail, as shown in Figure 6.27, the wheels are marked as 1,2,3,4 while the discrete supports are marked as  $s_1, \dots, s_n$ . If the excitation force is added at wheel 1, wheel 1 is replaced with a unit force. Taking the response of wheel 2 as an example, the generated displacement at wheel 2 can be given by Equation (6.13) as

$$u(z_2) = \alpha^{RT}(z_2, z_1) - Z_w u(z_2) \alpha^{RT}(z_2, z_2) - Z_w u(z_3) \alpha^{RT}(z_2, z_3) - Z_w u(z_4) \alpha^{RT}(z_2, z_4) + \sum_{n=s_1}^{s_n} p_{sn1} \alpha^{RT}(z_2, z_n) \quad (6.17)$$

Rearranging Equation (6.17) and obtaining the similar equations for other wheels, the resultant generated displacements at the wheel/rail interaction points are given in matrix form as

$$\mathbf{\alpha}_M \mathbf{u}_M = \mathbf{\alpha}'_{Me} \mathbf{F}_e - \mathbf{\alpha}'_M \mathbf{F} \quad (6.18)$$

where  $\mathbf{u}_M = [u(z_2); u(z_3); u(z_4)]$ ,  $\mathbf{\alpha}'_{Me} = [\alpha^{RT}(z_2, z_1); \alpha^{RT}(z_3, z_1); \alpha^{RT}(z_4, z_1)]$ ,

$\mathbf{F} = [p_{ss11}; p_{ss21}; \dots; p_{ssn1}]$ , and

$$\mathbf{\alpha}_M = \begin{bmatrix} 1 + Z_w \alpha^{RT}(z_2, z_2) & Z_w \alpha^{RT}(z_2, z_3) & Z_w \alpha^{RT}(z_2, z_4) \\ Z_w \alpha^{RT}(z_3, z_2) & 1 + Z_w \alpha^{RT}(z_3, z_3) & Z_w \alpha^{RT}(z_3, z_4) \\ Z_w \alpha^{RT}(z_4, z_2) & Z_w \alpha^{RT}(z_4, z_3) & 1 + Z_w \alpha^{RT}(z_4, z_4) \end{bmatrix} \quad (6.19)$$

$$\mathbf{\alpha}'_M = \begin{bmatrix} \alpha^{RT}(z_2, z_{s1}) & \dots & \alpha^{RT}(z_2, z_{sn}) \\ \alpha^{RT}(z_3, z_{s1}) & \dots & \alpha^{RT}(z_3, z_{sn}) \\ \alpha^{RT}(z_4, z_{s1}) & \dots & \alpha^{RT}(z_4, z_{sn}) \end{bmatrix} \quad (6.20)$$

Combining Equation (6.18) with (3.45) and (3.46), the displacements at the wheel positions  $\mathbf{u}_M$  can be obtained.

According to Equation (3.47) and (3.48), the rail displacement at the connection points with the rail pads are needed to calculate the connection forces. Thus, the displacements at the rail foot positions which are connected to the rail pads are given in matrix form as

$$\mathbf{u}_r + \mathbf{\alpha}_c \mathbf{u}_M = \mathbf{\alpha}'_e \mathbf{F}_e - \mathbf{\alpha}'_r \mathbf{F} \quad (6.21)$$

where  $\mathbf{u}_r = [u(z_{s1}); u(z_{s2}); \dots; u(z_{sn})]$ ,  $\mathbf{\alpha}'_e = [\alpha^{RT}(z_{s1}, z_1); \alpha^{RT}(z_{s2}, z_1); \dots; \alpha^{RT}(z_{sn}, z_1)]$  and

$$\mathbf{\alpha}_c = \begin{bmatrix} Z_w \alpha^{RT}(z_{s1}, z_2) & Z_w \alpha^{RT}(z_{s1}, z_3) & Z_w \alpha^{RT}(z_{s1}, z_4) \\ \vdots & \vdots & \vdots \\ Z_w \alpha^{RT}(z_{sn}, z_2) & Z_w \alpha^{RT}(z_{sn}, z_3) & Z_w \alpha^{RT}(z_{sn}, z_4) \end{bmatrix} \quad (6.22)$$

$$\mathbf{\alpha}'_r = \begin{bmatrix} \alpha^{RT}(z_{s1}, z_{s1}) & \dots & \alpha^{RT}(z_{s1}, z_{sn}) \\ \vdots & \ddots & \vdots \\ \alpha^{RT}(z_{sn}, z_{s1}) & \dots & \alpha^{RT}(z_{sn}, z_{sn}) \end{bmatrix} \quad (6.23)$$

Substituting Equation (3.47) and (6.18) into Equation (6.21) and rearranging, the rail displacement at the rail foot connection positions under multiple wheel/rail interactions can be obtained as



$$\mathbf{u}_r = (\mathbf{I} + \boldsymbol{\alpha}^r (\boldsymbol{\alpha}^p + \boldsymbol{\alpha}^s)^{-1} - \boldsymbol{\alpha}_c \boldsymbol{\alpha}_M^{-1} \boldsymbol{\alpha}_M^r (\boldsymbol{\alpha}^p + \boldsymbol{\alpha}^s)^{-1})^{-1} (\boldsymbol{\alpha}_e^r - \boldsymbol{\alpha}_c \boldsymbol{\alpha}_M^{-1} \boldsymbol{\alpha}_{Me}^r) F_e \quad (6.24)$$

Through Equations (6.24) and (3.47), the connection forces from discrete supports are obtained. Then, the track response at an arbitrary position on the rail head under multiple wheel/rail interactions can be given as

$$u_k^r = \alpha_{ke}^r F_e - Z_w \boldsymbol{\alpha}_{kc} \mathbf{u}_M - \boldsymbol{\alpha}_k^r \mathbf{F} \quad (6.25)$$

where  $\boldsymbol{\alpha}_k^r$  is the vector of receptances giving the response at point  $k$  on the free rail to a unit force at each spring location on the rail foot;  $\alpha_{ke}^r$  is the transfer receptance of the free rail from external force  $F_e$  to the response point  $k$ , and  $\boldsymbol{\alpha}_{kc}$  is the transfer receptance from passive force  $P_i$  to the response point  $k$ .

### 6.6.3 Numerical example

Calculations are carried out for the track with four wheels on it as shown in Figure 6.27. The wave reflections or the passive interactions from other wheels which are further away are weak enough to be neglected due to the wave attenuation. The parameters for the track and wheel are still same as the parameters given in Table 3.4 and Figures 4.2-4.3 respectively. The distances between wheels are set to 2.2 m and 3.85 m which are consistent with Desiro City Class 717 trains in the UK. A unit force acts at wheel 1. The results are shown in Figure 6.28 in terms of the point mobility of the rail compared with the point mobility of single wheel and the passive wheel/rail interaction force.

From Figure 6.28(a), the point mobility at low frequencies is found to be hardly affected by the presence of the wheels on the rail, compared with Figure 3.13. This is due to the high wave propagation decay rate in the rail at low frequencies, see Figure 3.16. The incident wave is much attenuated before reaching other wheels, so that the passive wheel/rail interaction is weak. At high frequencies, however, it fluctuates around the point mobility value of the rail without wheels on it. This fluctuation of the rail vibration is caused by the combination of the incident wave and the reflected waves between the wheels on the rail. For a certain position on the rail, the vibration amplitude may increase when the reflected wave constructively interferes with the incident wave, or decrease when the two waves destructively interfere [75]. As a result, the mobility amplitude fluctuates with frequency.

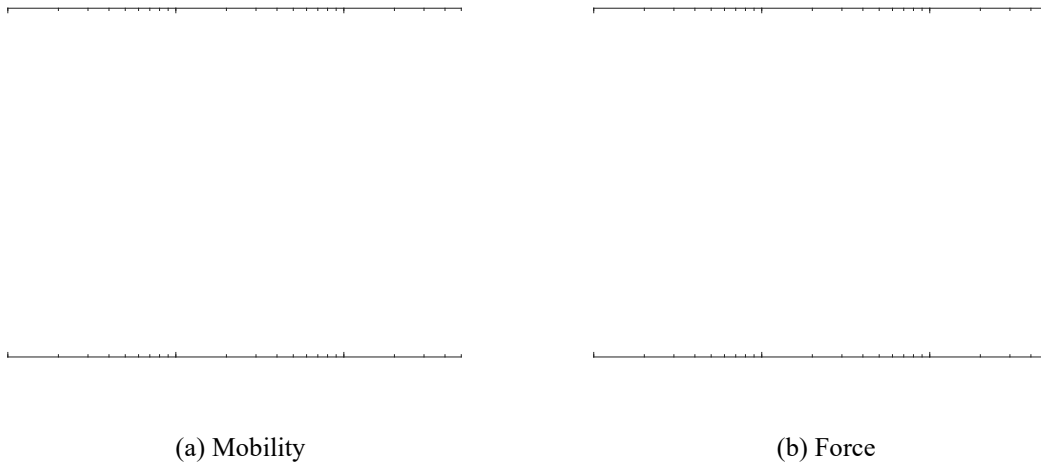


Figure 6.28 Amplitude of point and transfer mobility and passive interaction force at different wheel positions. Soft pads are used. A unit excitation force acts at the wheel 1 position and the excitation is above one of the sleepers.

The passive wheel/rail interaction forces shown in Figure 6.28(b) are small at low frequencies. This is due to the low dynamic stiffness combination of the wheel and the contact spring,  $Z_w$ , at low frequencies, and also due to the high decay rate in the rail. Surprisingly as also found in [75], at some frequencies the passive interaction force can be higher than the original excitation force. In particular, at around 800 Hz and 1100 Hz, the passive contact forces at wheels 3 and 4 are larger than the excitation force at wheel 1 (unity). Therefore, the passive interaction forces are important at high frequencies and cannot be neglected in the calculation of the whole wheel/rail contact force.

#### 6.6.4 Time-domain results

To investigate the effect of the multiple wheel/rail interactions on the generation of corrugation, similar cases are considered here to those in Section 6.4. First, the basic case with all three mechanisms is considered with multiple wheels rolling over a discretely supported track. Unlike the case in Section 6.4.4, here the moving Green's functions of the active wheels are derived from the track receptance that includes the effect of the multiple wheel/rail interactions. For the four positions shown in Figure 6.27, the track receptances at the first and fourth wheel-rail contact positions are similar, while the track receptances at second and third wheel-rail contacts are similar. The initial roughness is considered for each wheel-rail interaction individually, and the effect of roughness at other wheel-rail contacts is neglected. The dynamic characteristics of the wheels are the same as those established in Section 4.2. The radius of the curve is chosen as 300 m and the wheel running speed is 72 km/h (20 m/s) as previously. Other operational and steady-state curving parameters are same as for the case in Section 6.4.4.

Four wheel/rail interactions are considered here, as shown in Figure 6.27. The initial roughness is applied to each wheel, as in Section 6.2.1, but the phase of the roughness at each wheel is treated as a random variable which is assumed to be distributed in  $(-\pi, \pi)$ . According to the distances between the wheels, and the sleeper spacing of 0.65 m, when the first wheel is directly above the sleeper, the second wheel is 0.25 m away from the nearest sleeper, the third is 0.2 m away from the nearest sleeper and the fourth is also 0.2 m away from the nearest sleeper. The roughness spectra at various stages during the first 10,000 passages of the first and second wheel-rail interactions in this case are shown in Figure 6.29. The average roughness growth rates over the first 10,000 passages for the first and second wheel-rail interactions are shown in Figure 6.30.

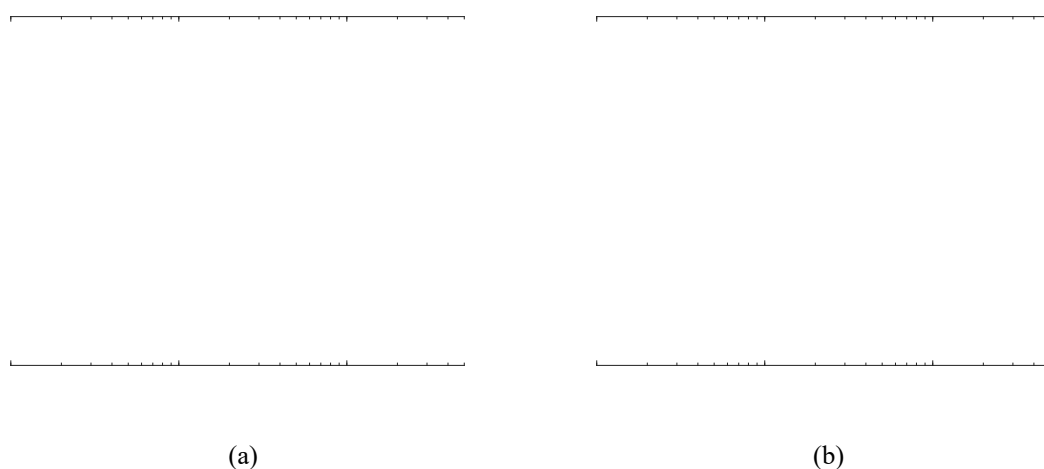


Figure 6.29 Roughness level spectra applying all three mechanisms considering multiple wheel-rail interactions in one third octave bands: (a) First wheel-rail interaction; (b) Second wheel-rail interaction

For the first wheel-rail interaction, compared with results of the original case with all three mechanisms in Figure 6.23, the main peaks observed in the resultant figures are modified. Due to the oscillations of the rail mobility at high frequency, the roughness growth rate at 1000 Hz increases a lot and the growth rate at 400 Hz drops. As for the roughness growth rate at 160 Hz and 250 Hz, they become zero in this case. From Figure 6.30(a), for the first wheel-rail interaction case, the effect of the self-excited vibration caused by falling friction is eliminated. The transient dynamic interaction mechanism becomes dominant, especially at high frequencies. The roughness develops mainly at high frequencies due to the rail oscillation.

For the second wheel-rail interaction, compared with the first wheel-rail interaction, the peaks of the roughness growth rate are more like the original case with all three mechanisms. Compared with the original case with all three mechanisms, the peaks at 160 Hz, 400 Hz and 1000 Hz are a little suppressed, while the roughness growth rate at 250 Hz

---

has nearly no change. Thus, unlike the first wheel, the oscillation of the rail mobility at high frequency has little effect on the second wheel (or the third wheel).

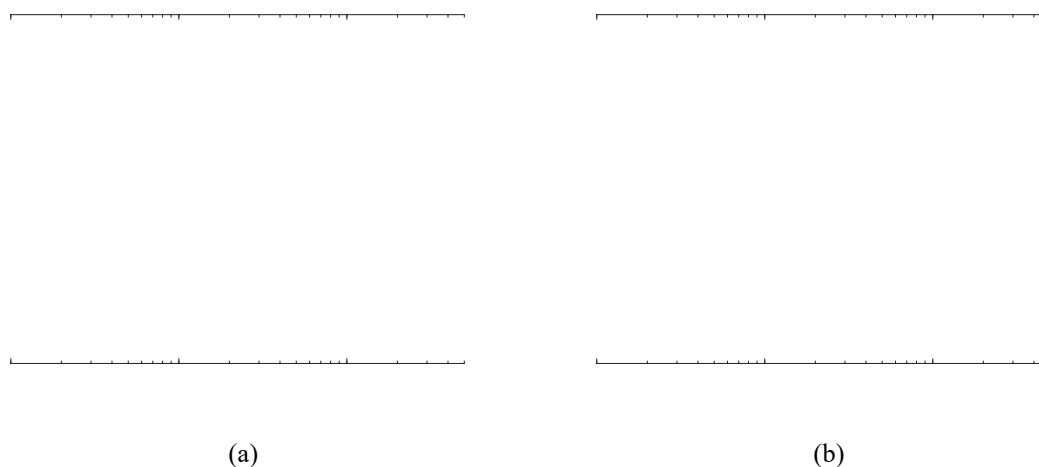


Figure 6.30 Roughness growth rates of first 10k passages applying all three mechanisms considering multiple wheel-rail interactions in one third octave bands: (a) First wheel-rail interaction; (b) Second wheel-rail interaction

## 6.7 Summary

At the beginning of this chapter, possible mechanisms accounting for the formation and development of rail corrugation presented in the literature were identified. The principles of each mechanism have been briefly presented. To further investigate which resonances contribute to the significant peaks in the roughness spectra, the values of the P2 resonance and the pinned-pinned resonance of the basic case applying all three mechanisms are preliminarily obtained before the investigations in the following parts. These values are found to be similar to some modal frequencies of the wheelset. In the following investigations, if significant peaks appear at these frequencies, it needs further investigations to identify which resonance contributes to the roughness development at this frequency.

The simulation model was then used to identify the dominant mechanism of a basic case. By including the different mechanisms, the resultant roughness development and growth rates are compared and the main mechanisms are identified. From the results it is seen that the self-excited vibration caused by falling friction and the transient dynamic interaction are the main mechanisms that account for the corrugation formation and development in this case. Rutting is one kind of corrugation whose typical frequency is between 250-400 Hz and mainly corresponds to the wheelset modes as introduced in Table 1.1. It appears that rutting corrugation is the main type of corrugation found in this case. The vertical pinned-pinned resonance also makes a small contribution to the corrugation formation,

---

while the P2 resonance appears not to contribute to the corrugation growth in this case.

The effects on the roughness development and growth rate of coupling between both wheels and rails, and of multiple wheel/rail interactions on a single rail, are also investigated. The coupling between both wheels and rails is found to have negligible effect. The inclusion of multiple wheel/rail interactions affects the track responses mainly in the high frequency range, especially for the outer wheels of a pair of bogies.



---

## **7 Influence of different parameters on roughness growth**

### **7.1 Introduction**

In this chapter, the model described in the preceding chapters is applied to a series of case studies to investigate the effects of various parameters on the development of the rail surface roughness. Results are presented in the form of roughness growth rate functions. This allows comparison between different operational conditions, as well as changes in different track and wheel parameters. Results are presented for changes in different operational parameters, such as curve radii, vehicle speeds and friction coefficients; for track parameters, such as pad stiffness, cant condition or a slab track; for vehicle parameters, such as normal load and different wheelset design. These parameters are important when studying the development of rail corrugation. Investigation of these parameters can help explain some phenomena and make the effects clear.

When using this model, the wear depth generated by the wheel-rail interaction can be calculated for a particular vehicle type on a particular track under particular operational conditions. The initial roughness profile used is the same in all the cases investigated in this chapter, which is based on the limit roughness spectrum in ISO 3095:2013 [133]. As in the previous chapter, the roughness growth is calculated for about a passage time of 2 seconds (corresponding to 60 sleeper bays for 72 km/h).

### **7.2 Influence of operational parameters**

#### **7.2.1 Curve radius**

The curve radius is a key parameter in this study since the research is focused on curved tracks. Thus, the curve radius is expected to have a significant effect on the formation of rail corrugation. Its influence is investigated here. The variation of the curve radius does not change the track vibration responses significantly, as explained in Chapter 3 [84]. The effect of curvature on the rail response is therefore neglected. The variation of the curve radius mainly affects the steady-state curving contact parameters.

The steady-state contact parameters of the vehicle negotiating a curved track are obtained in advance from the steady curving model. These parameters include the normal loads on

the two rails, the lateral wheel/rail contact positions, wheelset yaw angle, and steady creepages in the wheel/rail contacts on the high and low rails. These contact positions and creepages are then used in the time-domain prediction model. Since the steady lateral offset increases as the curve radii reduce, Figure 7.1 shows the creepages and wheel/rail contact positions plotted against curve radii.

(a) Creepage on inner wheel-rail against curve radius

(b) Offset against curve radius

Figure 7.1 Effects of curve radius on steady parameters when curving

The wheel/rail contact position and the creepages change rapidly with the curve radius when it is below 1000 m. Thus, to investigate the influence of the curve radius on the formation of corrugation, the values chosen are 200 m, 300 m (basic case considered above), 500 m and 800 m. To make the prediction results comparable, for different curve radii, although the balanced cants are different, the track cant is chosen to be 50 mm for all cases. The vehicle speed is 20 m/s as previously. Other steady-state parameters are listed in Table 7.1.

Table 7.1 Steady-state curving parameters for leading inner wheel under various curve radii

Curve radius	200 m	300 m	500 m	800 m
Wheelset lateral offset	-7.916mm	-7.775 mm	-7.618 mm	-7.495 mm
Yaw angle	-10.11 mrad	-7.347 mrad	-4.532 mrad	-2.782 mrad
Longitudinal creepage	0.3546%	0.3984%	0.3707%	0.2925%
Lateral creepage	1.001%	0.732%	0.4493%	0.2761%
Spin	-0.031	-0.034	-0.0367	-0.0386
Normal load	35.36 kN	35.58 kN	36.75 kN	37.99 kN

The resulting roughness spectra are given in Figure 7.2 when including all three mechanisms. It can be seen from Figure 7.2(a) that, for the 200 m radius curve, the roughness level increases rapidly at 160 Hz, 250 Hz and 400 Hz due to the large lateral



creepage in the tightly curved track. Meanwhile, the roughness level at 1000 Hz increases slowly compared to the other peaks and has a lower roughness level. For 300 m curve radius, the result in Figure 7.2(b) was discussed in the previous section. The roughness at 80, 160 and 1000 Hz shows a great increase while the roughness between 250 and 800 Hz increases gradually with the number of wheel passages. For 500 m curve radius in Figure 7.2(c) and 800 m curve radius in Figure 7.2(d), the roughness growth in the whole frequency range is very low for the current conditions. Basically, the roughness level grows in the whole frequency range or does not grow at any frequency.

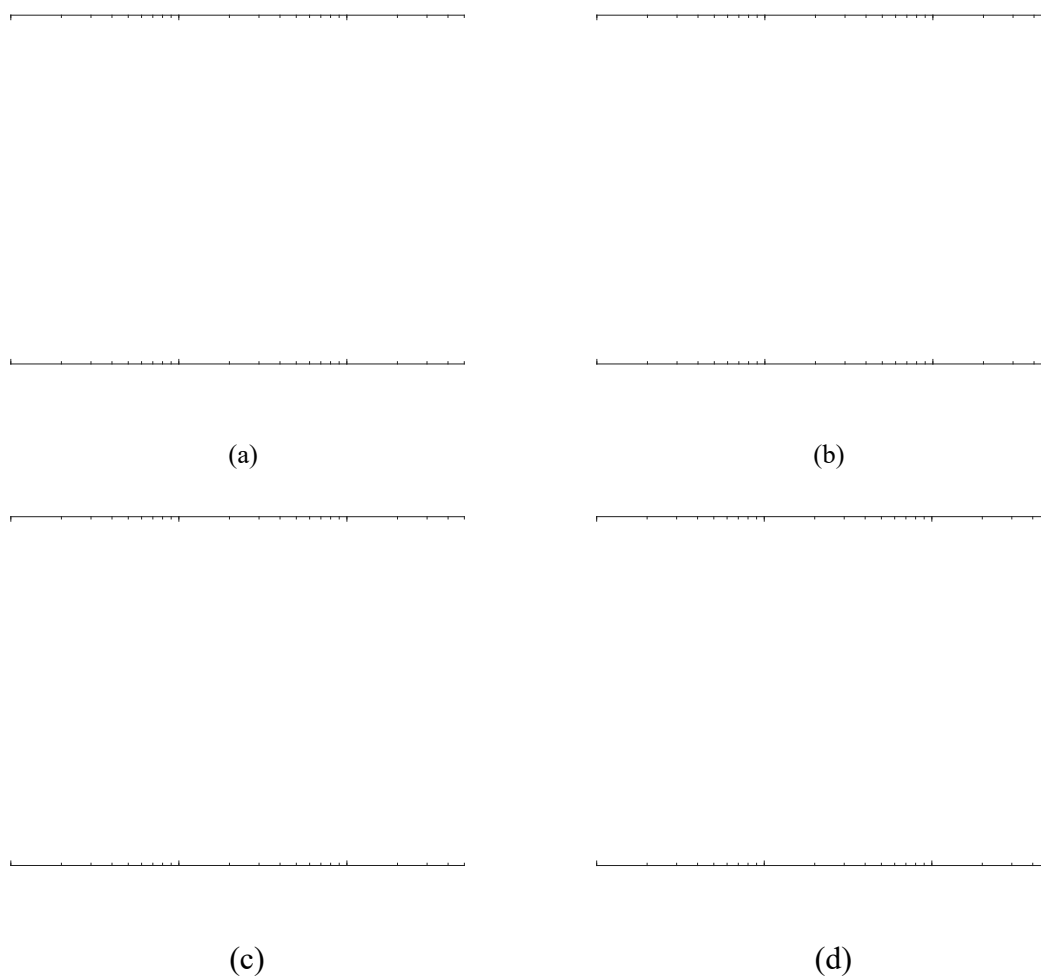


Figure 7.2 Roughness level spectra variation with number of the passages applying all three mechanisms on curved track with radius: (a) 200 m; (b) 300 m; (c) 500 m; (d) 800 m

Figure 7.3 shows the average roughness growth rate of the first 10,000 passages when including the different mechanisms for various curve radii. There is a general trend in all the cases that the roughness growth rate in the whole frequency range is decreasing as the track curve radius increases. For a track curve radius of 800 m, the roughness development on the low rail of curves is hardly found, which means the curving behaviour is not very severe (severe case is close to flange contact) and the rail corrugation does not grow

significantly. Neglecting the cases of 500 m and 800 m curve radii, the roughness level peaks of which are hard to find, the results of the 200 m and 300 m curve radii cases are mainly compared. For these tight curves, there are more peaks at lower frequencies when considering initial roughness (or with vertical-lateral cross terms) for tighter curves. When considering falling friction, the peaks at lower frequencies of tighter curves have higher levels. These peaks are related to the lateral wheelset modes. The results indicate that the tighter the track curve is, the more peaks and more higher roughness levels can be achieved. The importance of the stick-slip self-excited vibration due to falling friction also grows. The 1000 Hz peak is also increased as the track curve radius reduces. This frequency corresponds to one wheelset mode and the vertical pinned-pinned resonance. The results indicate the pinned-pinned resonance contributes more as track curve radius reduces.

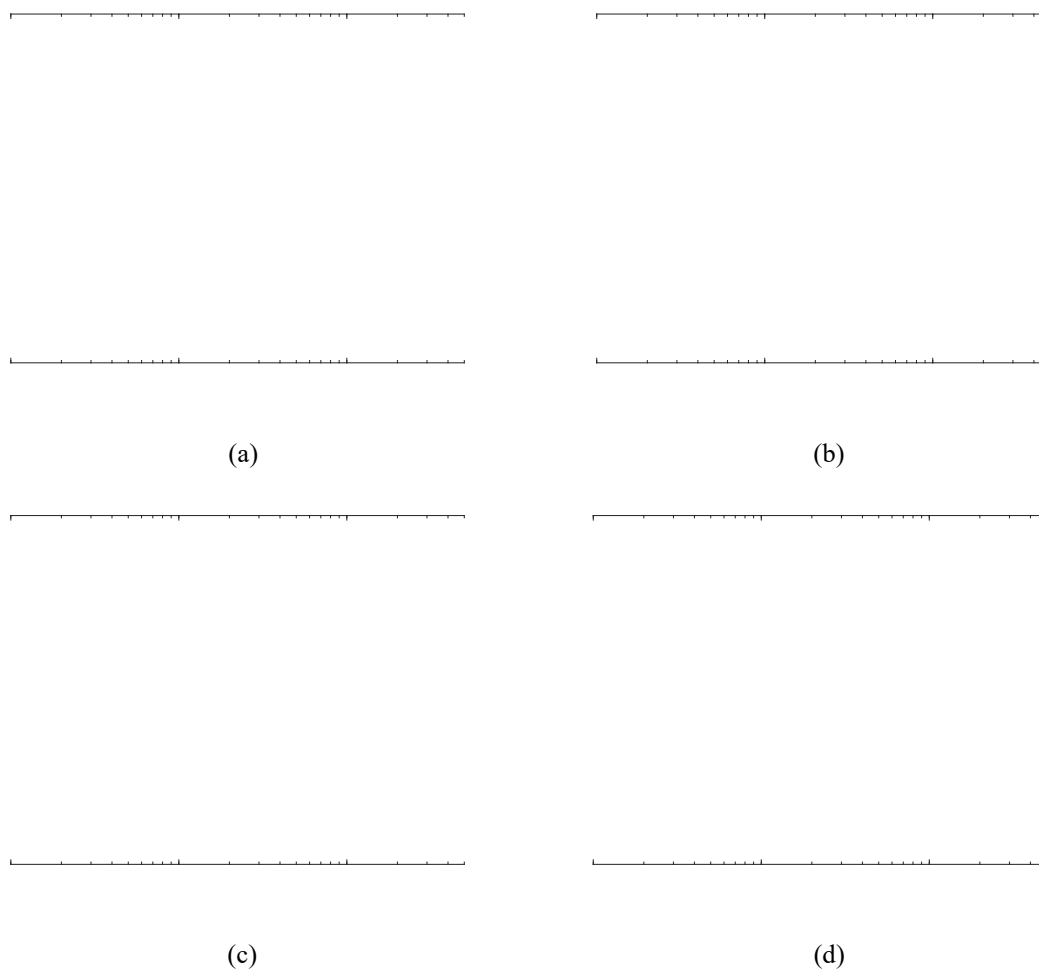


Figure 7.3 Roughness growth rates of first 10k passages under different track curve radii applying (a) only initial roughness; (b) initial roughness and vertical-lateral cross terms; (c) initial roughness and falling friction; (d) initial roughness, vertical-lateral cross terms and falling friction

Figure 7.4 shows the traction coefficient plotted against creepage and indicates the steady-state values for the different curve radii. When the curve radius is small, such as 200 m and

300 m, the creep force is beyond saturation under large lateral steady-state creepage. As the curve radius of the track increases, the creep force decreases to values below saturation, as shown in Figure 7.4. The dominant mechanism of the corrugation formation for small radius curves is the stick-slip self-excited vibration caused by falling friction, whereas the transient dynamic interaction becomes less important when the curve radius decreases.

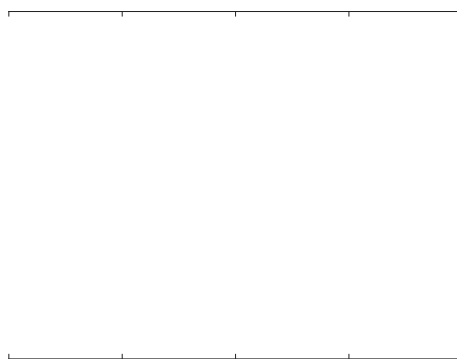


Figure 7.4 Traction coefficient against creepage

### 7.2.2 Vehicle speed

Vehicle speed is also an important factor in the formation of rail corrugation. Different from the curve radius, the vehicle speed can affect the pre-calculated moving Green's functions of the track. To keep a fixed distance passed in one time step in the time-domain prediction model, the time interval of each time step needs to be reduced when the vehicle speed increases. Consequently, the sampling frequency in the time-domain prediction model and the pre-calculated moving Green's functions of the track also need to be modified. Here the different vehicle speeds are chosen as 54 km/h (15 m/s), 72 km/h (20 m/s, basic case considered above) and 108 km/h (30 m/s). Other parameters are the same as the basic case. In basic case, the cant is 50 mm and the cant deficiency is 158 mm. In this section, the cant is also set to be 50 mm in all cases as the values may be unrealistic due to the modification of the vehicle speed if applying the same cant deficiency. The track curve radius considered here is 300 m. The steady-state parameters for various vehicle speed are listed in Table 7.2. The influence of cant is studied separately in Section 7.3.3.

Table 7.2 Steady-state curving parameters under various vehicle speed

Vehicle speed	54 km/h	72 km/h	108 km/h
Lateral offset	-7.705 mm	-7.755 mm	-7.807 mm
Yaw angle	-7.969 mrad	-7.347 mrad	-6.509 mrad
Longitudinal creepage	0.3495%	0.3984%	0.425%
Lateral creepage	0.7913%	0.732%	0.646%

Spin	-0.0345	-0.034	-0.03356
Normal load	36.68 kN	35.58 kN	35.26 kN

The roughness spectra are shown in Figure 7.5. For a vehicle speed of 54 km/h (15 m/s) given in Figure 7.5(a), it can be found that the roughness level at 160 Hz, 250 Hz and 400 Hz increases rapidly. These peaks are found in previous cases to be related to the lateral wheelset modes. In this case, the roughness at 250 Hz grows most rapidly. When the vehicle speed increases to 72 km/h (20 m/s) and 108 km/h (30 m/s), the roughness level at 160 Hz, 250 Hz and 400 Hz still increases rapidly but the frequency which has the fastest roughness growth is modified to be 400 Hz. Meanwhile, the roughness level at 1000 Hz becomes more significant and reaches a higher value under a higher vehicle speed. The 1000 Hz band is usually related to a wheelset mode and the vertical pinned-pinned resonance.

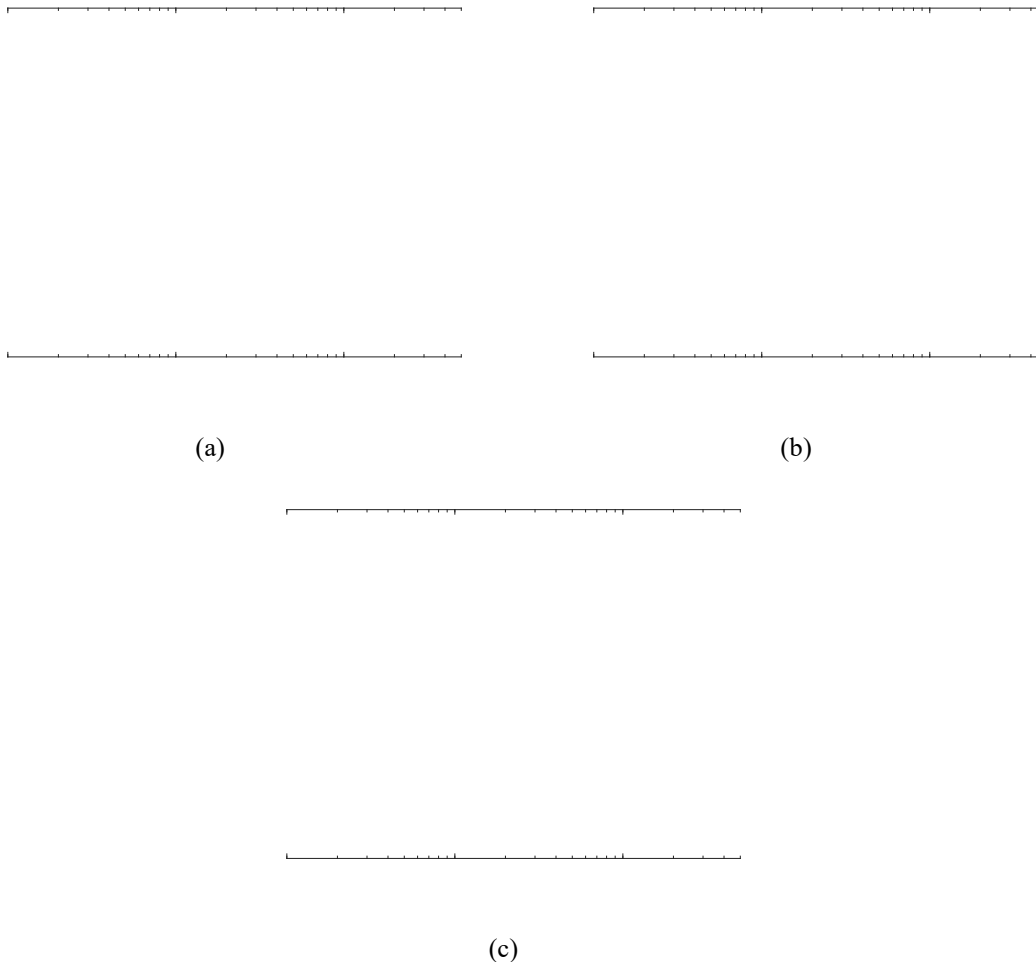


Figure 7.5 Roughness level spectra variation with the number of passages applying all three mechanisms for train speed of: (a) 15 m/s; (b) 20 m/s; (c) 30 m/s

Figure 7.6 shows the roughness growth rate of the first 10,000 passages under all three mechanisms at different vehicle speeds. As the vehicle speed increases, it can be seen that

the roughness growth rate at 160 Hz and 250 Hz decreases while that at 1000 Hz increases. The overall roughness growth rate basically remains stable. It is found in previous cases that the 160 Hz and 250 Hz peaks are caused mainly by the inclusion of falling friction, while the 400 Hz and 1000 Hz peaks are introduced mainly by transient dynamic interaction mechanism. This indicates that the transient dynamic interaction mechanism becomes more important while the effect of the stick-slip self-excited vibration caused by falling friction on roughness development reduces, as the vehicle speed increases. Corresponding lateral wheelset modes are related to these roughness growth rate peaks. The dominant mode frequencies shift to higher values as the vehicle speed grows.

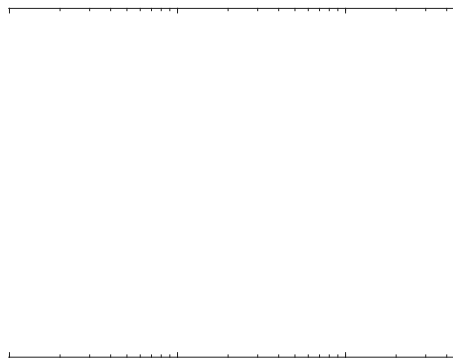


Figure 7.6 Roughness growth rates of the first 10,000 passages under different mechanisms under (a) 20 m/s; (b) 30 m/s; (c) 40 m/s

### 7.2.3 Friction coefficient

The influence of the friction coefficient on the formation of corrugation is investigated in this section. The friction coefficient is directly related to the tangential wheel/rail contact force limits and further the wear depth on the rail surface. Under different conditions, the value of the friction coefficient may vary. Here the friction coefficient is chosen as 0.2 (basic case considered above), 0.3, 0.5 and 0.8. To make the prediction results comparable, the variation of friction coefficient is investigated only in the time-domain prediction model whereas the steady-state curving parameters are kept the same. This is to investigate the effect of friction coefficient alone on the formation of corrugation. When considering the cases with the velocity-dependent friction coefficient, to achieve comparable friction coefficients at the nominal value of creepage as the corresponding cases with constant friction coefficient, the maximum friction coefficient is set to 0.3, 0.38, 0.65 and 1.0, respectively.

The roughness development under all three mechanisms with different friction coefficients is shown in Figure 7.7. When the friction coefficient value changes from 0.2 to 0.3, the effect of the transient dynamic interaction mechanism on the roughness development becomes less pronounced as the roughness at the corresponding 400 Hz wheelset mode develops more slowly. When the friction coefficient value changes to 0.5, the roughness at 80 Hz develops very rapidly. This may be due to the stick-slip self-excited vibration caused by mode coupling related to the 81 Hz wheelset mode, and this will be investigated in detail later in this section. The broadband roughness above 160 Hz also increases. For a friction coefficient value of 0.8, as well as the stick-slip self-excited vibration related to the 81 Hz wheelset mode, the broadband roughness at frequencies above 500 Hz grows significantly.

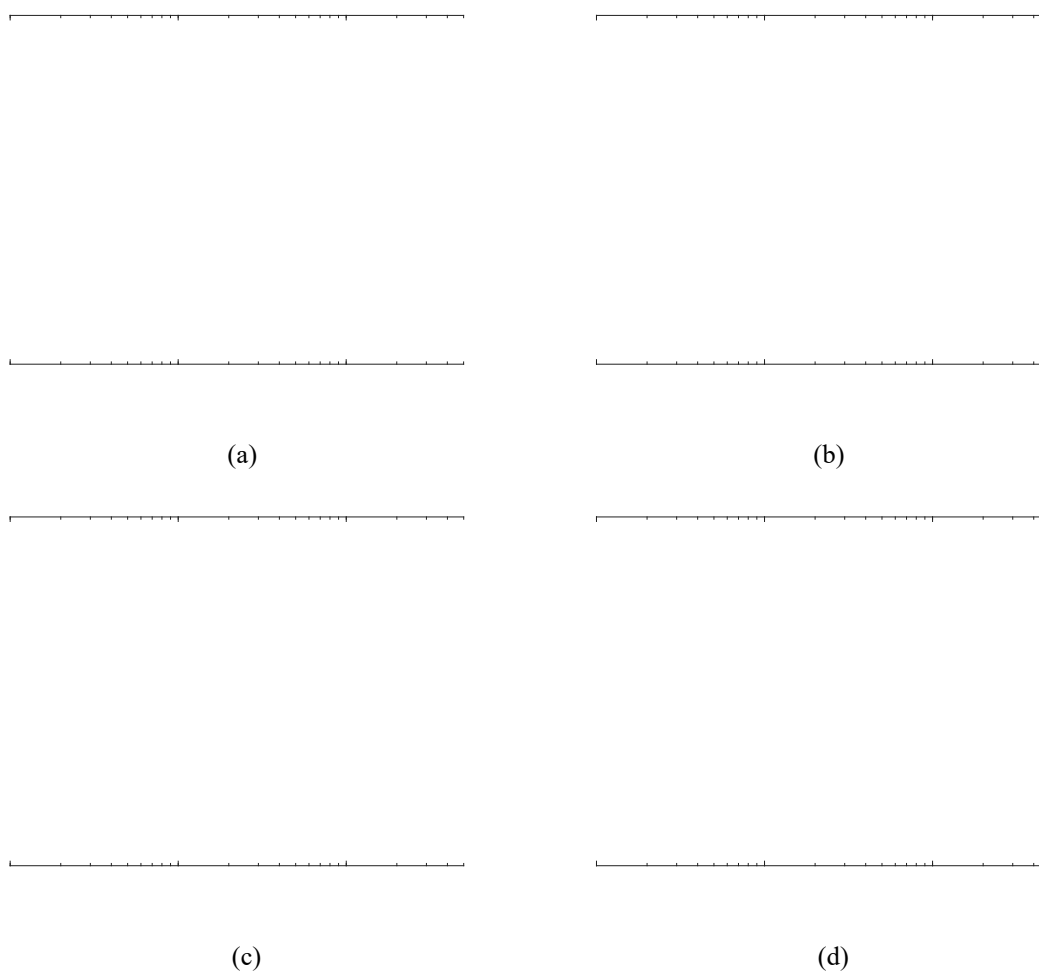


Figure 7.7 Roughness level spectra variation with number of the passages applying all three mechanisms and velocity-dependent friction coefficient whose actual value of (a) 0.2; (b) 0.3; (c) 0.5; (d) 0.8

To identify the 80 Hz peak in the roughness development spectra for friction coefficients of 0.5 and 0.8, the roughness growth rate results for a friction coefficient of 0.5 applying different mechanisms are shown in Figure 7.8. When considering only initial roughness, there is no peak at 80 Hz. When including the vertical-lateral cross terms, the peak at 80 Hz is very strong. Figure 7.9(a) gives the wheel and rail vertical displacement spectra of

this case. The P2 resonance appears at around 80 Hz (wheel vertical displacement is higher below 80 Hz and the rail vertical displacement is higher above 80 Hz). When including falling friction, there is also a roughness peak at 80 Hz but lower than that when including cross terms. In this case, the P2 resonance is identified to be at 100 Hz as shown for the basic case in Figure 7.9(b). This difference may indicate that under the current friction coefficient, the peak at 80 Hz is due to the stick-slip self-excited vibration caused by mode coupling related to the 81 Hz wheelset mode and the P2 resonance. Due to the vertical-lateral cross terms, the P2 resonance is shifted from 100 Hz to 80 Hz. The P2 resonance identified is also 80 Hz in the case of a friction coefficient value of 0.5 when applying all three mechanisms.

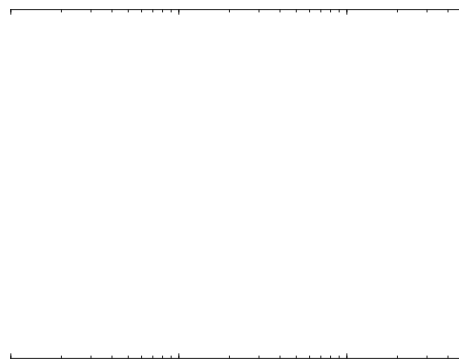


Figure 7.8 Roughness growth rates of the first 10,000 passages under different mechanisms and constant friction coefficient of 0.5

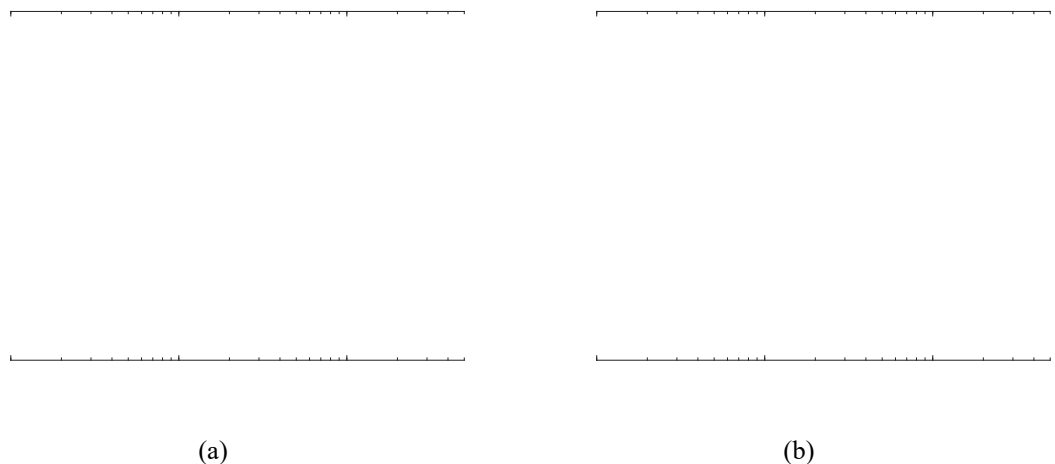


Figure 7.9 Wheel and rail vertical displacement spectra for case of friction coefficient of 0.5 due to: (a) initial surface roughness and vertical-lateral cross terms; (b) initial surface roughness and falling friction

Figure 7.10 shows the growth rates under different values of friction coefficient when including all three mechanisms. For the case with a velocity-dependent friction coefficient with actual value of 0.3, it can be seen that the resultant roughness growth rate under all

three mechanisms is reduced compared with a value of 0.2, but the dominant modes are still the 160 Hz, 250 Hz and 400 Hz lateral wheelset modes. In this case, the effect of the transient dynamic interaction mechanism on the roughness development is reduced. As the friction coefficient value grows, the dominant mode becomes the stick-slip self-excited vibration caused by mode coupling of the 81 Hz wheelset mode and the P2 resonance. At these values of friction coefficient, the effects of falling friction and the transient dynamic interaction mechanism are hardly found. The broadband roughness at higher frequencies also increases, especially for the highest value of friction coefficient.

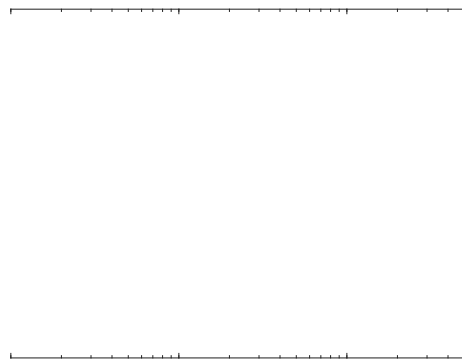


Figure 7.10 Roughness growth rates of the first 10,000 passages under all three mechanisms and different constant friction coefficient

The transient dynamic interaction and the stick-slip self-excited vibration caused by the velocity-dependent friction coefficient are the dominant mechanisms of rail corrugation formation for lower values of friction coefficient. For larger values of friction coefficient, saturation of the creep force is no longer reached under the value of creepage considered here. The ratio of creep force to normal load lies in the linear region instead of the falling region, as shown in Figure 7.11.

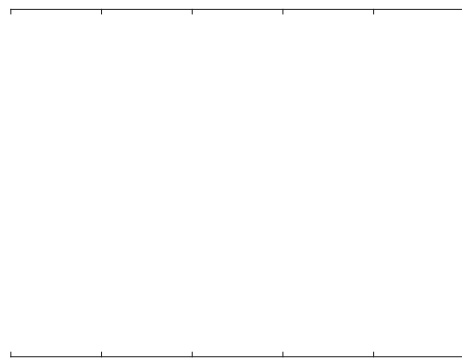


Figure 7.11 Traction coefficient against creepage with different friction coefficient



---

## 7.3 Influence of track parameters

### 7.3.1 Influence of rail pad stiffness

The rail pad stiffness is considered as an important factor that affects the initiation and growth of rail corrugation. Hempelmann [152] listed some pad parameters of ballasted track with concrete sleepers from measurements on unloaded or preloaded tracks and laboratory measurements. These pad parameters showed that the relation between the pad stiffness and the pad damping can be described by a linear function. This justifies the use of a constant loss factor to describe the pad damping here when investigating the effect of varying pad stiffness.

The pad stiffness used for the basic case in Chapter 6 is 120 MN/m in the vertical direction and 40 MN/m in the lateral direction. The loss factor is 0.25 for both directions. This is a relatively soft rail pad. To investigate the influence of the pad stiffness on the formation of corrugation, two stiffer rail pads and one softer rail pad are considered. The pad stiffnesses selected are 60 MN/m, 120 MN/m (basic case), 300 MN/m and 800 MN/m in the vertical direction. The lateral pad stiffness is chosen as 40 MN/m in all cases in this section. However, the rotational pad stiffness is proportional to the vertical stiffness [93]. Vertical and lateral mobilities are shown in Figure 7.12. The vertical pad stiffness mainly affects the vertical mobility by shifting the resonance from 200 to 600 Hz; the behaviour at low frequency and above 600 Hz is affected much less. The pinned-pinned modes remain at the almost same frequency. The lateral mobility is affected at low frequencies by the changes in rotational stiffness.

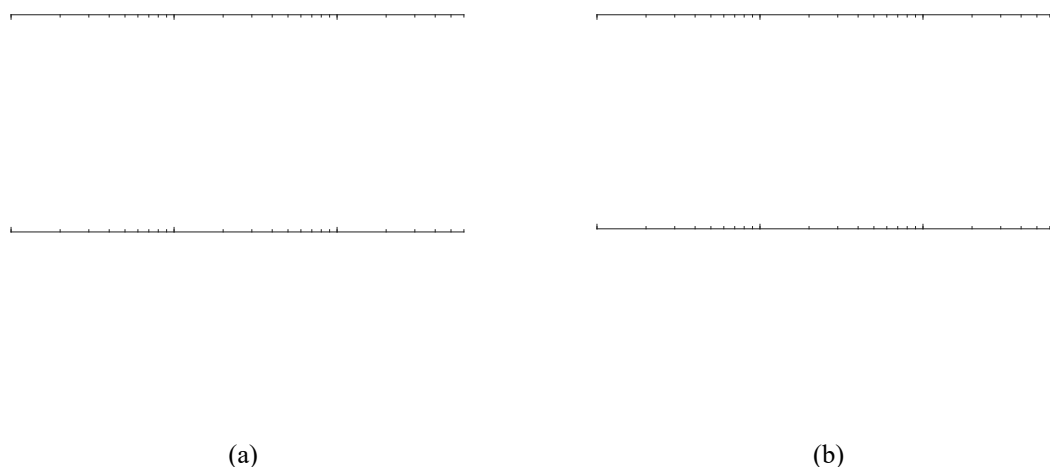


Figure 7.12 Point mobilities of tracks with different values of vertical pad stiffness: (a) vertical; (b) lateral

The cases considered here apply the same steady-state curving parameters as the basic case

given in Section 6.4. For a vertical stiffness of 60 MN/m, obvious roughness growth is found mainly at 250 and 400 Hz. However, the roughness levels are smaller than those of the basic case result, shown again here in Figure 7.13(b). For the higher pad stiffness values 300 MN/m and 800 MN/m, the roughness growth peaks are found at 160 Hz, 250 Hz and 400 Hz. The roughness levels are also nearly the same as the basic case of 120 MN/m. The 1000 Hz peak is less important for 60 MN/m or 800 MN/m than it is for 300 MN/ and especially 120 MN/m. From comparing results with the different mechanisms (not shown here) it is found that in the basic case that the 400 Hz and 1000 Hz peaks are caused mainly by the inclusion of initial roughness, while the 160 Hz and 250 Hz peaks are caused mainly by falling friction.

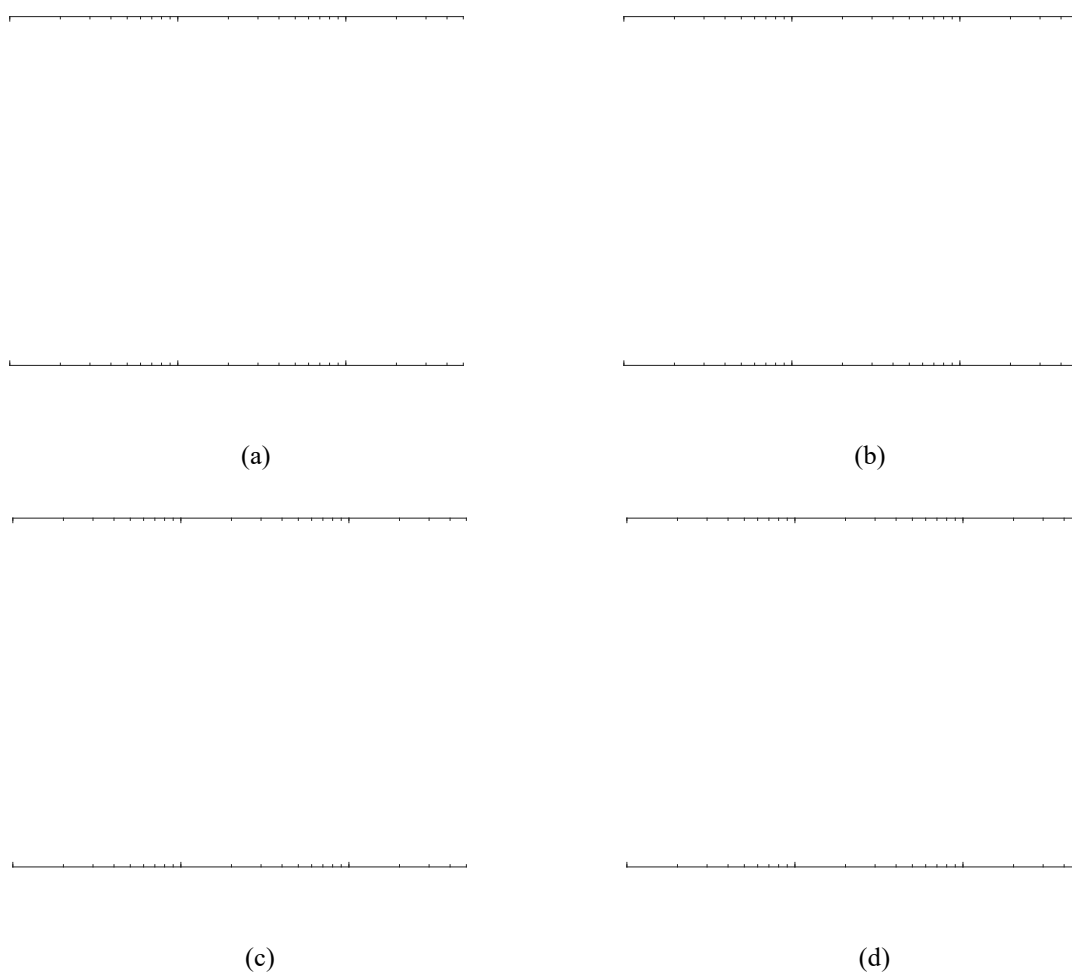


Figure 7.13 Roughness level development of the first 10,000 passages for different pad stiffnesses: (a) 60 MN/m; (b) 120 MN/m; (c) 300 MN/m; (d) 800 MN/m

The roughness growth rate of the first 10,000 passages for different values of pad stiffness are compared together in Figure 7.14; this again shows the results when applying all three mechanisms: initial roughness, vertical-lateral cross terms and falling friction. Here, stiffer pads cause higher roughness growth rate. When using soft pads (60 MN/m), the main peaks are at 250 Hz and 400 Hz, associated with lateral wheelset modes. As found in

---

previous cases, the 250 Hz peak is caused mainly by the inclusion of falling friction, while the 400 Hz peak is introduced mainly by transient dynamic interaction mechanism. As the pads become stiffer, the peak at 160 Hz becomes increasingly important. Analysed from the point of view of the dominant mechanisms, the transient dynamic interaction mechanism contributes more to the roughness development in the case with stiff pads, than the case with resilient pads. The roughness growth rates at 250 Hz, 400 Hz and 1000 Hz are almost independent of pad stiffness. This indicates that when the pad stiffness reaches a certain value, the roughness development does not further increase as the pad stiffness value increases. Only a very soft pad can have a significant effect on the roughness development.

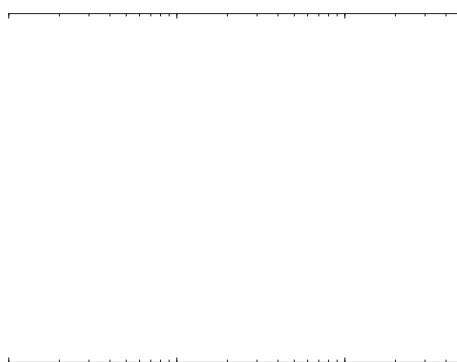


Figure 7.14 Roughness growth rates of the first 10,000 passages for different pad stiffnesses with initial roughness, cross terms and falling friction

### 7.3.2 Comparison with slab track

Slab track differs from ballasted track, considered in all other cases in this study. It is a type of railway track infrastructure in which the traditional elastic support provided by sleepers and ballast is replaced by a rigid construction of concrete. In track model, the sleepers and ballast are therefore considered as rigid and only the rail and rail pads are included. In practice, the stiffness of the rail pads used in slab track is lower than in ballasted track. Thus, a vertical pad stiffness of 60 MN/m is considered here and results are compared with the ballasted track with the same pad stiffness. The vehicle speed is still 20 m/s, track curve radius is 300 m and track cant is 50 mm. The steady-state parameters are the same as previously. The track mobility of slab track is compared with that of ballasted track in Figure 7.15. When applying the same pad stiffness value, the mobilities of the slab track and ballasted track have the same resonance, which corresponds to the rail mass vibrating on the rail pad stiffness, as well as the pinned-pinned resonances at higher frequency. The main difference is that the ballasted track has a resonance corresponding to

the rail and sleeper mass vibrating on the ballast stiffness below 100 Hz, which the slab track does not have. The mobilities are similar to each other above 300 Hz.

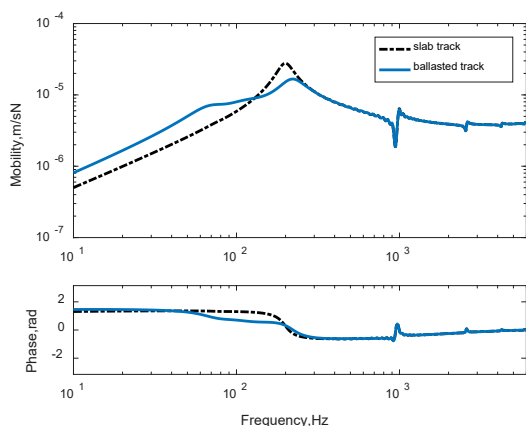


Figure 7.15 Vertical mobility of slab track and ballasted track with rail pad stiffness 60 MN/m

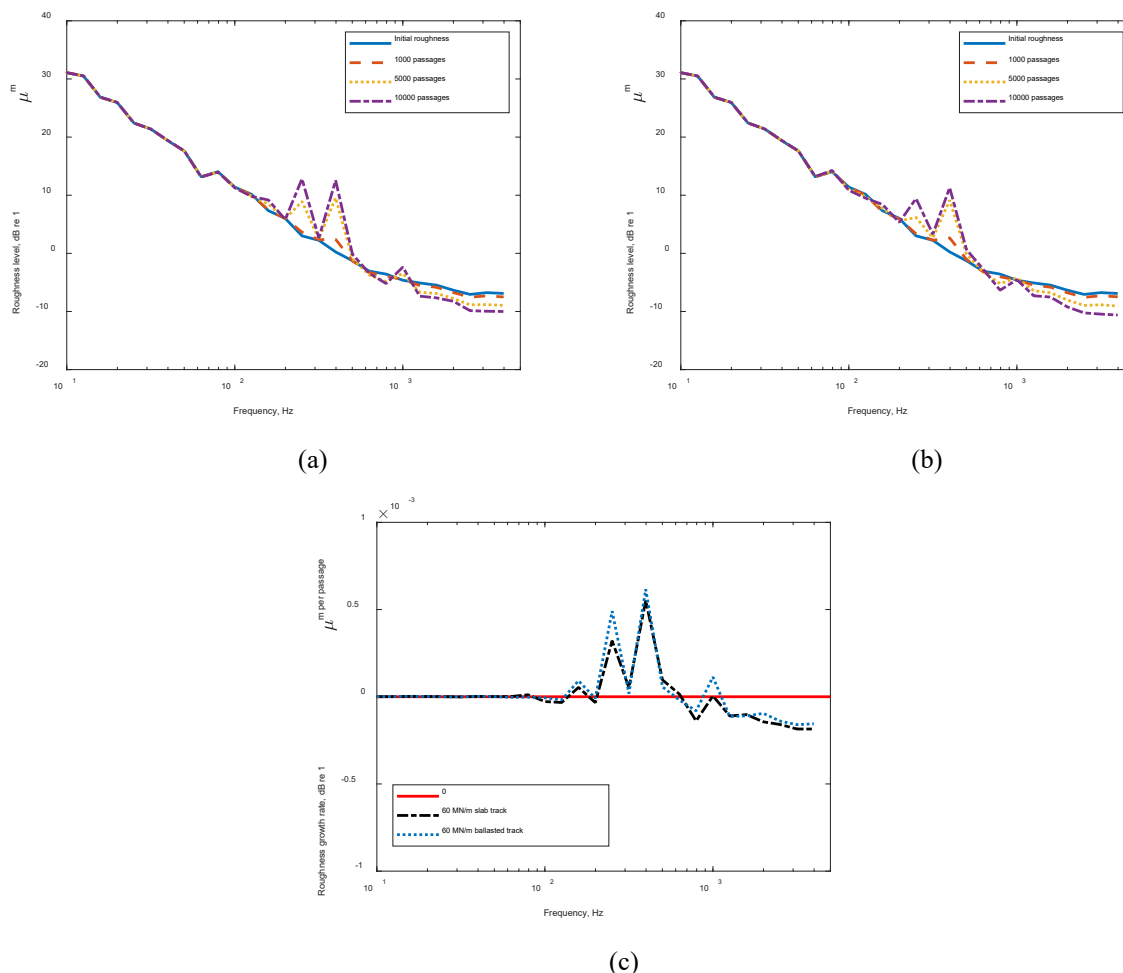


Figure 7.16 Roughness of the first 10,000 passages under all three mechanisms of a slab track with 60 MN/m pad stiffness: (a) Roughness level of concrete track; (b) Roughness level of slab track; (c) Roughness growth rate comparison between ballasted track and slab track

The roughness development spectra of slab track and ballasted track are given in Figure 7.16(a-b) and the roughness growth results are compared in Figure 7.16(c). The roughness

level peaks at 250 Hz and 400 Hz are found in both cases. These two peaks are related to lateral wheelset modes and are caused due to the stick-slip vibration caused by falling friction and transient dynamic interaction mechanisms. However, due to the differences in dynamic response at low frequency, the roughness growth rate of the slab track is lower than that of the ballasted track at these peaks. The roughness development of the ballasted track above 800 Hz is also a little greater than that of the slab track.

### 7.3.3 Influence of cant deficiency and cant excess

The track in a curve has an appropriate cant angle  $\psi_0$ , providing all or part of the centripetal force for curving. For a vehicle speed  $V_0$  and a curve radius  $R_0$ , the centripetal acceleration  $a_c$  required for balanced curving is

$$a_c = \frac{V_0^2}{R_0} \quad (7.1)$$

If the centripetal acceleration is totally provided by gravity, the cant angle must be

$$\psi_0 = \tan^{-1} \left( \frac{V_0^2}{R_0 g} \right) \quad (7.2)$$

where  $g$  is the acceleration due to gravity.

On a specific curved track with a vehicle speed  $V_0$  and a curve radius  $R_0$ , the fixed cant angle may provide less or more centripetal acceleration than required. These conditions are called cant deficiency or cant excess. Under these conditions, the wheel-rail contact forces will be involved in the balance of the lateral forces. In practical situations, the maximum value of cant (i.e. vertical height of outer rail relative to inner rail) is 150 mm. The corresponding cant angle, with cant deficiency or cant excess, is given as

$$\psi_1 = \tan^{-1} \left( \frac{l_0 \tan \psi_0 \pm d_0}{l_0} \right) \quad (7.3)$$

where  $l_0$  is the track gauge, and  $d_0$  is the extra cant vertical height difference. The sign before  $d_0$  is negative for cant deficiency, and positive for cant excess. In this section, since balanced cant cannot be achieved in the basic case, the cant excess cases cannot be investigated. Here, 0 mm, 50 mm (basic case), 100 mm and 150 mm cant values are considered (all the cant values considered here are cant deficiency cases). The curve radius considered here is still 300 m and the vehicle speed is 20 m/s (72 km/h). The corresponding steady-state curving parameters for different cant values are listed in Table 7.3.

Table 7.3 Steady-state curving parameters under various values of extra cant height

Cant value	0 mm	50 mm	100 mm	150 mm
Cant angle	0°	1.91°	3.81°	5.71°
Lateral offset	-7.775 mm	-7.755 mm	-7.724 mm	-7.696 mm
Yaw angle	-6.986 mrad	-7.347 mrad	-7.715 mrad	-8.0215 mrad
Longitudinal creepage	0.404%	0.3984%	0.3672%	0.3502%
Lateral creepage	0.6934%	0.732%	0.7662%	0.7959%
Spin	-0.0339	-0.034	-0.0344	-0.0345
Normal load	36.52 kN	35.58 kN	37 kN	37.25 kN

The roughness growth rates from the first 10,000 passages when including all three mechanisms are given in Figure 7.17 for the cases in which the cant value varies from small to large. It may be concluded from Figure 7.17 that, under the current curve radius and vehicle speed, the resultant roughness growth rate peaks are mainly at 160 Hz, 250 Hz and 400 Hz. As the cant value increases, the roughness develops quicker at these frequencies. As can be found in Table 7.3, the longitudinal creepage decreases and the lateral creepage increases as the cant value grows. The lateral curving behaviour is more severe under a large cant value, and thus the roughness develops quicker. The dominant corrugation mechanisms are still the stick-slip self-excited vibration caused by falling friction and transient dynamic interaction.

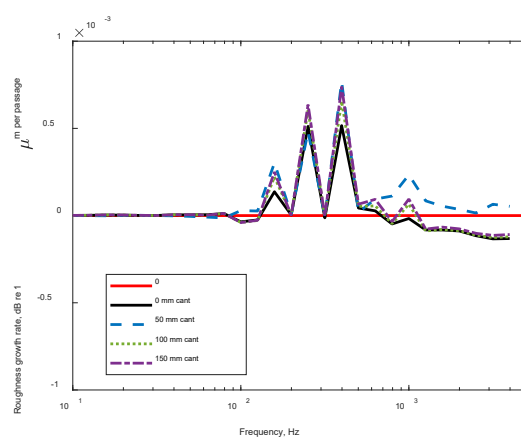


Figure 7.17 Roughness growth rates of the first 10,000 passages under all three mechanisms with various values of cant

## 7.4 Influence of vehicle parameters

### 7.4.1 Different wheelset designs

The influence of the wheelset design on the formation of corrugation is investigated here. The track is well damped by the rail pads and ballast, while the wheelset is very lightly damped. The previous simulations have been based on a wheel with a radius of 0.42 m and

---

straight web. Here, another wheel is considered, which has the same radius but a curved web.

The vertical, lateral and cross mobilities of the wheelset with curved web are shown in Figure 7.18. Due to the assumed identical elastic constraints from the vehicle and bogies, the rigid body modes of the two wheelsets are assumed to have the same frequency values of 20 Hz, 30 Hz and 40 Hz, while the corresponding damping ratios are 0.01. The method to obtain the dynamic response is the same as that introduced in Section 4.2. Comparing the mobilities of the two wheelsets in Figure 7.18, it can be found that the vertical and lateral mobilities of the two wheels are similar but the cross mobilities are different above 200 Hz.

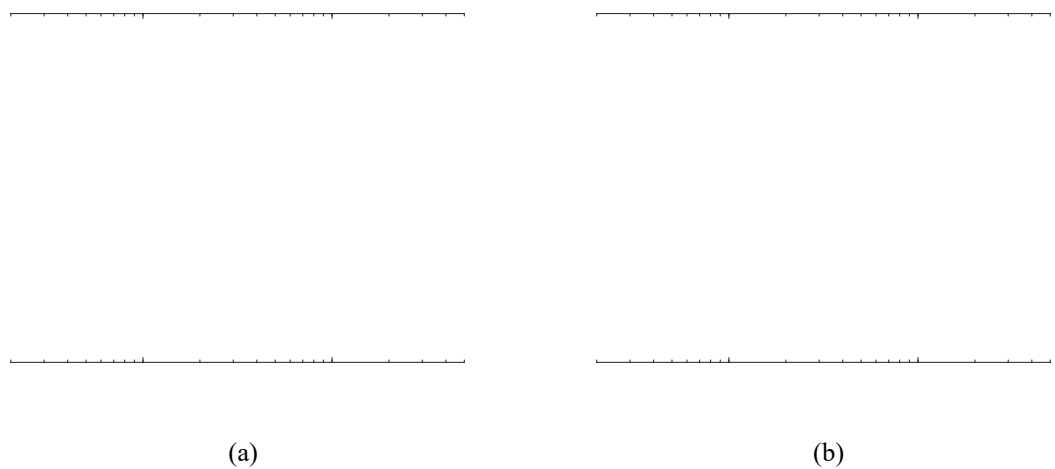


Figure 7.18 Mobilities of wheelset whose wheel (a) with straight web; (b) with curved web

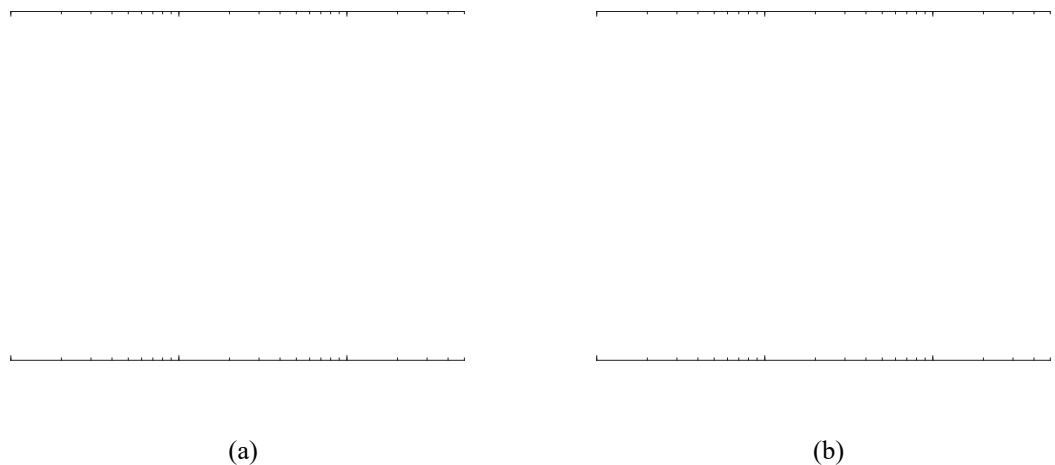


Figure 7.19 Roughness variation with the passage number with all three mechanisms of ballasted track in contact with wheel with curved web: (a) Roughness level spectra; (b) Comparison of roughness growth rate with results for wheel with straight web

Figure 7.19(a) shows the roughness development for the wheel with curved web, from which it can be seen that for the curved web wheel case, the roughness develops only at

---

400 Hz. In Figure 7.19(b), compared with the straight web wheel case, the roughness level growth at 400 Hz is lower and has no other peaks. This peak is related to a lateral wheelset mode of the wheelset. It is caused by both the stick-slip self-excited vibration caused by falling friction and transient dynamic interaction.

#### 7.4.2 Axle load

The influence of the axle load on the formation of corrugation is investigated here. In the basic case, the normal load on each wheel is around 40 kN. For investigation, the wheel load is set to 50 kN and 60 kN. To investigate the effect of the wheel load on the formation of corrugation alone, the variation of the wheel load is applied only in the time-domain prediction model, which means the steady-state curving contact parameters in different cases here are the same as the basic case.

The results are shown in Figure 7.20. This shows that higher axle loads cause lower global roughness growth rates under identical steady-state curving parameters, curve radius and speed. To help explain this, Figure 7.21 shows the traction coefficient (ratio of lateral creep force to normal contact force). Larger values compared in Figure 7.21 is to show more obvious difference between different cases. For lower axle loads, a lower creepage value is needed for the creep force to reach saturation and the traction coefficient enters the falling slope region. Under identical creepages, the traction coefficients for 40 kN and 60 kN are in the same falling slope region. Although the contact patch size is different due to the different normal load, the contact area is in the full slip region. However, for 80 kN, the traction coefficient is close to the saturation point. This would cause a smaller slip region within the contact patch and result in lower wear if it is not at the saturation point. For 100 kN, the traction coefficient is far below the saturation value.

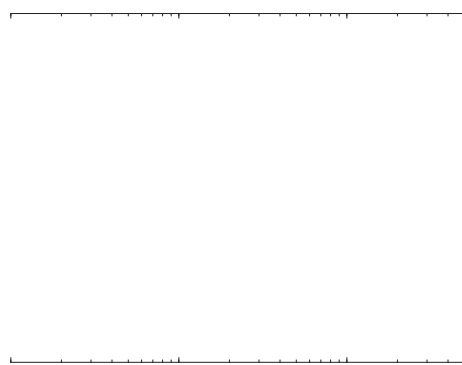


Figure 7.20 Roughness growth rates of first 10,000 passages under different wheel loads with all three mechanisms



Figure 7.21 Tangential/Normal force ratio variation with creepage

### 7.4.3 Traction force

The influence of the traction force on the formation of corrugation is investigated here. In the basic case, the external traction force applied is 0 kN. For investigation, the traction force applied to each wheel is set first to 1 kN and then to 2 kN. To investigate the effect of the traction force on the formation of corrugation, the variation of the traction force is applied in the steady-state curving model to obtain the corresponding steady-state curving contact parameters listed in Table 7.4, and then these are applied in the time-domain prediction model considering all three mechanisms. The other parameters are the same as the basic case.

Table 7.4 Steady-state curving parameters under various vehicle speed

Traction force	0 kN	1 kN	2 kN
Lateral offset	-7.755 mm	-7.750 mm	-7.746 mm
Yaw angle	-7.347 mrad	-7.351 mrad	-7.457 mrad
Longitudinal creepage	0.3984%	0.2658%	0.1623%
Lateral creepage	0.732%	0.7285%	0.7433%
Spin	-0.034	-0.0341	-0.0341
Normal load	35.58 kN	36.27 kN	37.07 kN

The roughness growth rate results for different values of traction force considering all three mechanisms are shown in Figure 7.22. As the applied traction increases, the roughness growth rate becomes higher at 250 Hz and the peak at 1000 Hz is suppressed. When the traction increases, the longitudinal dynamics become a bit more important and thus, the transient dynamic interaction.

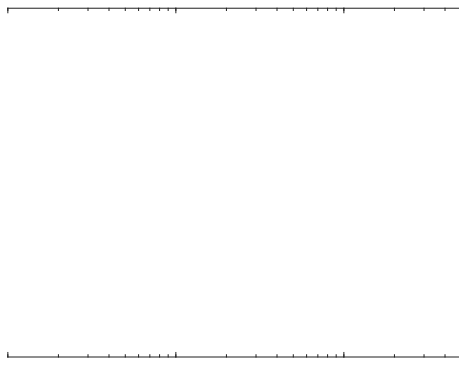


Figure 7.22 Roughness growth rates of first 10,000 passages under different tractions with all three mechanisms

## 7.5 Summary

A series of roughness growth rate calculations have been made to examine the development of acoustic roughness (roughness affecting the acoustic frequency range) over time under different conditions. The parameters used in these calculations are identical to those used in the basic case presented in Section 6.2.5 apart from the specific parameters investigated in each case, enabling the effects of each parameter to be identified. The effects of the operational, track and vehicle parameters on the roughness formation and development have been investigated.

The roughness development and growth rate have firstly been examined for different operational parameters. For tight curves, the dominant corrugation development mechanisms are the self-excited vibration caused by falling friction and the transient dynamic interaction. The rutting corrugation is main type of corrugation that is found, which is related to lateral wheelset modes. Changes of vehicle speed did not affect the wheel/rail contact position and creepages much; the corrugation wavelength remains approximately constant. Changes in the friction coefficient modify the friction limit of the creep force. As the friction coefficient grows, the dominant mechanism may become the stick-slip self-excited vibration caused by mode coupling.

When changing the rail pad stiffness, rutting is still found as the main type of corrugation. The self-excited vibration caused by falling friction and the transient dynamic interaction mechanism are the dominant mechanism. When the pad stiffness reaches a certain value, the effect of pad stiffness on the roughness development does not further increase as the pad stiffness value grows. Slab track is also considered for comparison with ballasted track but the results are similar for a given pad stiffness. When the cant is increased, the curving

---

behaviour is more important in the lateral direction since the lateral creepage grows, thus the roughness develops quicker.

For a different wheelset design, the roughness development rate and dominant mechanisms are similar, but the growth at the dominant frequency peaks are different. When applying a higher axle load with constant creepages, the roughness growth rate decreases. Applying traction forces enhances the transient dynamic interaction.



---

## 8 Conclusions and Recommendations

A time-domain wheel/rail interaction prediction model has been developed to give improved understanding of the mechanism of rutting corrugation development in curved track and to predict its growth. By making use of this model, time-domain results are obtained and different theoretical studies are carried out to give a detailed investigation of the dominant mechanism and relevant resonances in each case.

The conclusions of this thesis can be summarised as follows.

### 8.1 The updated and newly assembled time-domain prediction model

Steady-state curving parameters of the wheel/rail interaction are obtained by using a steady-state curving model. The steady-state curving model used in this thesis is based on Huang's work [69]. Some modifications are also applied here, introducing a velocity-dependent friction coefficient and the effect of the traction in the calculation of steady-state curving.

The wheel/rail dynamic interaction is then predicted in the time domain using a model comprising a flexible wheelset model, a semi-analytical track model with discrete supports and the non-Hertzian non-steady-state 3D wheel-rail contact model based on the variational theory by Kalker [14]. Wear calculation is performed with Braghin's wear model [134] by using the contact parameters obtained from the wheel-rail contact model to compute the material loss on the running surfaces of the two rails. The wheel/rail interaction forces can also be used in TWINS to predict the rolling noise generated by each part in the wheel/rail interaction as well as the overall radiated noise.

For the track model, by applying the receptance-coupling method, the frequency domain response of the discretely supported track system is obtained. Each part of the track model is validated with examples from the literature. The transfer functions from one rail to the other are also validated using measurements. The coupling between the two rails is found to have little effect on the track response. However, the inclusion of torsion and warping are found to have significant effects on the lateral track responses compared to the Timoshenko beam theory. The track responses from the semi-analytical model are converted to moving Green's functions and then combined with a numerical wheelset model to obtain the wheel-rail interaction forces. The equations of motion of the wheelset are solved in the time domain using a state-space approach. This combination of using a

---

moving Green's function method for the track and a state-space method for wheelset is believed to be novel. A three-dimensional contact model explained by Kalker in his variational method has been implemented in MATLAB. The contact model can solve normal and tangential stress distributions throughout the contact area. Stress distributions can be used to predict wear depth and the resultant interaction force can be used to predict rolling noise.

## 8.2 Corrugation growth mechanisms

Several possible mechanisms accounting for the formation and development of rail corrugation presented in the literature are included in the model. Then, the simulation model is used to identify the dominant mechanism in a chosen situation. This basic case includes a wheelset with a straight web in contact with track with 60E1 rail and 120 MN/m rail pads. The train is negotiating a 300 m radius curve under 20 m/s vehicle speed and 50 mm cant, with 158 mm cant deficiency. The friction coefficient is 0.2 and the normal load is 40 kN. By including the different mechanisms separately, the resultant roughness development and growth rates are compared. From the results it is seen that the self-excited vibration caused by falling friction and the transient dynamic interaction are the main mechanisms that account for the corrugation formation and development in this case. The inclusion of vertical/lateral coupling (i.e. mode coupling) is a relevant mechanism when the friction coefficient is large enough. The dominant peaks are found to be in the 160 Hz, 250 Hz, 400 Hz and 1000 Hz one-third octave bands and are related to lateral wheelset modes. Thus, rutting corrugation is the main type of corrugation found in this case, while the vertical pinned-pinned resonance (at around 1000 Hz) also makes a small contribution to the corrugation formation. The P2 resonance appears not to contribute to the corrugation growth in this case.

The effects on the roughness development and growth rate of (i) the coupling between both wheels and rails and (ii) multiple wheel/rail interactions on a single rail are also investigated. The coupling between both wheels and rails is found to have negligible effect on the response and hence on the roughness growth. The inclusion of multiple wheel/rail interactions on a single rail affects the track responses mainly in the high frequency range. For the outer wheels of a pair of bogies, the roughness growth at high frequency is greatly increased and other peaks are suppressed. However, the effect of multiple wheel/rail interactions is found to be small for the wheels in the middle positions.

---

### 8.3 Effect of relevant parameters on corrugation

The effects of the operational, track and vehicle parameters on the roughness formation and development are investigated by comparing the results with those of basic case.

As the curve radius of the track is increased, the creepages in the wheel/rail contact gradually decrease. For large curve radii, the curving behaviour is not very severe (the creep force reaches saturation) and there is little or no rail corrugation growth. For tight curves, the dominant corrugation development mechanisms are the self-excited vibration caused by falling friction and the transient dynamic interaction, and the transient dynamic interaction becomes less important when the curve radius decreases. For tight curves, the rutting corrugation is main type of corrugation, which is related to various wheelset modes. Changes of vehicle speed did not affect the wheel/rail contact position and steady-state creepages much. The dominant frequency increases as the vehicle speed grows, suggesting that the corrugation wavelength remains approximately constant.

Changes of the friction coefficient modify the friction limit of the creep force and also increase the wear. The larger the friction coefficient is, the higher the resultant roughness level is. When keeping the creepages constant, the corresponding creep force also changes from the saturation region to below saturation. As the friction coefficient value grows, the dominant mechanism changes from the self-excited vibration caused by falling friction and the transient dynamic interaction, to the stick-slip self-excited vibration caused by mode coupling related to the 81 Hz wheelset mode and the P2 resonance.

As the rail pad stiffness increases, rutting is still the main type of corrugation, while the self-excited vibration caused by falling friction and transient dynamic interaction are the dominant mechanisms. But as the pad stiffness increases, the transient dynamic interaction also gradually shows more importance. When the pad stiffness reaches a certain value, the roughness development does not further increase as the pad stiffness value grows. From a comparison of a slab track with ballasted track with the same pad stiffness, the roughness level peaks are identical, but the growth rate of the slab track is a little lower. When the cant increases, the curving behaviour leads to higher lateral creepage, and thus the roughness develops quicker.

Considering a different wheelset design with a curved web, the roughness development rate and dominant mechanisms are similar, but the dominant frequency peaks are reduced. When applying a higher axle load with constant creepages, the roughness growth rate

---

decreases since a higher creepage value is needed for the creep force to reach saturation and the traction coefficient enters the falling slope region.

## **8.4 Summing up**

Three different mechanisms for rail corrugation formation and development have been explained and explored through theoretical modelling. Reviewing all the cases and parameters investigated, for a vehicle negotiating tightly curved tracks, the creep force is usually beyond saturation. In these cases, the dominant mechanism is usually found to be the stick-slip vibration caused by falling friction as well as the transient dynamic interaction. The frequency of the dominant peak may differ in different cases, but is usually related to lateral wheelset modes, which corresponds to rutting corrugation. In these cases, in which the creep force is beyond saturation, the pinned-pinned resonance corrugation can also be found and has a small contribution to the resultant corrugation. The change of some parameters can change the wear depth in the time domain, and thus, the resultant roughness level and growth rate. If the creep force is changed to be below saturation, the importance of the transient dynamic interaction mechanism may be more pronounced. The P2 and pinned-pinned resonance corrugations may then also have more contribution to the resultant corrugation. Self-excited vibration caused by mode coupling can be found in cases with higher friction coefficient.

## **8.5 Recommendations for future work**

Measurements of roughness development over time are required to validate the time-domain roughness prediction model and to understand the mechanisms of roughness growth. A useful long-term experiment would be to take roughness measurements at regular intervals over many months or years at locations with initially low roughness levels where roughness growth is expected. Other factors that should ideally be monitored in addition to the roughness itself include traffic axle load, lateral forces, traction and braking forces. However, these would be more difficult (perhaps impossible) to collect on the time scales of roughness development. Details are also required of the wheelset and track dynamic properties.

One of the main limitations of most analytical track models, including the present one, is the neglect of cross-sectional deformations. Although the current model is sufficient for frequencies up to 1 kHz, which is acceptable for most corrugation modelling, it could be useful to extend it to higher frequencies. The step required to improve the frequency limits



---

of applicability of such models, is to incorporate the cross-sectional deformations, mainly those of web bending and double web bending that affect the lateral response. This could be achieved either by considering the cross-sectional flexibility in the fundamental theory, or potentially by introducing additional degrees of freedom at the centroid to correct for the cross-sectional behaviour (e.g. similar to warping).

The effect of multiple wheel/rail interactions on the corrugation formation and development has been investigated using a simplified approach in this thesis. In practice, the rail surface roughness is affected by multiple wheel/rail interactions simultaneously in the time domain. This means all the wheels should be considered as active to themselves and passive to other wheels. This needs more complicated considerations in the time-domain model and higher calculation capacity.

In the railway field, the wear of the wheel is a common phenomenon after long-term operation of the train. The radius can be reduced with reprofiling by up to 50 mm. As the wheel wears, the mode shapes and natural frequencies will change. The coupling between wheel modes can be affected which may lead to self-excited vibration of the wheel and thus, corrugation. The effect of the wheel wear on the mode coupling should therefore be investigated. Different wheels with different degrees of wear can be considered to see how wheel wear affects the likelihood of corrugation.

As well as rail corrugation, wheels can develop tonal roughness known as polygonization. The models in this thesis could also be used to study the development of roughness on the surface of wheels.

Investigation into the effects of temperature on rail vibration could be considered. The main influence of temperature on rolling noise occurs due to the variation of the rail pad stiffness with temperature. Temperature effects, though, can also be considered in the rail, by the introduction of tensional/compressional forces. These loads affect both the bending and torsional dynamic behaviour of the rail, and if the loads reach significantly high values, they might influence the corrugation generated.



# Appendices

## Appendix A. Flexible sleeper model [84]

When modelling a flexible sleeper, the damping properties of the sleeper are important for its dynamic behaviour. In order to include these, the Young's modulus and shear modulus are made complex by introducing a material damping loss factor. The wavenumbers also become complex. For the following formulation, the local coordinate axes of the sleeper are considered, where  $x$  is the axis along the sleeper length. A rotation matrix is used to convert the local dynamic stiffness matrix to the global (rail) coordinate system.

Two models of a flexible sleeper resting on an elastic foundation are considered, one is accounting for lateral bending and torsion, the other is accounting for vertical bending and extension. The flexible sleeper can be considered as uniform flexible beam with finite length supported on a damped elastic layer to represent the ballast. Thus the method presented in the Section 2.3.1 can also be applied here to the flexible sleeper to model its dynamic behaviour.

Figure A.1 shows a flexible sleeper supported by an elastic foundation. The waves are indicated that account for lateral bending and torsion.

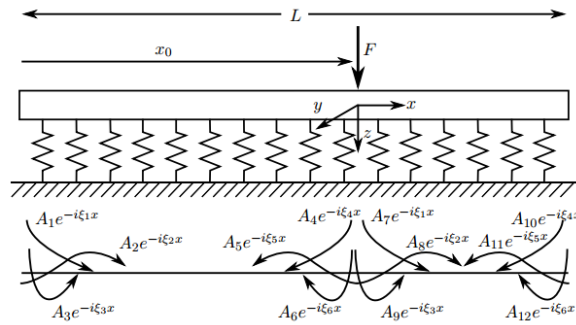


Figure A.0.1 Lateral/torsional waves on a sleeper excited by a point force at  $x_0$  [69]

The equations of motion for a beam in lateral bending and torsion are given as

$$\begin{aligned}
 -F'_y + \rho A \ddot{u}_y + \tilde{F}_y^R &= 0 \\
 -M'_z + F_y + \rho I_z \ddot{\theta}_z + \tilde{M}_z^R &= 0 \\
 -\frac{\partial M_x}{\partial x} + \rho I_p \ddot{\theta}_x + \tilde{M}_x^R &= 0
 \end{aligned} \tag{A.1}$$

with the internal forces

$$\begin{aligned}
F_y &= GA\kappa_y(u'_y + \theta_z) \\
M_z &= EI_z\theta'_z \\
M_x &= GJ\theta'_x
\end{aligned} \tag{A.2}$$

and the foundation forces, here representing the ballast, arising from

$$\begin{Bmatrix} \tilde{F}_y^R \\ \tilde{M}_z^R \\ \tilde{M}_x^R \end{Bmatrix} = \begin{bmatrix} 1 & 0 & z_b \\ 0 & 1 & 0 \\ 0 & 0 & 1 \end{bmatrix}^T \begin{bmatrix} k_{b,y} & 0 & 0 \\ 0 & k_{b,rz} & 0 \\ 0 & 0 & k_{b,rx} \end{bmatrix} \begin{bmatrix} 1 & 0 & z_b \\ 0 & 1 & 0 \\ 0 & 0 & 1 \end{bmatrix} \begin{Bmatrix} u_y \\ \theta_z \\ \theta_x \end{Bmatrix} \tag{A.3}$$

where  $z_b$  is the centroid of the cross-section of the sleeper at the excitation point  $x_0$ ,  $k_{b,y}$  is the lateral ballast stiffness,  $k_{b,rz}$  and  $k_{b,rx}$  are the torsional stiffness of the ballast around  $z$  and  $x$  axis. The dash ' represents the partial differential with respect to position  $x$  and the dot  $\dot{\phantom{x}}$  represents the partial differential with respect to time  $t$ .

When the sleeper is excited at a location  $x_0$  from the left sleeper end, three waves are generated for each direction away from the excitation point, along with three reflected waves at each end due to the finite length of the sleeper (as shown in Figure A.1). In total there are six waves. The wavenumbers  $\zeta_n$  can be obtained by Equation (2.8).

The sleeper is divided into two parts at the force location  $x = 0$  and the forced response is determined directly, with the displacements written as

$$u_{y-} = \sum_{n=1}^6 A_n e^{-i\zeta_n x} \quad \text{for } -x_0 \leq x \leq 0 \tag{A.4}$$

$$u_{y+} = \sum_{n=1}^6 A_{n+6} e^{-i\zeta_n x} \quad \text{for } 0 \leq x \leq L-x_0 \tag{A.5}$$

Similarly, the rotation of the sleeper around the  $y$  and  $x$  axis can be written as

$$\theta_{z-} = \sum_{n=1}^6 B_n e^{-i\zeta_n x} \quad \text{for } -x_0 \leq x \leq 0 \tag{A.6}$$

$$\theta_{z+} = \sum_{n=1}^6 B_{n+6} e^{-i\zeta_n x} \quad \text{for } 0 \leq x \leq L-x_0 \tag{A.7}$$

$$\theta_{x-} = \sum_{n=1}^6 C_n e^{-i\zeta_n x} \quad \text{for } -x_0 \leq x \leq 0 \tag{A.8}$$

$$\theta_{x+} = \sum_{n=1}^6 C_{n+6} e^{-i\zeta_n x} \quad \text{for } 0 \leq x \leq L-x_0 \tag{A.9}$$

where  $A_n$ ,  $B_n$  and  $C_n$  are the complex amplitudes of the respective degrees of freedom for a given wavenumber  $\zeta_n$ .

Three boundary conditions are required at each end of the beam. The shear force is zero at each end:

$$\begin{aligned} GA\kappa_y \left( \frac{\partial u_y}{\partial x} + \theta_z \right) \Big|_{x=-x_0} &= 0 \\ GA\kappa_y \left( \frac{\partial u_y}{\partial x} + \theta_z \right) \Big|_{x=L-x_0} &= 0 \end{aligned} \quad (\text{A.10})$$

Similarly, the bending moment is zero at each end:

$$\begin{aligned} EI_z \frac{\partial \theta_z}{\partial x} \Big|_{x=-x_0} &= 0 \\ EI_z \frac{\partial \theta_z}{\partial x} \Big|_{x=L-x_0} &= 0 \end{aligned} \quad (\text{A.11})$$

and the torsional moment is also zero at each end:

$$\begin{aligned} GJ \frac{\partial \theta_x}{\partial x} \Big|_{x=-x_0} &= 0 \\ GJ \frac{\partial \theta_x}{\partial x} \Big|_{x=L-x_0} &= 0 \end{aligned} \quad (\text{A.12})$$

Six more conditions apply at  $x = 0$  which are the continuity of displacements, rotation and torsion:

$$\begin{aligned} u_{y-}(0) &= u_{y+}(0) \\ \theta_{z-}(0) &= \theta_{z+}(0) \\ \theta_{x-}(0) &= \theta_{x+}(0) \\ F_{y-}(0) &= F_{y+}(0) \\ M_{z-}(0) &= M_{z+}(0) \\ M_{x-}(0) &= M_{x+}(0) \end{aligned} \quad (\text{A.13})$$

This gives 12 boundary conditions. Although there are 36 unknown amplitudes, they are interrelated as the amplitudes  $B_n$  and  $C_n$  can be written as a function of the amplitudes  $A_n$  for a given wave  $n$ . Since there are six waves at either side of the applied load, 24 more equations are obtained for the amplitudes  $B_n$  and  $C_n$ . If combined with the 12 boundary conditions, they can be written as a  $36 \times 36$  matrix of equations and solved to find the wave amplitudes  $A_n$ ,  $B_n$  and  $C_n$ . The equations have to be solved separately for a unit force, unit bending moment and unit torsion moment to give the receptance matrix. The receptance matrix  $\mathbf{R}_{s,l}(\omega)$  at a general position  $x$  is then given by Equations (A.4)-(A.9).

Similarly, for the vertical bending and extension of the flexible sleeper, the equations of motion are given as:

$$\begin{aligned}
-F'_z + \rho A \ddot{u}_z + \tilde{F}_z^R &= 0 \\
-M'_y + F_z + \rho I_y \ddot{\theta}_y + \tilde{M}_y^R &= 0 \\
-\frac{\partial F_x}{\partial x} + m \ddot{u}_x + \tilde{F}_x^R &= 0
\end{aligned} \tag{A.14}$$

with the internal forces

$$\begin{aligned}
F_z &= GA \kappa_z (u'_z - \theta'_y) \\
M_y &= EI_y \theta'_y \\
F_x &= EA u'_x
\end{aligned} \tag{A.15}$$

and the foundation forces, here representing the ballast, arising from

$$\begin{Bmatrix} \tilde{F}_z^R \\ \tilde{M}_y^R \\ \tilde{F}_x^R \end{Bmatrix} = \begin{bmatrix} 1 & 0 & 0 \\ 0 & 1 & 0 \\ 0 & -z_b & 1 \end{bmatrix}^T \begin{bmatrix} k_{b,z} & 0 & 0 \\ 0 & k_{b,ry} & 0 \\ 0 & 0 & k_{b,x} \end{bmatrix} \begin{bmatrix} 1 & 0 & 0 \\ 0 & 1 & 0 \\ 0 & -z_b & 1 \end{bmatrix} \begin{Bmatrix} u_z \\ \theta_y \\ u_x \end{Bmatrix} \tag{A.16}$$

where  $k_{b,z}$  and  $k_{b,x}$  are the vertical and longitudinal ballast stiffness,  $k_{b,ry}$  is the torsional stiffness of the ballast around  $y$  axis.

Again, when an excitation is applied at location  $x_0$  from the left sleeper end, three waves are generated for each direction away from the excitation point, along with three reflected waves at each end due to the finite length of the sleeper. Similar to the lateral and torsion case, in total there are six waves. The wavenumber  $\zeta_n$  can also be obtained by Equation (2.8), by which the obtained wavenumbers for the vertical bending of sleeper are different with the lateral and torsion case.

The sleeper is again divided into two parts at the force location  $x = 0$  and the forced response is determined directly, with the displacements written as

$$u_{z-} = \sum_{n=1}^6 D_n e^{-i\zeta_n x} \quad \text{for } -x_0 \leq x \leq 0 \tag{A.17}$$

$$u_{z+} = \sum_{n=1}^6 D_{n+6} e^{-i\zeta_n x} \quad \text{for } 0 \leq x \leq L-x_0 \tag{A.18}$$

Similarly, the rotation around the  $y$  and  $x$  axis of the sleeper can be written as

$$\theta_{y-} = \sum_{n=1}^6 E_n e^{-i\zeta_n x} \quad \text{for } -x_0 \leq x \leq 0 \tag{A.19}$$

$$\theta_{y+} = \sum_{n=1}^6 E_{n+6} e^{-i\zeta_n x} \quad \text{for } 0 \leq x \leq L-x_0 \tag{A.20}$$

$$u_{x-} = \sum_{n=1}^6 F_n e^{-i\zeta_n x} \quad \text{for } -x_0 \leq x \leq 0 \tag{A.21}$$

$$u_{x+} = \sum_{n=1}^6 F_{n+6} e^{-i\xi_n x} \quad \text{for } 0 \leq x \leq L-x_0 \quad (\text{A.22})$$

where  $D_n$ ,  $E_n$  and  $F_n$  are the complex amplitudes of the respective degrees of freedom for a given wavenumber  $\xi_n$ .

Three boundary conditions are required at each end of the beam. The vertical force is zero at each end:

$$\begin{aligned} GA\kappa_z \left( \frac{\partial u_z}{\partial x} - \theta_y \right) \Big|_{x=-x_0} &= 0 \\ GA\kappa_z \left( \frac{\partial u_z}{\partial x} - \theta_y \right) \Big|_{x=L-x_0} &= 0 \end{aligned} \quad (\text{A.23})$$

Similarly, the bending moment is zero at each end:

$$\begin{aligned} EI_y \frac{\partial \theta_y}{\partial x} \Big|_{x=-x_0} &= 0 \\ EI_y \frac{\partial \theta_y}{\partial x} \Big|_{x=L-x_0} &= 0 \end{aligned} \quad (\text{A.24})$$

and the axial force is also zero at each end:

$$\begin{aligned} EA \frac{\partial u_x}{\partial x} \Big|_{x=-x_0} &= 0 \\ EA \frac{\partial u_x}{\partial x} \Big|_{x=L-x_0} &= 0 \end{aligned} \quad (\text{A.25})$$

Six more conditions apply at  $x = 0$  which are the continuity of displacements, rotation and torsion:

$$\begin{aligned} u_{z-}(0) &= u_{z+}(0) \\ \theta_{y-}(0) &= \theta_{y+}(0) \\ u_{x-}(0) &= u_{x+}(0) \\ F_{z-}(0) &= F_{z+}(0) \\ M_{y-}(0) &= M_{y+}(0) \\ F_{x-}(0) &= F_{x+}(0) \end{aligned} \quad (\text{A.26})$$

This gives 12 boundary conditions. Although there are 36 unknown amplitudes, they are interrelated as the amplitudes  $E_n$  and  $F_n$  can be written as a function of the amplitudes  $D_n$  for a given wave  $n$ . Since there are six waves at either side of the applied load, 24 more equations are obtained for the amplitudes  $E_n$  and  $F_n$ . If combined with the 12 boundary conditions, they can be written as a  $36 \times 36$  matrix of equations and solved to find the wave amplitudes  $D_n$ ,  $E_n$  and  $F_n$ . The equations have to be solved separately for a unit force, unit bending moment and unit torsion moment to give the receptance matrix. The receptance

matrix  $\mathbf{R}_{s,v}(\omega)$  at a general position  $x$  is then given by Equations (A.17)-(A.22).

By combining the vertical and lateral flexible sleeper models, the resulting receptance matrix  $\mathbf{R}_{s,local}(\omega)$  is assembled from the two derived receptance matrices,  $\mathbf{R}_{s,l}(\omega)$  and  $\mathbf{R}_{s,v}(\omega)$  in the local coordinate system of the sleeper. Since the inertial properties of the sleeper are already incorporated in the receptance matrix  $\mathbf{R}_{s,local}(\omega)$ , no separate sleeper mass matrix is required for the flexible sleeper model.

To account for the difference in orientation of the rail and sleeper beams, the receptance matrix must be converted from the local (sleeper) coordinate system to the global (rail) coordinate system. This is performed by applying a rotation matrix:

$$\mathbf{R}_s^D = (\mathbf{T}_g^T \mathbf{R}_{s,local}^D \mathbf{T}_g) / l_{ss} \quad (\text{A.27})$$

where

$$\mathbf{T}_g^T = \begin{bmatrix} 0 & 0 & -1 & 0 & 0 & 0 \\ 0 & 1 & 0 & 0 & 0 & 0 \\ 1 & 0 & 0 & 0 & 0 & 0 \\ 0 & 0 & 0 & 0 & 0 & -1 \\ 0 & 0 & 0 & 0 & 1 & 0 \\ 0 & 0 & 0 & 1 & 0 & 0 \end{bmatrix} \quad (\text{A.28})$$

The division by  $l_{ss}$  is performed in equation (A.27) in order to obtain properties per unit length, for a continuous support layer under the sleeper. This is not applied in the current thesis as the discrete supports are considered.



## Appendix B. Fundamentals of beam theories [84]

In Figure B.1 an infinitesimal element of length  $dx$  is shown along with the forces and moments acting on it, which will be used for the formulation of force equations. The external forces and moments per unit length are assumed to act in the positive direction of the coordinate system and consist of excitation forces and reaction forces due to the foundation. Here  $k_x$ ,  $k_y$  and  $k_z$  are the translational stiffness per unit length along the respective axis, while  $k_{rx}$ ,  $k_{ry}$  and  $k_{rz}$  are the corresponding rotational stiffnesses.

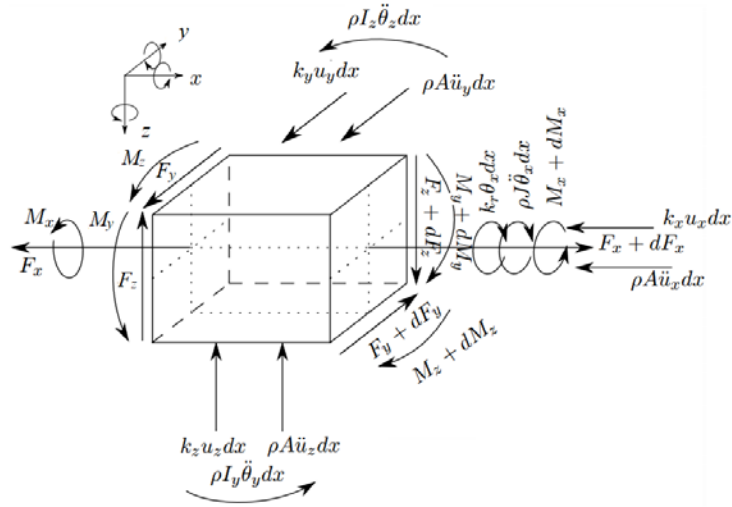


Figure B.0.2 Forces and moments on an infinitesimal element

According to Love [109], the linear components of strain in Cartesian coordinates are given as

$$\varepsilon_{xx} = \frac{\partial u_x}{\partial x} \quad (\text{B.1})$$

$$\gamma_{xy} = \frac{\partial u_y}{\partial x} + \frac{\partial u_x}{\partial y} \quad (\text{B.2})$$

$$\gamma_{xz} = \frac{\partial u_z}{\partial x} + \frac{\partial u_x}{\partial z} \quad (\text{B.3})$$

while other strains, namely  $\varepsilon_{yy}$ ,  $\varepsilon_{zz}$  and  $\gamma_{yz}$ , are assumed to be zero for the given beam model. The normal and shear stresses are then calculated using the Young's modulus  $E$  and shear modulus  $G$ , based on the generalized Hooke's law.

As the equations for the strain-displacement and stress-displacement are obtained, the stress resultants acting on the cross-section can be calculated by integrating the stresses over the cross-sectional area.

---

## B.1 Classical beam theory

The classical beam theory, also known as Euler-Bernoulli beam theory, is often used to study the out-of-plane vibration of beams. The main assumptions of this theory are that the cross-section does not deform and it remains plane and normal to the deformed axis (centroid). Considering an infinitesimal element as given in Figure B.1, the result of summing the forces in the vertical direction is obtained as

$$-\frac{\partial F_z}{\partial x} + k_z u_z + \rho A \ddot{u}_z = F_{z,ex} \quad (\text{B.4})$$

The first term in the equation represents the effect of the flexural rigidity of the beam as Equation (B.5) shows, the second term is the resistance due to the foundation, the third term is the inertial resistance due to the beam mass and the final term is the external force.

$$-\frac{\partial F_z}{\partial x} = EI_y \frac{\partial^3 u_z}{\partial x^3} \quad (\text{B.5})$$

When the beam is assumed as a free beam with no external force applied, the right-hand side is equal to 0. Moreover, the vertical displacement of the cross-section due to bending of the beam can be written in a complex form as  $u_z = u_0 e^{i\omega t} e^{-i\xi x}$ . By substituting this form of response into the equation of motion, the frequency-wavenumber relationship is obtained as

$$EI_y \xi^4 - \rho A \omega^2 = 0 \quad (\text{B.6})$$

where  $\xi$  is the complex wavenumber and  $\omega$  is the circular frequency.

## B.2 Timoshenko beam theory

When the higher frequency range is under consideration, the wavelength of the beam becomes shorter. Both rotational inertia and shear deformations become more significant. These are included in the Timoshenko beam theory. Figure B.2 shows the bending of a beam with shear schematically.

In Figure B.2,  $\theta_y$  denotes the angle between the  $x$ -axis and the normal to the plane of the infinitesimal element, while  $\gamma_{xy}$  denotes the angle between the normal to the plane of the infinitesimal element and the tangent to the beam centreline. For small rotations, it can be obtained that

$$\frac{\partial u_z}{\partial x} = \theta_y + \gamma_{xz} \quad (\text{B.7})$$

This equation gives the shear strain for a Timoshenko beam in bending. The shear force can be given as

$$F_z = GA\kappa_z\gamma_{xz} \quad (\text{B.8})$$

where  $\kappa_z$  is a correction factor depending on the cross-section known as the shear coefficient, which accounts for the effective shear area in the  $z$  direction.

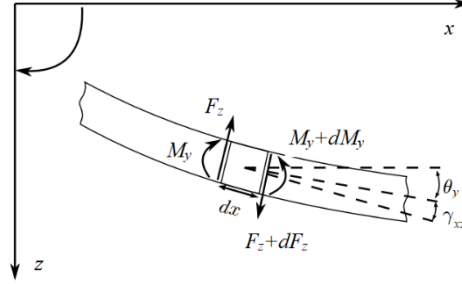


Figure B.0.3 Bending of beam with shear

Taking the sum of all the moments acting in the positive direction in Figure B.1 gives

$$-\frac{\partial M_y}{\partial x} - F_z + \rho I_y \ddot{\theta}_y = M_{z,ex} \quad (\text{B.9})$$

Combining with Equation (B.4) and substituting from Equation (B.7) & (B.8), two coupled equations of motion of a free rail are obtained as

$$-GA\kappa_z(u_z'' - \theta_y') + \rho A \ddot{u}_z = F_{z,ex} \quad (\text{B.10})$$

$$-EI_y \theta_y'' - GA\kappa_z(u_z' - \theta_y) + \rho I_y \ddot{\theta}_y = M_{y,ex} \quad (\text{B.11})$$

which constitute the classical dynamic equilibrium equations for a Timoshenko beam.

To obtain the dispersion relationship for the Timoshenko beam, the displacement and rotation of the cross-section due to bending of the beam are written in complex form, as above. By substituting this form of response back into the equations of motion and collecting terms for the complex amplitudes, the frequency-wavenumber relationship can be written as

$$\mathbf{A}(\zeta, \omega) \tilde{\mathbf{U}}(\zeta, \omega) = \tilde{\mathbf{F}}(\zeta, \omega) \quad (\text{B.12})$$

where  $\mathbf{U}$  contains the complex amplitudes of displacement and rotation,  $\mathbf{F}$  contains the corresponding forces, while the dynamic stiffness matrix  $\mathbf{A}$  is a  $2 \times 2$  matrix of coefficients dependent on  $\zeta$  and  $\omega$  for the Timoshenko beam. By collecting terms within  $\mathbf{A}$  for  $\zeta$  and

$\omega$ ,  $\mathbf{A}$  can be written as

$$\mathbf{A}=(\mathbf{K}_0+\mathbf{K}_p-\omega^2\mathbf{M})-i\zeta\mathbf{K}_1-\zeta^2\mathbf{K}_2 \quad (\text{B.13})$$

where  $\mathbf{K}_0=\begin{bmatrix} 0 & 0 \\ 0 & GA\kappa_z \end{bmatrix}$ ,  $\mathbf{K}_1=\begin{bmatrix} 0 & GA\kappa_z \\ -GA\kappa_z & 0 \end{bmatrix}$ ,  $\mathbf{K}_2=\begin{bmatrix} -GA\kappa_z & 0 \\ 0 & -EI_y \end{bmatrix}$ ,  $\mathbf{M}=\begin{bmatrix} \rho A & 0 \\ 0 & \rho I_y \end{bmatrix}$ ,

$\mathbf{K}_p=\begin{bmatrix} k_z & 0 \\ 0 & k_{yz} \end{bmatrix}$ . If a free rail with no foundation is considered, the stiffness matrix  $\mathbf{K}_p$  is empty. To obtain the dispersion relation, the free vibration which  $\mathbf{F} = 0$  is considered. For this case, non-trivial solutions require  $|\mathbf{A}|=0$ . A similar process can be carried out for the vertical or lateral bending of the beam.

### B.3 Warping and arbitrary excitation forces [84]

Usually, in analytical models the cross-section of the beam is assumed not to deform. In the Saint-Venant theory for uniform torsion, no extension or shearing occurs in the plane of cross-section and the cross-section is free to warp. The Saint-Venant torsional moment is given as:

$$M_x^p = GJ\theta_x' \quad (\text{B.14})$$

To obtain a consistent system of equations, the stresses can be decomposed into primary stresses accounting for the shear stresses due to uniform torsion (Saint-Venant theory) and secondary stresses accounting for the shear stresses that arise in the non-uniform torsion theory. The deformation of the cross-section is described by a warping function that is defined to be dependent only on the vertical and lateral directions. However, by taking the stress equilibrium equation in the axial direction in Figure B.1, the warping function is found also to be a function of axial direction which contradicts its definition. The warping function can also be decomposed with the primary warping function being consistent with that in the Saint-Venant theory, while the secondary warping function being additionally a function of axial direction.

Similarly to the axial displacement, the twisting moment  $M_x$  can also be decomposed as

$$M_x = M_x^p + M_x^s \quad (\text{B.15})$$

where  $M_x^p$  is the Saint-Venant torsional moment due to the uniform torsion, while  $M_x^s$  is the non-uniform torsion moment due to warping which takes the form:

$$M_x^s = -EI_w\theta_x''' \quad (\text{B.16})$$

where the warping constant is calculated by

$$I_w = \int (\phi_s^p)^2 dA \quad (B.17)$$

Thus, the equation of motion for the twisting of a free beam is given as

$$EI_w \theta_x'''' - GJ \theta_x'' + \rho I_p \dot{\theta}_x = M_{x,ex} \quad (B.18)$$

Similarly, the normal stress will cause a new stress resultant, called the warping moment as

$$M_w = -EI_w \theta_x'' \quad (B.19)$$

To obtain the equation of motion for the warping degree of freedom, the variation of the warping moment in the beam needs to be considered. If external force and inertia due to warping are considered, then the equation of motion for the warping component can be obtained as

$$-\frac{\partial M_w}{\partial x} + M_x^s + \rho I_w \dot{f}_w = M_{w,ex} \quad (B.20)$$

The secondary torsional moment is not only based on the normal stresses. Like the Timoshenko theory for shear deformation in bending, shear deformation can also be induced by warping. The rotation of the section can be decomposed as primary and secondary twist:

$$\theta_x = \theta_x^p + \theta_x^s \quad (B.21)$$

with the secondary torsional curvature given as

$$\frac{d\theta_x^s}{dx} = \frac{M_x^s}{GJ_s} \quad (B.22)$$

in which the secondary torsional constant  $J_t$  is [105]

$$J_t = \kappa_s (I_p - J) \quad (B.23)$$

$\kappa_s$  is a correction factor for the effective shear area undergoing torsion, similar to  $\kappa_z$  for bending. For open cross-sections such as I-beams, the secondary torsional moment has only a small influence on the torsional behaviour of the beam [106]. Thus, the value of the correction factor  $\kappa_s$  will not significantly influence the response of the beam. However, the inclusion of this value will lead to a more accurate result.

In Figure 3.1, the eccentricity between the shear centre and the centroid mainly affects the

displacements in vertical and lateral directions, as well as the rotations around  $y$  and  $z$  directions,

$$\begin{aligned}
 u_{x,c} &= u_{x,s} \\
 u_{y,c} &= u_{y,s} - e_z \theta_{x,s} \\
 u_{z,c} &= u_{z,s} + e_y \theta_{x,s} \\
 \theta_{x,c} &= \theta_{x,s} \\
 \theta_{y,c} &= \theta_{y,s} + e_y f_w \\
 \theta_{z,c} &= \theta_{z,s} + e_z f_w \\
 f_c &= f_w
 \end{aligned}
 \tag{B.24}$$

where the subscript  $c$  represents centroid, while  $s$  represents shear centre. The offset  $e_y$  and  $e_z$  are shown in Figure 3.1.

The excitation forces are assumed to be applied at the centroid of the rail. In practice, the forces are often applied with some eccentricity, both vertically and laterally from the centroid, as shown in Figure B.3. The external force at the excitation point is assumed to be applied in three directions. Due to the lateral offset  $y_e$  and vertical offset  $z_e$  between the excitation point and the centroid, the following expressions can be derived for the external excitation forces:

$$\tilde{\mathbf{F}} = [\tilde{F}_x, \tilde{F}_y, \tilde{F}_z, z_e \tilde{F}_y - y_e \tilde{F}_z, z_e \tilde{F}_x, y_e \tilde{F}_x, \phi_h \tilde{F}_x]^T
 \tag{B.25}$$

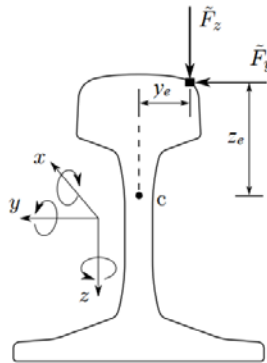


Figure B.0.4 Excitation forces applied with offsets from the centroid

The required response positions also have offsets in vertical and lateral directions with the rail centroid. After obtaining the responses at the centroid, a transformation matrix between the centroid and the response position is applied to determine the responses at the response position. Considering the lateral offset  $y_r$  and vertical offset  $z_r$  between the response point and the centroid, the transformation matrix is given as

---


$$\mathbf{T}_f = \begin{bmatrix} 1 & 0 & 0 & 0 & -z_r & y_r & \varphi_r \\ 0 & 1 & 0 & z_r & 0 & 0 & 0 \\ 0 & 0 & 1 & -y_r & 0 & 0 & 0 \\ 0 & 0 & 0 & 1 & 0 & 0 & 0 \\ 0 & 0 & 0 & 0 & 1 & 0 & 0 \\ 0 & 0 & 0 & 0 & 0 & 1 & 0 \\ 0 & 0 & 0 & 0 & 0 & 0 & 1 \end{bmatrix} \quad (\text{B.26})$$

When considering curved railway tracks, the effect of the curvature should also be considered. However, the effect of the curvature on the coupling between vertical, lateral, axial and torsional directions becomes significant only when the curve radius is very small [74]. For the considered curve radii in this research, the effect of curvature on the rail response is negligible.

---

## Appendix C. Initial broadband roughness

For the investigations in this chapter, an initial broadband roughness of the rails is used as the input. The limit roughness spectrum on the running surfaces of rails established in ISO 3095:2013 [133] is implemented to reproduce a realistically low level of roughness containing a broadband spectrum of wavelengths, ranging from 0.00315 m to 0.4 m. This standard indicates the roughness level  $L_{ri}$ , in decibels, for the central wavelength  $\lambda_i$  of twenty-two 1/3 octave bands

$$\lambda_i = 0.1 \times 10^{k/10}, \text{ with } k = -15, -14, \dots, 6 \text{ and } i = 1, \dots, 22 \quad (\text{C.1})$$

The initial roughness profile can be calculated as the superposition of sinusoidal functions, the amplitudes of which are calculated for each 1/3 octave band from the levels of the rail roughness spectrum

$$z_0(x) = \sum_{i=1}^{N_{\text{oct}}} a_i \left[ \sum_{j=1}^{N_{\text{func}}} \sin \left( \frac{2\pi x}{\lambda_{ij}} + \varphi_{ij} \right) \right] \quad (\text{C.2})$$

where  $N_{\text{oct}}$  is the number of 1/3 octave bands and  $N_{\text{func}}$  is the number of sinusoidal functions in each band used to obtain the roughness profile. The  $N_{\text{oct}}$  amplitudes  $a_i$ , in  $\mu\text{m}$ , associated with each band are calculated as a function of the roughness level corresponding to the band

$$a_i = \sqrt{\frac{2}{N_{\text{func}}}} 10^{L_{ri}/20} \quad (\text{C.3})$$

The phase angles  $\varphi_{ij}$  are obtained as random numbers uniformly distributed from 0 to  $2\pi$ . The  $N_{\text{func}}$  wavelengths in each band  $\lambda_{ij}$  are calculated by taking into account a constant increment of the wave number

$$\Delta\kappa_i = \frac{2\pi}{N_{\text{func}}} \left( \frac{1}{\lambda_i^{\text{min}}} - \frac{1}{\lambda_i^{\text{max}}} \right) \quad (\text{C.4})$$

with  $\lambda_i^{\text{min}}$  and  $\lambda_i^{\text{max}}$  being the wavelengths of the extremes of each band, which are calculated from the centre wavelength of each band  $\lambda_i$  as follows

$$\lambda_i^{\text{max}} = \lambda_i 2^{1/6} \quad \lambda_i^{\text{min}} = \lambda_i / 2^{1/6} \quad (\text{C.5})$$



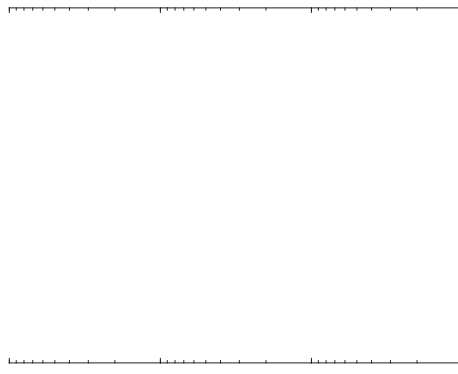


Figure C.0.5 Broadband roughness spectrum of the initial roughness generated

In the cases in this chapter, twenty-two  $1/3$  octave bands and 1000 sine functions for each octave band are considered to represent the initial roughness profile. Figure C.1 shows one randomly generated broadband initial roughness spectrum derived from a sample of length 2 m.

---

## Appendix D. Effect of track curvature on rolling noise

Although the main scope of this thesis is the calculation of corrugation growth, the wheel-rail interaction models that have been developed in the time domain allow the calculation of wheel and track vibration in curved track. The opportunity is therefore taken to extend these calculations to study the influence of curving on rolling noise.

When a railway vehicle negotiates a tight curve, high levels of vibration and noise usually arise. The rolling noise radiated by the vibration of the wheel and rail is generally more severe than on straight track. Rolling noise on tangent track have been studied for a long time. Remington [153] developed early theoretical models of rolling noise. Thompson [154] extended Remington's theory and developed the model into a computer program called TWINS [91,155]. The sources of rolling noise and the importance of the surface roughness in railway noise have been thoroughly investigated by using TWINS.

For curved track, Torstensson et al. [124] simulated wheel/track interaction on small radius curves. A time-domain model was used to simulate the low-frequency vehicle dynamics due to curving and vehicle-track dynamics up to at least 200 Hz. The structural flexibility of the wheelsets and track was accounted for by using the finite element method. Time-domain Green's function is also a sufficient method to deal with interactions between wheels and track [128]. Zhang et al. [85] extended this method based on time-domain moving Green's functions to include the flexibility and rotation of the wheelset. This approach was employed to calculate wheel/rail interaction forces at high speed. The frequency content of the high-speed wheel/rail forces was shown for a number of typical excitation cases. The effects of wheelset rotation and multiple wheelsets were also investigated, but curved track was not considered.

In the current analysis, the force time-histories are obtained using the variational method described in Chapter 5. The sound radiation is calculated in a post-processing step. To achieve this the forces are converted to the frequency domain and applied in the TWINS model to calculate the wheel and track vibration and their noise radiation. A constant frequency resolution of 0.2 Hz is used which ensures sufficient resolution around the wheel resonances. It is essential that the wheel modal basis used in TWINS corresponds exactly to that used in the time-domain simulations.

A curved track with radius 300 m is firstly considered here. The operational velocity of the vehicle negotiating the curve is 72 km/h (20 m/s). The static friction coefficient is 0.3. The

dynamic characteristics of the wheel and discretely supported track used are those established in Sections 3.5 and 4.2. An initial calculation of 5 s is used to allow the wheel/rail contact to reach steady-state, after which the roughness is introduced for a further 0.5 seconds. The roughness spectrum used is a broadband roughness corresponding to the limit curve from ISO 3095-2013 [133]. The wheel/rail interaction forces obtained in the presence of the roughness are plotted as one-third octave spectra for comparison. To reveal the difference in interaction forces between tangent and curved tracks, the results of these two cases are compared in Figure D.1(a). For the tangent track case, the same curve radius and vehicle speed are used as for the curved track case listed above. The curve radius has some effects on the track dynamic properties [84]. However, the effect of curvature can be neglected for radii greater than 100 m. Thus, the Green's functions used for the curved track are the same as for the tangent track. For the steady-state parameters for the tangent track case, the wheel/rail contact position is assumed to be at the nominal contact position. The normal load is 1/8 the mass of the whole vehicle multiplied by the gravity coefficient for each wheel. The steady-state longitudinal and lateral creepages are obtained from the wheel/rail contact model in Chapter 5 with the curve radius set to infinity.



Figure D.0.6 Interaction force spectra comparison of different track types: (a) Curved track with radius 300 m and tangent track; (b) Curved track with radius 300 m with and without coupling between two wheels/rails

Several important frequencies can be identified in the 1/3 octave spectra of the interaction forces in Figure D.1(a). The peak at around 90 Hz is the P2 resonance (the vehicle unsprung mass bouncing on the track stiffness). The 200-300 Hz frequency range is dominated by the track receptance which contains the resonance frequency of the rail mass on the rail pad stiffness, seen as a dip in the interaction force. The vertical interaction forces of the two cases show little difference except around 20 Hz, associated with rigid body modes of the wheelset. For the tightly curved track, the steady lateral creepage is

---

large enough to make the lateral interaction force reach saturation. Since a constant friction coefficient was applied, the saturated value is equal to the vertical interaction force multiplied by the friction coefficient. Thus, the lateral interaction force of the tightly curved track shows mainly the characteristics of the vertical wheel/rail dynamics. For the tangent track, only the dynamic lateral creepage is considered and the interaction force is mainly related to the characteristics of the lateral wheel/rail dynamics. Above 1.6 kHz the effect of track curvature on the lateral forces is much smaller, which is where the wheel component of noise is important.

Section 3.4.6 introduced the transfer functions between the two rails mounted on the same series of sleepers. Similarly, the transfer functions between two wheels within a wheelset can also be obtained from the wheelset modal information. To investigate the effects on the interaction forces of the coupling between the two wheels and rails, Figure D.1(b) shows the force spectra for the curved track with and without this coupling. The coupling mainly introduces differences in the frequency range around the P2 resonance and the 200-300 Hz frequency range.



Figure D.0.7 Total sound pressure level comparison: (a) between curved track and tangent track; (b) among curved tracks with different radii

Figure D.2(a) compares the total sound pressure spectrum (single wheel considered, averaged over 100 m, three microphone positions at 3 m from the near rail, at heights of 0.5, 1.2 and 2.5 m above the rail head) of the tangent track and curved track (on the inner side) with 300 m curve radius; for the curved track, results are shown with or without considering the coupling between the two wheels and rails. These results include the sound radiated by the wheel, sleepers, vertical and lateral vibration of the track. The rolling noise in the curved track is higher than on the tangent track between 100 and 1250 Hz due to the higher lateral forces. The effect of the coupling between the two wheels and rails is mainly

---

found in the range 80-300 Hz, similar to the contact force.

Figure D.2(b) shows results for different curve radii. The sound pressure level decreases between 100 and 1250 Hz as the curve radius increases. As the curve radius is increased, the steady-state wheel/rail contact position shifts back to the nominal position and the steady lateral creepage value becomes lower. Consequently, the sound radiated by the lateral vibration of the track is reduced. The A-weighted sound pressure level of each component is plotted against curve radius in Figure D.3 (The total A-weighted SPL for tangent track is 78.3 dB(A)).



Figure D.0.8 A-weighted SPL of each component plotted against curve radius

Figure D.4 gives sound pressure spectra of the rail, wheel and sleeper for tangent track and curved track with 300 m radius. The overall A-weighted sound pressure at low frequencies is dominated by the track.

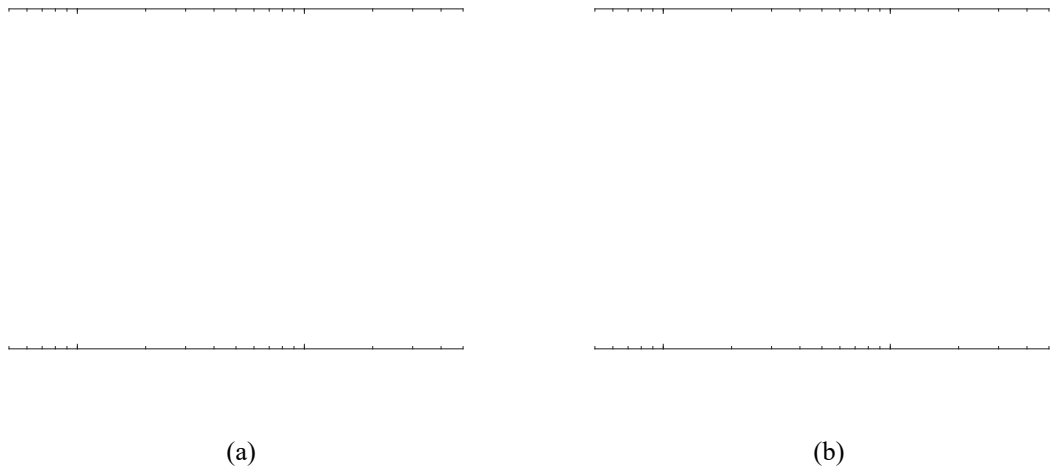


Figure D.0.9 Sound pressure level of each part of: (a) tangent track; (b) curved track with 300 m radius



---

## References

- [1] D.J. Thompson, C.J.C. Jones. Chapter 10. Noise and vibration from railway vehicles; Iwnicki, S. (ed.), Handbook of railway vehicle dynamics. CRC Press, 2006.
- [2] D.J. Thompson. On the relationship between wheel and rail surface roughness and rolling noise. *Journal of Sound and Vibration*. 193 (1996) 149-160.
- [3] S.L. Grassie. Rail irregularities, corrugation and acoustic roughness: characteristics, significance and effects of reprofiling. *Proceedings of the Institution of Mechanical Engineers Part F: Journal of Rail and Rapid Transit* 226 (2012) 542–557.
- [4] X.S. Jin, Z.F. Wen. Effect of discrete track support by sleepers on rail corrugation at a curved track. *Journal of Sound and Vibration* 315 (2008) 279–300.
- [5] S.L. Grassie, Rail corrugation: characteristics, causes, and treatments, *Proceedings of the Institution of Mechanical Engineers Part F: Journal of Rail and Rapid Transit* 223 (2009) 581–596.
- [6] S.L. Grassie. The corrugation of railway rails: I. Introduction and mitigation measures. *Proceedings of the Institution of Mechanical Engineers Part F: Journal of Rail and Rapid Transit* 237 (2023) 588–596.
- [7] W. Li, H. Wang, Z. Wen, X. Du, L. Wu, X. Li, X. Jin. Generation Mechanism and Development Characteristics of Rail Corrugation of Cologne Egg Fastener Track in Metro. *Proceedings of the Institution of Mechanical Engineers Part F: Journal of Rail and Rapid Transit* 230 (2016) 1025–1039.
- [8] G.X. Chen, X.L. Cui, W.J. Qian. Investigation into rail corrugation in high-speed railway tracks from the viewpoint of the frictional self-excited vibration of a wheel-rail system. *Journal of Modern Transportation* 24 (2016) 124-131.
- [9] X. Cui, G. Chen, J. Zhao, W. Yan, H. Ouyang, M. Zhu. Field investigation and numerical study of the rail corrugation caused by frictional self-excited vibration. *Wear* 376-377 (2017) 1919-1929.
- [10] A.B. Wang, Z.Q. Wang, P. Zhang, N. Xu, Z. Zhang, K. He. Study on the mechanism of discontinuous support stiffness on the development of rail corrugation. *Proceedings of the 21st International Congress on Sound and Vibration (ICSV '14)* pp. 1926–1933, Beijing, China, July 2014.
- [11] C. Zhao, P. Wang, M. Xing. Research on the Matching of Fastener Stiffness Based on Wheel-Rail Contact Mechanism for Prevention of Rail Corrugation. *Mathematical Problems in Engineering* (2017) 21:1-13.
- [12] C. Zhao, P. Wang, X. Sheng, D. Meng. Theoretical Simulation and Experimental Investigation of a Rail Damper to Minimize Short-Pitch Rail Corrugation. *Mathematical Problems in Engineering* (2017) 1:1-14.
- [13] J.J. Kalker. A fast algorithm for the simplified theory of rolling contact. *Vehicle System Dynamics* 11 (1982) 1-13.
- [14] J.J. Kalker. *Three-dimensional Elastic Bodies in Rolling Contact*. Dordrecht, Kluwer Academic Publishers. 1990.
- [15] S.L. Grassie, K.L. Johnson. Periodic microslip between a rolling wheel and a corrugated rail. *Wear* 101(1985) 291-309.
- [16] C.O. Frederick, A rail corrugation theory. In *Proceedings of the International Symposium on Contact Mechanics and Wear of Rail-Wheel Systems, II*, 1986, pp. 181–211.

- 
- [17] K. Hempelmann, K. Knothe. An extended linear model for the prediction of short pitch corrugation. *Wear* 191 (1996) 161-169.
- [18] S. Müller, A linear wheel-track model to predict instability and short pitch corrugation. *Journal of Sound and Vibration* 227 (1999) 899–913.
- [19] J.C.O. Nielsen, R. Lunden, A. Johansson, T. Verneresson. Train-track interaction and mechanisms of irregular wear on wheel and rail surfaces. *Vehicle System Dynamics* 40 (2003) 3-54.
- [20] C. Andersson, A. Johansson. Prediction of rail corrugation generated by three-dimensional wheel-rail interaction. *Wear* 257 (2004) 423-434.
- [21] R. Robles, N. Correa, E.G. Vadillo, J. Blanco-Lorenzo. Comprehensive efficient vertical and lateral track dynamic model to study the evolution of rail corrugation in sharp curves. *Journal of Sound and Vibration* 545 (2023) 117448.
- [22] X.S. Jin, Z.F. Wen, K.Y. Wang, Z.R. Zhou, Q.Y. Liu, C.H. Li. Three-dimensional train-track model for study of rail corrugation. *Journal of Sound and Vibration* 293 (2006) 830–855.
- [23] I. Gomez, E.G. Vadillo. A linear model to explain short pitch corrugation on rails. *Wear* 255 (2003) 1127-1142.
- [24] J.B. Nielsen. Evolution of rail corrugation predicted with a non-linear wear model. *Journal of Sound and Vibration* 227 (1999) 915–933.
- [25] M. Ciavarella, J. Barber. Influence of longitudinal creepage and wheel inertia on short-pitch corrugation: a resonance-free mechanism to explain the roaring rail phenomenon. *Proceedings of the Institution of Mechanical Engineers Part J: Journal of Engineering Tribology* 222 (2008) 171–181.
- [26] L. Afferrante, M. Ciavarella. Short-pitch corrugation: A possible resonance-free regime as a step forward to explain the “enigma”? *Wear* 266 (2009) 934-944.
- [27] T.X. Wu, D.J. Thompson. An investigation into rail corrugation due to micro-slip under multiple wheel/rail interactions. *Wear* 258 (2005) 1115–1125.
- [28] H. Ilias. The influence of railpad stiffness on wheelset/track interaction and corrugation growth. *Journal of Sound and Vibration* 227 (1999) 935-948.
- [29] L. Baeza, F.J. Fuenmayor, J. Carballeira and A. Roda. Influence of the wheel-rail contact instationary process contact parameters. *Journal of Strain Analysis for Engineering Design* 42 (2007) 377-387.
- [30] L. Baeza, P. Vila, A. Roda, J. Fayos. Prediction of corrugation in rails using a non-stationary wheel-rail contact model. *Wear* 265 (2008) 1156-1162.
- [31] A. Alonso, J.G. Gimenez. Non-steady state modelling of wheel-rail contact problem for the dynamic simulation of railway vehicle. *Vehicle System Dynamics* 46 (2008) 179-196.
- [32] K. Knothe, A. Gross-Thebing. Short wavelength rail corrugation and non-steady-state contact mechanics. *Vehicle System Dynamics* 46 (2008) 49-66.
- [33] G. Xie, S.D. Iwnicki. Calculation of wear on a corrugated rail using a three-dimensional contact model. *Wear* 265 (2008) 1238-1248.
- [34] G. Xie, S.D. Iwnicki. Simulation of wear on a rough rail using a time-domain wheel-track interaction model. *Wear* 265 (2008) 1572-1583.
- [35] P. Vila, J. Fayos, L. Baeza. Simulation of the evolution of rail corrugation using a rotating flexible wheelset model. *Vehicle System Dynamics* 49 (2011) 1749-1769.
- [36] P. Vila, L. Baeza, J. Martinez-Casas, J. Carballeira. Rail corrugation growth accounting for the



- 
- flexibility and rotation of the wheel set and the non-Hertzian and non-steady-state effects at contact patch. *Vehicle System Dynamics* 52 (2014) 92-108.
- [37] P.T. Torstensson, M. Schilke. Rail corrugation growth on small radius curves-Measurements and validation of a numerical prediction model. *Wear* 303 (2013) 381-396.
- [38] P.T. Torstensson, A. Pieringer, J.C.O. Nielsen. Simulation of rail roughness growth on small radius curves using a non-Hertzian and non-steady wheel-rail contact model. *Wear* 314 (2014) 241-253.
- [39] R.A. Clark, G.A. Scott, W. Poole, Short wave corrugations-an explanation based on stick-slip vibrations. In *Proceedings of the Applied Mechanics Rail Transportation Symposium* (1988) 141-148.
- [40] C.A. Brockley, P.L. Ko. An investigation of rail corrugation using friction-induced vibration theory. *Wear* 128 (1988) 99-105.
- [41] A. Matsumoto, Y. Sato, H. Ono, M. Tanimoto, Y. Oka, E. Miyauchi. Formation mechanism and countermeasures of rail corrugation on curved track. *Wear* 253 (2002) 178-184.
- [42] S.L. Grassie, J.W. Edwards. Development of corrugation as a result of varying normal load. *Wear* 265 (2008) 1150-1155.
- [43] Y.Q. Sun, S. Simson. Wagon-track modeling and parametric study on rail corrugation initiation due to wheel stick-slip process on curved track. *Wear* 265 (2008) 1193-1201.
- [44] B. Ding. The mechanism of railway curve squeal. PhD thesis, University of Southampton, 2018.
- [45] B. Kurzeck. Combined friction induced oscillations of wheelset and track during the curving of metros and their influence on corrugation. *Wear* 271 (2011) 299-310.
- [46] G.X. Chen, Z.R. Zhou, H. Ouyang, X.S. Jin, M.H. Zhu, Q.Y. Liu. A finite element study on rail corrugation based on saturated creep force-induced self-excited vibration of a wheelset-track system. *Journal of Sound and Vibration* 329 (2010) 4643-4655.
- [47] W.J. Qian, G.X. Chen, H. Ouyang, M.H. Zhu, W.H. Zhang, Z.R. Zhou. A transient dynamic study of the self-excited vibration of a railway wheel set-track system induced by saturated creep forces. *Vehicle System Dynamics: International Journal of Vehicle Mechanics and Mobility* 52 (2014) 1115-1138.
- [48] X. Cui, G. Chen, H. Yang, H. Ouyang, W. Yan. A case study of rail corrugation phenomenon based on the viewpoint of friction-induced oscillation of a wheelset-track system. *Journal of Vibroengineering* 19 (2017) 4516-4530.
- [49] E.G. Vadillo, J. Tárrego, G.G. Zubiaurre, C.A. Duque. Effect of sleeper distance on rail corrugation. *Wear* 217 (1998) 140-145.
- [50] P.A. Meehan, W.J.T. Daniel, T. Campey. Prediction of the growth of wear-type rail corrugation. *Wear* 258 (2005) 1001-1013.
- [51] Z. Yan, V. Markine, A. Gu, Q. Liang. Optimisation of the dynamic properties of ladder track to minimise the chance of rail corrugation. *Proceedings of the Institution of Mechanical Engineers Part F: Journal of Rail and Rapid Transit* 228 (2014) 285-297.
- [52] X. Song, Y. Qian, K. Wang, P. Liu. Effect of Rail Pad Stiffness on Vehicle-Track Dynamic Interaction Excited by Rail Corrugation in Metro. *Transportation Research Record* 2674 (2020) 1-19.
- [53] R. Robles, N. Correa, E.G. Vadillo, J. Blanco-Lorenzo. Predicting rail corrugation in a real line by means of a fast non-linear vertical and lateral model. *Wear* 524-525 (2023) 204896.
- [54] X. Sheng, D.J. Thompson, C.J.C. Jones, G. Xie, S.D. Iwnicki, P. Allen, S.S. Hsu. Simulations of roughness initiation and growth on railway rails. *Journal of Sound and Vibration* 293 (2006) 819-829.

- 
- [55] A. Igeland. Railhead corrugation growth explained by dynamic interaction between track and bogie wheelsets. *Proceedings of the Institution of Mechanical Engineers Part F: Journal of Rail and Rapid Transit* 210 (1996) 11–20.
- [56] K. Manabe. A hypothesis on a wavelength fixing mechanism of rail corrugation. *Proceedings of the Institution of Mechanical Engineers Part F: Journal of Rail and Rapid Transit* 214 (2000) 21–26.
- [57] A. Johansson, J.C.O. Nielsen. Rail corrugation growth – influence of powered wheelsets with wheel tread irregularities. *Wear* 262 (2007) 1296-1307.
- [58] P.A. Meehan, W.J.T. Daniel. Effects of wheel passing frequency on wear-type corrugations. *Wear* 265 (2008) 1202-1211.
- [59] P.A. Bellette, P.A. Meehan, W.J.T. Daniel. Effects of variable pass speed on wear-type corrugation growth. *Journal of Sound and Vibration* 314 (2008) 616-634.
- [60] P.A. Meehan, R.D. Batten, P.A. Bellette. The effect of non-uniform train speed distribution on rail corrugation growth in curves-corners. *Wear* 366-367 (2016) 27-37.
- [61] P.A. Bellette, P.A. Meehan, W.J.T. Daniel. Validation of a tangent track corrugation model with a two disk test rig. *Wear* 271 (2011) 268-277.
- [62] D.T. Eadie, M. Santoro, K. Oldknow, Y. Oka. Field studies of the effect of friction modifiers on short pitch corrugation generation in curves. *Wear* 265 (2008) 1212–1221.
- [63] S.L. Grassie. The corrugation of railway rails: II. Monitoring and conclusions. *Proceedings of the Institution of Mechanical Engineers Part F: Journal of Rail and Rapid Transit* 237 (2023) 597–605.
- [64] B.E. Croft, C.J.C. Jones, D.J. Thompson. Modelling the effect of rail dampers on wheel–rail interaction forces and rail roughness growth rates. *Journal of Sound and Vibration* 323 (2009) 17–32.
- [65] T.X. Wu. Effects on short pitch rail corrugation growth of a rail vibration absorber-damper. *Wear* 271 (2011) 339-348.
- [66] B.W. Wu, G.X. Chen, J.Z. Lv, Q. Zhu, X.N. Zhao, X. Kang. Effect of the axlebox arrangement of the bogie and the primary suspension parameters on the rail corrugation at the sharp curve metro track. *Wear* 426-427 (2019) 1828-1836.
- [67] X.L. Cui, G.X. Chen, H.G. Yang, Q. Zhang, H. Ouyang, M.H. Zhu. Effect of the wheel-rail contact angle and the direction of the saturated creep force on rail corrugation. *Wear* 330-331 (2015) 554-562.
- [68] O. El Beshbichi, C. Wan, S. Bruni, E. Kassa. Complex eigenvalue analysis and parameters analysis to investigate the formation of railhead corrugation in sharp curves. *Wear* 450-451 (2020) 203150.
- [69] Z. Huang. Theoretical modelling of the railway curve squeal. University of Southampton. Doctoral Thesis. 2007.
- [70] A.H. Wickens. *Fundamentals of Rail Vehicle Dynamics – Guidance and Stability*. Swets & Zeitlinger Publishers, Lisse, 2003.
- [71] J. Mackenzie. Resistance on railway curves as an element of danger. *Minutes of the Proceedings of the Institution of Civil Engineers* 74 (1883) 1-57.
- [72] S.R.M. Porter. *The mechanics of a locomotive on curved track*. The Railway Gazette, London, 1935.
- [73] J.A. Elkins, R.J. Gostlling. A general quasi-static curving theory for railway vehicles. *Vehicle System Dynamics* 6 (1977) 100-106.
- [74] K.L. Johnson. *Contact Mechanics*, Cambridge University Press, 1985.
- [75] T.X. Wu, D.J. Thompson. Vibration analysis of railway track with multiple wheels on the rail.

- [76] J.L. Meriam, L.G. Kraige. Engineering mechanics: dynamics, John Wiley & Sons, 2012.
- [77] S. Andersson, A. Söderberg, S. Björklund. Friction models for sliding dry, boundary and mixed lubricated contacts, *Tribology International*, 40 (2007) 580-587.
- [78] G. Xie, P.D. Allen, S.D. Iwnicki, A. Alonso, D.J. Thompson, C.J.C Jones, Z.Y. Huang. Introduction of falling friction coefficients into curving calculations for studying curve squeal noise. *Vehicle System Dynamics* 44 (2006) 261-271.
- [79] M. Spiryagin, O. Polach and C. Colin. Creep force modelling for rail traction vehicles based on the Fastsim algorithm. *Vehicle System Dynamics* 51 (2013) 1765-1783.
- [80] O. Polach. Creep forces in simulations of traction vehicles running on adhesion limit. *Wear* 258 (2005) 992–1000.
- [81] O. Polach. Influence of locomotive tractive effort on the forces between wheel and rail. *Vehicle System Dynamics* 35 (2001) 7–22.
- [82] M. Ertz, F. Bucher. Improved creep force model for wheel/rail contact considering roughness and temperature. *Vehicle System Dynamics* 37 (2002) 314–325.
- [83] F. Bucher, K. Knothe, A. Theiler. Normal and tangential contact problem of surfaces with measured roughness. *Wear* 253 (2002) 204–218.
- [84] D. Kostovasilis. Analytical modelling of the vibration of railway track. University of Southampton, Doctoral Thesis, 2017.
- [85] X. Zhang, D.J. Thompson, Q. Li, D. Kostovasilis, M.G.R. Toward, G. Squicciarini, J. Ryue. A model of a discretely supported railway track based on a 2.5D finite element approach. *Journal of Sound and Vibration* 438 (2019) 153-174.
- [86] A. Pieringer. Time domain modelling of high-frequency wheel/rail interaction. PhD thesis, Chalmers University of Technology, 2011.
- [87] P.J. Remington. Wheel/rail rolling noise I: theoretical analysis, *Journal of Acoustical Society of America* 81 (1987) 1805-1823.
- [88] D.J. Thompson, N. Vincent. Track dynamic behaviour at high frequencies. Part 1: theoretical models and laboratory measurements. *Vehicle System Dynamics* 24 (1995) 86-99.
- [89] K.L. Knothe, S.L. Grassie. Modelling of railway track and vehicle/track interaction at high frequencies. *Vehicle System Dynamics* 22 (1993) 209-262.
- [90] N. Vincent, D.J. Thompson. Track dynamic behaviour at high frequencies. Part 2: results and comparisons with theory. *Vehicle System Dynamics* 24 (1995) 100-114.
- [91] D.J. Thompson, B. Hemsworth, N. Vincent. Experimental validation of the TWINS prediction program for rolling noise, Part 1: description of the model and method. *Journal of Sound and Vibration* 193 (1996) 123-135.
- [92] S.L. Grassie, R.W. Gregory, D. Harrison, K.L. Johnson. The dynamic response of railway track to high frequency vertical excitation. *Journal of Mechanical Engineering Science* 24 (1982) 77-90.
- [93] M.A. Heckl. Railway noise-Can random sleeper spacings help? *Acustica* 81 (1995) 559-564.
- [94] M.A. Heckl. Coupled waves on a periodically supported Timoshenko beam. *Journal of Sound and Vibration*. 252 (2002) 849-882.
- [95] T.X. Wu, D.J. Thompson. A double Timoshenko beam model for vertical vibration analysis of railway track at high frequencies. *Journal of Sound and Vibration* 224 (1999) 329-348.

- 
- [96] T.X. Wu, D.J. Thompson. Analysis of lateral vibration behavior of railway track at high frequencies using a continuously supported multiple beam model. *Journal of Acoustical Society of America*. 106 (1999) 1369–1376.
- [97] D.J. Thompson. *Railway noise and vibration: mechanisms, modelling and means of control*. Elsevier Science, Oxford, UK, 2009.
- [98] K.L. Knothe, Z. Strzyzakowski, K. Willner. Rail vibrations in the high frequency range. *Journal of Sound and Vibration* 169 (1994) 111–123.
- [99] J. Ryue, D.J. Thompson, P.R. White, D.R. Thompson. Investigations of propagating wave types in railway tracks at high frequencies. *Journal of Sound and Vibration* 315 (2008) 157–175.
- [100] C.M. Nilsson, C.J.C. Jones, D.J. Thompson, J. Ryue. A waveguide finite element and boundary element approach to calculating the sound radiated by railway and tram rails. *Journal of Sound and Vibration* 321 (2009) 813–836.
- [101] W. Li, R.A. Dwight, T. Zhang. On the study of vibration of a supported railway rail using the semi-analytical finite element method. *Journal of Sound and Vibration* 345 (2015) 121–145.
- [102] A. Bhaskar, K.L. Johnson, G.D. Wood, J. Woodhouse. Wheel-rail dynamics with closely conformal contact. Part 1: dynamic modelling and stability analysis. *Proceedings of the Institution of Mechanical Engineers. Part F: Journal of Rail Rapid Transit* 211 (1997) 11–26.
- [103] B. Betgen, G. Squicciarini, D.J. Thompson. On the prediction of rail cross mobility and track decay rates using finite element models, in: *Proceedings of the 10th European Congress and Exposition on Noise Control Engineering (EURONOISE2015)*, Maastricht, Netherlands, EAA-NAG-ABAV, 2015, 2019–2024.
- [104] S.L. Grassie, S.J. Cox. The dynamic response of railway track with flexible sleeper to high frequency vertical excitation. *Proceedings of the Institution of Mechanical Engineers* 198D (1984) 117–124.
- [105] J.C.O. Nielsen, A. Igeland. Vertical dynamic interaction between train and track-influence of wheel and track imperfections. *Journal of Sound and Vibration* 187 (1995) 825–839.
- [106] S.L. Grassie. Dynamic modelling of concrete railway sleepers. *Journal of Sound and Vibration* 187 (1995) 799–813.
- [107] R. Ferrara, G. Leonardi, F. Jourdan. A contact-area model for rail-pads connections in 2-D simulations: sensitivity analysis of train-induced vibrations. *Vehicle System Dynamics*. 51 (2013) 1342–1362.
- [108] M.Y. Kim, S.B. Kim, N.I. Kim. Spatial stability of shear deformable curved beams with non-symmetric thin-walled sections. I: stability formulation and closed-form solutions, *Computers and Structure* 83 (2005) 2525–2541.
- [109] A.E.H. Love. *A treatise on the mathematical theory of elasticity*. Dover Publications, New York, 4<sup>th</sup> edition, 1944.
- [110] E.J. Sapountzakis, V.J. Tspiras. Shear deformable bars of doubly symmetrical cross section under nonlinear nonuniform torsional vibrations application to torsional postbuckling configurations and primary resonance excitations. *Nonlinear Dynamics* 62 (2010) 967–987.
- [111] M. Oregui, Zili Li, R. Dollevoet. An investigation into the vertical dynamics of tracks with monobloc sleepers with a 3D finite-element model. *Proceedings of the Institution of Mechanical Engineers Part F: Journal of Rail and Rapid Transit* 230 (2015) 891–908.

- 
- [112] C.J.C. Jones, D.J. Thompson, R.J. Diehl. The use of decay rates to analyse the performance of railway track in rolling noise generation. *Journal of Sound and Vibration* 293 (2006) 485–495.
- [113] British Standards Institution. BS EN 15461:2008 A1:2010: Railway applications – Noise emission - Characterization of the dynamic properties of track selections for pass by noise measurements, 2010.
- [114] R.A. Clark, P.A. Dean et al. Investigation into the dynamic effects of railways vehicles running on the corrugated rails. *Journal of Mechanical Engineering Science* 24 (1982) 65-76.
- [115] L. Baeza, A. Roda, J.C.O Nielson. Railways vehicle/track interaction analysis using a model substructuring approach. *Journal of Sound and Vibration* 293 (2006) 112-124.
- [116] M. Heckl. Proposal for a railway simulation program. *A Workshop on Rolling Noise Generation* (1989) 128-148.
- [117] J. Fayos, L. Baeza, F. D. Denia, J. E. Tarancón. An Eulerian coordinate-based method for analysing the structural vibrations of a solid of revolution rotating about its main axis. *Journal of Sound and Vibration* 306 (2007) 618-635.
- [118] L. Baeza, J. Fayos, A. Roda, R. Insa. High frequency railway vehicle-track dynamics through flexible rotating wheelsets. *Vehicle System Dynamics* 46 (2008) 647-659.
- [119] T. Szolc. Medium frequency dynamic investigation of the railway wheelset–track system using a discrete–continuous model. *Archive of Applied Mechanics* 65 (1998) 30–45.
- [120] T. Szolc. Simulation of bending-torsional-lateral vibrations of the railway wheelset–track system in the medium frequency range. *Vehicle System Dynamics* 30 (1998) 473–508.
- [121] T. Meinders. Modeling of a railway wheelset as a rotating elastic multibody system. *Machine Dynamics Problems* 20 (1998) 209–219.
- [122] L. Baeza, P. Vila, G. Xie et al. Prediction of rail corrugation using a rotating flexible wheelset coupled with a flexible track model and a non-Hertzian/non-steady contact model. *Journal of Sound and Vibration*. 330 (2011) 4493–4507.
- [123] K. Popp, H. Kruse, I. Kaiser. Vehicle/track dynamics in the midfrequency range. *Vehicle System Dynamics* 31 (1999) 423–463.
- [124] P.T. Torstensson, J.C.O. Nielson. Simulation of dynamic vehicle-track interaction on small radius curves. *Vehicle System Dynamics* 49 (2010) 1711-1732.
- [125] D.J. Ewins, *Modal testing: theory and practice*. Research studies press Letchworth, 1984.
- [126] J.C.O. Nielsen. High-frequency vertical wheel-rail contact forces – validation of a prediction model by field testing. *7<sup>th</sup> International Conference on Contact Mechanics and Wear of Rail/Wheel Systems*, Brisbane, Australia, 2006.
- [127] C. Andersson, T. Abrahamsson. Simulation of interaction between a train in general motion and a track. *Vehicle System Dynamics* 38 (2002) 433-455.
- [128] A. Pieringer, W. Kropp, J.C.O. Nielsen. A time-domain model for wheel/rail interaction aiming to include non-linear contact stiffness and tangential friction. *Noise and Vibration Mitigation for Rail Transportation Systems Proceedings of the 9<sup>th</sup> International Workshop on Railway Noise*, Munich, Germany, 4-8 September 2007: 285-291, Springer: Berlin.
- [129] H. Hertz. On the contact of elastic solids. *Papers by H. Hertz*, Jones and Schott Macmillan London, 166-171, 1896.
- [130] P. Remington, J. Webb. Estimation of wheel/rail interaction forces in the contact area due to roughness. *Journal of Sound and Vibration* 193 (1996) 83–102.

- 
- [131] D.J. Thompson. The influence of the contact zone on the excitation of wheel/rail noise. *Journal of Sound and Vibration* 267 (2003) 523–535.
- [132] P.J. Remington. Wheel/rail noise IV: Rolling noise, *Journal of Sound and Vibration* 46 (1975) 419-436.
- [133] “Acoustics – Railway applications – Measurement of noise emitted by railbound vehicles”. ISO 3095-2013. Geneva: International Standards Organization.
- [134] F. Braghin, R. Lewis, R.S. Dwyer-Joyce, S. Bruni. A mathematical model to predict railway wheel profile evolution due to wear. *Wear* 261 (2006) 1253-1264.
- [135] K.L. Johnson. *Contact Mechanics*, Cambridge University Press.
- [136] S. Hao, L.M. Keer. Rolling contact between rigid cylinder and semi-infinite elastic body with sliding and adhesion. *Transactions of the ASME. Journal of Tribology* 129 (2007) 481-494.
- [137] F. Bucher, K. Knothe, A. Theiler. Normal and tangential contact problem of surfaces with measured roughness. *Wear* 253 (2002) 204-218.
- [138] K. Knothe. History of wheel-rail contact mechanics: from Redtenbacher to Kalker. *Vehicle System Dynamics* 46 (2008): 9-26.
- [139] B. Croft. The development of the rail-head acoustic roughness. University of Southampton, Doctoral Thesis, 2009.
- [140] L. Baeza, D.J. Thompson, G. Squicciarini, F.D. Denia. Method for obtaining the wheel-rail contact location and its application to the normal problem calculation through ‘Contact’. *Vehicle System Dynamics* 56 (2018) 1734-1746.
- [141] T.G. Pearce, N.D. Sherratt. Prediction of wheel profile wear, *Wear* 144 (1991) 343–351.
- [142] N. Correa, O. Oyarzabal, et al. Rail corrugation development in high speed lines. *Wear* 271 (2011) 2438–2447.
- [143] C.A. Brockley, P.L. Ko. An investigation of rail corrugation using friction-induced vibration theory. *Wear* 128 (1988) 99–106.
- [144] J.F. Archard, W. Hirst. The wear of metals under unlubricated conditions, *Proceedings of the Royal Society of London Series A. Mathematical and Physical Sciences* 236 (1956) 397–410.
- [145] W. Zhang, J. Chen, X. Wu, X. Jin. Wheel/rail adhesion and analysis by using full scale roller rig. *Wear* 26 (2002) 61-79.
- [146] O. Polach. Creep forces in simulations of traction vehicle running on adhesion limit. *Wear* 258 (2005) 992-1000.
- [147] N. Hoffmann, M. Fischer, R. Allgaier, L. Gaul. A minimal model for studying properties of the mode-coupling type instability in friction induced oscillations. *Mechanics Research Communications*, 29 (2002) 197-205.
- [148] N. Hoffmann, L. Gaul. Effects of damping on mode-coupling instability in friction induced oscillations. *ZAMM*, 83 (2003) 524-534.
- [149] I.L. Singer, H. Pollock. *Fundamentals of friction: acrosopic and microscopic processes*, Springer Science & Business Media, 2012.
- [150] K. Mannabe. A hypothesis on a wavelength fixing mechanism of rail corrugation. *Proceedings of the Institution of Mechanical Engineers Part F: Journal of Rail and Rapid Transit* 214 (2000) 21–26.
- [151] T.X. Wu, D.J. Thompson. Behaviour of the normal contact force under multiple wheel/rail interaction. *Vehicle System Dynamics* 37 (2002) 157-174.

- 
- [152] K. Hempelmann. Short pitch corrugation on railway rails: a linear model for prediction. VDI-Verlag, 1994.
- [153] P.J. Remington. Wheel/rail rolling noise: What do we know? What don't we know? Where do we go from here? *Journal of Sound and Vibration* 120 (1988) 203-226.
- [154] D.J. Thompson. Wheel-rail noise generation, Part IV: Contact zone and results. *Journal of Sound and Vibration* 161 (1993) 447-466.
- [155] D.J. Thompson, P. Fodiman, H. Mahe. Experimental validation of the TWINS prediction program for rolling noise, Part 2: results. *Journal of Sound and Vibration* 193 (1996) 137-147.